The Pennsylvania State University

The Graduate School

College of Engineering

Modeling and Control of Two-Phase Flow in Direct Methanol Fuel Cells

A Dissertation in

Mechanical Engineering

by

Seung Hun Jung

Submitted in Partial Fulfillment
of the Requirements
for the Degree of

Doctor of Philosophy

August 2010

The dissertation of Seung Hun Jung was reviewed and approved* by the following:

Chao-Yang Wang
Distinguished Professor of Mechanical Engineering
Distinguished Professor of Chemical Engineering
Professor of Material Science and Engineering
Dissertation Advisor
Chair of Committee

John M. Cimbala
Professor of Mechanical Engineering

Seungjin Kim
Assistant Professor of Mechanical and Nuclear Engineering

Michael A. Hickner
Assistant Professor of Materials Science and Engineering

Karen A. Thole
Department Head of Mechanical and Nuclear Engineering
Professor of Mechanical Engineering

* Signatures are on file in the Graduate School

ABSTRACT

A direct methanol fuel cell (DMFC) involves two-phase flow on both anode and cathode sides. On the anode side, methanol-water solution is oxidized to produce carbon dioxide (CO_2), whereas gaseous oxygen from air is reduced to form liquid water on the cathode side. Prediction and control of two-phase flow is of paramount importance for performance and fuel efficiency of DMFC in portable application. This dissertation aims to accurately predict and control two-phase flow in the channel and porous media of a DMFC to enable novel design and selection of components.

CO_2 gas produced during methanol oxidation reaction in a DMFC is the reason for the two-phase flow in the anode. This CO_2 gas is typically removed through the anode channel for steady cell operation, which makes a strong two-phase flow in the anode channel. As this channel two-phase flow causes a large pressure drop which is not desired, the present work modeled a CO_2 breathing DMFC which directly vents CO_2 to the ambient through the porous surface film. Although the CO_2 breathing DMFC shows similar cell performance with the conventional DMFC, the net power throughput and the system efficiency are improved since required pumping power is reduced due to reduced anode pressure. The role of CO_2 in controlling water and methanol transport in a DMFC is elucidated with a computational method for the first time. It is found that the amount of CO_2 in the anode (CO_2 level) determines capillary diffusion which dominates water transport in a DMFC. In addition, the multi-D DMFC model explains that methanol is transported not only by molecular diffusion but also by capillary diffusion in the anode porous media, and both transport mechanisms are strong functions of the CO_2 level.

The present study predicted a significant cell performance loss due to severe non-uniform distribution of methanol concentration under ultra-low anode stoichiometry condition. After identifying the controlling parameters of the anode non-uniformity, two strategies to mitigate the anode non-uniformity and to boost cell performance as well as fuel efficiency are proposed. First, streamline-graded structures (SGS) which control methanol transfer resistance are devised and studied through a statistical analysis. Second, an interdigitated fuel distributor which converts the fuel transport mechanism from diffusive to convective is developed. It is found that cell performance and fuel efficiency are improved by mitigating fuel concentration non-uniformity due to reduced methanol crossover in the inlet region and improved fuel supply in the outlet region.

TABLE OF CONTENTS

LIST OF FIGURES

LIST OF TABLES

Nomenclature

Acronyms and abbreviations

A	area (m^2)
a	specific reaction are (1/m), activity
ABP (abp)	anode bipolar plate
ACL (acl)	anode catalyst layer
AGDL (agdl)	anode gas diffusion layer
AMPL (ampl)	anode micro-porous layer
C	molar concentration (mol/m^3)
CBP (cbp)	cathode bipolar plate
CCL (ccl)	cathode catalyst layer
CGDL (cgdl)	cathode gas diffusion layer
CMPL (cmpl)	cathode micro-porous layer
D	diffusivity (m^2/s)
F	Faraday constant, force
g	Gibbs free energy (kJ/kg), gravity (m/s^2)
G	mass flux (kg/m^{2}s)
h	enthalpy (kJ/kg)
i, I	current density (A/m^2 or mA/cm^2), current (A)
j	mass flux (kg/m^{2}s), phase diffusion flux (mol/m^{2}s), volumetric transfer current density (A/m)
K	permeability (m^2)
m	mass (kg)
M	molar weight (g/mol), mol concentration (mol/L)
MEM (mem)	membrane
N	molar flux (mol/m^{2}s)
p	pressure (Pa)
R	gas constant
s	liquid saturation, entropy
S	volumetric source term
u	velocity (m/s)
T	temperature (K)
v	specific volume (m^3/kg)
V	volume (m^3)
W	mass flow rate (kg/s), width (m)
x	quality

Y	species mass fraction

Greek letters

α	water transfer coefficient, void fraction, transfer number
ε	porosity
δ	thickness
κ	ionic conductivity
ρ	density
τ	shear stress
γ	advection correction factor
η	overpotential, efficiency
Φ	potential
θ	angle
λ	mobility, water content
σ	surface tension
μ	dynamic viscosity (N-s/m^2)
ν	kinematic viscosity (m^2/s), molar stoichiometry number

Superscript and subscript

a	anode
c	cathode, contact
capill	capillary
d	drag
diff	diffusion
e	electrolyte phase
eff	effective
g	gas
k	species
l	liquid
m	mass
mem	membrane, methanol
ref (or 0)	reference
s	solid phase
u	velocity
tot	total
xover	crossover

Acknowledgments

I am most grateful and indebted to my thesis advisor, Professor Chao-Yang Wang, for the invaluable guidance and encouragement he has shown me during my time at Penn State. I thank my other committee members, Professor John M. Cimbala, Professor Seungjin Kim and Professor Michael A. Hickner for their service on my doctoral committee and for their suggestions and insightful comments on my thesis work.

I thank my family for their love, support and understanding, and for making it possible to complete my research.

Finally, I would also like to thank ECEC members and all others who were not mentioned above and have given me all kinds of help that contributed to the success of this work.

Seung Hun Jung

Chapter 1

Introduction

1.1 Background and Motivation

Keeping pace with the advancing speed of information technologies, demands for portable power sources are increasing. However, conventional batteries which are widely used as portable power sources reveal the limitation. As batteries are not power generators but energy storage devices, they need to be replaced once the power is depleted or recharged by nearby rechargers. People who require extensive portable power sources, for example, military soldiers carrying out missions or wilderness expeditions must carry many Li-ion batteries with them. Those batteries are heavy, bulky and expensive. It is considered that portable fuel cells may replace batteries in the future because fuel cells can operate continuously as far as fuel supply lasts. The direct methanol fuel cell (DMFC) is a promising candidate for future portable power source since it uses liquid fuel which has high volumetric energy density.

Although much research on DMFC has been conducted, there are still several obstacles to overcome before commercializing DMFC. O'Hayre *et al.* [1] stressed four methods to improve cell performance based on Eq. (1-1) describing the exchange current density.

$$i_{o} = nFC_{R}f_{1}e^{-\Delta G_{1}/(RT)} \tag{1-1}$$

i) Decrease the activation barrier ΔG_{I} by increasing catalyst loading

ii) Increase the reactant concentration C_{R}

iii) Increase the cell temperature; T

iv) Increase the number of possible reaction sites

Although the above four methods are applicable to hydrogen PEMFC, there are several problems when they are applied to DMFC, as follows.

Method *i*): Currently, most DMFC use several times higher amounts of catalyst loading than hydrogen PEMFC because anode reaction kinetics of methanol in DMFC is very sluggish compared to the hydrogen reaction rate of PEMFC. Reducing novel catalyst loading or replacing it with other less expensive catalysts is an important issue to reduce manufacturing cost for DMFC.

Method *ii*): Figure [1-1] shows the polarization curve of DMFC compared to that of hydrogen PEMFC. Significant voltage loss from fuel (methanol) crossover through the membrane is observed in DMFCs. As the anode reaction is dominated by 0th order reaction when methanol concentration is greater than the threshold value (around 0.1 M), increasing methanol concentration near the anode catalyst layer (ACL) degrades the cell performance by mixed potential loss on the cathode side. Moreover, as methanol crossover degrades fuel efficiency of DMFC by combustion on the cathode side, this is considered as the top priority to resolve before commercializing DMFC.

Method *iii*): Although high temperature is good for activating reactions, it also increases methanol crossover by increasing methanol diffusion. Therefore, typical DMFC operate at low temperature range (around 60 °C).

Water management is another important issue to solve. In contrast to hydrogen PEM fuel cells (PEMFC), DMFC need water as reactant on the anode side. DMFC systems will not be sustainable if water is being lost on the cathode side and it is difficult to replenish water frequently. Therefore, much research is under way to prevent water loss.

In order to apply DMFC to portable devices, DMFC system size should be as small as possible. To reduce system size, we should carefully control two important gases. One is CO_2, a byproduct of methanol oxidation reaction (MOR) on the anode side. The other is oxygen necessary for oxygen reduction reaction (ORR) on the cathode side. Gas management is closely related to the channel design. Channel size is an important design parameter. Although a thin channel will help in reducing the entire system size, it may cause trouble in removing CO_2 or water droplets in the channel. Therefore, removing CO_2 effectively from DMFC and supplying air effectively to DMFC is the key to success in building compact DMFC. Table [1-1] is a summary of major issues to resolve before future commercialization of DMFC.

1.2 Principles of DMFC Operation

1.2.1 DMFC structure

Figure [1-2] shows a schematic of DMFC configuration. Similar to typical batteries, the DMFC has anode, cathode and electrolyte. The major structural difference from conventional batteries is the anode/cathode channels which supply fuel and oxidizer continuously from external source to reaction sites, making the fuel cell a power generator, not an energy storage device.

Roughly, conventional DMFC consist of membrane electrode assembly (MEA) and current collectors (or bipolar/monopolar plates) which are usually made of graphite to enhance electron transport and prevent corrosion. Flow channels are machined into the bipolar plates and there are several kinds of shapes depending on their purposes. Although the parallel shaped flow field induces less pressure drop than serpentine channel (in particular, large pressure drop occurs in anode channel due to two-phase flow), CO_2 slugs may cause clogging in some regions and this may lead to dead channels. Hence, most DMFC adopt serpentine channels because of CO_2 removal problems, even though there are several advantages in parallel channels.

MEA consist of gas diffusion layer (GDL), catalyst layers (CL) and membrane. Depending on the cell design, micro porous layer (MPL) can be inserted between CL and GDL. GDL made of porous conducting materials such as carbon paper (or carbon cloth) performs two important roles. One is to facilitate mass transport of fuel, oxidizer and byproduct on each side. The other is to serve as a bridge for electron transport between bipolar plate and catalyst layer.

The catalyst layer is where electrochemical reactions occur. Electrochemical reaction is an interfacial phenomenon and takes place only in the triple phase boundary that includes electrolyte, catalyst and molecules in DMFC. For this purpose, the catalyst layers consist of a complex mixture including catalyst. Typically, Platinum (Pt) is used as the base catalyst which reduces the activation energy of reactants and it is supported by carbon to increase the effective area. In the anode of DMFCs, additional catalyst such as Ruthenium (Ru) is added to mitigate CO poisoning. As the catalyst layer must conduct not only electrons but also protons, ionomers such as Nafion® is added to catalyst layer.

In order to alleviate methanol crossover and water loss through the membrane, MPL can be inserted between catalyst and GDL. It is known that MPL helps to reduce contact resistance between GDL and catalyst layer also.

Electrolyte, usually called membrane in DMFC or PEMFC, plays an important role as a proton conductor and as an anode/cathode separator to divert electron flow to external load in order to generate useful electricity by blocking electrons from moving directly from anode to cathode. Desirable membrane characteristics are mechanical/chemical durability, electrical insulation and high ionic conductivity. In addition, especially for DMFC, low methanol permeability is required. As Nafion® has good durability and high ionic conductivity when hydrated, due to the hydrophilic property of sulfonic acid group (HSO_3), Nafion® is widely used as a membrane material for PEMFC and DMFC. However, its high methanol permeability causes poor fuel efficiency and prompts many researchers to develop other kinds of material for DMFC membranes.

1.2.2 Principle of DMFC operation

In order to operate a DMFC, liquid fuel mixture (water and methanol) is supplied to the anode channel by forced feeding using mechanical pump (or passive feeding using a cartridge). Although dilute fuel mixture (around 2 M or 2000 mol/m^3) is used to reduce methanol crossover, neat methanol will be ideal to maximize fuel density and minimize total system size. Air is supplied to cathode by forced feeding using a fan or passive feeding (air-breathing), depending on the cell design. Fuel mixture in the anode channel diffuses into the anode catalyst layer via gas diffusion layer. In the anode catalyst layer, methanol and water react to form protons and electrons with gaseous CO_2, which is called methanol oxidation reaction (MOR). Protons produced in the anode catalyst layer move

directly through electrolyte to react with oxygen in the cathode catalyst layer, and electrons move to current collector via gas diffusion layer which has large electron conductivity. As gas hardly penetrates solid electrolyte, produced gaseous CO_2 is removed through the anode channel, which induces strong two-phase flow. Supplied oxidizer (typically air) combines with protons coming from the membrane and electrons coming from the current collector to form water molecules in the cathode catalyst layer, which is called oxygen reduction reaction (ORR). Electric power is generated and transferred to a load while electrons form an outer circuit connecting anode and cathode. Eq. (1-2) shows overall reactions occurring in DMFC.

$$
\begin{array}{ll}
CH_3OH + H_2O \rightarrow CO_2 + 6H^+ + 6e^- & \text{(MOR)} \\
6H^+ + 6e^- + \dfrac{3}{2}O_2 \rightarrow 3H_2O & \text{(ORR)} \\
\hline
CH_3OH + \dfrac{3}{2}O_2 \rightarrow 2H_2O + CO_2 & \text{(Overall)}
\end{array}
\tag{1-2}
$$
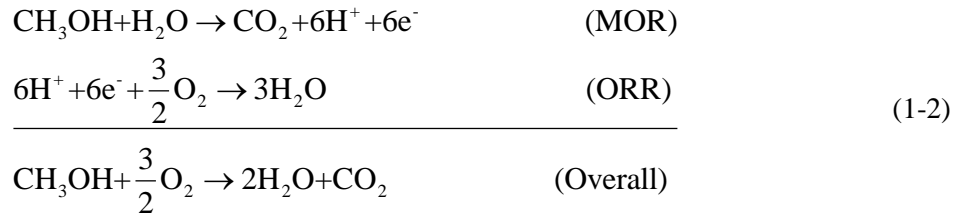
1.2.3 Important parameters

Water is a necessary reactant in MOR and plays an important role to dilute liquid fuel to mitigate methanol crossover through the membrane. Therefore, water management in DMFC is as important as that of PEMFC in order to achieve water balance through the membrane for steady operation. Water balance through the membrane can be expressed by 'water transport coefficient (α)' defined in Eq. (1-3) [2]. Water transport coefficient consists of three terms: electro-osmosis drag (EOD) term, water diffusion term and hydraulic permeation term. As the net proton flow moves from the anode to cathode, EOD term is always positive. Water diffusion is governed by water concentration gradient, and hydraulic permeation is determined by capillary pressure gradient across the

membrane. Therefore both of them will be determined by water content distribution across the membrane, which means diffusion term and hydraulic permeation term could be positive or negative in Eq. [1-3] depending on MEA design and operating conditions. By examining the water transport coefficient, we can find out whether water is being lost or gained on each anode or cathode side. Experimentally, water transport coefficient can be found by measuring water coming from cathode channel.

$$\alpha \ = \ N_{mem}^{H_2O} \frac{F}{i} = (N_{mem,EOD}^{H_2O} + N_{mem,diff}^{H_2O} + N_{mem,pl}^{H_2O}) \frac{F}{i} = n_d^{H_2O} + \alpha_{mem,diff} + \alpha_{mem,pl} \qquad (1\text{-}3)$$

$$\text{where} \begin{cases} n_d^{H_2O} = N_{m,EOD}^{H_2O} \dfrac{F}{i} = f(T) \\[2ex] \alpha_{m,diff} = N_{m,diff}^{H_2O} \dfrac{F}{i} = D_{mem}^{H_2O} \left(\dfrac{\rho_{mem}}{EW_{mem}} \right) \dfrac{d\lambda}{dx} \dfrac{F}{i} \ = D_{mem}^{H_2O} \left(\dfrac{\rho_{mem}}{EW_{mem}} \right) \left(\dfrac{\lambda_a - \lambda_c}{\delta_{mem}} \right) \dfrac{F}{i} \\[3ex] \alpha_{m,pl} = N_{m,pl}^{H_2O} \dfrac{F}{i} = \left(\dfrac{\rho_l K_{mem}}{M_1 \mu_1} \right) \left(\dfrac{p_{l,a} - p_{l,c}}{\delta_{mem}} \right) \dfrac{F}{i} \end{cases}$$

Crossover current density measures the amount of methanol crossed over through the membrane. Therefore, crossover current density expresses fuel efficiency of DMFC. Electro-osmosis drag, diffusion and hydraulic permeation (convection) contribute to the methanol crossover (as dilute fuel mixture is assumed, convection term is neglected here). The crossover current density is defined as follows:

$$i_{xover} = 6FN_{mem}^{MeOH}$$
$$\text{where} \quad N_{mem}^{MeOH} = \frac{i_{xover}}{6F} = n_d^{MeOH} \frac{i}{F} + D_{mem}^{MeOH} \frac{C_{acl}^{MeOH}}{\delta_{mem}} \qquad (1\text{-}4)$$

Electro-osmosis drag coefficient of methanol shown in the above equation is correlated with water concentration as follows:

$$n_d^{\text{MeOH}} = n_d^{\text{H}_2\text{O}} \frac{C_1^{\text{MeOH}}}{C_1^{\text{H}_2\text{O}}} \tag{1-5}$$

Another way to express fuel efficiency of DMFC is methanol crossover rate (MCO) defined as follows:

$$MCO = \frac{i_{\text{xover}}}{i + i_{\text{xover}}} \tag{1-6}$$

1.2.4 Thermodynamics and efficiency

Table [1-2] compares thermodynamics data between hydrogen PEFMC and DMFC. The thermodynamic standard state reversible voltage in Table [1-2] is calculated as follows:

$$E^0 = -\frac{\Delta g}{nF} = -\frac{\Delta h - T\Delta s}{nF} \tag{1-7}$$

Thermodynamic reversible voltage changes depending on temperature, pressure and species concentration, which is called non-standard state reversible voltage as is expressed as follows considering Nernst equation:

$$E = E^T - \left[\frac{RT}{nF}\right] \ln \frac{\Pi a_{\text{products}}^{\upsilon_k}}{\Pi a_{\text{reactants}}^{\upsilon_k}} \tag{1-8}$$

$$\text{where } E^T = E^0 + \frac{\Delta s}{nF}\left(T - T^0\right)$$

The maximum possible electrical work that can be extracted from the total chemical energy is $W_{\text{elec}} = -\Delta g$. Thus, we define the thermodynamic efficiency of a fuel cell as follows:

$$\eta_{\mathrm{rev}} = \frac{\Delta g}{\Delta h} = -\frac{nFE}{\Delta h} \qquad (1\text{-}9)$$

However, actual voltage is much lower than this reversible voltage because of several voltage losses like ohmic loss, concentration loss and activation loss. Thus, we use a more practical expression as follows:

$$\eta_{\mathrm{voltaic}} = \frac{V_{\mathrm{cell}}}{E} \qquad (1\text{-}10)$$

As we discussed previously, there is fuel loss due to methanol crossover in DMFC. So we define fuel efficiency as follows:

$$\eta_{\mathrm{fuel}} = \frac{i}{i + i_{\mathrm{xover}}} \qquad (1\text{-}11)$$

Part of power generated by the cell is used for driving the system such as fuel pumping and air blowing. So we define the mechanical efficiency as follows:

$$\eta_{\mathrm{mech}} = \frac{W_{\mathrm{cell}} - W_{\mathrm{a}} - W_{\mathrm{c}}}{W_{\mathrm{cell}}} \quad \text{where} \begin{cases} W_{\mathrm{cell}} = IV & \text{(cell power output)} \\ W_{\mathrm{a}} = \Delta p_{\mathrm{a}} u_{\mathrm{a}} A_{\mathrm{a}} & \text{(fuel pumping power)} \\ W_{\mathrm{c}} = \Delta p_{\mathrm{c}} u_{\mathrm{c}} A_{\mathrm{c}} & \text{(air pumping power)} \end{cases} \qquad (1\text{-}12)$$

Finally, the total energy efficiency of a fuel cell can be expressed by:

$$\eta = \eta_{\mathrm{rev}} \eta_{\mathrm{voltaic}} \eta_{\mathrm{fuel}} \eta_{\mathrm{mech}} \qquad (1\text{-}13)$$

In order to increase the total fuel cell efficiency, we must increase operating cell voltage and decrease crossover current density.

1.3   MEA Design for Portable DMFC

Low-α MEA for modern DMFC are composed of several layers as shown in Figure [1-2]: two GDLs, two hydrophobic MPLs, two CLs and a proton exchange membrane (PEM). Desirable operating conditions for DMFC is to utilize highly concentrated methanol to increase energy density with low stoichiometry to minimize parasite arising from fuel pumping or air blowing. In order to achieve those goals, each component should be optimized to fulfill its role perfectly in harmony with other components. Major properties of each layer are *i*) thickness, *ii*) wettability, *iii*) porosity and permeability. As there are 7 components in a MEA, property combinations for experiments (or number of MEAs) will be huge. If we also consider operating conditions (cell temperature, fuel concentration, operating current density), the number of combinations will increase even more. Moreover, manufacturing MEAs requires much time, effort and cost. Hence, it is difficult to cover all cases of property combination by experiments. Numerical simulation will be a good tool to accomplish this.

1.4 CO_2 Management of DMFC

During electrochemical reaction in DMFC, water is produced in the cathode from ORR and CO_2 is produced in the anode from MOR as byproducts. In order to maintain steady cell operation, produced CO_2 should be removed from the cell. Produced CO_2 in the anode catalyst layer is basically in gas phase and typically removed through the anode channel of DMFC out of the cell (see Figure [1-2]). As liquid fuel mixture is supplied from the anode channel to porous layers, CO_2 removal occurs in counter-flow direction to the liquid flow. During this CO_2 removal process, it is known that CO_2 gas brings on

strong two-phase flow (bubbly flow or slug flow) in the anode channel as shown in Figure [1-3], which causes a large pressure drop along the anode channel and makes study of DMFC difficult. In addition, typically at high current density operation, CO_2 gas forms slugs which may block the interface between the anode channel and gas diffusion layer, which prevent the liquid fuel from spreading well into anode porous layers. For the above reason, it is important to consider CO_2 removal for channel design. For example, typical DMFC hardly uses parallel channels on the anode side, although parallel channels have advantages of less pressure drop or even species distribution than serpentine channels. The reason is possible CO_2 slugs that block some anode flow channels and may cause dead regions in the cell.

The liquid mixture in the anode channel is typically recycled in order to improve the fuel efficiency and to collect water. For those purposes, most of DMFCs have liquid/gas separator which makes the DMFC system complex and bulky.

Figure [1-4] shows experimental data of a DMFC operating at constant current densities. Large voltage fluctuations are found when the cell is operated at high current density. It is considered that this fluctuation is caused by two reasons. One reason might be flooding in the cathode. If liquid blocks the reaction site, reactant gas cannot reach there. Therefore, severe voltage drop can occur due to concentration loss. The other reason can be found on the anode side. Cyclic CO_2 bubble build-up and removal processes inside the cell can affect both methanol concentration loss (where methanol concentration is low) and methanol crossover (where methanol concentration is high). Although Liu *et al*. [3] achieved great success in improving cell performance by reducing methanol crossover with the application of micro-porous layers, their cell still shows this

voltage fluctuation. Definitely, this fluctuation is bad for the fuel cell as it reduces cell performance, power quality. For these reasons, it is desirable to quickly remove CO_2 in anode porous layers during cell operation at high current density in order to avoid cyclic phenomena of CO_2 removal. Several techniques have been proposed to remove gaseous CO_2 from the face of the bipolar plate, instead of accumulating in the anode channel. These include a hydrophobic porous plate, a perforated plate covered with highly hydrophobic GDL/MPL [4] and adding chemical agents which helps produced CO_2 to dissolve in liquid fuel [5]. However, is that still valid for cells operating at low or intermediate current densities? We cannot simply answer this question because there is the role of CO_2 in anode porous layers which is barely reported up to now. Actually, the amount of CO_2 in anode porous layers directly affects the methanol concentration and the saturation distribution in anode porous layers, which have a direct influence on the cell performance.

For the above reasons, it is important not only to develop efficient ways to remove CO_2 in the anode channel but also to investigate the role of CO_2 in DMFC in order to find out the optimum DMFC design and operating condition.

1.5   Operating DMFC with Ultra-Low Stoichiometry

Operating a DMFC with low flow rate is desirable to minimize the parasite loss arising from fuel pumping and air blowing. However, cell performance is strongly affected by the fuel flow rate (anode stoichiometry) and typically low stoichiometry leads to low cell performance or even cell shut-down. In order to achieve both high cell

performance and low parasite loss, we need to identify the details of fuel transport mechanism, especially under ultra-low stoichiometry condition.

1.6   Obstacles to Overcome for Commercialization of DMFC

As summarized in Table [1-1], many problems still remain to be solved before commercializing DMFC. Lu and Wang [6] focused on the energy density of DMFC to compete with lithium-ion battery in the future. They addressed four key challenges to overcome: *i*) low rate of methanol oxidation kinetics on the anode, *ii*) methanol crossover through the polymer membrane, *iii*) water management, and *iv*) heat management. A brief summary about efforts to overcome the above obstacles are introduced here.

Slow methanol oxidation problem

As the fuel mixture is supplied in the form of liquid phase which has a strong molecular bonding force, methanol oxidation is several times slower than the hydrogen oxidation in PEMFCs. Therefore, significant voltage loss occurs due to the kinetic loss in the anode (around 0.3 ~ 0.4 V). In order to promote the methanol oxidation or to reduce the activation barrier, large amount of catalyst is used for DMFCs. Typically, the anode catalyst loading of a DMFC is around 5 mg/cm^2 which is 10 times larger amount compared to a typical PEMFC. As carbon monoxide (CO) which strongly poisons platinum (Pt) catalyst may evolve during MOR, typically ruthenium (Ru) is added to the anode catalyst compound. Many material scientists are working on developing more active catalyst to reduce the catalyst loading and cell manufacturing cost.

Methanol crossover problem

One of serious problems of DMFC is methanol crossover through the membrane. In order to reduce methanol crossover, various approaches have been tried experimentally and numerically to date. Developing new membrane material could be one such approach. As widely used Nafion® has relatively high methanol permeability, some other polymers (polyamides, poly ether imides, polysulphones etc.) [7] or hydrocarbon-based materials are being investigated although they have relatively low ionic conductivity at present. Applying composite membrane can be another option. Bauer *et al.* [8] suggested a hybrid membrane made of zirconium and phosphate which showed low methanol permeability and high water permeation. However, the ideal membrane for DMFC which has low methanol permeability and high ionic conductivity has not yet been developed. Recently, those technical problems are being approached from a different standpoint: fundamental study of cell design and operating method. Liu and Wang [3] modified the conventional DMFC design by using a catalyzed diffusion medium (CDM) on the anode side to act as a methanol diffusion barrier in order to reduce methanol crossover, which has proven very effective. Combining micro-porous layer on the anode side with thin membrane (Nafion®112) proved to be an effective way to reduce methanol crossover [9].

Water management

For DMFC, water is as important a reactant as methanol to build MOR in the anode catalyst layer. One typical method to supply water to the anode catalyst layer is using fuel mixture made of methanol and water. In this case, fuel mixture should be very dilute (less than 10 M) to suppress methanol crossover. One problem from this dilute solution is

its low energy density due to large portion of water, which makes the DMFC system bulky. In order to develop a compact DMFC system, highly concentrated methanol is desirable. Another problem is loss of anode side water to the cathode side due to water diffusion, electro-osmosis and hydraulic permeation through membrane. In order to prevent losing water to the cathode, using additional MPL between cathode catalyst layer and cathode diffusion medium was discussed by Pasaogullari and Wang [10]. This cathode MPL blocks water flux moving from cathode catalyst layer to cathode diffusion media and it builds hydraulic pressure to induce water backflow to the anode. However, if water content is too high in the cathode catalyst layer (cathode flooding), oxygen supply to the cathode catalyst layer will be blocked by liquid water and the cell will suffer from cathode concentration loss. On the contrary, if water content is too low in the cathode catalyst layer, cathode resistance will increase too much and cell performance will decrease again. Therefore, it is important to balance water in DMFC. All efforts to solve water problems listed above are called water management. Liu *et al.* [3] stressed the importance of water management in DMFC. They inserted a hydrophobic cathode MPL between the cathode catalyst layer and cathode diffusion medium and achieved good experimental results showing small α (less than 0.8) at 60 °C with 3 M methanol solution. Combining with catalyzed diffusion medium on the anode side, they attained cell voltage of 0.4 V with power density of 60 mW/cm^2 maintaining high fuel efficiency around 80%. Liu and Wang [11] studied the effect of anode MPL properties on water/methanol crossover. They found that wettability of the anode MPL has a dramatic effect on water crossover through the membrane.

Passive DMFC systems

Adopting vapor-fed fuel delivery system with highly concentrated methanol could be helpful to increase energy density of a DMFC. MTI MicroFuel Cells Inc. disclosed their technique using vapor feed DMFC [12-14]. They invented a passive fuel delivery system using polydiymethlysiloxane (PDMS) membrane. PDMS membrane has an ability to selectively transport organic molecules (methanol) while it blocks polar molecules (water). Absorbed liquid methanol from the fuel tank vaporizes when it leaves the other side of the PDMS membrane. The methanol vapor chamber facing the anode diffusion medium could maintain about 1.0 M methanol concentration, low enough to hold methanol crossover. However, it was difficult for this passive system to control fuel delivery to achieve steady operation of DMFC. In addition, when liquid methanol vaporizes, the temperature of the membrane drops, causing water vapor to condense and build water film on the surface of the anode diffusion medium. Faghri's group carried out intensive study of vapor-fed DMFC experimentally and numerically [15-16]. Basically, their concept of vapor feeding is a modification of MTI's design. In order to prevent temperature drop in evaporation pad from latent heat loss, they added heating source on the evaporation pad. Instead of using dilute fuel solution, they used a fuel tank that contains neat methanol and a water tank. Wicks from each tank are connected to the vapor chamber to make a vapor mixture of methanol and water. However, their cell still shows low power density (lower than 16 mW/cm^2) compared to the forced feed DMFC.

1.7 Objectives of the Present Research

This study aims to predict and control two-phase flow in a DMFC and subsequently suggest novel cell designs as well as use of new materials and components.

Firstly, the baseline two-phase, non-isothermal DMFC model will be introduced, which has the newly implemented capability such as, *i*) simulating saturation jump at the interface of two different porous media, *ii*) simulating non-isothermal behavior such as latent heat effect and thermal diffusion, and *iii*) simulating full-scale DMFCs.

Secondly, the CO_2 breathing DMFC which can build pure liquid flow in the anode channel by venting CO_2 gas directly to the ambient through the surface film will be introduced. The role and effect of CO_2 on the cell performance will be investigated for the first time.

Thirdly, the fundaments of the anode non-uniformity which is crucial for the cell operation under ultra-low stoichiometry condition will be enlightened. Subsequently, strategies to mitigate the anode non-uniformity and to boost cell performance and fuel efficiency will be discussed.

Finally, summary and future work will be presented.

TABLES

Table [1-1]   Obstacles to overcome before commercialization of DMFC

Category	Problems	Consequences
Anode catalyst	Methanol oxidation kinetics	Large amount of catalyst loading is required
	Catalyst poisoning	Reduces DMFC lifetime
Cathode catalyst	Oxygen reduction kinetics	Large amount of catalyst loading is required
	Catalyst poisoning	Reduces DMFC lifetime
Membrane	Methanol crossover	Degrade cell performance, fuel efficiency
	Low ionic conductivity	Degrades cell performance
Water management	Low concentrated fuel	Volumetric energy density of DMFC is low
	Large water crossover	Not sustainable for steady operation
Fuel management	Low flow rate is required	Not sustainable for steady operation
Gas management (anode)	CO_2 removal	Causes strong two-phase flow Large anode stoichiometry, voltage fluctuation
Gas management (cathode)	Air supply	Pumping power is required Mechanism becomes complex and bulky

Table [1-2]   Thermodynamic data of fuel cell reactions at 25℃ 1atm [17]

Reaction	T(K)	Δg (kJ/kg)	Δh (kJ/kg)	Δs (kJ/kgK)	n	ΔE (V)	η_{rev}
PEFC	298	-237	-285	-162	2	1.23	0.83
DMFC	298	-704	-727	-77	6	1.21	0.97

PEFC: $H_2 + 1/2O_2 \rightarrow H_2O$ DMFC: $CH_3OH + 3/2O_2 \rightarrow CO_2 + H_2O$

FIGURES
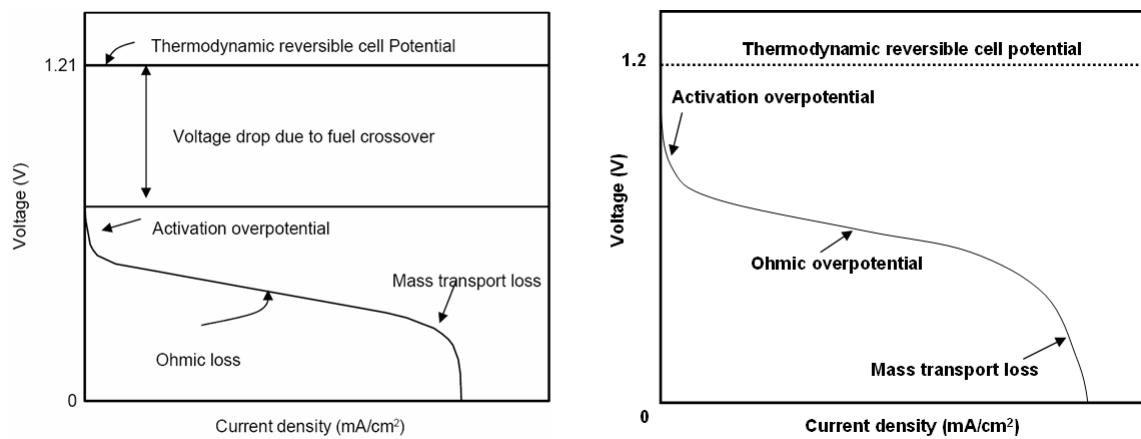
Figure [1-1]   Performance comparison between DMFC (left [18]) and PEMFC (right)

1.	Anode bipolar plate	6.	Cathode bipolar plate
2.	Anode diffusion layer	7.	Cathode diffusion layer
3.	Anode micro-porous layer	8.	Cathode micro-porous layer
4.	Anode catalyst layer	9.	Cathode catalyst layer
5.	Membrane		
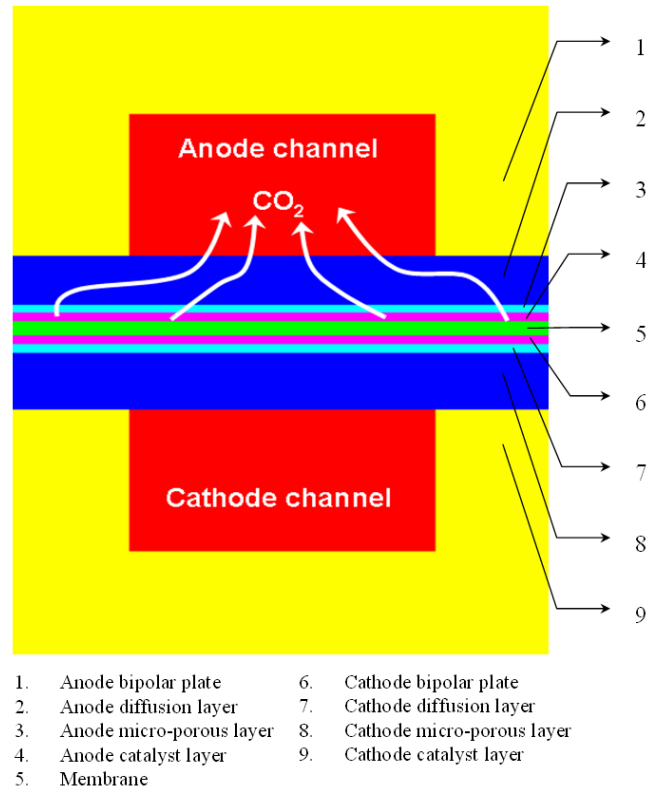
Figure [1-2]   Schematic of a typical DMFC structure
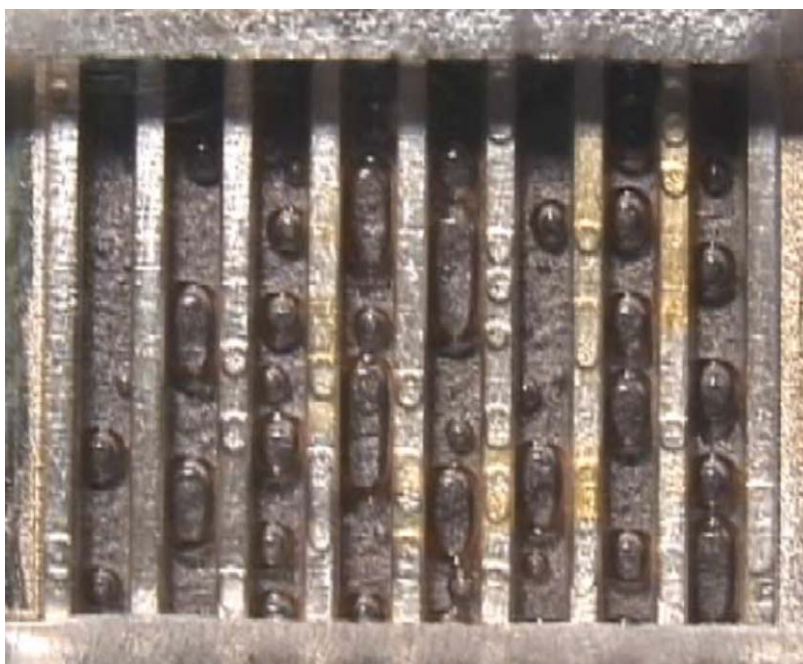
Figure [1-3]   CO$_2$ bubbles in anode channel with hydrophobic carbon paper [34]
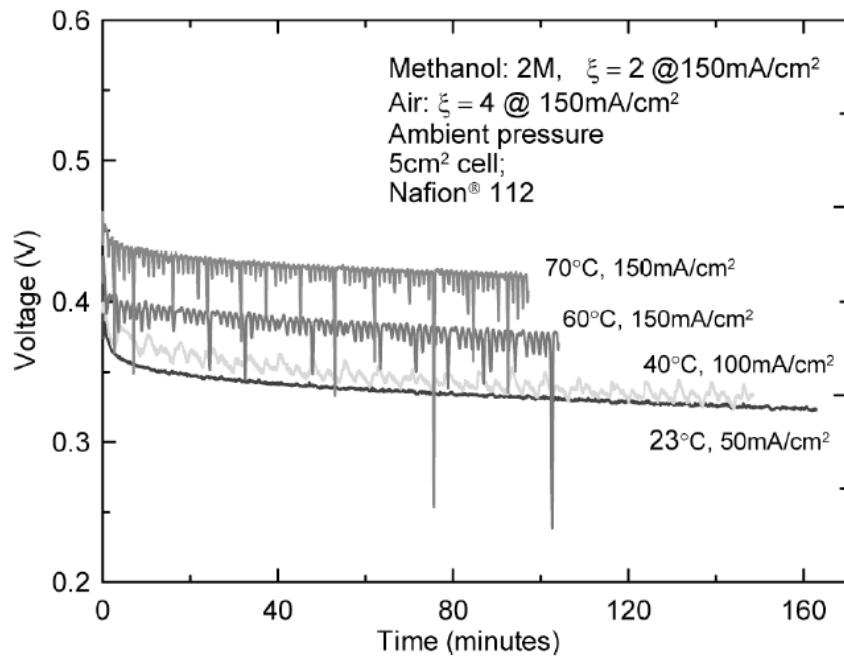
Figure [1-4]   Evolution in cell voltage during constant current loading [9]

Chapter 2

Non-Isothermal Multi-D Model with Micro-Porous Layers to Mitigate Water/Methanol Crossover

2.1 Introduction

Inside a direct methanol fuel cell (DMFC) several transport phenomena related to electrochemical reactions occur simultaneously. The methanol oxidation reaction (MOR) occurs in the anode, whereas the oxidation reduction reaction (ORR) occurs in the cathode. One mol of water species is consumed by MOR in the anode and three mol of water is produced by ORR in the cathode (see Eq. [1-2]). Therefore, theoretically, it is possible to operate a DMFC without any external water supply from the anode side because the water production is greater than the water consumption. This is very desirable because users should carry only pure methanol without water, which significantly reduces the volume and weight of the DMFC system. However, in reality, a large amount of water is supplied to the anode side to prevent methanol crossover and a large amount of water is lost due to water crossover (positive α value). Therefore, many studies about reducing α value have been conducted, experimentally and numerically.

In order to construct an ideal DMFC which has negative α value, it is important to know the fundamentals of transport phenomena which occur three-dimensionally in a DMFC. Many experimental studies about these transport phenomena in fuel cells have been conducted. However, there is limitation of fuel cell experiments because it is difficult to visualize and measure the species transport inside porous media of a fuel cell, which three-dimensionally occurs in very small scale (thickness of typical porous media

is around 0.3 mm). The multi-dimensional fuel cell model incorporated with computational fluid dynamics (CFD) is a powerful tool for understanding the fundamentals of transport phenomena in a fuel cell.

Multi-dimensional DMFC model framework was firstly established by Wang and Wang [19]. Their model was two-dimensional and isothermal. Liu and Wang [20] extended two-dimensional model to three-dimensional but it was still an isothermal model. Capability of non-isothermal modeling is important for predicting non-uniform behavior such as evaporation/condensation of water and latent heat effect on heat removal in a fuel cell. In addition, both previous models did not consider the effect of micro-porous layer which is proved to be very effective for minimizing water/methanol crossover by generating saturation jumps at the interface of two different porous media.

In this chapter, first, we introduce the two-phase non-isothermal multi-dimensional DMFC model, which is developed to identify and simulate transport phenomena and to predict cell performance and fuel efficiency. Second, with the developed model, effect of micro-porous layer on water/methanol crossover is simulated and visualized by applying saturation jump model. Third, non-isothermal behavior such as cathode side heat removal by heat-pipe effect is simulated and discussed. Finally, full-scale DMFC models simulating actual DMFCs are introduced with experimental validation.

2.2   Physical Model

The present multi-D DMFC model is extended from the work by Liu and Wang [20] and based on the M^2 formulation of Wang and Cheng [21]. Important extended capabilities are saturation jump, non-isothermal behavior and large-scale simulation with

parallel processing. Basic assumptions for the model are: *i*) ideal gas law, *ii*) laminar flow, and *iii*) homogeneous flow in the channels.

The structure of the single channel DMFC is shown in Figure [2-1] and [2-2] which is created for multi-D simulation. On the anode side, liquid fuel mixture is introduced from the inlet of the anode channel by a liquid pump. Introduced liquid fuel is transported to the anode GDL surface and spread throughout the anode porous media, then consumed in the anode catalyst layer by MOR. On the cathode side, oxidizer (typically air) is introduced from the inlet of the cathode channel by a blower. Introduced oxidizer diffuses throughout the cathode porous media and it is consumed in the cathode catalyst layer by ORR.

2.2.1 *Governing equations*

The present multi-D model consists of six coupled PDEs (mass, momentum, species, proton transport, electron transport and heat equations) with source terms as summarized in Appendix A. Constitutive relationships, important parameters and cell geometry of the baseline cell are listed in Appendix B and C, respectively.

Mass continuity equation

The following mass continuity equation is used for channels and porous media in the present multi-D model. There is no mass flow in both solid bipolar plates.

$$\nabla \cdot (\rho \vec{u}) = \dot{m}'''$$

(2-1)

There are mass sinks and sources in the catalyst layers where electrochemical reaction occurs as follows:

$$\dot{m}_{acl}''' = M^{MeOH}S^{MeOH} + M^{H_2O}S^{H_2O} + \frac{M^{CO_2}j}{6F}$$

$$\dot{m}_{ccl}''' = M^{H_2O}S^{H_2O} + M^{O_2}S^{O_2} + \frac{M^{CO_2}j_{xover}}{6F}$$

(2-2)

Anode mass source term ($\dot{m}_{acl}'''$) consists of methanol consumption, water consumption and CO_2 production whereas cathode mass source term ($\dot{m}_{ccl}'''$) consists of water production, oxygen consumption and CO_2 production due to methanol crossover.

Momentum equation

In the flow channels, a conventional Navier-Stokes type equation is applied, whereas Darcy's law is applied in the porous media as follows:

$$\nabla \cdot (\rho \vec{u}\vec{u}) = -\nabla p + \nabla \cdot \vec{\tau} + S^u$$

where $S^u = -\dfrac{\mu}{K}\vec{u}$ (in porous media domain)

(2-3)

Generic species equation

A general form of multi-phase species equation by M^2 model [21] can be expressed as follows:

$$\nabla \cdot (\gamma \rho \vec{u} Y^k) = \nabla \cdot \left[\rho_l D_{l,eff}^k \nabla Y_l^k + \rho_g D_{g,eff}^k \nabla Y_g^k \right] - \nabla \cdot \left[\left(Y_l^k - Y_g^k \right) \vec{j}_l \right] + M^k S^k$$

(2-4)

The left term represents convectional term which is significant in the flow channel region. The first term on the right hand side represents the molecular diffusive term and the second term is phase-diffusive term or capillary flux, which is significant in the porous region. As the molecular diffusion is strongly affected by porosity and each phase volume (saturation), the following semi-empirical relationships are used in the present model.

$$D_{l,eff}^{k} = D_{l}^{k} s^{n} \varepsilon^{n}$$

$$D_{g,eff}^{k} = D_{g}^{k} (1-s)^{n} \varepsilon^{n}$$

$$\text{where } \varepsilon = \frac{V_{pore}}{V}$$

(2-5)

Liquid saturation shown above is defined as follows [21]:

$$s = \frac{V_{l}}{V_{pore}} = 1 - \frac{V_{g}}{V_{pore}} = \frac{\rho_{g} Y^{k} - \rho_{g} Y_{g}^{k}}{\rho_{l} Y_{l}^{k} - \rho_{l} Y^{k} + \rho_{g} Y^{k} - \rho_{g} Y_{g}^{k}}$$

(2-6)

Capillary flux of liquid phase shown in Eq. (2-4) is calculated by Darcy's law as follows:

$$\vec{j}_{l} = \frac{\lambda_{l} \lambda_{g} K}{\nu} \nabla p_{c}$$

(2-7)

Note that capillary flux is driven by capillary pressure gradient that is defined as follows:

$$p_{c} = p_{g} - p_{l} = \sigma \cos \theta_{c} \left(\frac{\varepsilon}{K} \right) J(s)$$

(2-8)

Leverette's *J*-function (see Appendix A) shown up above equation empirically expresses that capillary pressure is a function of liquid saturation and λ_{l} and λ_{g} express relative mobility of liquid and gas, respectively.

$$\lambda_{l} = \frac{K_{rl}}{\nu_{l}} \nu = \frac{K_{rl}/\nu_{l}}{K_{rl}/\nu_{l} + K_{rg}/\nu_{g}} \quad \text{and} \quad \lambda_{g} = 1 - \lambda_{l}$$

$$\text{where } \nu = \left(\frac{K_{rl}}{\nu_{l}} + \frac{K_{rg}}{\nu_{g}} \right)^{-1}$$

(2-9)

Relative permeabilities of each phase are expressed by semi-empirical Bruggeman relationship with liquid saturation as follows:

$$K_{rl} = s^n \text{ and } K_{rg} = (1-s)^n \tag{2-10}$$

Finally, by combining the above equations, capillary flux of liquid phase is reformulated as the following equation.

$$
\begin{aligned}
\vec{j}_l &= \frac{\lambda_g \lambda_l K}{\nu} \nabla p_c = \frac{\lambda_g \lambda_l K}{\nu} \nabla \left[\sigma \cos(\theta_c) \left(\frac{\varepsilon}{K} \right)^{1/2} J(s) \right] = \frac{\lambda_g \lambda_l \sigma \cos(\theta_c) (K\varepsilon)^{1/2}}{\nu} \frac{dJ}{ds} \nabla s \\
&= \frac{\lambda_g \lambda_l \sigma \cos(\theta_c) (K\varepsilon)^{1/2}}{\nu} \frac{dJ}{ds} \frac{\rho_l \left(\rho_g Y_l^k - \rho_g Y_g^k \right)}{\left(\rho_l Y_l^k - \rho_l Y^k + \rho_g Y^k - \rho_g Y_g^k \right)^2} \nabla Y^k
\end{aligned}
\tag{2-11}
$$

Water species equation

As typical DMFCs operate below the water boiling point (100 $^\circ$C at 1 bar), water exists in two-phase (liquid water and water vapor) and the water vapor concentration is saturated. The gradient of mass fraction in the liquid phase is almost zero due to the dilute solution assumption. Therefore, the water transport equation can be derived from Eq. (2-4) with Eq. (2-11) as follows:

$$\nabla \cdot \left(\gamma \rho \vec{u} Y^{H_2O} \right) = \nabla \cdot \left[\rho D_{capill} \nabla Y^{H_2O} \right] + M^{H_2O} S^{H_2O} \tag{2-12}$$

This equation shows the water is transported by capillary diffusion in the porous media with the capillary diffusivity being

$$D_{capill} = \frac{1}{\rho} \left(Y_l^{H_2O} - Y_g^{H_2O} \right) \frac{\lambda_g \lambda_l \sigma \left| \cos(\theta_c) \right| (K\varepsilon)^{1/2}}{\upsilon} \frac{dJ}{ds} \frac{\rho_l \left(\rho_g Y_l^{H_2O} - \rho_g Y_g^{H_2O} \right)}{\left(\rho_l Y_l^{H_2O} - \rho_l Y^{H_2O} + \rho_g Y^{H_2O} - \rho_g Y_g^{H_2O} \right)^2} \tag{2-13}$$

Capillary diffusivity shown above is based on mass fraction. It can be expressed in other terms such as concentration:

$$D_{\text{capill,C}} = \left(\frac{C_{\text{sat}}^{H_2O} M^{H_2O}}{\rho_g} - 1 \right) \left(\frac{1}{\rho_l - C_{\text{sat}}^{H_2O} M^{H_2O}} \right) \frac{\lambda_g \lambda_l \sigma \cos \theta_c \left(K\varepsilon \right)^{1/2}}{\nu} \frac{dJ}{ds} \tag{2-14}$$

Or it can be expressed in term of liquid saturation as follows:

$$D_{\text{capill,S}} = D_{\text{capill,C}} \left(\frac{\rho_l}{M^{H_2O}} - C_{\text{sat}}^{H_2O} \right) \tag{2-15}$$

Water species source term arises from: *i*) MOR, *ii*) ORR, *iii*) MCO, and iv) α. Therefore, water source terms can be expressed as follows:

$$S_{\text{acl}}^{H_2O} = -\frac{j}{6F} - \frac{j}{F}\alpha$$

$$S_{\text{ccl}}^{H_2O} = \frac{j}{2F} + \frac{j_{\text{xover}}}{3F} + \frac{j}{F}\alpha \tag{2-16}$$

Methanol species equation

Assuming vapor-liquid equilibrium of methanol in the anode, methanol mass fraction can be expressed by Henry's law as follows:

$$Y_g^{MeOH} = \frac{\rho_l}{\rho_g k_H} Y_l^{MeOH} \tag{2-17}$$

where k_H is the Henry's constant. Therefore, methanol mass fraction can be expressed as

$$Y^{MeOH} = \frac{\rho_l}{\rho} \left(s + \frac{1-s}{k_H} \right) Y_l^{MeOH} \tag{2-18}$$

and methanol transport equation can be summarized from Eq. (2-4) as follows:

$$\nabla \cdot \left(\rho \vec{u} Y_l^{MeOH} \right) = \nabla \cdot \left[\rho_l \left(D_{l,\text{eff}}^{MeOH} + \frac{D_{g,\text{eff}}^{MeOH}}{k_H} \right) \nabla \cdot Y_l^{MeOH} \right] - \nabla \cdot \left[\left(Y_l^{MeOH} - Y_g^{MeOH} \right) \vec{j}_l \right] + M^{MeOH} S^{MeOH} \tag{2-19}$$

Methanol species source term arises from MOR and MCO as follows:

$$S_{\text{acl}}^{\text{MeOH}} = -\frac{j}{6F} - \frac{j_{\text{xover}}}{6F}$$

(2-20)

Oxygen species equation

As the present model assumes very low oxygen solubility in the water, oxygen species equation can be derived as follows:

$$\nabla \cdot \left(\gamma \rho \vec{u} Y^{O_2} \right) = \nabla \cdot \left[\rho \left(\frac{\rho_g}{\rho} D_{g,\text{eff}}^{O_2} \right) \nabla Y^{O_2} \right] + \nabla \cdot \left[Y^{O_2} \vec{j}_1 \right] + M^{O_2} S^{O_2}$$

(2-21)

Oxygen is consumed in the cathode catalyst layer as follows:

$$S_{\text{ccl}}^{O_2} = -\frac{j}{4F} - \frac{j_{\text{xover}}}{4F}$$

(2-22)

Heat transfer equation

As liquid water and water vapor coexist in a DMFC, water concentration is strongly affected by temperature whereas temperature is affected by the latent heat due to water phase change (condensation and evaporation). Therefore, species equation and energy equation are strongly coupled in the present multi-D model. Standard energy equation for the present DMFC model is derived from M^2 model (see Appendix E).

$$\nabla \cdot \left(\rho \vec{u} c_p T \right) = \nabla \cdot (k \nabla T) + \nabla \cdot \left(h_{\text{fg}}^{\text{o}} \rho_1 \vec{u}_1 \right) + S_{\text{sen}}^{\text{T}}$$

(2-23)

There are three sensible heat sources in the anode: *i*) irreversible heat of the electrochemical reaction, *ii*) reversible entropic heat, and *iii*) Joule heating. In the membrane, only Joule heating exists since electrochemical reaction does not occur there.

31

$$S_{\text{sen,acl}}^{\text{T}} = j\left(\eta + T\frac{dU_0}{dT}\right) + \frac{I^2}{\kappa^{\text{eff}}}$$

$$S_{\text{sen,mem}}^{\text{T}} = \frac{I^2}{\kappa^{\text{eff}}}$$

$$S_{\text{sen,ccl}}^{\text{T}} = j\left(\eta + T\frac{dU_0}{dT}\right) + \frac{I^2}{\kappa^{\text{eff}}} + S_{\text{xover}}^{\text{T}}$$ (2-24)

$$S_{\text{xover}}^{\text{T}} = j_{\text{xover}}\left(\eta + T\frac{dU_0}{dT}\right)$$

The influences of methanol crossover on energy balance is added ($S_{\text{xover}}^{\text{T}}$), which generates additional heat in CCL where crossed over methanol reacts.

Latent heat effect is included in the model as the following equation, which is derived from M^2 model (see Appendix E).

$$\begin{aligned}
S_{\text{lat}}^{\text{T}} = \dot{m}_{\text{fg}}''' h_{\text{fg}}^{\text{o}} &= \nabla \cdot \left(h_{\text{fg}}^{\text{o}} \rho_1 \vec{u}_1\right) \\
&= \nabla \cdot \left(h_{\text{fg}}^{\text{o}} \frac{\lambda_1 \lambda_{\text{g}} \sigma \cos(\theta_{\text{c}})}{\nu}(K\varepsilon)^{1/2}\frac{dJ}{ds}\nabla s - h_{\text{fg}}^{\text{o}}\lambda_1 \frac{K}{\nu}\nabla p\right)
\end{aligned}$$ (2-25)

where $\dot{m}_{\text{fg}}'''$ is the phase-changing rate (kg/m³s)

This source term arises from heat release or absorption due to water condensation or evaporation in two-phase flow region. Evaporation occurs in near surface area of GDL where air flow carries moisture away. Condensation occurs in cold region (under the land region) and CCL region where water is being produced by ORR. Because the present model assumes water is produced in vapor form at first, excessive water which is greater than saturation value must be condensed as liquid form.

Proton transport equation

In order to know the proton potential field which is required for calculating overpotentials and cell voltage, the following proton transport equation is implemented in the present multi-D model.

$$0 = \nabla \cdot (\kappa_{e,eff} \nabla \phi_e) + S_e^\phi$$

$$\text{where} \quad \begin{cases} S_{e,acl}^\phi = j \\ S_{e,ccl}^\phi = -j_c + j_{xover} \end{cases} \tag{2-26}$$

Protons are produced in the anode catalyst layer by MOR and consumed in the cathode catalyst layer by ORR. Therefore, the proton transport equation is valid in both catalyst layers and membrane.

Electron transport equation

The electron potential field is required also in order to examine the effect of electric ohmic loss and cell voltage.

$$0 = \nabla \cdot (\kappa_{s,eff} \nabla \phi_s) + S_s^\phi$$

$$\text{where} \quad \begin{cases} S_{s,acl}^\phi = -j \\ S_{s,ccl}^\phi = j_c - j_{xover} \end{cases} \tag{2-27}$$

Electrons produced by MOR in the anode catalyst layer move through the external electron-conductive route (load). Then, electrons are consumed in the cathode catalyst layer by ORR.

Electrochemical reaction equations

Electrochemical reaction in a DMFC, including the methanol oxidation reaction and oxygen reduction reaction are treated using proper source/sink terms in the species concentration, and proton and electron transport equations. The transfer current densities in these equations are expressed by the Tafel approximation of Butler-Volmer equation in the anode and cathode, respectively, as follows:

$$j_a = \frac{aj_{0,a}^{ref} C_{acl}^{MeOH} \exp(\frac{\alpha_a F}{RT}\eta_a)}{C_{acl}^{MeOH} + K \exp(\frac{\alpha_a F}{RT}\eta_a)}$$

$$\text{where} \quad \eta_a = \phi_s - \phi_e - U_a^0$$

(2-28)

C_{acl}^{MeOH} and K are the local methanol concentration at the anode catalyst and a reaction constant, respectively. It is known that methanol oxidation reaction (MOR) is 0th order when the methanol concentration is high enough and 1st order when the methanol concentration approaches the depletion limit. Eq. (2-28) simulates a smooth transition from 0th order kinetics to 1st order kinetics in the present multi-D model [22-24].

On the cathode side, ORR is assumed to be proportional to oxygen concentration. Flooding effect is considered by adding $(1-s)^n$ in Eq. (2-29).

$$j_c = aj_{0,c}^{ref} \left(\frac{C_{ccl}^{O_2}}{C_{ref}^{O_2}} \right)(1-s)^n \exp\left(-\frac{\alpha_c F}{RT}\eta_c \right)$$

$$\text{where} \quad \eta_c = \phi_s - \phi_e - U_c^0$$

(2-29)

Volumetric crossover current density (j_{xover}) in the multi-D model can be found by the net methanol crossover flux through the membrane, which consists of electro-osmotic drag and diffusion as follows:

$$\frac{j_{\text{xover}}}{6F} = \nabla \cdot \left(n_{\text{d}}^{\text{MeOH}} \frac{i}{F} \right) + \frac{\left(D_{\text{mem}}^{\text{MeOH}} \dfrac{C_{\text{acl}}^{\text{MeOH}}}{\delta_{\text{mem}}} \right)}{\delta_{\text{acl}}} \tag{2-30}$$

The electronic and electrolyte phase potential fields found by Eq. (2-26) and Eq. (2-27) are used for calculating overpotentials as follows:

$$\begin{aligned}
\eta_{\text{a}} &= \phi_{\text{s}}\big|_{\text{a}} - \phi_{\text{e}}\big|_{\text{a}} - U_0\big|_{\text{a}} \quad \text{(anode overpotential)} \\
\eta_{\text{c}} &= \phi_{\text{s}}\big|_{\text{c}} - \phi_{\text{e}}\big|_{\text{c}} - U_0\big|_{\text{c}} \quad \text{(cathode overpotential)}
\end{aligned} \tag{2-31}$$

Above anode/cathode overpotentials are coupled with transfer current densities. Hence, they are calculated iteratively. Neglecting the contact resistance, the terminal voltage is found by the electronic potential difference between anode and cathode current collectors as follows:

$$V_{\text{cell}} = \phi_{\text{s}}\big|_{\text{abp}} - \phi_{\text{s}}\big|_{\text{cbp}} \quad \text{(terminal voltage)} \tag{2-32}$$

Description of mass transport on the GDL surface

In this section, we further discuss the mass transfer mechanism between the channel and porous media. Wang *et al.* [25] explained mass transfer on the GDL surface by convective mass transfer coefficient, which can be obtained by heat transfer analogy.

$$N = h_{\text{m}}(C_{\text{A}} - C_{\text{B}}) = \frac{ShD}{\delta}(C_{\text{A}} - C_{\text{B}})$$
$$\text{where } Sh \begin{cases} = f(Re) \\ = 2.693 \quad \text{(Fully developed laminar flow)} \end{cases} \tag{2-33}$$

However, basic assumption of such a description is 'permeable surface'. There is no information about hydrophobicity or permeability in this description. In other words, this

expression works well when GDL surface has no hydrophobicity. Nevertheless, many experimental results show good agreement with this description because actual GDL surface is not ideally hydrophobic or hydrophilic since it is a mixture of carbon (hydrophilic) and PTFE (hydrophobic). If the GDL surface is ideally hydrophobic (liquid impermeable), this description fails.

Another way to explain mass transport is applying hydraulic pressure acting on the GDL surface. Displacing gas-phase by liquid-phase in hydrophobic porous media is called 'drainage'. Three methods exist to cause drainage: *i*) gravitation, *ii*) centrifugal force, and *iii*) externally applied liquid pressure. In a fuel cell, first and second methods are not applicable. In order to fill ideally hydrophobic porous media with liquid, we should apply high liquid pressure externally which is called 'break-through pressure' and it is defined as follows:

$$p_b = \frac{4\sigma \cos\theta_c}{d_p} \tag{2-34}$$

where d_p is the particle diameter of the porous medium. Breakthrough pressure of GDL can be estimated as follows:

$$p_{b,gdl} = \frac{4\sigma \cos\theta_{c,gdl}}{d_{p,gdl}} = \frac{4 \times 0.06 \times \cos 110^o}{10^{-5}} = 8.2 \text{ kPa} \tag{2-35}$$

This is a very high value compared to the pressure applied in the anode channel of a conventional DMFC. In addition, CO_2 gas pressure exists in the anode. If external liquid pressure is applied to permeate the GDL surface, it should be at least,

$$p_l > p_b + p_g \tag{2-36}$$

36

But, actual mass transfer at the channel/GDL interface occurs without such a high external pressure. Therefore, surface liquid transport of a conventional DMFC can be explained by convective mass transfer description. If the GDL surface is ideally hydrophobic (convective mass transfer fails) and the channel is not pressurized enough (less than the breakthrough pressure of the GDL surface), then liquid transport is theoretically impossible and the anode will not be wet.

On the cathode, as water is continuously produced by ORR, liquid water should be removed from the reaction side. Otherwise, liquid water will block the reaction sites and ORR will be hindered. Liquid water removal from the cathode catalyst layer to the surface of the cathode channel can be easily explained with hydraulic pressure built by ORR water production. As it is difficult for liquid water to permeate proton exchange membrane which has very low hydraulic permeability (or very high breakthrough pressure), liquid water produced in the cathode catalyst layer must move towards cathode GDL which has relatively lower breakthrough pressure. In addition, as the applied gas (air) pressure in the cathode is almost constant (~ ambient pressure), liquid water can move through the hydrophobic GDL by drainage.

Boundary conditions

As the present multi-D model solves eight equations (mass, momentum, three species, electron, proton and heat), there are ten unknowns. The following explains their boundary conditions.

i) Anode and cathode channel inlet velocity is determined according to the flow stoichiometry and inlet concentration as follows:

$$\vec{u}_{a,in} = \xi_a \left(\frac{i_{ref}}{6FC_{in}^{MeOH}} \right) \left(\frac{A_{mem}}{A_{in}} \right)$$

$$\vec{u}_{c,in} = \xi_c \left(\frac{i_{ref}}{6FC_{in}^{O_2}} \right) \left(\frac{A_{mem}}{A_{in}} \right)$$

(2-37)

Stoichiometry 1 means required mass for operating the cell at the reference current density (i_{ref} = 150 mA/cm^2 in this study). At the outlet surface, zero gradient boundary condition is applied.

ii) Species (water, methanol, oxygen) inlet concentration value is given according to the specified cell operating condition.

iii) Electron: Cathode current collector surface has the reference cell voltage (zero) and anode current collector surface has electric current flux boundary condition as follows:

$$\phi_s \big|_{cbp} = 0, \qquad \frac{d\phi_s}{dx} \bigg|_{abp} = \frac{I}{A_{mem}} = i$$

(2-38)

As the membrane is electrically insulated, zero gradient boundary condition is applied on both sides of the membrane surface.

iv) Proton: Proton equation is valid only for MEA (ACL/MEM/CCL). Hence, zero gradient boundary condition is applied at both CL/MPL interfaces.

v) Heat: Constant temperature boundary condition is applied on the surface of both current collectors.

2.2.2 Saturation jump model

Qi and Kaufman [26] experimentally showed the effect of micro-porous layer (MPL) inserted between GDL and CL on the water transport and distribution in fuel cells. As

this MPL is made of finer and more hydrophobic materials than other porous layers, a discontinuity in the liquid saturation across the interface of two layers occurs while the liquid pressure at the interface is continuous. Anode MPL has the effect of reducing saturation level in the anode catalyst layer by blocking water flow from the anode channel whereas cathode MPL has the effect of increasing saturation level in the cathode catalyst layer by reserving produced water. Therefore, water flux from the anode to cathode is greatly reduced.

Nam and Kaviany [27] theoretically explained the saturation discontinuity effect with a 1-D mathematical model, the so called saturation jump model. Passaogullari and Wang [10] further investigated the effect of saturation jump with MPL on the water transport in the porous media of a fuel cell. Shaffer and Wang [28] conducted a theoretical discussion about the effect of hydrophobic MPL on the cell performance and the fuel efficiency of DMFCs by simulating 1-D model.

In order to minimize water/methanol crossover, most of recently developed DMFCs have two MPLs with thin proton exchange membrane, so called 'low-α MEA'. Experimental results by Liu and Wang [29] showed that cell performance and fuel efficiency can be improved with properly selected MPLs.

As Nam and Kaviany [27] and Shaffer and Wang [28]'s 1-D model directly solved flux-based liquid saturation equation with above relationship, their model easily shows through-plane saturation profile. However, as the present multi-D model solves species equation instead of saturation equation, saturation distribution is acquired from species distribution. Furthermore, several parameters and constitutive relationships of the multi-D

39

model are dependent on saturation, which means saturation and species fractions are strongly coupled in the multi-D model.

Ju [30] first implemented the saturation jump concept between cathode catalyst layer and cathode MPL in a multi-D PEMFC model. Here, we introduce how to implement saturation jump in the present multi-D DMFC model. Figure [2-3(a)] shows the interface of two different porous layers (GDL and MPL). The capillary pressure should be continuous at this interface as follows:

$$\sigma \cos \theta_{c,1} \left(\frac{\varepsilon_1}{K_1} \right) J\left(s_{int,1} \right) = \sigma \cos \theta_{c,2} \left(\frac{\varepsilon_2}{K_2} \right) J\left(s_{int,2} \right) \tag{2-39}$$

When the saturation of one layer is given, the saturation of the other layer can be found by solving following equation. Calculation result is shown in Figure [2-3(b)].

$$J\left(s_{int,1} \right) = \beta_2 / \beta_1 \, J\left(s_{int,2} \right) \quad \text{where} \quad \begin{cases} \beta_1 = \sigma \cos\left(\theta_1\right) \left(\dfrac{\varepsilon_1}{K_1} \right)^{1/2} \\[4mm] \beta_2 = \sigma \cos\left(\theta_2\right) \left(\dfrac{\varepsilon_2}{K_2} \right)^{1/2} \end{cases} \tag{2-40}$$

However, the multi-D model calculates liquid saturation in each mesh (s_1 and s_2) and interfacial liquid saturation (s_{int}) is not given. Therefore, interfacial liquid saturation should be determined by s_1 and s_2 with considering water flux continuity (liquid phase and vapor phase) at the mesh interface as follows (Note D_S is saturation-based capillary diffusivity shown in Eq. (2-15)):

$$N_{int} = N_{1,int} = N_{2,int}$$
$$D_{S,1} \frac{s_{1,int} - s_1}{\Delta x_1} + D_1^g \frac{C_{g,int} - C_{g,1}}{\Delta x_1} = D_{S,1} \frac{s_2 - s_{2,int}}{\Delta x_2} + D_2^g \frac{C_{g,2} - C_{g,int}}{\Delta x_2} \tag{2-41}$$

Then from Eq. (2-41), we have,

$$s_{\text{int},2} = A s_{\text{int},1} + B \tag{2-42}$$

where

$$A = -\frac{D_{S,1}}{D_{S,2}} \frac{\Delta x_2}{\Delta x_1}$$

$$B = \left(D_{S,1} \frac{s_1}{\Delta x_1} + D_{S,2} \frac{s_2}{\Delta x_2} - f_{g1} + f_{g2} \right) \frac{\Delta x_2}{D_{S,2}}$$

$$f_{g1} = D_{g1} \frac{C_{g,\text{int}} - C_{g,1}}{\Delta x_1}$$

$$f_{g2} = D_{g2} \frac{C_{g,2} - C_{g,\text{int}}}{\Delta x_2}$$

Now we combine Eq. (2-40) and Eq. (2-42) to get interfacial liquid saturation and interfacial liquid flux. Interfacial liquid saturation does not explicitly show up in the multi-D model. Instead, we add or subtract interfacial liquid flux found above in the mesh 1 and 2 as follows:

$$M^{\text{H}_2\text{O}} S_1^{\text{H}_2\text{O}} = -\nabla \cdot \left(\rho D_{\text{capill}} \nabla Y^{\text{H}_2\text{O}} \right) + M^{\text{H}_2\text{O}} \nabla \cdot N_{\text{int}}$$

$$M^{\text{H}_2\text{O}} S_2^{\text{H}_2\text{O}} = -\nabla \cdot \left(\rho D_{\text{capill}} \nabla Y^{\text{H}_2\text{O}} \right) - M^{\text{H}_2\text{O}} \nabla \cdot N_{\text{int}} \tag{2-43}$$

Finally, above water source term is put to the water equation (Eq. (2-12)).

2.2.3 Non-isothermal behavior

In a typical DMFC, heat transfer in the anode is mostly carried out by liquid flow in the channel which has large convective heat transfer coefficient (liquid cooling). However, in the cathode, heat conduction and heat-pipe effect is important since there is no liquid flow in the channel. The heat pipe effect was first proposed and explored by

Wang and Wang [31] and Suman *et al.* [32] investigated the phase change and heat-pipe effect in a PEMFC. They showed the cell operating condition (relative humidity of the inlet gas) and material property (heat conductivity of GDL) have a strong influence on phase change and temperature distribution by quantifying phase-changing rate and portion of heat transfer by heat-pipe effect. In this chapter, we reproduce the non-isothermal behavior with the heat-pipe effect in a DMFC by adopting Suman's methodology. As DMFC and PEMFC have almost the same cathode structure, although PEMFC produces more heat since it operates at higher current, we can assume similar heat transfer phenomena may occur in DMFCs also.

Figure [2-4] shows how heat transfer occurs in the cathode by heat-pipe effect. As CCL is hot due to reaction and land is cold, major heat flow direction is from CCL to GDL/land interface. Water vapor near CCL is transported to GDL/land interface by thermal diffusion and it condenses there due to lower temperature. Condensed water near GDL/land interface moves towards the gas channel and finally it evaporates since dry air flow carries moisture away. By considering heat balance near GDL/land interface, the heat conduction equation becomes,

$$\frac{d}{dx}\left[\left(k_{gdl} + h_{fg}^{o} M^{H_2O} D_{g,eff}^{H_2O} \frac{dC_{sat}^{H_2O}}{dT}\right)\frac{dT}{dx}\right] = \frac{d}{dx}\left(k_{eff}\frac{dT}{dx}\right)$$

$$\text{where } \begin{cases} D_{g,eff}^{H_2O} = D_g^{H_2O}\left(1-s\right)^n \varepsilon^n \\ k_{eff} = k_{gdl} + h_{fg}^{o} M^{H_2O} D_{g,eff}^{H_2O} \frac{dC_{sat}^{H_2O}}{dT} \end{cases} \quad (2\text{-}44)$$

Wang and Wang [31] derived above effective thermal conductivity (k_{eff}) which explains the contribution of thermal diffusion. Eq. (2-44) implies that heat-pipe effect increases the effective thermal conductivity, which improves heat release.

In addition to heat transfer effect, heat-pipe effect includes water transport effect also. When a cell is non-isothermal, thermal vapor diffusion occurs due to water vapor concentration gradient in two-phase region. As this thermal vapor diffusion occurs from hot to cold region, liquid saturation in the hot region decreases and it increases in the cold region, which means water removal from the cathode porous media to the cathode channel is enhanced. As water is transported by both capillary diffusion and non-isothermal vapor diffusion in two-phase region, we can expect net water transfer coefficient will increase. Contrary to the heat equation, those two water transport mechanisms (capillary diffusion and thermal vapor diffusion) are not compatible. Hence, they cannot be incorporated in a single diffusion term. Therefore, we introduce an additional water source term to reflect the thermal vapor diffusion as follows:

$$M^{H_2O}S_{diff}^{H_2O} = \int_{V} \nabla \cdot \left\{ \rho_g \bar{D}_{g,eff}^{H_2O} Y_{sat}^{H_2O}(T) \right\}$$

(2-45)

This term is added to the water equation Eq. (2-12).

2.2.4   Flow field configuration

DMFC model with parallel channel configuration

Figure [2-2] shows the 3-D mesh used for the present multi-D DMFC modeling, which simulates a single channel (75 mm length) of a 28 cm^2 DMFC which has 18 parallel channels. In order to save computational time, we assume every single channel is identical in the parallel cell configuration without any channel clogging by CO_2 bubbles. Therefore, this single channel can be considered to represent the entire DMFC cell area. A detailed cell specification is listed in Appendix C.

DMFC model with serpentine channel configuration

Many DMFCs adopt a serpentine channel configuration in order to avoid the channel clogging problem although serpentine channel causes larger pressure drop than the parallel configuration. On the cathode side, removed water from GDL surface may be condensed in the cathode channel, which may clog the channel and hinder air supply although it is not so much severe as the anode side since a typical DMFC operates at low current compared to PEMFC. Therefore, DMFC with serpentine channel configuration will have non-uniform distribution of species, current and temperature compared to DMFC with parallel channel configuration.

Figure [2-5] shows 3-D mesh of the full-scale DMFC model (28 cm^2). Anode has a single-pass serpentine channel in order to sweep away CO_2 bubbles whereas cathode has a two-pass serpentine channel. As air volumetric flow rate is much larger than liquid fuel flow rate, pressure drop in the cathode channel is greater than that of the anode channel. In order to reduce pressure drop due to large air flow rate, 2 ~ 4 serpentine passes are arranged to grasp both reduced pressure drop and better removal of water droplets. Anode channel and cathode channel are arranged as cross-flow configuration in order to minimize non-reactive region and promote uniform distribution. Figure [2-6] shows 3-D mesh of the actual DMFC for experimental validation.

2.3   Implementation

All derived sets of governing equations, parameters and constitutional relations discussed above are implemented into commercial CFD solver, STAR-CD$^{®}$. AMG (algebraic multi-grid method) based on finite volume method (FVM) is used for

discretization and SIMPLE algorithm is applied for solving governing equations. It is considered that convergence is achieved when the residuals reach 10^{-6}. Parallel computing is used for the full-scale simulation.

2.4 Results and Discussion

2.4.1 Single channel model

Effect of flow stoichiometry on cell performance and fuel efficiency

As flow stoichiometry increases, methanol concentration in the anode increases also, as shown in Figure [2-7]. The region under the channel has higher methanol concentration than the region under the land due to short diffusion length. As defined in Eq. (1-4), crossover current density (methanol crossover) is strongly affected by methanol concentration near membrane/ACL interface. Therefore, crossover current density distribution is similar to methanol concentration distribution as shown in Figure [2-8].

Figure [2-9] shows current density distribution in the single channel model according to fuel stoichiometry. When fuel supply is large enough, current density is uniformly distributed in flow stream direction as shown Figure [2-9(c)] and the highest current density is observed under the land region. In a DMFC, when methanol supply is large enough, MOR is 0th order, which means MOR is not affected by methanol concentration in ACL. However, excessive methanol transported to the cathode side (under the channel region) degrades cell performance by producing mixed potential, which results in lower current density under the channel region where methanol crossover is high. When fuel stoichiometry is low, MOR is affected by methanol concentration in ACL and the highest

current density is observed under the channel region as shown in Figure [2-9(a)]. When fuel supply is intermediate, the highest current density shows up under the land in the inlet region and it is observed under the channel in the outlet region, as shown in Figure [2-9(b)]. Although large stoichiometry produces better cell performance, fuel efficiency decreases due to large MCO. In addition, operating a cell with large stoichiometry requires much pumping power (parasitic loss). Contrarily, overly low stoichiometry may lead to large local concentration overpotential due to anode non-uniformity which significantly degrades the cell performance although fuel efficiency is good and parasitic loss is minimal. This will be discussed in detail in Chapter 4 and 5.

Finally, Figure [2-10] shows the current density distribution in the entire cell area when we assume that every single channel is identical without any channel clogging. Parallel, strip-shaped distribution is observed due to the channel configuration. Again, large flow stoichiometry results in more uniform distribution of current density.

Liquid saturation distribution and effect of MPL

Figure [2-11] shows liquid saturation distribution in the cell cross-section according to the MPL configuration. Anode porous media are gradually getting gaseous in the channel direction since produced CO_2 gas accumulates whereas cathode porous media become wetter since produced water accumulates. In the anode, under the channel region is wetter than under the land region. This is because CO_2 removal is blocked by the land and the region under the channel directly faces channel liquid flow. Contrarily, the region under the land on the cathode side is wetter than the region under the land since liquid water removal from the cathode catalyst layer to the cathode channel is blocked there. Therefore, it is expected that water transfer coefficient will be positive under the channel

46

and negative (or small) under the land. When there are no MPL, two weak saturation jumps are observed at CL/GDL interface as shown in Figure [2-11(a)].

When the anode MPL is inserted between the anode GDL and ACL, we can see a strong saturation jump at the interface between the anode MPL and ACL, which effectively blocks liquid flow from the anode GDL to the anode catalyst layer and lowers the net water transfer to the cathode (see Figure [2-11(b)]). In addition, the anode MPL plays as a methanol transport barrier which reduces methanol concentration in the anode catalyst layer and lowers methanol crossover.

Figure [2-11(c)] shows the effect of cathode MPL inserted between the cathode GDL and CCL. By reserving liquid water inside CCL, the cathode MPL builds up hydraulic pressure and increases water back-diffusion to the anode side, which lowers water transfer coefficient. Three saturation jumps are observed in this case. Note that liquid saturation in CCL is especially increased. Cathode MPL does not have the effect of reducing methanol crossover.

When a cell has two MPLs, four saturation jumps can be observed as shown in Figure [2-11(d)]. Performance comparison according the MPL configuration is summarized in Table [2-2]. Both MPLs have the effect of lowering water crossover but only the anode MPL has additional effect of lowering methanol crossover. Case D, which has two MPLs, shows the lowest water/methanol crossover. Figures [2-12] and [2-13] show the effect of MPL in a different viewpoint as a form of saturation profile. Saturation jumps are more clearly noticed. When the cathode MPL is inserted, liquid saturation level in the cathode GDL is lowered due to the increased water back-diffusion. This may result in wet-to-dry transition near outlet region as shown in Figure [2-12(c)] and [2-12(d)].

47

Effect of thermal diffusion and phase-change on heat and water management

Figures [2-14(a)] and [2-14(b)] compare temperature distribution and thermal diffusion rate in the cathode according to the heat conductivity of the cathode GDL. Low heat conductivity of GDL (Figure [2-14(a)]) results in higher temperature difference than the high heat conductivity case (Figure [2-14(b)]). This high temperature difference drives more water thermal diffusion from the hot region (near CCL) to the cold region (GDL/CBP interface region). Note that negative value denotes water is being lost whereas positive value denotes water is being supplied there. Water transported to the region GDL/CBP interface is carried away by air flowing through the cathode channel. As the higher temperature difference causes much more water transport (higher water transfer coefficient value), it can be concluded that low GDL heat conductivity leads to higher water transfer coefficient (α). Effect of supply air humidity on the thermal diffusion rate is presented by Figures [2-14(a)] and [2-14(c)]. When highly humidified air is flowing in the cathode channel, less thermal diffusion occurs due to the reduced water concentration difference. Therefore, less water is transported from CCL to the channel, which results in lower water transfer coefficient value ($\alpha = 0.58$) compared to the dry air case (RH = 10 %) that induces more water to the cathode side ($\alpha = 1.2$).

Phase-change rate is presented in Figure [2-15]. Positive value denotes condensation whereas negative value denotes evaporation. Water vapor transported from CCL to CBP/GDL interface by thermal diffusion condenses and it moves towards the cathode channel and evaporates. Phase-change rate is affected by both material property (heat conductivity, k) and operating condition (relative humidity, RH). When heat conductivity is low (Figure [2-15(a)]), more water condenses at CBP/GDL interface and evaporates at

the channel/GDL interface compared to the high heat conductivity case (Figure [2-15(b)]), since more water is transported by increased temperature difference with low heat conductivity. Effect of air humidity on phase-change rate is compared by Figure [2-15(a)] and [2-15(c)]. Increased relative humidity of the air flowing through the cathode channel results in higher liquid saturation and lowered saturation gradient in the cathode porous media, which leads to lowered phase-change rate (see Eq. (2-25)).

2.4.2 *Serpentine channel model (28 cm² cell)*

In order to see the effect of flow stoichiometry, three cases are simulated. Simulation conditions are listed in Table [2-3].

Pressure drop in the channel

Pressure distribution in the anode and the cathode channel according to flow stoichiometry is presented in Figures [2-16] and [2-17], respectively. Although case A and C have the same anode flow rate (ξ_a = 2.0), case C shows lower anode pressure because large air flow rate (ξ_c = 5.0) in the cathode channel carries more water away in addition to more methanol loss due to larger MCO. Cathode pressure drop is greater than anode pressure drop due to greater volumetric flow rate for the same mass stoichiometry.

Methanol concentration and crossover current distribution

Figure [2-18] shows methanol concentration distribution in the ACL. Case B (ξ_a = 1.4) shows severe non-uniform distribution of methanol concentration, which implies that the outlet region may suffer from methanol shortage trouble. As crossover current density

is a strong function of methanol concentration, crossover current density shown in Figure [2-19] has a similar distribution trend as Figure [2-18].

Current density distribution

As shown in the single channel model, current density distribution becomes more uniform when flow stoichiometry increases (see Figure [2-20]). For the same anode/cathode stoichiometry condition with counter-flow configuration, the highest current density is found on the cathode side (low half region in case A). This is because ORR is more active than MOR and anode inlet region suffers from methanol crossover which degrades cell performance. Note that cathode inlet port (region B in Figure [2-20(a)]) and outlet port region (region A in Figure [2-20(a)]) show relatively lower current density than other regions when anode stoichiometry is large enough (case A and C). First, those regions are corners of the anode channel where fuel concentration is greater than neighboring region due to improved mixing effect (see Figure [2-18]). Second, those regions have the widest cathode channel area (three times larger area than a single channel area) since two cathode channels merge together there, which means oxygen is widely spread there (more cathode-active). Therefore, the large amount of methanol that crossed over to the cathode side reacts very actively with oxygen there, which degrades cell performance.

Temperature distribution

As the cathode catalyst generates more heat than the anode catalyst, temperature distribution follows the cathode channel shape as shown in Figure [2-21]. The left half region is hotter than right half region since methanol crossover concentrated in the left

50

half region generates additional heat. Again, hot spots are found in region A and B where methanol crossover is strong and cathode area is wide.

2.4.3   Serpentine channel model (12cm² cell) with experimental validation

In order to see the influence of the flow direction (co-flow vs. counter-flow) and flow stoichiometry, an actual 12 cm² DMFC is modeled (Figure [2-22]) and validated with experiment data that were provided by Panasonic Inc. (Figure [2-23]).

Experimental results show similar distribution of current density as shown in Figure [2-23(a)]. When the fuel and the oxidizer flow in the same direction (co-flow), the highest current density appears just after the inlet port. When the fuel and the oxidizer flow in the opposite direction (counter-flow), the highest current is found on the cathode side since methanol crossover in the anode inlet region degrades cell performance as discussed.

When anode stoichiometry is very low ($\xi_a = 1.4$), current density distribution is not so uniform in both co-flow and counter-flow configuration. Although this non-uniformity can be mitigated by increasing flow stoichiometry, it results in more parasite power and fuel loss due to increased methanol crossover.

2.5   Conclusion

Through the developed non-isothermal multi-D DMFC model which is capable of simulating saturation jump, the effectiveness of both the anode and cathode MPL is confirmed. Non-isothermal behavior including thermal diffusion and phase change is discussed and it is found that heat and water management are strongly coupled to each

other by the material property (heat conductivity) and the cell operating condition (temperature and inlet air humidity). Finally, the developed model is extended to the full-scale DMFC model and validated with the experimental data, which show good agreement with each other.

FIGURES
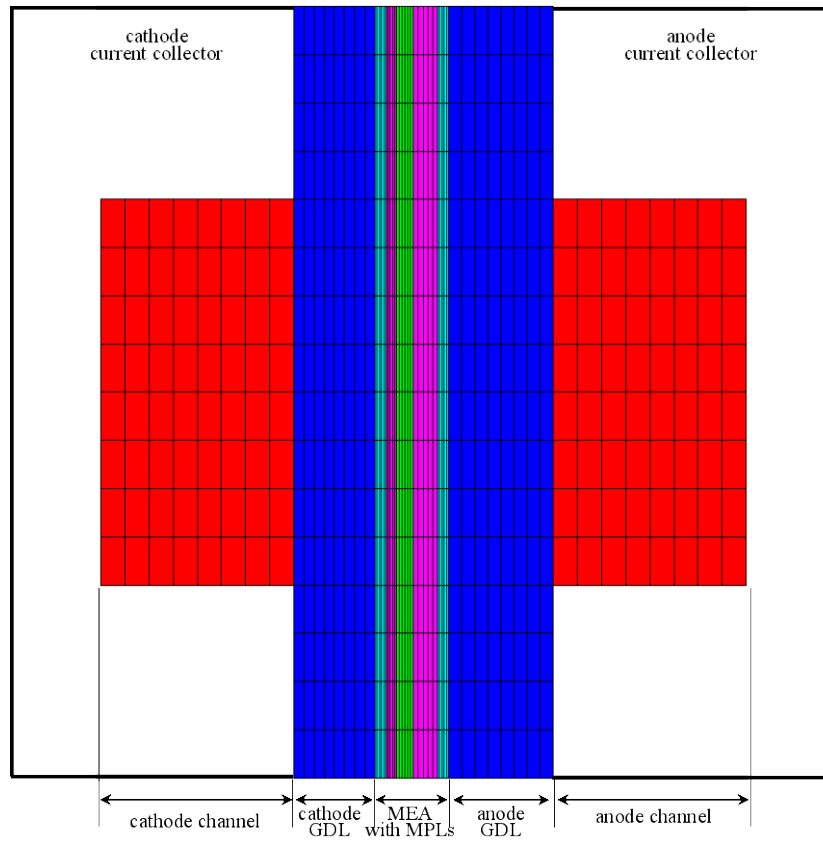
Figure [2-1]   Cell cross-section showing the sandwich configuration of the DMFC for the present study
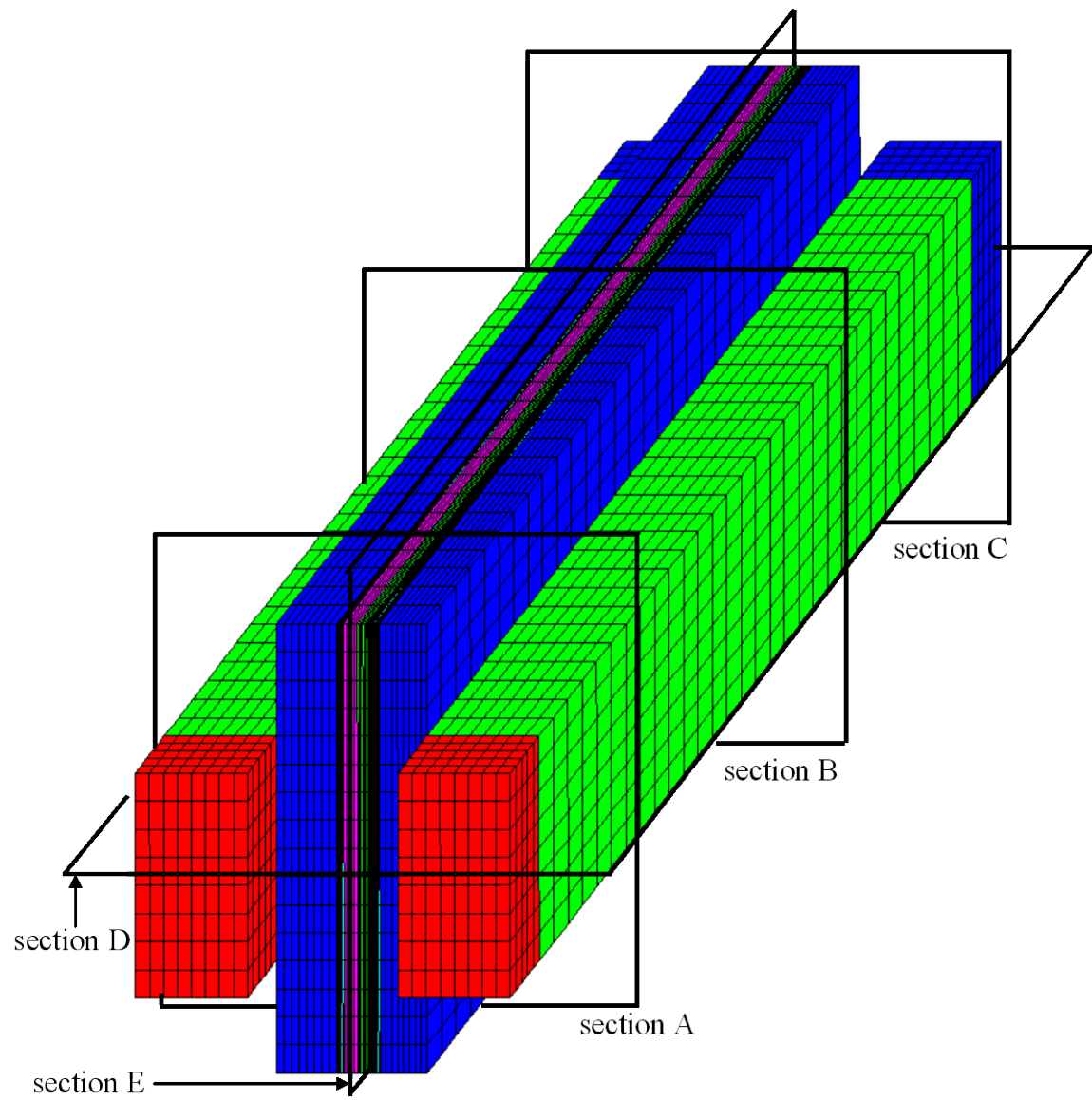
Figure [2-2]   Three-dimensional mesh of the single channel DMFC model for the present study
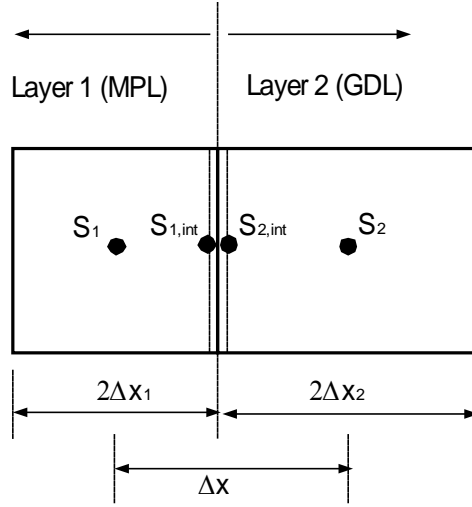
(a) Schematic of GDL/MPL interface for calculation
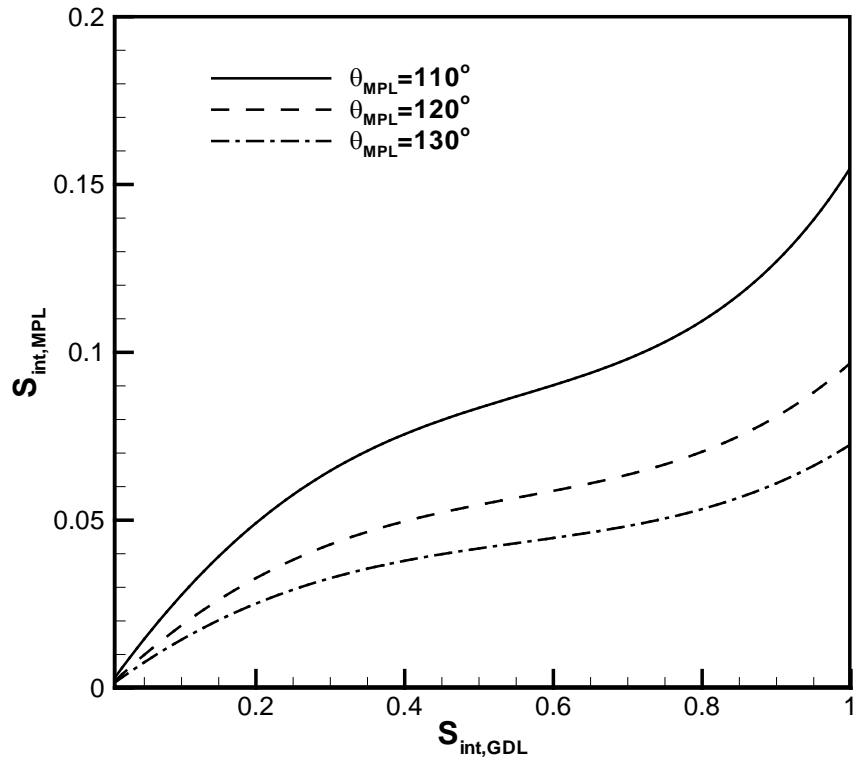
(b) Interfacial saturation discontinuity when $\theta_{gdl} = 100^o$

Figure [2-3]   Discontinuity of the liquid saturation at MPL/GDL interface
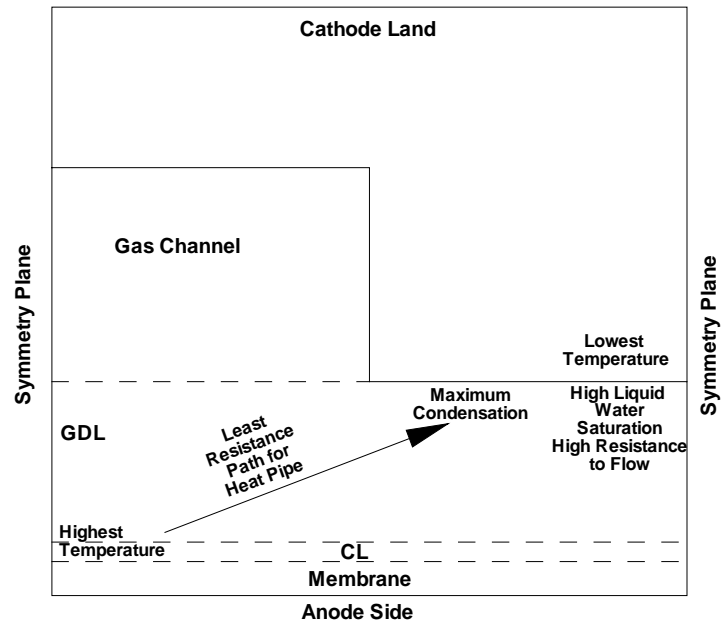
Figure [2-4]   Schematic showing heat-pipe effect [32]
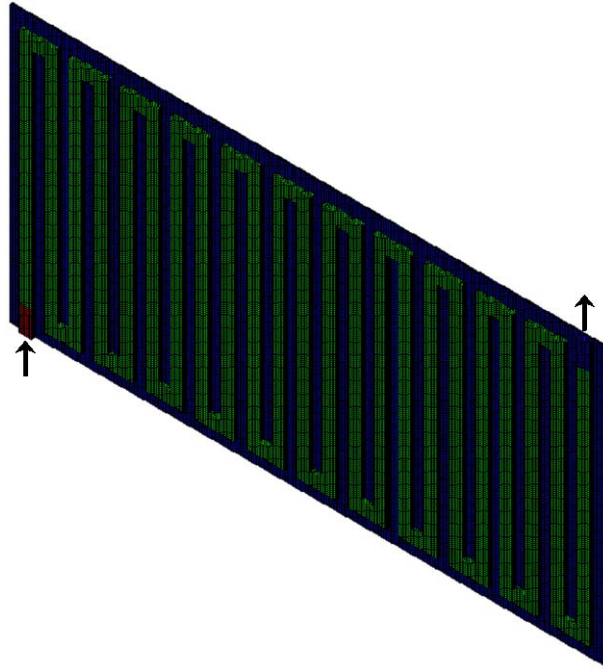
(a) Anode mesh (single-pass)
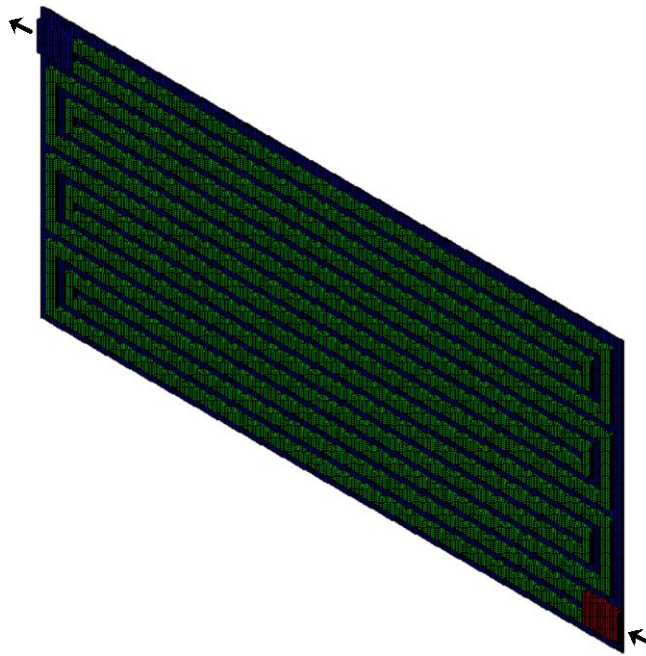
(b) Cathode mesh (two-passes)

Figure [2-5]   Three-dimensional mesh of the full-scale DMFC model (28 cm^2) which has serpentine channel configuration
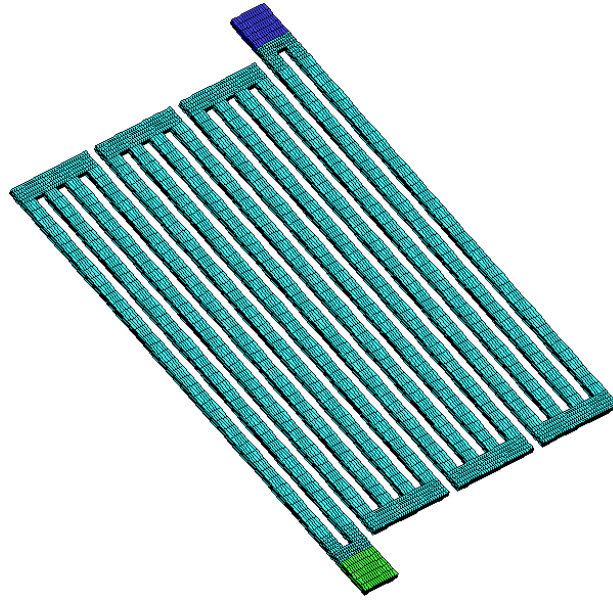
(a) Anode mesh (two-passes)
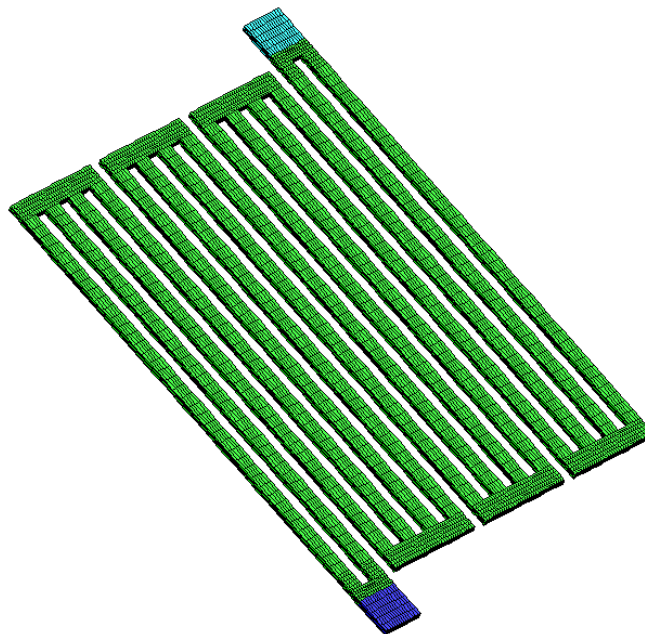
(b) Cathode mesh (two-passes)

Figure [2-6]   Three-dimensional mesh of the full-scale DMFC model (12 cm^2) which has serpentine channel configuration
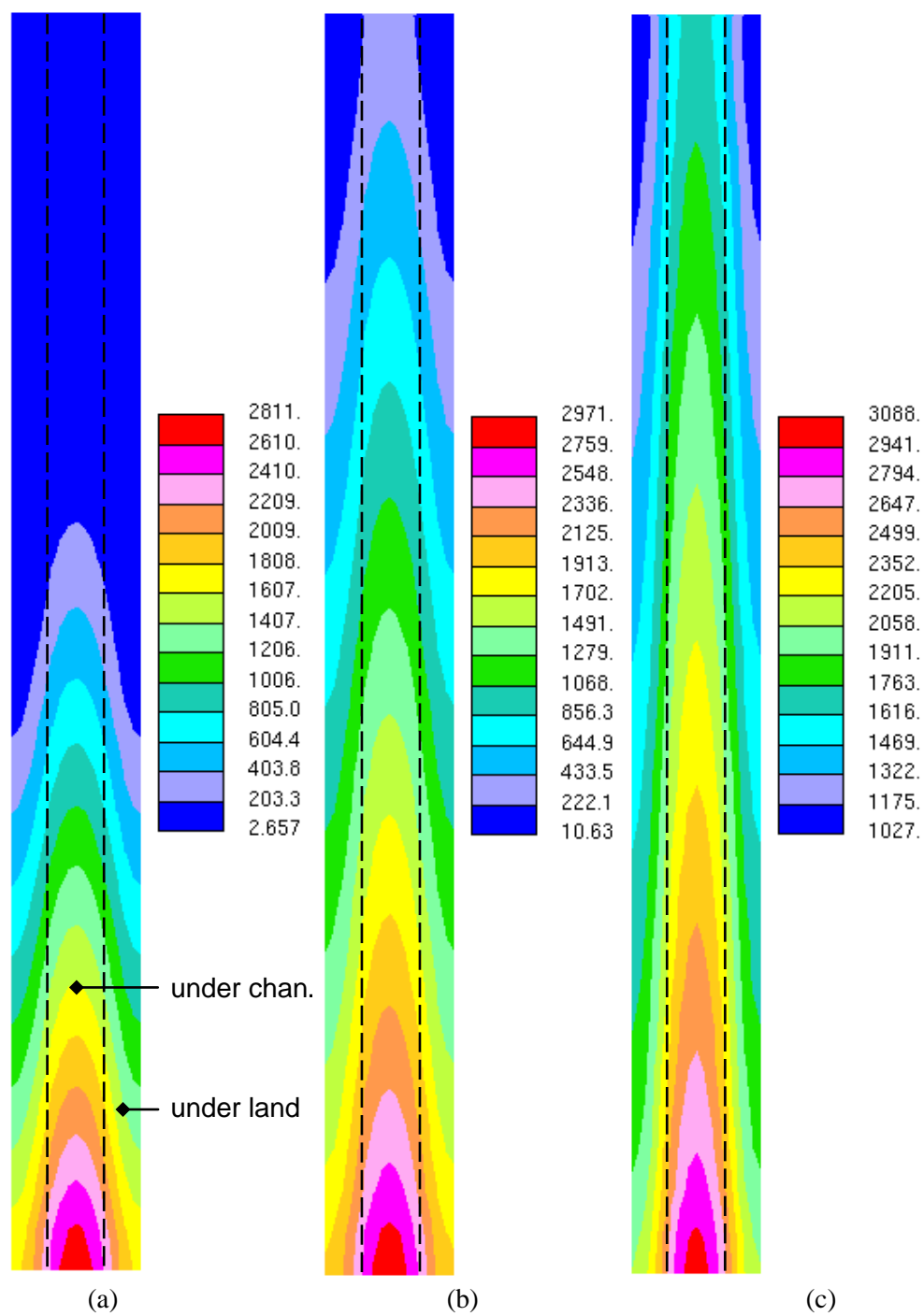
Figure [2-7]   Methanol concentration (mol/m^3) in the ACL of the single channel cell model according to flow stoichiometry, (a) T_{cell}=313K, ζ= a1.4c2.0, (b) T_{cell}=313K, ζ=a2.4c2.4, (c) T_{cell} =313K, ζ=a5.0c5.0
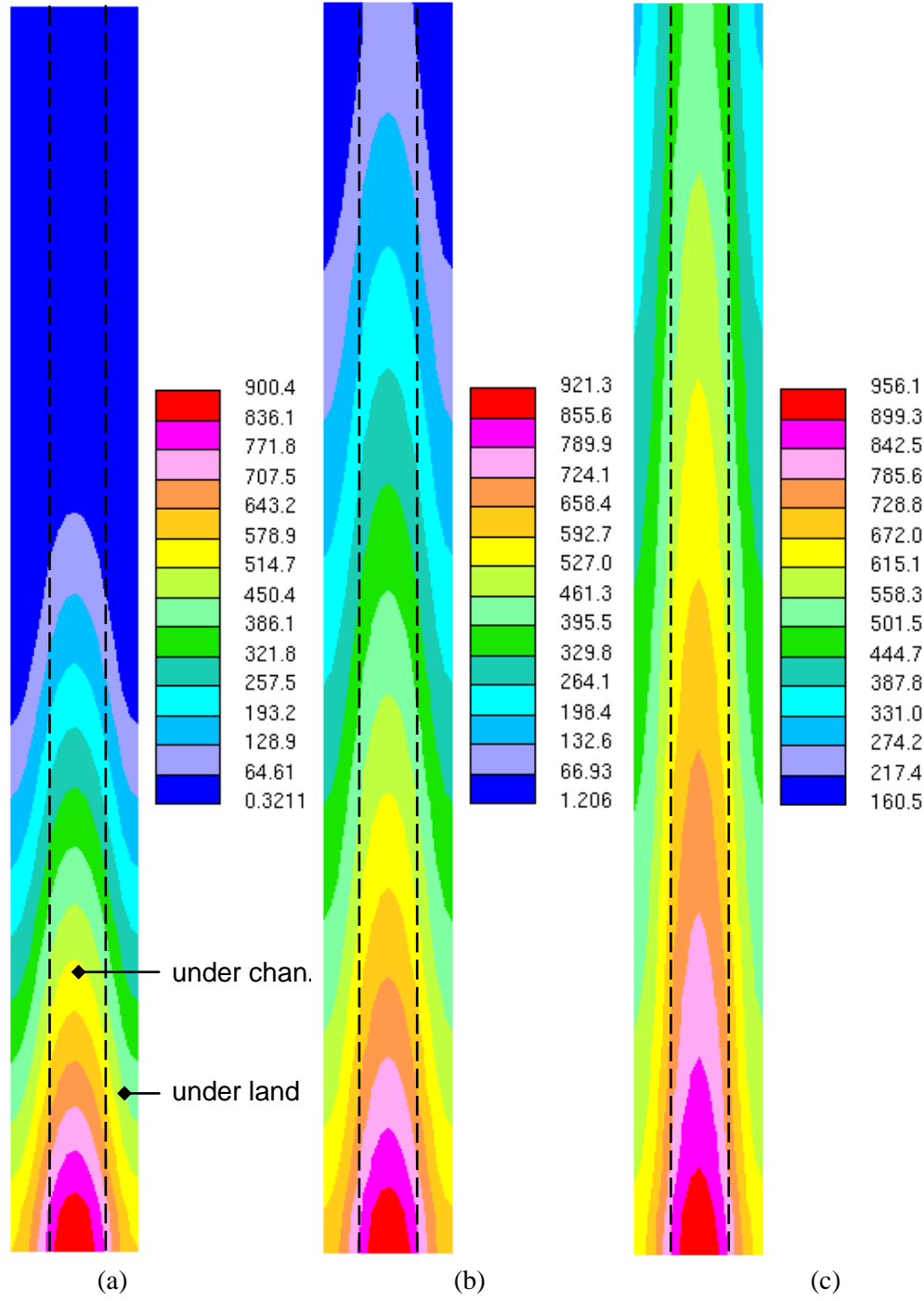
Figure [2-8]   Crossover current density distribution (A/m^2) of the single channel cell model according to flow stoichiometry, (a) T_{cell}=313K, ζ= a1.4c2.0, (b) T_{cell}=313K, ζ=a2.4c2.4, (c) T_{cell} =313K, ζ=a5.0c5.0
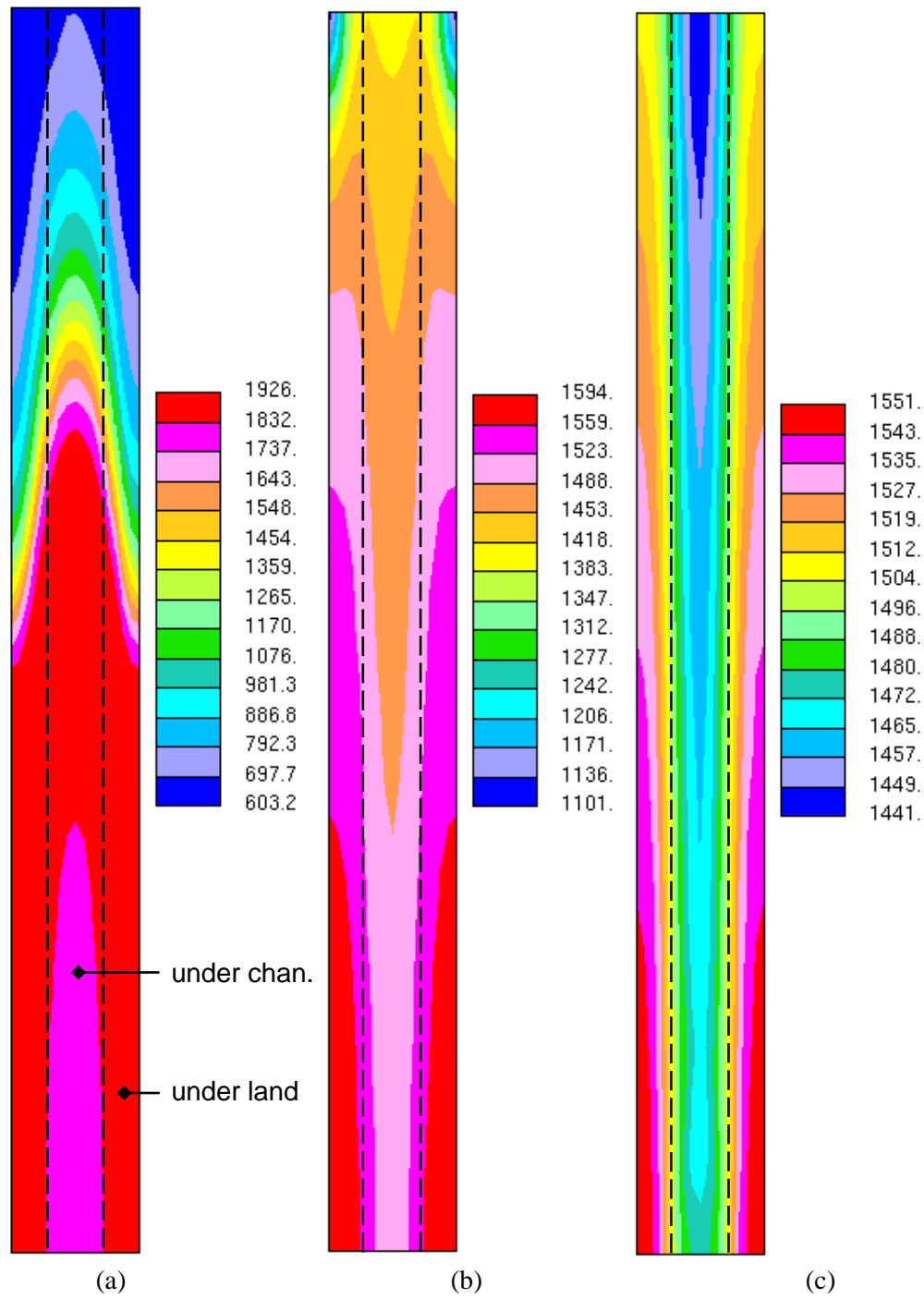
Figure [2-9]   Current density distribution (A/m^2) of the single channel cell model according to flow stoichiometry, (a) T$_{cell}$=313K, ζ= a1.4c2.0, (b) T$_{cell}$=313K, ζ=a2.4c2.4, (c) T$_{cell}$ =313K, ζ=a5.0c5.0
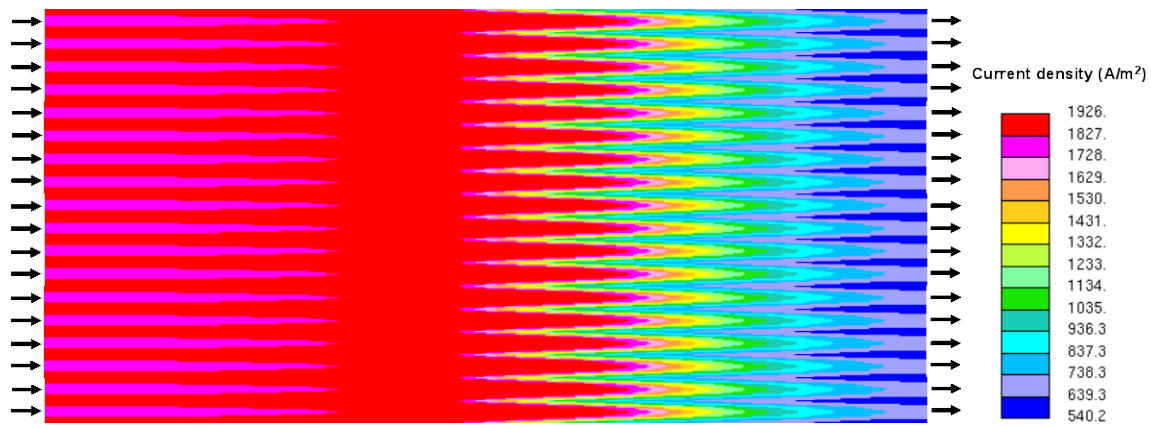
(a) T_{cell}=313K, ζ= a1.4c2.0
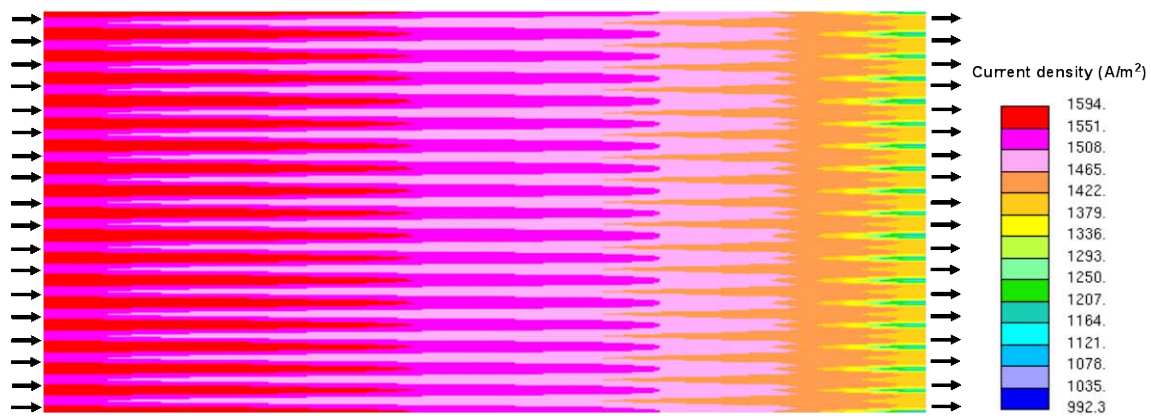
(b) T_{cell}=313K, ζ=a2.4c2.4
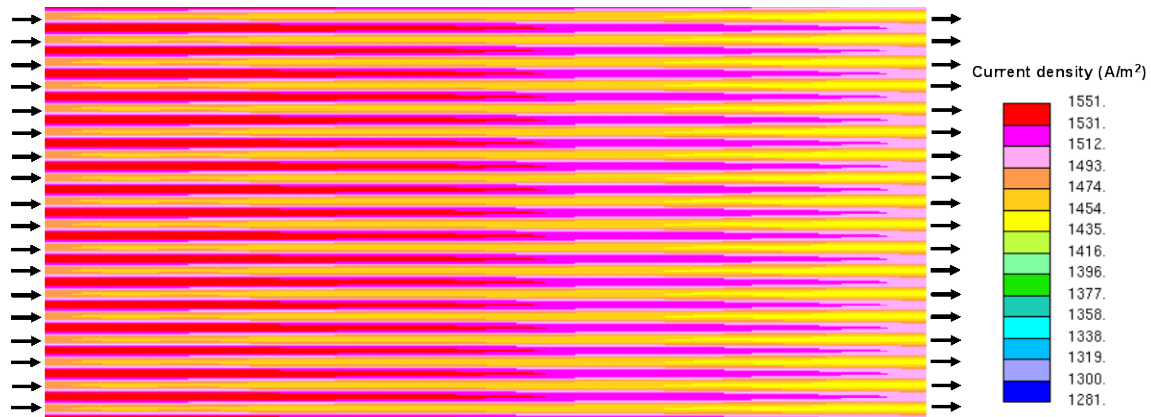
(c) T_{cell} =313K, ζ=a5.0c5.0

Figure [2-10]   Current density distribution in the cell with parallel channel configuration according to flow stoichiometry
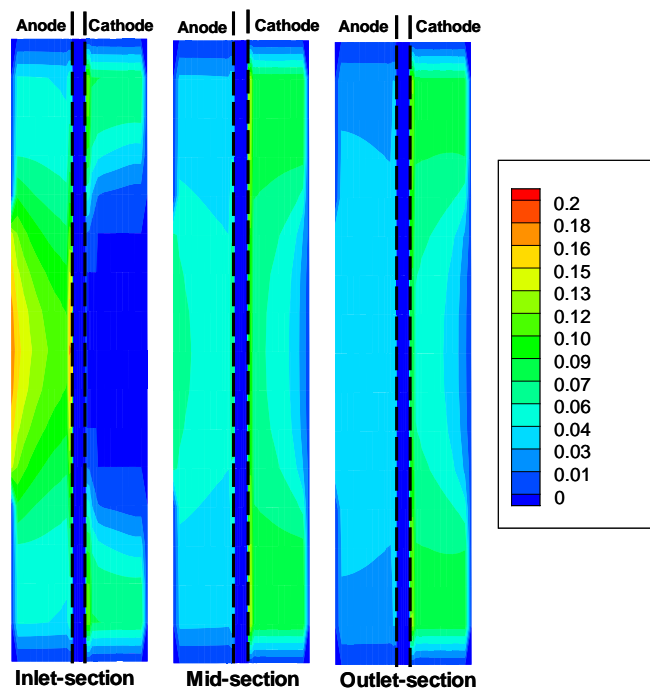
(a) No MPL
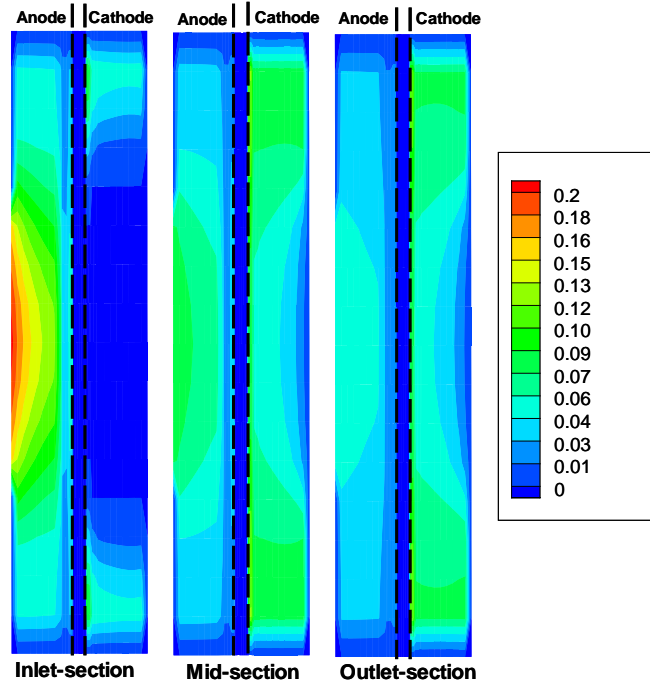
(b) Anode MPL only
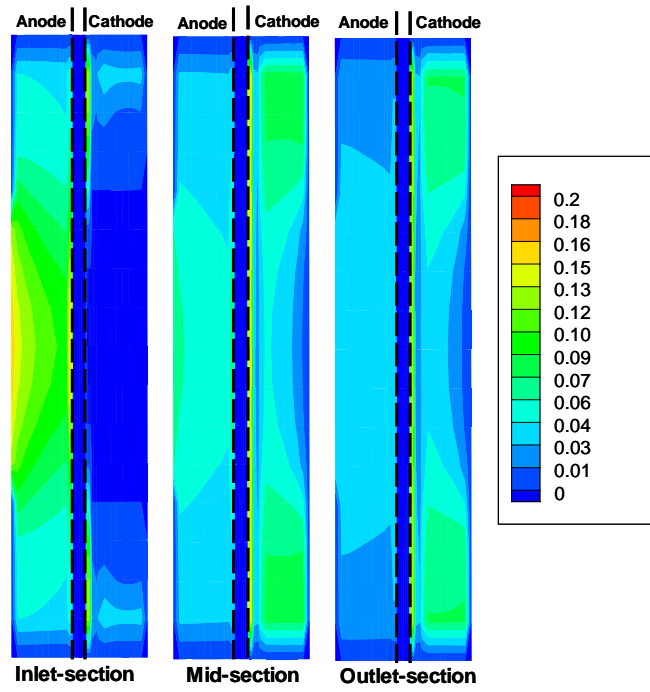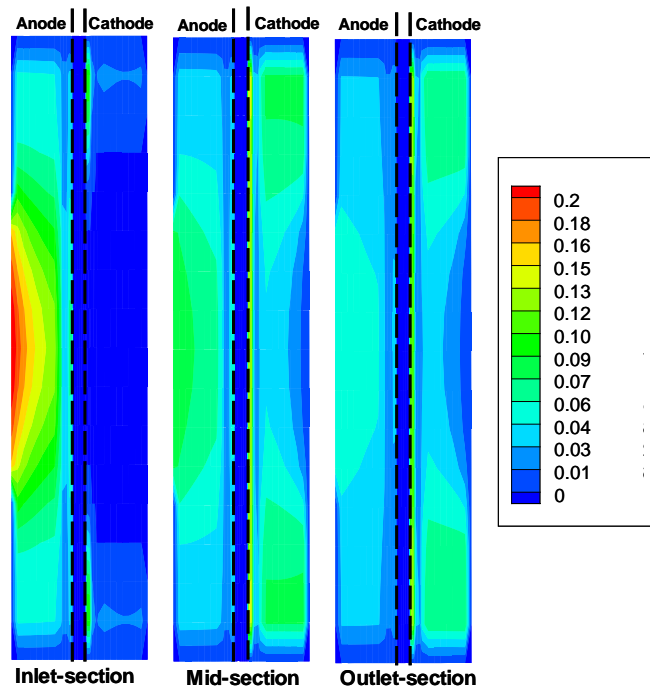
(c) Cathode MPL only

(d) Anode and cathode MPLs

Figure [2-11]   Liquid saturation distribution at the cross-section A, B, C according to the MPL configuration
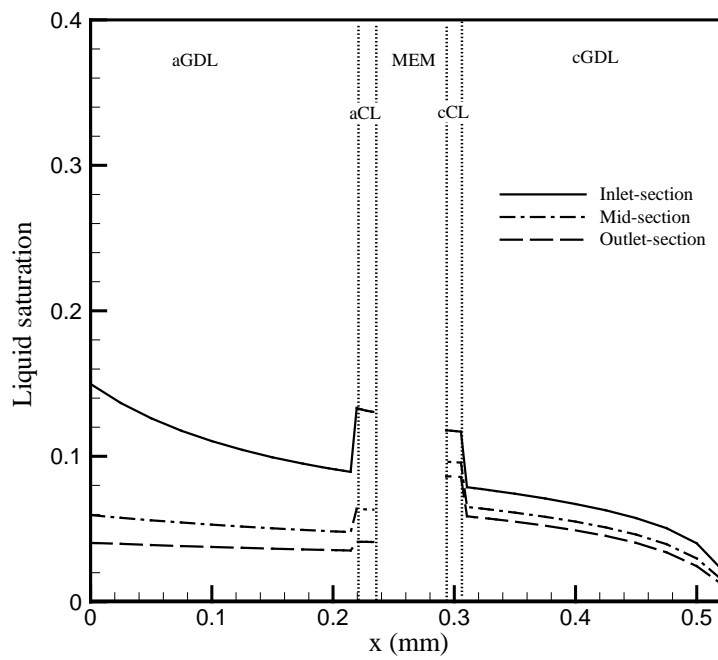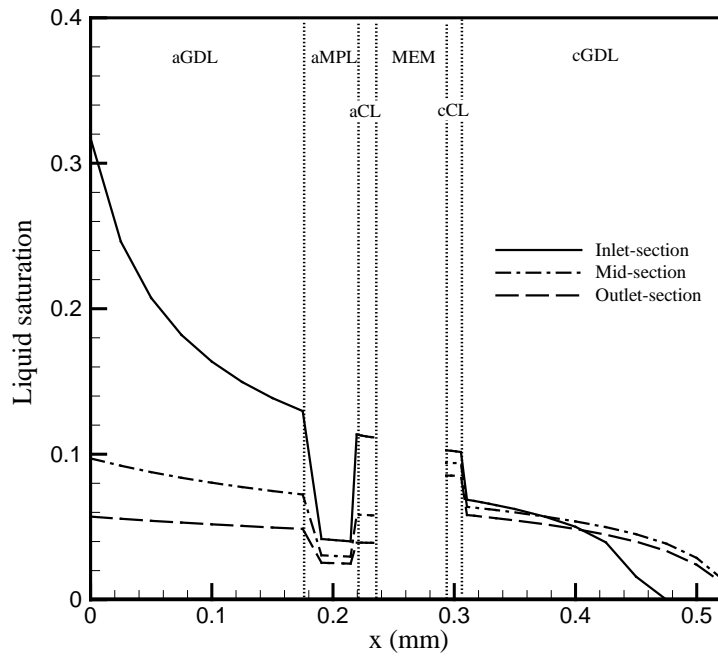
(a) No MPL
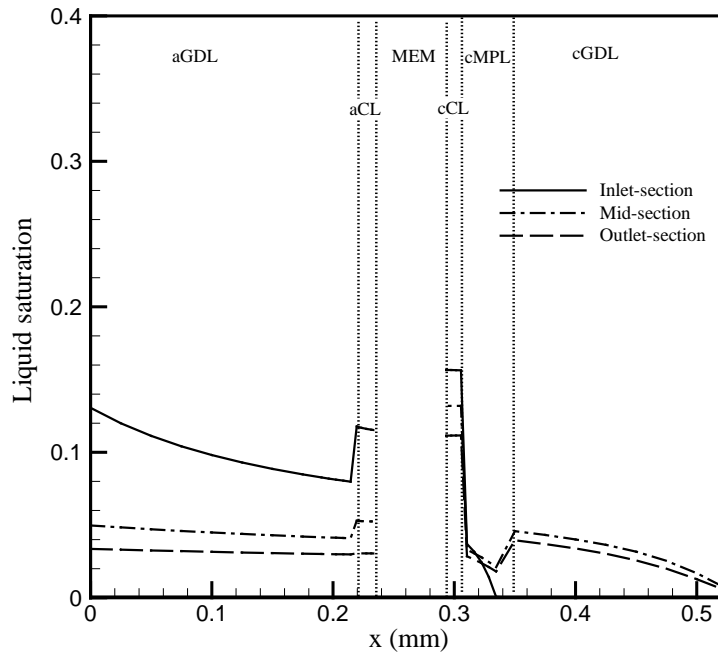
(b) Anode MPL only
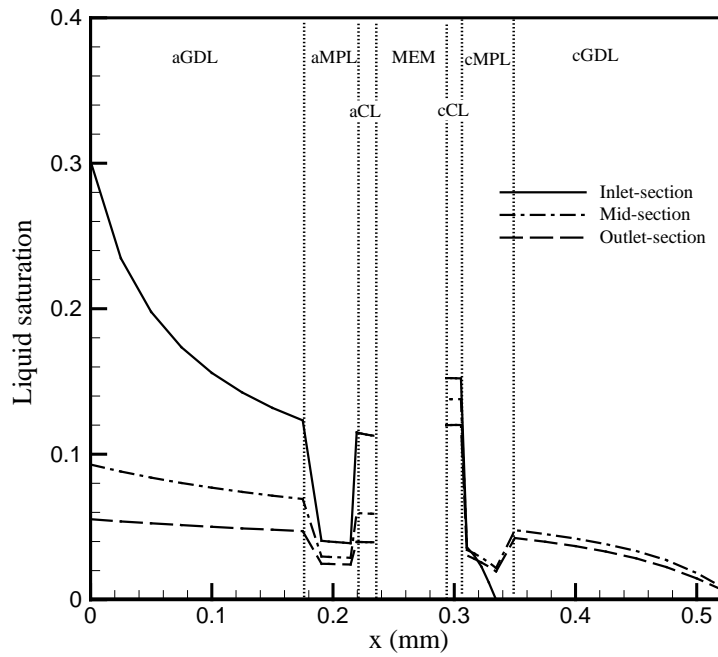
(c) Cathode MPL only

(d) Anode/cathode MPLs

Figure [2-12]   Liquid saturation profile under the channel at the cross-section A, B, C according to the MPL configuration

(a) No MPL

(b) Anode MPL only

67
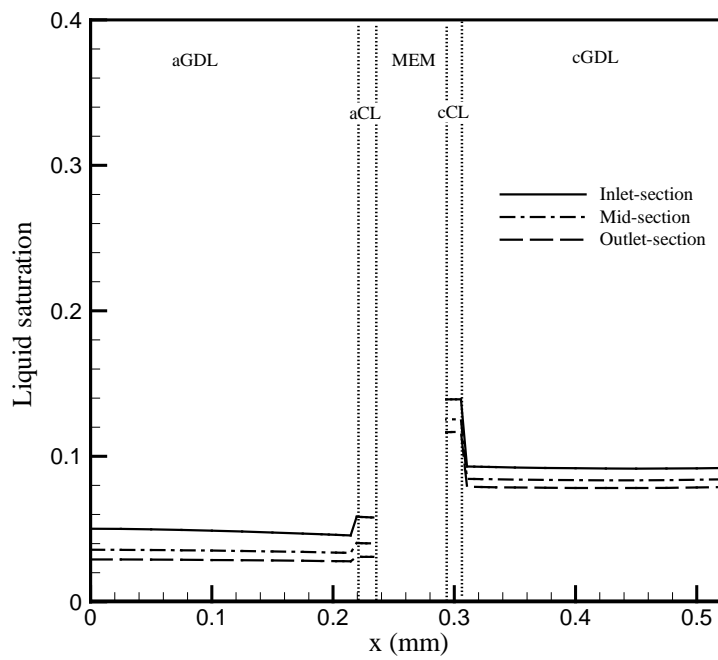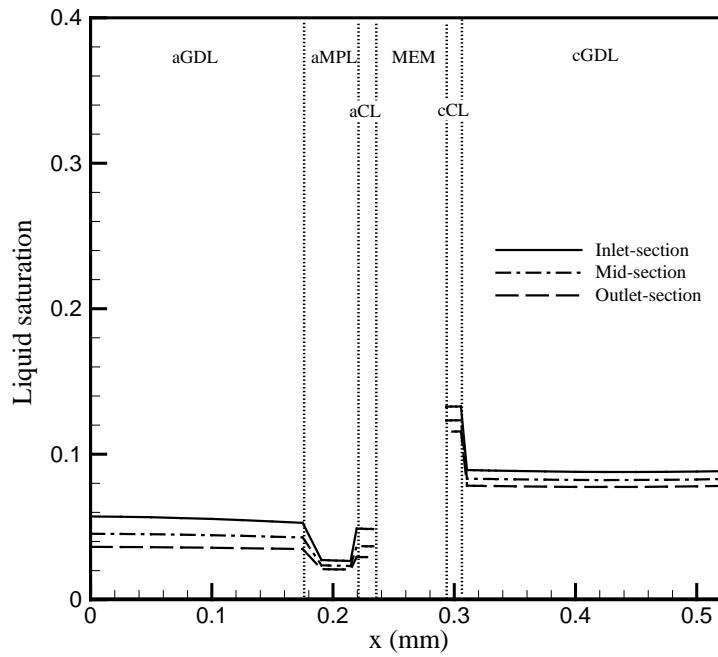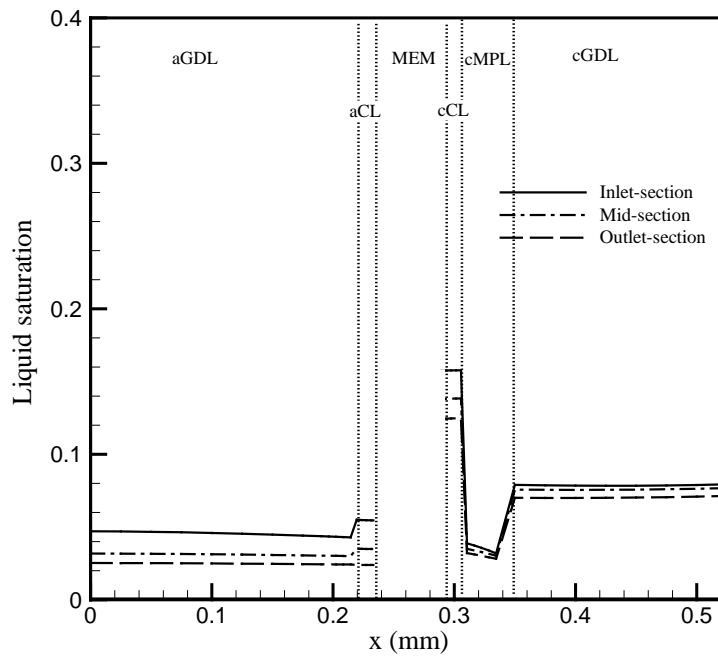
(c) Cathode MPL only
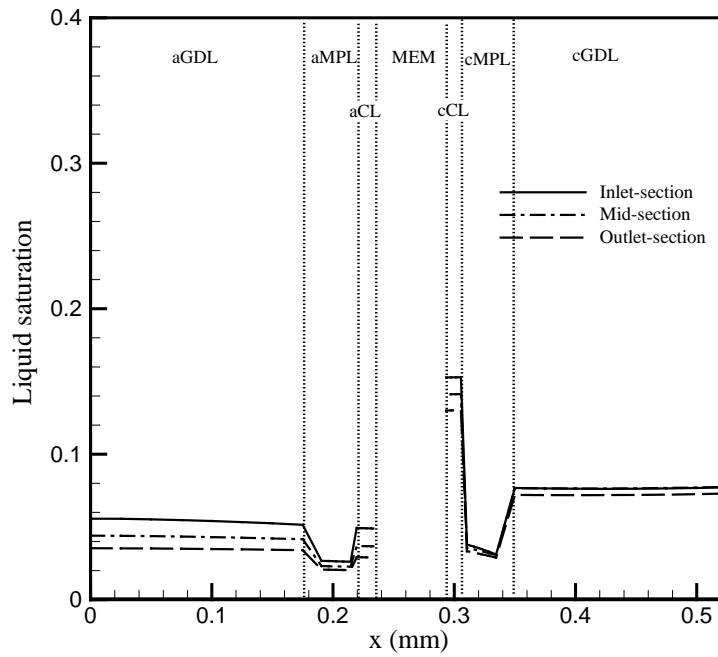
(d) Anode and cathode MPLs

Figure [2-13]   Liquid saturation profile under the land at the cross-section A, B, C according to the MPL configuration

(a) $k_{gdl} = 1$ W/mK, RH = 30 %

(b) $k_{gdl} = 3$ W/mK, RH = 30 %

(c) $k_{gdl} = 1$ W/mK, RH = 70 %
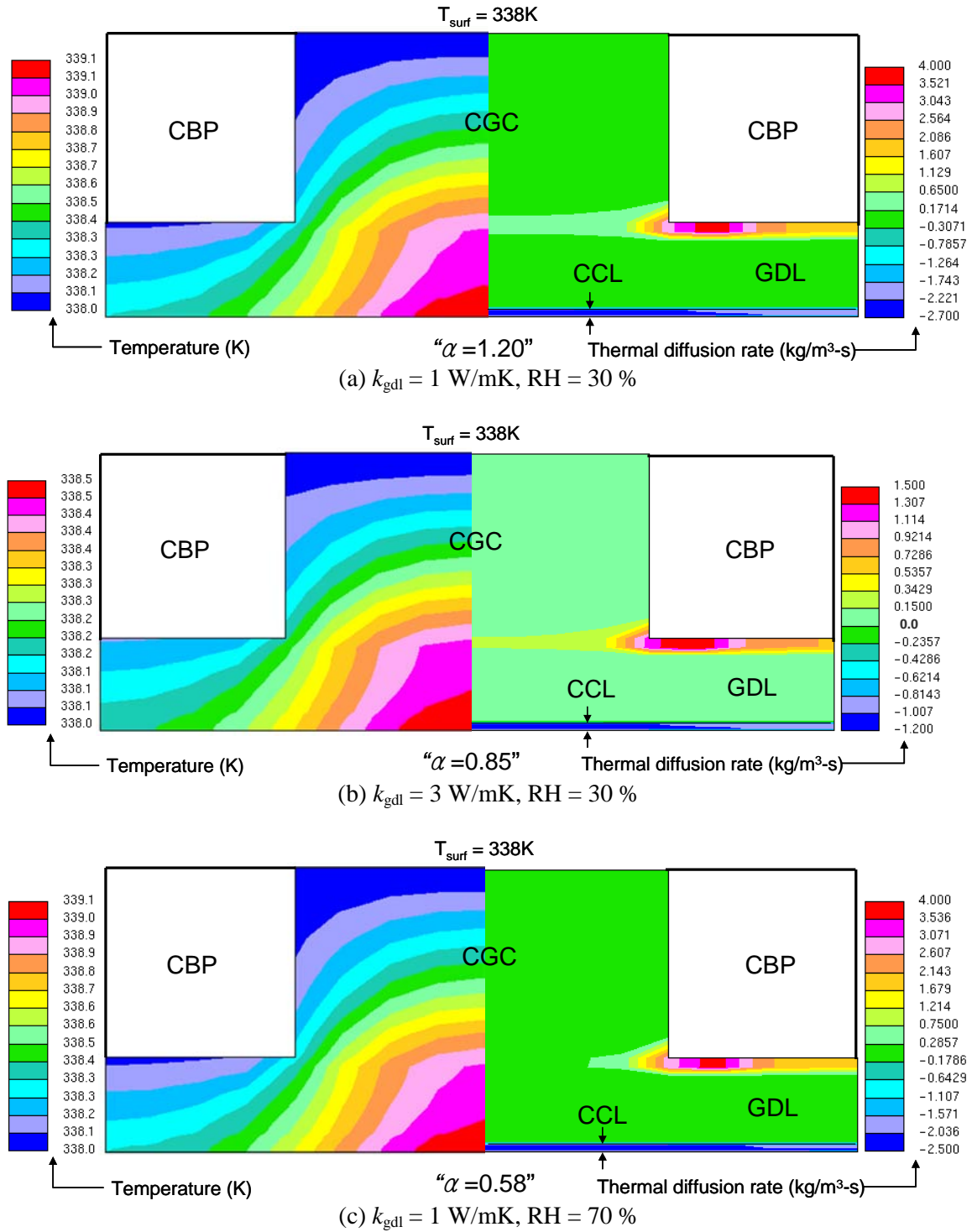
Figure [2-14]   Thermal diffusion rate in the cathode according to the material property (GDL heat conductivity) and operating condition (relative humidity of the inlet air)
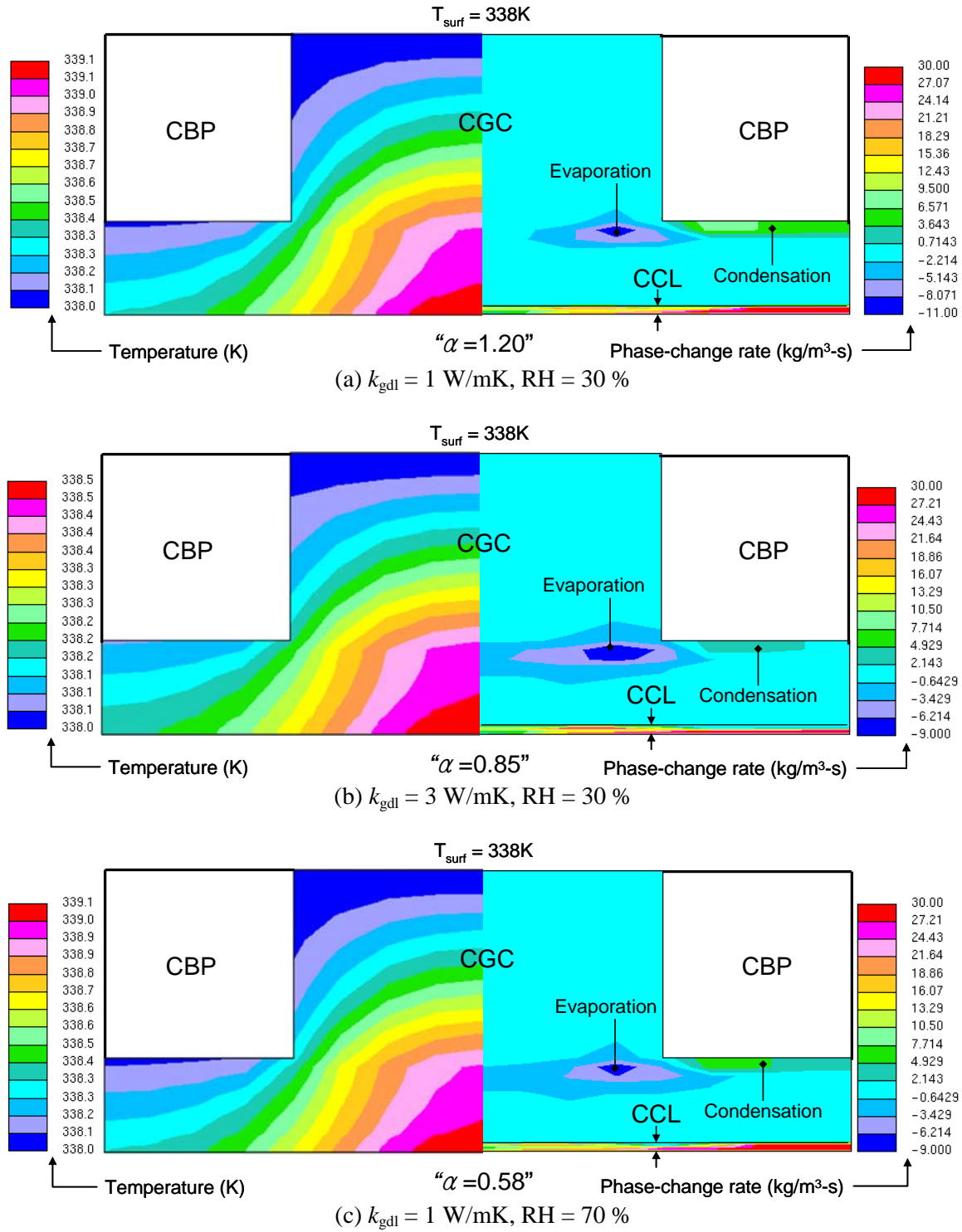
Figure [2-15]   Temperature and phase-change rate in the cathode according to the material property (GDL heat conductivity) and operating condition (relative humidity of the inlet air)
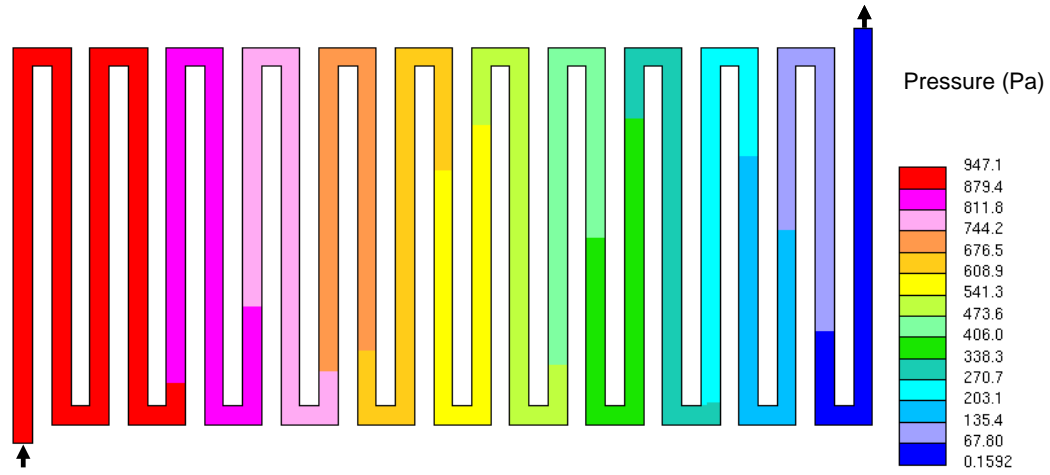
(a) Case A: $\zeta_a = 2.0$, $\zeta_c = 2.0$
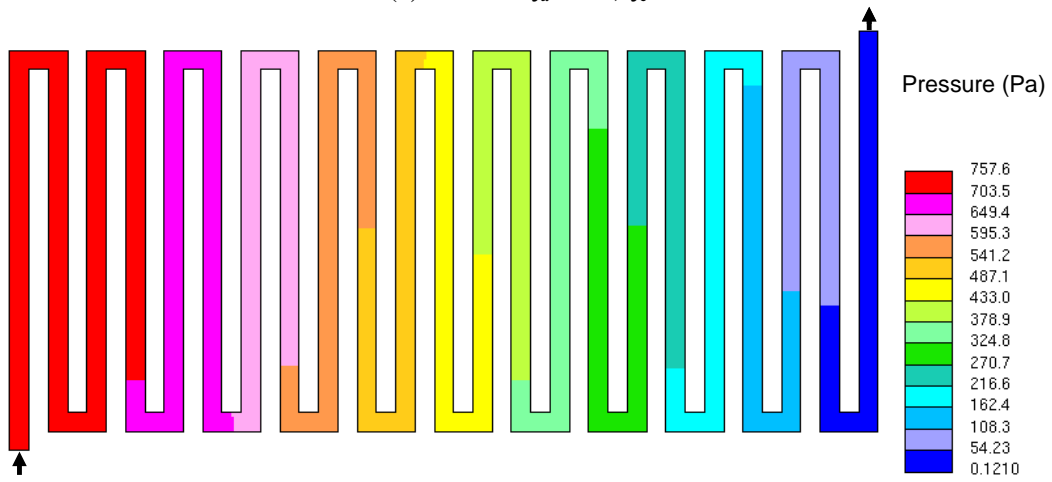
(b) Case B: $\zeta_a = 1.4$, $\zeta_c = 2.0$
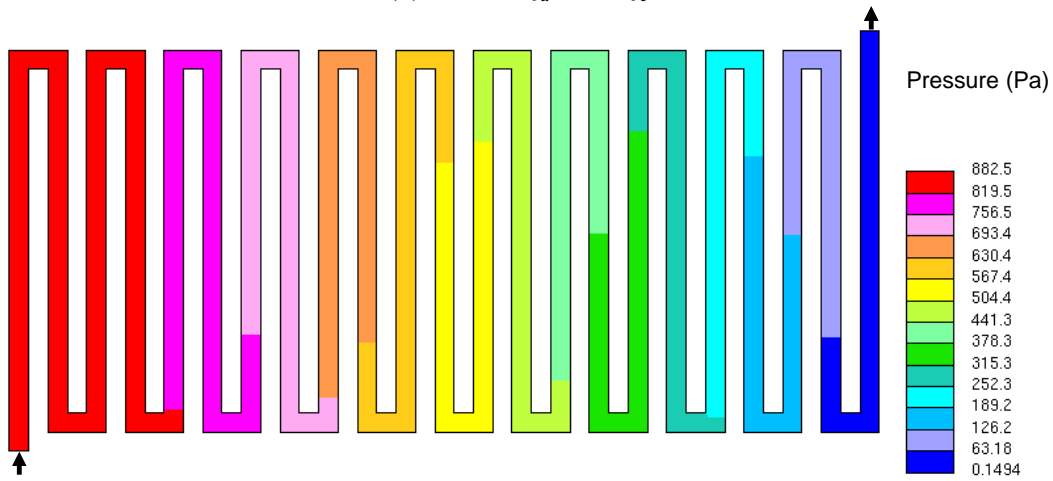
(c) Case C: $\zeta_a = 2.0$, $\zeta_c = 5.0$

Figure [2-16]   Pressure distribution in the anode channel
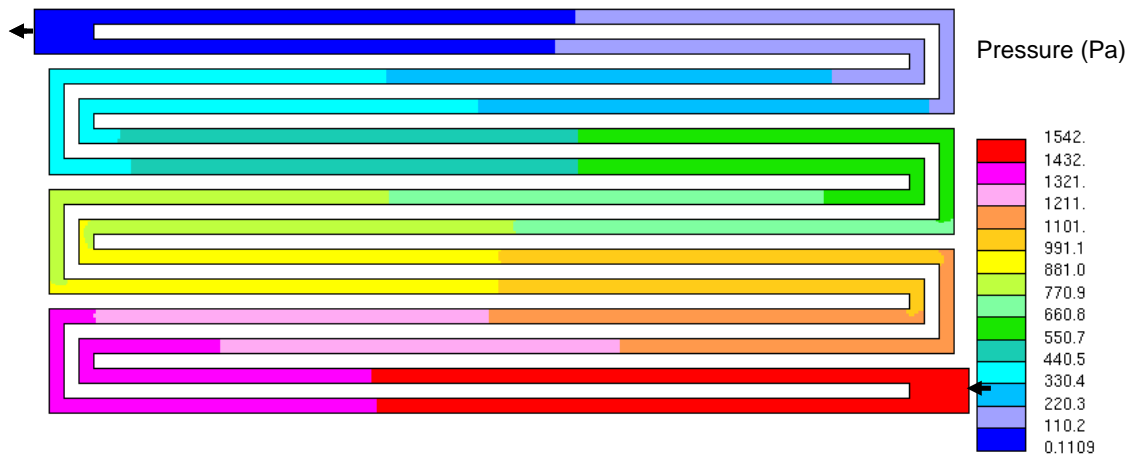
(a) Case A: $\zeta_a = 2.0$, $\zeta_c = 2.0$
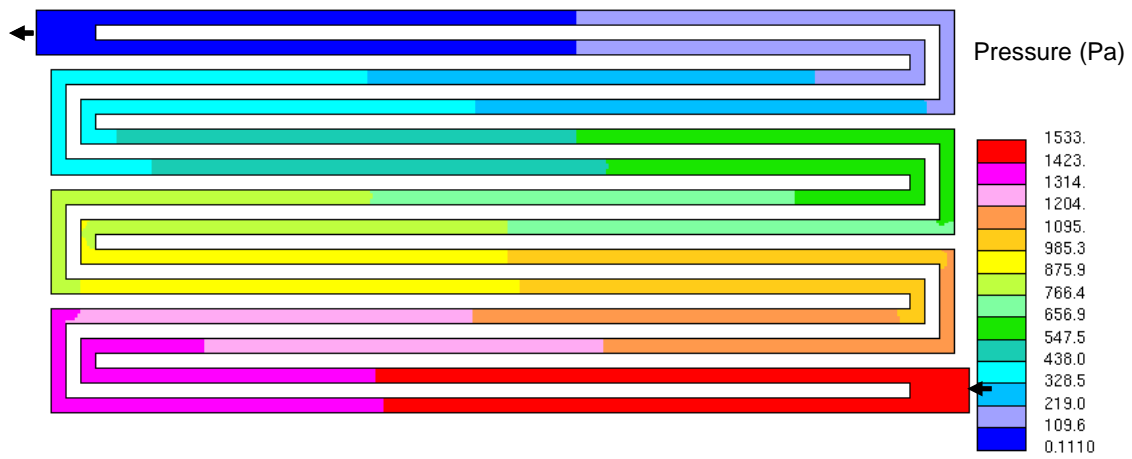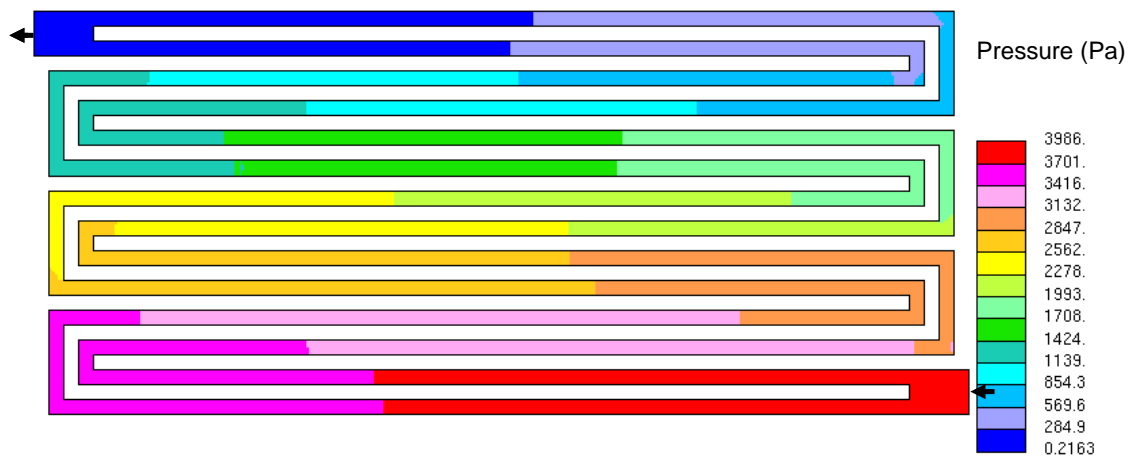
(b) Case B: $\zeta_a = 1.4$, $\zeta_c = 2.0$

(c) Case C: $\zeta_a = 2.0$, $\zeta_c = 5.0$

Figure [2-17]   Pressure distribution in the cathode channel
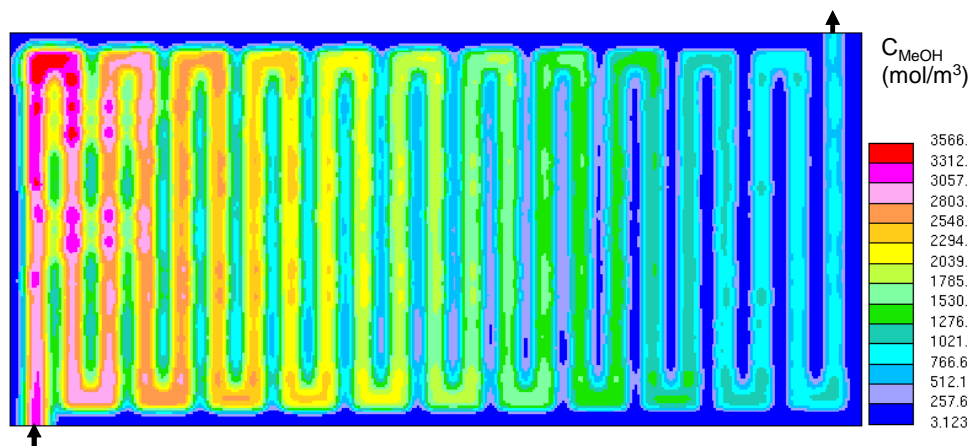
(a) Case A: $\zeta_a = 2.0$, $\zeta_c = 2.0$
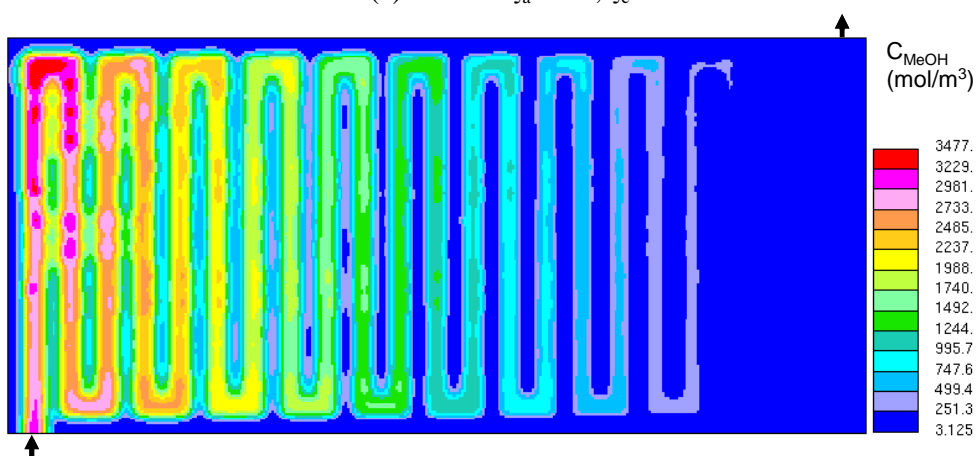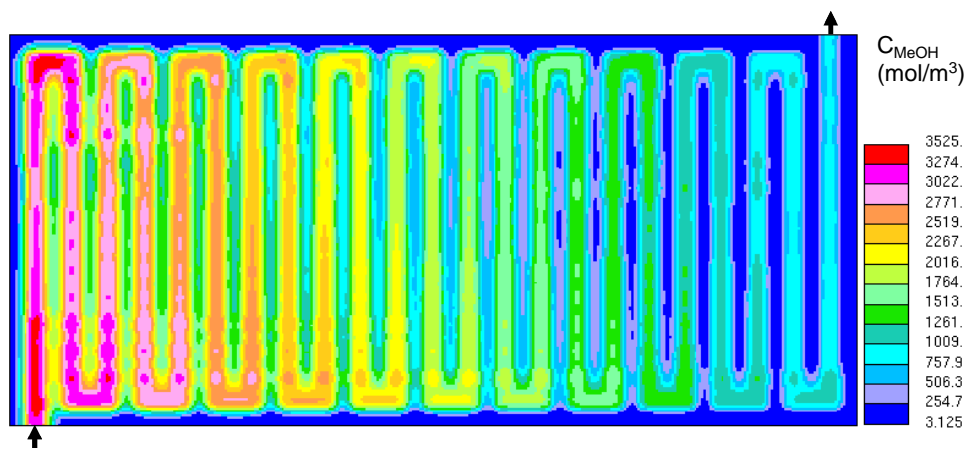
(b) Case B: $\zeta_a = 1.4$, $\zeta_c = 2.0$

(c) Case C: $\zeta_a = 2.0$, $\zeta_c = 5.0$

Figure [2-18]   Methanol concentration in ACL according to the operating condition

(a) Case A: ζ_a= 2.0, ζ_c=2.0

(b) Case B: ζ_a= 1.4, ζ_c=2.0
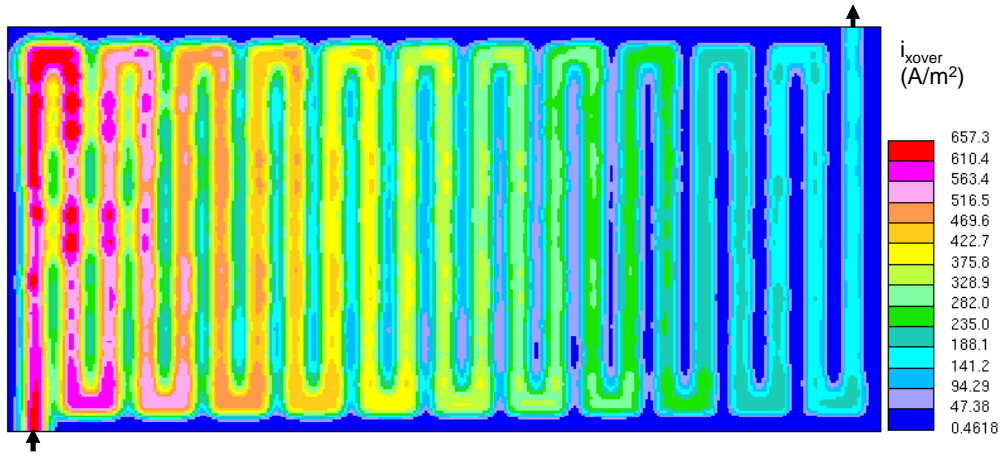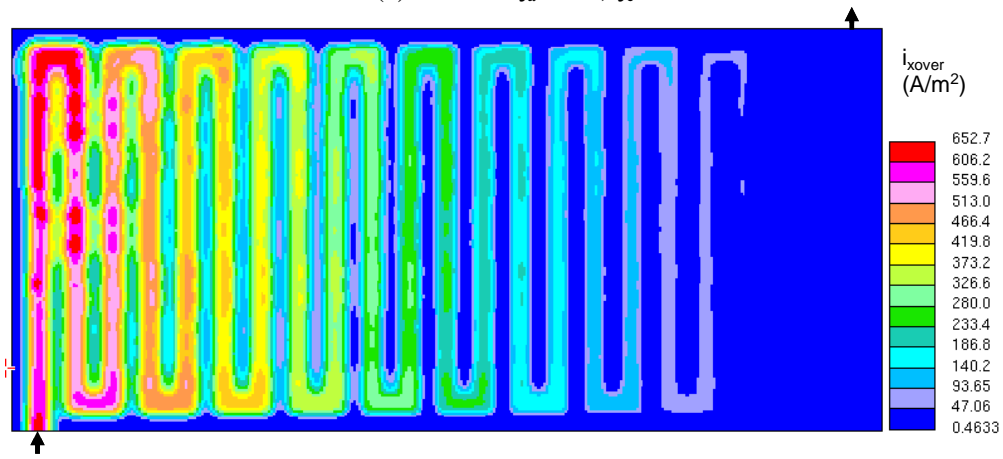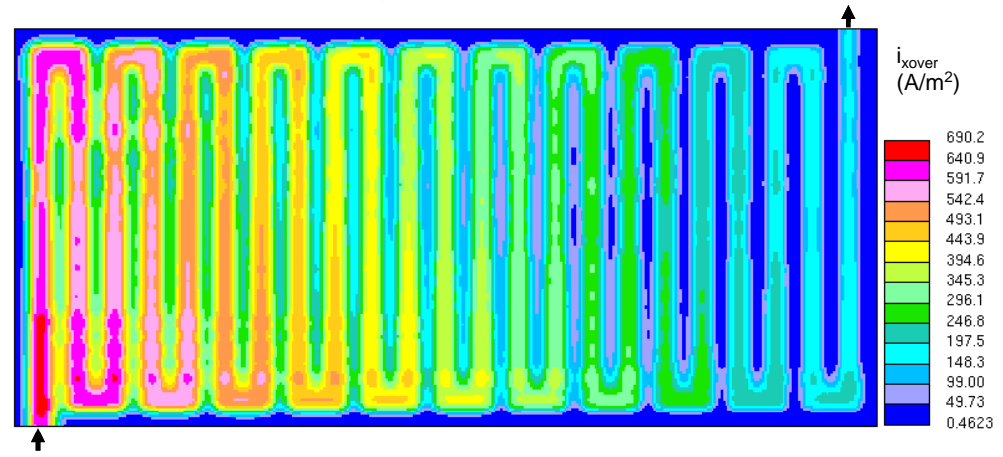
(c) Case C: ζ_a= 2.0, ζ_c=5.0

Figure [2-19]   Crossover current density distribution

(a) Case A: $\zeta_a = 2.0$, $\zeta_c = 2.0$

(b) Case B: $\zeta_a = 1.4$, $\zeta_c = 2.0$
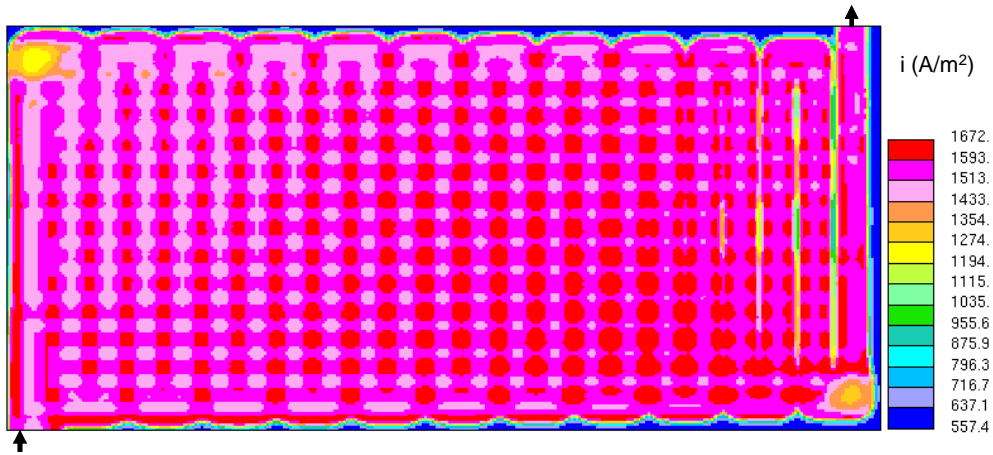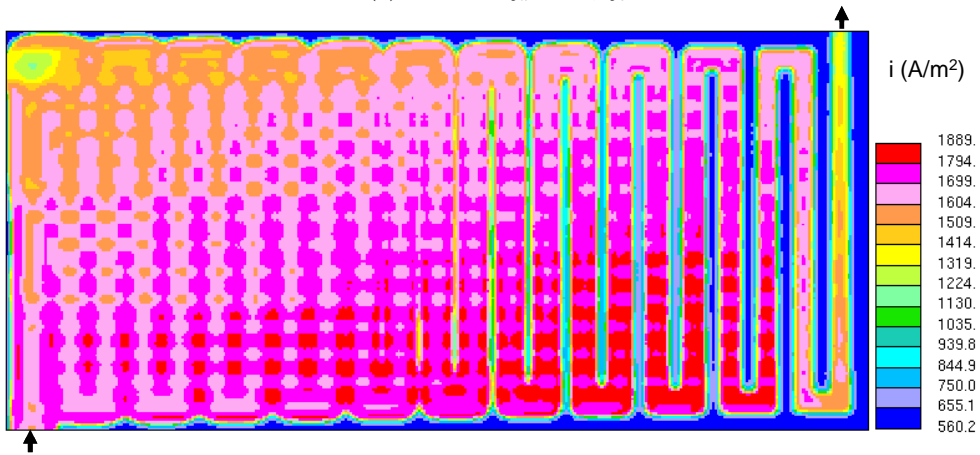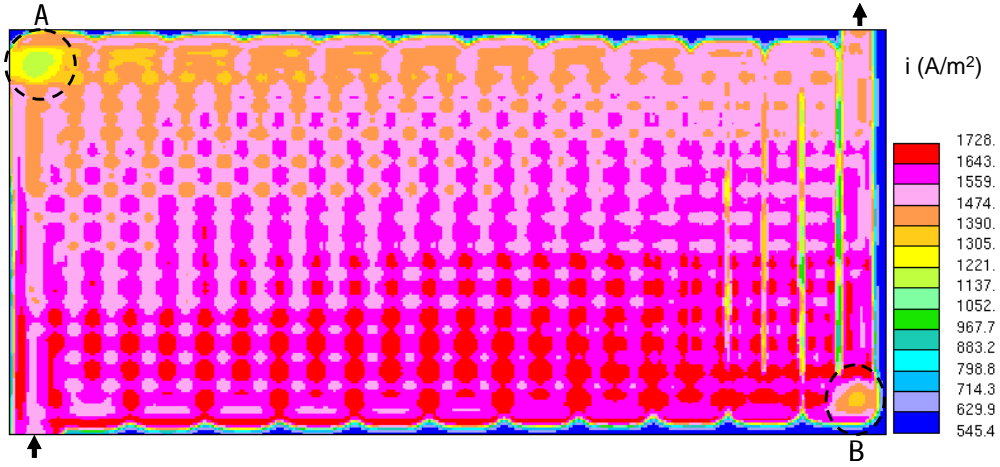
(c) Case C: $\zeta_a = 2.0$, $\zeta_c = 5.0$

Figure [2-20]   Current density distribution in the membrane

(a) Case A: ζ_a= 2.0, ζ_c=2.0

(b) Case B: ζ_a= 1.4, ζ_c=2.0
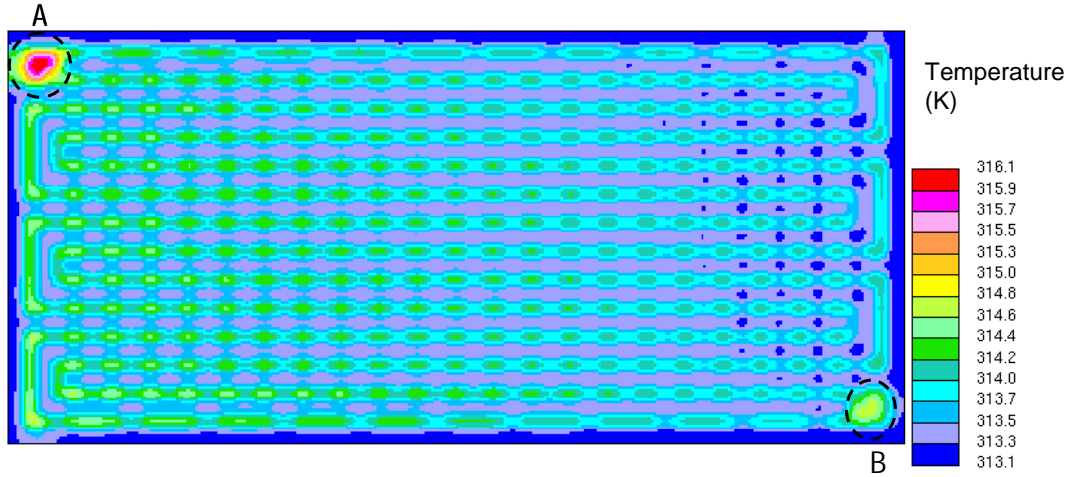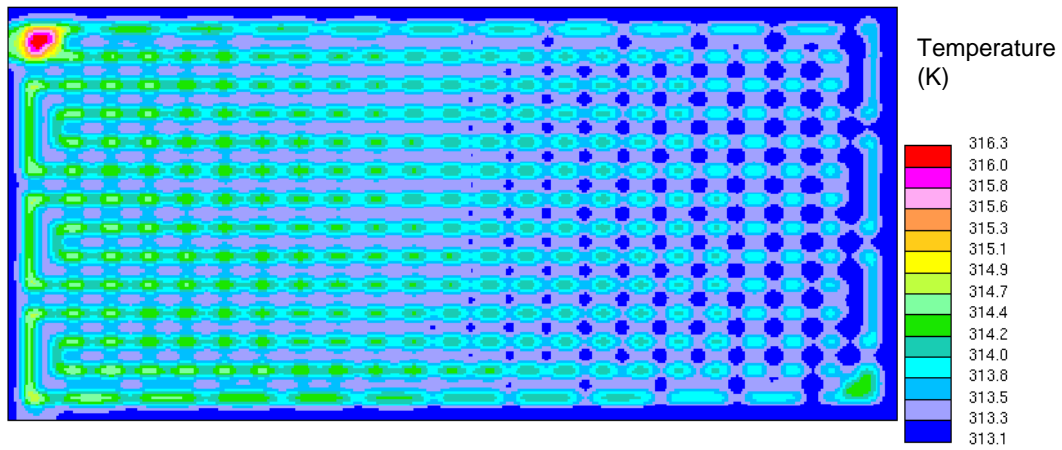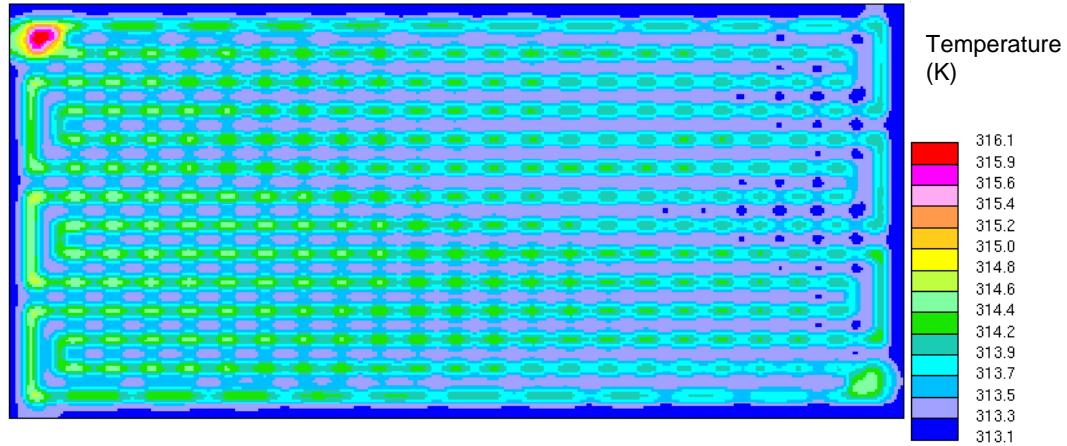
(c) Case C: ζ_a= 2.0, ζ_c=5.0

Figure [2-21]   Temperature distribution in the membrane

76
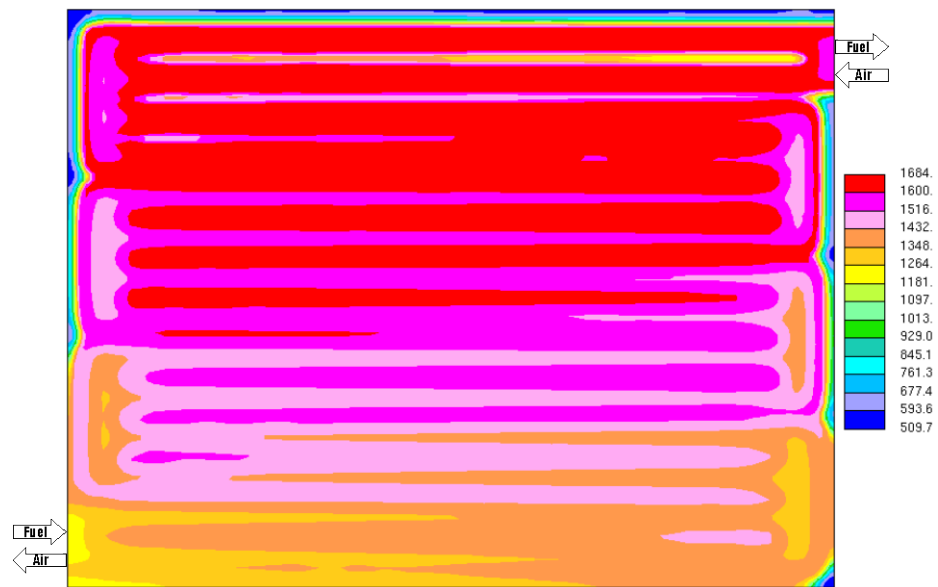
(a) co-flow

(b) counter-flow

Figure [2-22]   Current density (A/m^2) distribution of 12 cm^2 cell ($\zeta_a = 2.0$, $\zeta_c = 2.0$)
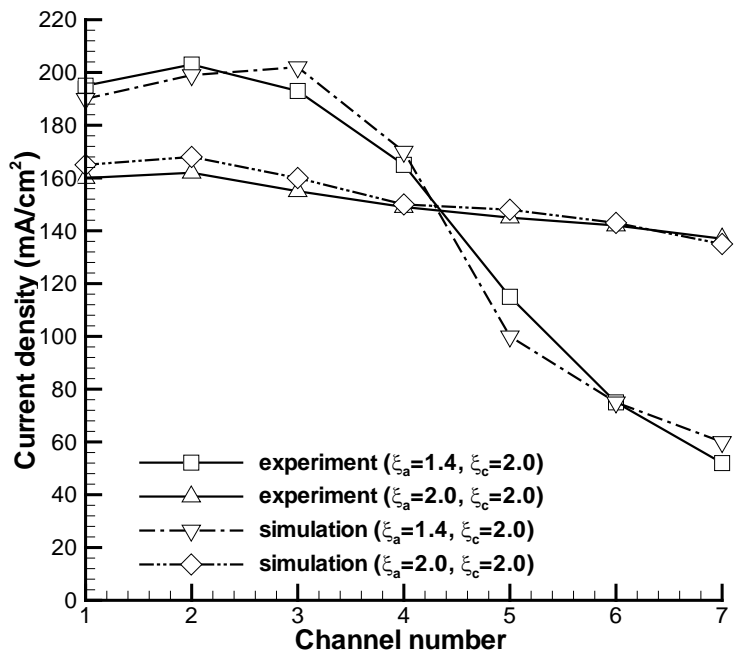
(a) co-flow
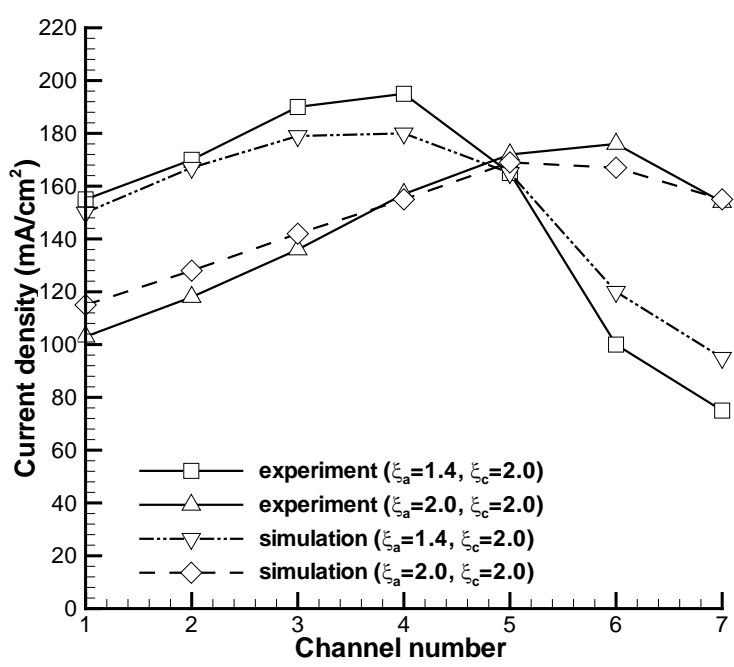
(b) counter-flow

Figure [2-23]   Current density distribution of 12 cm^2 cell (comparison experimental data with simulated result). Experimental data provided by Panasonic Inc.

TABLES

Table [2-1]   Effect of flow stoichiometry on cell performance (single channel model)

	T_{cell} (K)	RH (%)	C_{MeOH} (M)	ζ_a	ζ_c	I (mA/cm^2)	V_{cell} (V)	MCO (%)
Case A	313	10	4	1.4	2	150	0.409	12.0
Case B	313	10	4	2.4	2.4	150	0.455	19.1
Case C	313	10	4	5	5	150	0.461	28.1

Table [2-2]   Effect of MPL on cell performance (single channel model)

	Anode MPL	Cathode MPL	T_{cell} (K)	RH (%)	C_{meoh} (M)	ζ_a	ζ_c	I (mA/cm^2)	V_{cell} (V)	Alpha	MCO (%)
Case A	NO	NO	333	90	2.0	3.0	3.0	150	0.399	0.61	0.25
Case B	YES	NO	333	90	2.0	3.0	3.0	150	0.407	-0.08	0.20
Case C	NO	YES	333	90	2.0	3.0	3.0	150	0.400	0.55	0.25
Case D	YES	YES	333	90	2.0	3.0	3.0	150	0.407	-0.20	0.20

Table [2-3]   Calculation summary of full-scale DFMC simulation with serpentine channels (28 cm^2)

	T_{cell} (K)	RH (%)	C_{MeOH} (M)	ζ_a	ζ_c	I (mA/cm^2)	V_{cell} (V)	MCO (%)
Case A	313	10	4	2	2	150	0.459	13.7
Case B	313	10	4	1.4	2	150	0.428	9.2
Case C	313	10	4	2	5	150	0.466	14.4

Chapter 3

CO$_2$ Breathing DMFC and Role of CO$_2$ in Controlling Two-Phase Mass Transport in DMFC

3.1 Introduction

CO$_2$ production and problems in DMFC

During electrochemical reaction in a direct methanol fuel cell (DMFC), water is produced in the cathode from the oxygen reduction reaction (ORR) and CO$_2$ is produced in the anode from the methanol oxidation reaction (MOR) as a byproduct. In order to maintain steady cell operation, produced CO$_2$ should be removed from the cell. Produced CO$_2$ in ACL is basically in gas phase and is typically removed out of the cell through the anode flow field. As liquid fuel mixture is supplied from anode channel to porous media, CO$_2$ removal occurs in counter-flow direction to liquid flow direction. During this CO$_2$ removal process, it is observed that CO$_2$ gas brings on strong two-phase flow (bubbly flow or slug flow) in the anode flow field as shown in Figure [3-1], which causes large pressure drop. In addition, typically at high current density operation, CO$_2$ gas forms slugs which may block the interface between anode channel and gas diffusion media, which prevent liquid fuel from spreading into anode porous media, especially in the parallel channel.

Literature reviews about CO$_2$ in DMFC

There are some experimental studies about CO$_2$ in DMFC. Most of them focus on CO$_2$ flow behavior in the anode channel [33-40] or effective methods to remove CO$_2$

from DMFC [4, 5]. Some conducted experimental study about formation of CO_2 bubbles on the surface of gas diffusion layer and slug elongation, movement through the channel by using different manifold designs or gas diffusion layers in order to find better anode flow field for good removal of CO_2. Relatively few numerical studies focusing on CO_2 in DMFC have been published [41-44].

Argyropoulos *et al.* [33] stressed importance of CO_2 gas management. They conducted a visualizing experimental study using two DMFCs with different flow field designs. One was a simple parallel flow channel concept and the other was a cross-flow channel design concept. While the simple parallel channel design showed a tendency for gas slug formation blocking the anode channel, the cross-flow channel design showed bubbly flow characteristics rather than slug formation. In addition, they reported that large stoichiometry (or high anode velocity) is good for gas removal in the anode channel, which suggests that serpentine channel design is better than parallel channel design from a standpoint of gas removal. Scott *et al.* [4] studied the feasibility of using stainless steel mesh material as flow beds for DMFC in order to facilitate CO_2 removal. However, their cell didn't show significant performance improvement even though it was operated at 90ºC.

Lu *et al.* [34] observed that the pattern of CO_2 bubble generation is different according GDL material type. They conducted experiments with two kinds of MEA with transparent cells for flow visualization. One had GDL made of hydrophobic carbon paper and the other had GDL made of hydrophilic carbon cloth. With GDL made of the hydrophobic carbon paper (treated by PTFE), bubbles nucleated at certain locations non-uniformly. Due to the strong surface tension of hydrophobic GDL surface, bubbles grew

81

large and the bubble detachment was delayed to hinder efficient CO_2 removal. MEA made of carbon cloth showed tiny (~ 0.5 mm), uniform bubble generation on its surface, resulting in weak two-phase flow or good gas management characteristics.

Following Lu *et al.* [34], Yang *et al.* [35] conducted further visualization study of CO_2 behavior by placing DMFC in three different directions (vertical, anode-above MEA, anode-below MEA). They concluded vertical direction is best for cell performance because buoyancy force assists the removal of gas bubbles in the anode channel. In their succeeding paper [36], they conducted a parametrical study of the effect of anode flow field design on cell performance with serpentine channel design and parallel channel design by changing channel sizes. They reported that serpentine channel design with 50 % open ratio showed best performance. Parallel channel design showed CO_2 blockage and degraded the cell performance. Mench *et al.* [37] observed gas bubble emergence /detachment on the surface of gas diffusion layer with video microscopy. They explained that CO_2 removal occurs by two mechanisms: flow-induced removal and bubble coalescence. Bewer *et al.* [38] devised a unique method to simulate CO_2 bubble behavior in anode flow field using H_2O_2 solution without actual DMFC equipment. They tested flow field structures with several manifold designs and concluded that grid structure with splayed manifold is best for bubble discharge behavior from the cell. Liao *et al.* [39] studied the dynamic behavior of CO_2 gas bubbles by using a transparent cell. They observed the periodic process of emergence, growth, coalescence, detachment and sweeping of the gas bubble in detail. In addition, they explained that the period of this process strongly depends on anode flow rate (affects drag force on CO_2 bubbles), feed temperature (affects solubility of CO_2 bubbles) and cathode pressure (convective effect).

Wong *et al.* [40] conducted further study about the dynamic behavior of CO_2 gas bubbles in anode channel. They examined the residence time of CO_2 bubbles in anode channel by changing the channel size and found that gas slug size and residence time increase with reduction of anode channel size. Although the narrow channel impedes gas management due to its long gas residence time, it has higher mass transfer coefficient than wide channels. Therefore, there is balance between gas residence time with negative effect on cell performance and mass transfer coefficient with positive effect on cell performance. Their experimental result supported those ideas by showing that there is optimum channel size for cell performance and this result agrees with Yang *et al.*'s [36]. Lundin *et al.* [5] introduced a unique method to reduce CO_2 bubble formation in the anode channel by adding chemical agents like LiOH or KOH which increase CO_2 solubility to liquid fuel mixture. However, they didn't mention possible adverse consequences which may occur by adding such alkaline agents into fuel.

CO_2 breathing DMFC

In order to overcome problems caused by CO_2 flow in the anode channel, several methods have been suggested. MTI Microfuel Cells Inc. claimed two patents about CO_2 separation method. One uses gas permeable/liquid impermeable membrane which covers anode channels [45]. The other removes CO_2 through the composite membrane which plays as both proton conducting membrane and CO_2 separator [46]. Both cell designs remove CO_2 gas directly to the ambient, not through the anode channel. This is different from the conventional method which requires CO_2 separator outside of the cell. By adopting this kind of CO_2 removal method, the DMFC system can become very compact. Meng and Kim [47] developed a unique cell design which uses produced CO_2 as the

driving force delivering liquid fuel. CO_2 is finally removed from the anode channel to the ambient through porous membrane in their cell. From now on, we call this kind of DMFC which directly vents CO_2 to the ambient 'CO$_2$ breathing DMFC'.

The left figure in Figure [3-1(b)] shows the schematic of the CO_2 breathing DMFC designed for the present study by S.H. Jung and Y.J. Leng at ECEC group in The Pennsylvania State University. By attaching a gas-permeable/liquid-impermeable membrane such as PTFE film on the top of the anode bipolar plate, CO_2 can be directly removed to the ambient and almost pure liquid flows through the anode channel as shown the right figure.

Role of CO_2 in DMFC

This study investigates the role of CO_2 in a DMFC by conducting numerical modeling, which is important for two-phase transport of water and methanol.

3.2   Physical model

The present multi-D model is extended from the baseline model introduced in Chapter 2. Multi-D model consists of coupled PDEs (mass, momentum, species, proton transport and electron transport equations) with source terms as summarized in Appendix A. Constitutive relationships and parameters used in the model are listed in Appendix B. The present study focuses on the role of CO_2 in two-phase transport of water and methanol in a DMFC. The same cell geometry with the single channel model in Chapter 2 is used.

3.2.1 *Pressure drop in the anode channel*

In this part, two-phase pressure drop in the anode channel is estimated with one dimensional model. Figure [3-2] shows the schematic of the anode channel. Liquid fuel mixture is supplied to the channel inlet, and CO_2 gas produced (uniform production is assumed along the channel) in the catalyst layer is added to the channel flow. Therefore, void fraction in the channel increases and two-phase flow evolves along the channel. Our goal is to estimate the channel pressure drop according to the CO_2 amount.

For a control volume of Figure [3-2], gas mass flow rate (kg/s) is calculated by

$$\dot{m}_{g,k} = \frac{M^{CO_2}}{6F} i(y) W_{mem} y \tag{3-1}$$

and liquid mass flow rate is calculated by species consumption from MOR and methanol crossover as follows:

$$\dot{m}_{l,k} = \dot{m}_{l,k-1} - \frac{i(y)}{6F}\left(M^{H_2O} + M^{MeOH}\right)W_{mem}dy - D_{mem}^{MeOH}M^{MeOH}W_{mem}dy\frac{C_{acl}^{MeOH}(y)}{\delta_{mem}} \tag{3-2}$$

Then, gas mass fraction at location y becomes,

$$Y_g(y) = \frac{\dot{m}_g(y)}{\dot{m}_l(y)+\dot{m}_g(y)} \tag{3-3}$$

And liquid saturation, void fraction, and quality are found by,

$$
\begin{aligned}
s_l(y) &= \frac{\rho_g Y_l}{\rho_l(1-Y_l)+\rho_g Y_l} \\
\alpha(y) &= 1 - s_l(y) \\
x(y) &= \frac{\rho_g(1-s_l(y))}{\rho}
\end{aligned}
\tag{3-4}
$$

Therefore, velocities can be found as follows:

$$u_1(y) = \frac{\dot{m}_1(y)}{\rho_1 A_1(y)} = \frac{\dot{m}_1(y)}{\rho_1 A(y) s_1(y)}$$

$$u_g(y) = \frac{\dot{m}_g(y)}{\rho_g A_g(y)} = \frac{\dot{m}_g(y)}{\rho_1 A(y)(1 - s_1(y))}$$

$$u(y) = s_1 u_1 + (1 - s_1) u_g$$

(3-5)

The two-phase flow pattern parameters ($\rho_1 j_1^2$ and $\rho_g j_g^2$) are plotted in Figure [3-2(b)] according to the above model. Figure [3-3] shows the flow pattern maps developed by Hewitt and Roberts [48] and Mandhane [49]. Although flow pattern maps are not valid under all of flow conditions, the present anode channel is considered to belong to churn flow or slug flow for upward vertical flow configuration and stratified flow for horizontal flow configuration. However, as the channel flow rate is very low ($Re < 100$) and the channel is near micro-scale ($D_h < 1$ mm), actual flow pattern in a DMFC is more complex as shown in Figure [3-1].

According to the separated flow model, mass and momentum equation becomes as follows [50]:

$$W = GA = \rho Au$$

(3-6)

$$-\frac{dp}{dy} = \frac{1}{A}\frac{dF}{dy} + \frac{W^2}{A}\frac{d}{dy}\left[\frac{1}{A}\left\{\frac{x^2 v_g}{\alpha} + \frac{(1-x)^2 v_1}{1-\alpha}\right\}\right] + \left[(1-\alpha)\rho_1 + \alpha\rho_g\right]g\sin\theta$$

(3-7)

Assuming homogeneous flow, above momentum equation is simplified as [51],

$$-\frac{dp}{dy} = \frac{1}{A}\frac{dF}{dy} + \frac{W}{A}\frac{du}{dy} + \frac{g\sin\theta}{v} = -\frac{dp}{dy}\bigg|_{\text{friction}} - \frac{dp}{dy}\bigg|_{\text{ineritial}} - \frac{dp}{dy}\bigg|_{\text{gravity}}$$

$$\text{where } v = \frac{1}{\rho} = \frac{1}{\rho_g \alpha + \rho_l(1-\alpha)}$$

(3-8)

The frictional term in the above equation is simplified as,

$$-\frac{dp}{dy}\bigg|_{\text{friction}} = \frac{2fG^2}{D_h\rho} \quad \text{where} \begin{cases} Re = \dfrac{GD_h}{\mu} \\[2mm] G = \rho u \\[2mm] \dfrac{1}{\mu} = \dfrac{x}{\mu_g} + \dfrac{1-x}{\mu_l} \quad (McAdam\text{'s model}) \\[2mm] f = \dfrac{16}{Re} \quad (\text{laminar: } Re < 100) \\[2mm] x = \dfrac{\rho_g(1-s_l)}{\rho} \quad (\text{quality}) \end{cases}$$

(3-9)

If the flow is assumed to be separated-flow with high Reynolds number (turbulent flow), the frictional term becomes as follows:

$$-\frac{dp}{dy}\bigg|_{\text{friction}} = \frac{2f_{f0}G^2}{D_h\rho}\phi_{f0}^2 \quad \text{where} \begin{cases} G = \rho u \\[2mm] f_{f0} \quad (\text{friction factor of pure liquid flow}) \\[2mm] \phi_{f0}^2 \quad (\text{two-phase frictional multiplier}) \\[2mm] x = \dfrac{\rho_g(1-s_l)}{\rho} \quad (\text{quality}) \end{cases}$$

(3-10)

By assuming turbulent-turbulent two-phase flow in a circular pipe, Martinelli and Nelson [52] experimentally found that two-phase frictional multiplier (ϕ_{f0}^2) is a strong function of pressure and quality. Under the ambient pressure condition (1 bar), two-phase frictional multiplier (ϕ_{f0}^2) can be as high as 500 depending on the quality (x).

When cross-section is constant, the inertial term is simplified as,

$$-\frac{dp}{dy}\bigg|_{\text{inertial}} = G^2 v_{\text{fg}} \frac{dx}{dy}$$

(3-11)

Gravity term is ignored here. Total pressure drop in the anode channel is found by integrating above equation and Figure [3-4] shows the calculation result. 100% CO_2 removal means the CO_2 breathing DMFC which has almost pure liquid flow in the anode channel whereas 0% CO_2 removal means the conventional DMFC which exhausts CO_2 through the channel outlet (gaseous channel). As the CO_2 removal rate increases, the channel pressure drop decreases significantly. In other words, required pumping power for fuel supply will be minimized with the CO_2 breathing DMFC.

3.2.2   *Two-phase water transport and relationship with CO_2*

A general form of multi-phase species equation by M^2 model [21] can be expressed as follows.

$$\nabla \cdot (\gamma \rho \vec{u} Y^k) = \nabla \cdot \left[\rho_l D_{l,\text{eff}}^k \nabla Y_l^k + \rho_g D_{g,\text{eff}}^k \nabla Y_g^k \right] - \nabla \cdot \left[\left(Y_l^k - Y_g^k \right) \vec{j}_l \right] + M^k S^k$$

(3-12)

The left term represents convectional term which is significant in the flow channel region. The first term on the right hand side represents the molecular diffusive term and second term is phase-diffusive term or capillary flux, which is significant in the porous region. Capillary flux of liquid phase is driven by capillary pressure, which forms by the result of liquid saturation gradient as

$$\vec{j}_l = \frac{\lambda_g \lambda_l K}{v} \nabla p_c = \frac{\lambda_g \lambda_l K}{v} \nabla \left[\sigma \cos(\theta_c) \left(\frac{\varepsilon}{K} \right)^{1/2} J(s) \right] = \frac{\lambda_g \lambda_l \sigma \cos(\theta_c)(K\varepsilon)^{1/2}}{v} \frac{dJ}{ds} \nabla s$$

(3-13)

and the liquid saturation shown above equation is defined as follows:

$$s = \frac{V_l}{V_{pore}} = 1 - \frac{V_g}{V_{pore}} = \frac{\rho_g \left(1 - Y^{CO_2}\right)}{\rho_l Y^{CO_2} + \rho_g \left(1 - Y^{CO_2}\right)} \tag{3-14}$$

Note that the CO_2 fraction has a strong influence on the liquid saturation in Eq. (3-14) since the large amount of gas in the anode consists of CO_2. If there is no CO_2, liquid saturation in the anode channel becomes almost 1. In addition, it can be easily conjectured that the large amount of CO_2 in the anode will lead to lower water crossover to the cathode side by building dry condition in porous media. CO_2 amount in the anode is defined as CO_2 level as follows in this study.

$$CO_2 \text{ Level} = \int_V \frac{\rho_g \left(1 - s_l\right)}{\sum_k M^k X^k} \left(1 - \frac{C_{sat}^{H_2O} M^{H_2O}}{\rho_g^{H_2O}} - \frac{C_l^{MeOH} M^{MeOH}}{\rho_g^{MeOH} k_H}\right) \ [\text{mol/m}^3] \tag{3-15}$$

By plugging Eq. (3-14) into Eq. (3-13), capillary diffusive flux can be reformed as follows:

$$\vec{j}_l = \frac{\lambda_g \lambda_l \sigma \cos(\theta_c)(K\varepsilon)^{1/2}}{\nu} \frac{dJ}{ds} \frac{\rho_l \left(\rho_g Y_l^{H_2O} - \rho_g Y_g^{H_2O}\right)}{\left(\rho_l Y_l^{H_2O} - \rho_l Y^{H_2O} + \rho_g Y^{H_2O} - \rho_g Y_g^{H_2O}\right)^2} \nabla Y^{H_2O} \tag{3-16}$$

Assuming water concentration in gas phase is always saturated and gradient of mass fraction in liquid phase is almost zero due to dilute solution, water transport equation can be derived from Eq. (3-12) with Eq. (3-16) as follows:

$$\nabla \cdot \left(\gamma \rho \vec{u} Y^{H_2O}\right) = \nabla \cdot \left[\rho D_{capill} \nabla Y^{H_2O}\right] + M^{H_2O} S^{H_2O} \tag{3-17}$$

This equation explains how water is transported by capillary diffusion in porous media with capillary diffusivity

$$D_{\text{capill}} = \frac{1}{\rho}\left(Y_1^{H_2O} - Y_g^{H_2O}\right)\frac{\lambda_g\lambda_1\sigma\left|\cos(\theta_c)\right|(K\varepsilon)^{1/2}}{\nu}\frac{dJ}{ds}\frac{\rho_1\left(\rho_gY_1^{H_2O} - \rho_gY_g^{H_2O}\right)}{\left(\rho_1Y_1^{H_2O} - \rho_1Y^{H_2O} + \rho_gY^{H_2O} - \rho_gY_g^{H_2O}\right)^2} \quad (3\text{-}18)$$

Capillary diffusivity shown above is a complex function of material properties (porosity, permeability and contact angle), species composition and liquid saturation. Since liquid saturation is determined by the amount of CO_2 in porous media, it is predicted that a large amount of CO_2 may reduce capillary transport in porous media.

3.2.3   Two-phase methanol transport and relationship with CO_2

Assuming vapor-liquid equilibrium of methanol in the anode, methanol mass fraction can be expressed by Henry's law as follows:

$$Y^{\text{MeOH}} = \frac{\rho_1}{\rho}\left(s + \frac{1-s}{k_H}\right)Y_1^{\text{MeOH}} \quad (3\text{-}19)$$

Therefore, the methanol transport equation can be summarized from Eq. (3-12).

$$\nabla\cdot\left(\rho\vec{u}Y_1^{\text{MeOH}}\right) = \nabla\cdot\left[\rho_1\left(D_{\text{l,eff}}^{\text{MeOH}} + \frac{D_{\text{g,eff}}^{\text{MeOH}}}{k_H}\right)\nabla\cdot Y_1^{\text{MeOH}}\right] - \nabla\cdot\left[\left(Y_1^{\text{MeOH}} - Y_g^{\text{MeOH}}\right)\vec{j}_1\right] + M^{\text{MeOH}}S^{\text{MeOH}} \quad (3\text{-}20)$$

Examining the above equation, methanol transport in porous media is controlled by two important physics. The first term on the right hand side in Eq. (3-20) expresses the two-phase molecular diffusion. Since molecular diffusion of methanol is carried out by both liquid phase and gas phase, we define two-phase molecular diffusivity of methanol as follows:

$$D_{\text{mol}}^{\text{MeOH}} = \frac{\rho_1}{\rho}\left(D_{\text{l,eff}}^{\text{MeOH}} + \frac{D_{\text{g,eff}}^{\text{MeOH}}}{k_H}\right) = \frac{\rho_1}{\rho}\left(D_1^{\text{MeOH}}s^n + \frac{D_g^{\text{MeOH}}(1-s)^n}{k_H}\right)\varepsilon^n \quad (3\text{-}21)$$

Two-phase molecular diffusivity of methanol is a strong function of liquid saturation, and porosity as shown in Figure [3-5]. The second term on the right hand side of Eq. (3-20) represents capillary diffusion of methanol, which is difficult to deal with as it is. We transform this term to a unified diffusive term as follows: First, combining Eq. (3-16) and Eq. (3-18), liquid phase flux becomes,

$$\vec{j}_l = \frac{\rho D_{\text{capill}}}{Y_l^{H_2O} - Y_g^{H_2O}} \nabla Y^{H_2O} \tag{3-22}$$

Therefore, methanol capillary term becomes,

$$M^{\text{MeOH}} S_{\text{capill}}^{\text{MeOH}} = -\nabla \cdot \left[\left(Y_l^{\text{MeOH}} - Y_g^{\text{MeOH}} \right) \vec{j}_l \right] = \nabla \cdot \left[Y_l^{\text{MeOH}} \left(\frac{\rho_l}{\rho_g k_H} - 1 \right) \vec{j}_l \right]$$

$$= -\nabla \cdot \left[Y_l^{\text{MeOH}} \left(1 - \frac{\rho_l}{\rho_g k_H} \right) \frac{\rho D_{\text{capill}}}{Y_l^{H_2O} - Y_g^{H_2O}} \nabla Y^{H_2O} \right] = \nabla \cdot \left[\rho \nabla D_{\text{capill}}^{\text{MeOH}} Y_l^{\text{MeOH}} \right] \tag{3-23}$$

Methanol capillary diffusivity in the above equation is expressed as:

$$D_{\text{capill}}^{\text{MeOH}} = D_{\text{capill}} \psi$$

$$\text{where} \quad \psi = \left(1 - \frac{\rho_l}{\rho_g k_H} \right) \frac{Y_l^{\text{MeOH}}}{Y_l^{H_2O} - Y_g^{H_2O}} \tag{3-24}$$

In the above equation, CO_2 level affects liquid phase capillary diffusivity (D_{capill}) whereas cell temperature and methanol concentration strongly affects methanol capillary factor (ψ). Figure [3-6] shows that the methanol capillary factor becomes large when the liquid mixture is highly concentrated and temperature is low. However, even though methanol capillary factor is high, methanol capillary diffusivity may remain low if the cell operates at very low flow stoichiometry. This is because liquid phase diffusivity becomes very low under such a gaseous condition (or high CO_2 level environment). In contrast, there will be

no methanol capillary diffusion also if the porous media is filled with pure liquid. Finally, the methanol transport equation becomes,

$$\nabla \cdot \left(\rho \vec{u} Y_l^{\text{MeOH}} \right) = \nabla \cdot \left[\rho D_{\text{eff}}^{\text{MeOH}} \nabla \cdot Y_l^{\text{MeOH}} \right] + M^{\text{MeOH}} S^{\text{MeOH}} \tag{3-25}$$

The effective methanol diffusivity in the above equation is,

$$D_{\text{eff}}^{\text{MeOH}} = D_{\text{mol}}^{\text{MeOH}} + D_{\text{capill}}^{\text{MeOH}} \tag{3-26}$$

It is important to identify which transport physics dominates in fuel delivery in order to control fuel delivery and optimize the anode design under given operational condition. For example, under ultra-low anode flow rate condition, the anode becomes very gaseous and fuel delivery is dominated by molecular diffusion.

3.2.4 CO_2 surface removal

In reality, CO_2 removal amount through the surface film is affected by the material properties of the surface film such as porosity and permeability. Instead, the present study simulates CO_2 surface removal amount by applying a CO_2 species sink near the surface film. When this removal amount is zero, the model represents a conventional DMFC which removes all of CO_2 gas through the outlet port, whereas 100 % amount of CO_2 surface removal represents the ideal CO_2 breathing DMFC which has a pure liquid flow in the anode channel.

3.3   Results and Discussion

3.3.1   CO₂ removal and pressure drop

In a conventional DMFC, produced CO_2 accumulates and void fraction increases in the channel direction. This two-phase flow causes a large pressure drop in the channel. The present multi-D model described here applies a homogeneous flow model in the anode flow channel. This assumes the gas and liquid phase are completely mixed and they move with the same velocity. When CO_2 is directly removed to the ambient through the surface film, CO_2 accumulation is reduced and average liquid saturation increases. Channel void fraction according to anode flow stoichiometry and CO_2 removal amount are presented in Figure [3-7].

When CO_2 surface removal rate is large, channel void fraction becomes relatively uniform compared to the conventional cell. Figures [3-8] and [3-9] show the liquid saturation distribution in the anode. Liquid saturation in the anode GDL of CO_2 breathing cell is very uniform compared to the conventional cell. By avoiding strong two-phase flow in the channel, pressure drop in the channel can be significantly reduced as shown in Figure [3-10]. It is estimated that CO_2 breathing cell which completely removes CO_2 through the surface film requires only 10 % of the pumping power of the conventional DMFC, which contributes to improving the new power throughput. In addition, reduced pumping power leads to smaller pump and reduced manufacturing cost.

3.3.2   Role of CO₂ in water management

The conventional cell shows gradually decreasing saturation along the channel whereas the CO_2 breathing cell shows very uniform saturation in the GDL since CO_2 is

93

not accumulated as shown in Figure [3-8]. In other words, the CO_2 breathing cell has a wetter anode than the conventional cell. In both cases, the region under the anode land is gaseous (low liquid saturation) since CO_2 removal from ACL is blocked there. On the contrary, the region under the cathode land is quite wet (high liquid saturation) since water removal from CCL is blocked by the cathode land. Therefore, water back-diffusion strongly occurs under the land region, which leads to a lower local water transfer coefficient value there. Figure [3-9] shows saturation distribution in a different view. Overall, the CO_2 breathing cell shows uniformly wetter anode porous media compared to the conventional cell since CO_2 surface removal occurs uniformly everywhere on the surface film, which implies that the CO_2 breathing cell has more uniform and larger water transfer coefficient than the conventional cell. Local water transfer coefficients of both cells are presented in Figure [3-11]. The conventional cell shows a large water transfer coefficient value at the inlet region where the anode is very wet and cathode is dry. In contrast, the CO_2 breathing cell shows relatively uniform distribution of water transfer coefficient value due to minimal CO_2 accumulation. This means more water is lost to the cathode than in the conventional cell. In both cells, the water transfer coefficient is low under the land region due to gaseous environment in the anode and wet environment in the cathode.

As the operating current density increases, the anode becomes more gaseous due to the large amount of CO_2 production by MOR in ACL as shown in Figure [3-12(a)] and, definitely, CO_2 level decreases as CO_2 surface removal increases. Figure [3-12(b)] shows that the water transfer coefficient becomes large as CO_2 level decreases or CO_2 surface

removal increases. This simply implies that maintaining high CO_2 level helps to reduce the water transfer coefficient.

3.3.3 Role of CO_2 in methanol transport

Controlling methanol transport is important for steady operation of a DMFC. Too much methanol supply results in severe methanol crossover which degrades both cell performance and fuel efficiency. In contrast, the cell may shut down if too little methanol is delivered to the catalyst layer. As discussed, methanol is transported by molecular diffusion and capillary diffusion in the anode. CO_2 plays an important role for both two-phase transport mechanisms, depending on the cell operating condition such as flow rate, temperature and methanol concentration. Effective methanol diffusivity, consisting of two-phase molecular diffusivity and capillary diffusivity, expresses methanol delivery capability in anode porous media.

Methanol diffusivity analysis in the anode is shown in Figure [3-13] according to cell temperature and CO_2 surface removal rate. CO_2 level affects the capillary diffusivity (see Eq. (3-18)) and cell temperature strongly affects methanol capillary factor (see Eq. (3-24)). When the cell operates at high temperature (333K) without CO_2 surface removal (conventional DMFC), two-phase molecular diffusion is the dominant mechanism of methanol transport as shown in Figure [3-13(a)]. Capillary diffusion is strong only at the inlet region and rapidly decreases since the anode becomes gaseous due to CO_2 accumulation (low liquid phase capillary diffusivity) and methanol concentration decreases in the channel direction by methanol consumption, i.e., methanol capillary factor decreases. As vapor/liquid molecular diffusivity of methanol becomes high at high temperature and two-phase molecular diffusivity of methanol is high under gaseous

environment (see Figure [3-5]), two-phase molecular diffusivity of methanol increases in the channel direction and becomes the dominant mechanism of methanol transport. In the case of the CO_2 breathing cell operating at high temperature (Figure [3-13(b)]), two-phase molecular diffusivity remains almost uniform in the channel direction due to CO_2 surface removal. Although liquid saturation level is uniform in the channel direction, methanol capillary diffusivity linearly decreases because methanol concentration decreases due to methanol consumption by MOR. When the cell temperature is low, methanol molecular diffusivity decreases but methanol capillary diffusivity increases. Overall effective diffusivity is reduced compared to the high temperature case in the conventional cell (Figure [3-13(c)]). Methanol capillary diffusion becomes dominant in the CO_2 breathing cell at low temperature as shown in Figure [3-13(d)]. Methanol concentration distributions in the anode of both cells operating under base condition (T_{cell} = 333 K, I=150 mA/cm^2, ξ_a=3.0, ξ_c=3.0) are compared in Figure [3-14]. As both cells have similar effective methanol diffusivity, methanol concentration distributions are similar also.

CO_2 contributes to improving methanol molecular diffusion but prohibits methanol capillary diffusion. Although two-phase molecular diffusivity and capillary diffusivity of methanol are significantly affected by CO_2 level, effective methanol diffusivity which is the sum of both diffusivities, does not vary so much as shown in Figure [3-13]. This implies that the anode performance of the CO_2 breathing DMFC should be not so different than that of the conventional DMFC. If there is no CO_2 in the anode porous media, there is no methanol capillary transport since saturation is uniform everywhere and molecular diffusion occurs solely in liquid-phase, which is very low. Therefore, net

methanol transport will be very poor. In that sense, maintaining some level of CO_2 inside the anode porous media is necessary for facilitating fuel transport. Even the CO_2 breathing DMFC, which has almost pure liquid flow in the anode channel, has a significant level of CO_2 inside the anode porous media, which enables the CO_2 breathing DMFC to have similar anode performance to the conventional DMFC.

3.3.4   Current density and crossover current density

When the cathode condition is the same, methanol concentration distribution strongly affects current density and crossover current density distribution for the conventional cell and CO_2 breathing cell. As shown in Figure [3-14], both cells have similar distribution of methanol concentration since they have similar effective methanol diffusivity. Current density and crossover current density distribution of the conventional cell operating under base condition are presented in Figure [3-15(a)] and [3-15(b)]. Since the CO_2 breathing cell shows similar result with the conventional cell, it is neglected here. Calculation results show that current density is high under the land region rather than under the channel region. This is because stoichiometry is large enough. Excessive amount of methanol, especially under the channel region, negatively acts by increasing methanol crossover, which leads to large anode overpotential and lower current density. As methanol concentration under the channel region is high, crossover current density is high there.

3.3.5   DMFC system efficiency

Polarization curves according to CO_2 surface removal and cell temperature are plotted in Figure [3-16]. In low current regime, lower temperature is better for cell performance

97

than higher temperature. When the cell operates at low current, methanol concentration near the anode catalyst layer becomes high since methanol consumption is low. This high methanol concentration leads to high methanol crossover. In addition, if the cell temperature is high, methanol diffusivity of the membrane becomes large. Therefore, crossover current density becomes larger and cell voltage drops a bit.

Although the conventional cell and the CO_2 breathing cell show similar polarization curves, one interesting difference is noted between the low temperature case and the high temperature case. Under the high temperature condition, the conventional cell shows a bit better performance than the CO_2 breathing cell at high current regime, whereas the CO_2 breathing cell shows better performance at low temperature. In the conventional cell, the methanol molecular diffusivity is always dominant over the methanol capillary diffusivity. Therefore, high temperature acts positively for the methanol transport. However, in the CO_2 breathing cell, methanol capillary diffusivity becomes dominant over the methanol molecular diffusivity at low temperature, which extends the limiting current density.

Figure [3-17(a)] shows the net power throughput according to the CO_2 removal amount. Although the cell polarization curve of the CO_2 breathing DMFC is similar to that of the conventional DMFC, cell performance is improved by saving pumping power required for fuel supply. The total system efficiency calculated by Eq. (1-13) according to the CO_2 removal is presented in Figure [3-17(b)].

3.4   Experimental validation

The present CO_2 breathing DMFC was design by Y.J. Leng and S.H. Jung at ECEC. Cell fabrication and experiment were conducted by Y.J. Leng. Experimental results were

used for the model validation. Leng's test cell is specially constructed to compare the CO_2 breathing cell with the conventional cell. By covering the anode channel with a solid block, the conventional DMFC which removes CO_2 to the outlet port is simulated. By replacing the solid block with a gas-permeable (and liquid-impermeable) surface film made of PTFE, the CO_2 breathing cell which directly removes CO_2 gas through the surface film can be simulated. Experimental setup is shown in Figure [3-18]. Experimental results are presented in Figure [3-19]. The CO_2 breathing cell shows similar or slightly better performance compared to the conventional cell at 313K. This result agrees with the numerical prediction, which says the effect of methanol capillary diffusion becomes stronger when CO_2 is removed through the surface film under low temperature condition.

3.5   Conclusion

By venting CO_2 gas directly to the ambient through the surface film, CO_2 breathing DMFC could avoid strong channel two-phase flow and significantly reduce channel pressure drop, and it is expected that the CO_2 breathing DMFC will be free of channel clogging problem caused by CO_2 slugs in the anode channel.

The role of CO_2 in water transport in a DMFC is investigated through the multi-D modeling study. As CO_2 level decreases, the water transfer coefficient is estimated to increase since CO_2 level controls capillary diffusivity and low CO_2 level builds wet condition in the anode, which drives much more water flux to the cathode side. The CO_2 breathing DMFC has uniformly wet anode porous media since CO_2 does not accumulate

along the channel, which results in a larger water transfer coefficient than the conventional DMFC.

Fundamental analysis of two-phase methanol transport in a DMFC and the role of CO_2 in methanol transport are first elucidated. Methanol transport in a DMFC is carried out by two-phase molecular diffusion and methanol capillary diffusion. It is found that CO_2 level controls molecular diffusion and capillary diffusion of methanol. When CO_2 level is high, two-phase molecular diffusion is enhanced while methanol capillary diffusion is suppressed. However, it is also found that CO_2 surface removal does not have as much effect on the methanol transport because the sum of molecular diffusivity and capillary diffusivity (the effective methanol diffusivity) is maintained at constant level, especially at high temperature. Therefore, the calculation result shows that the cell performance of the conventional cell and CO_2 breathing cell is not so much different although operating temperature has some effect in high current density regime, which agrees with the trend of experimental results. Improvement of the net energy efficiency came from the increased mechanical efficiency due to lowered anode pressure drop.

As the present CO_2 breathing DMFC has a unit cell, the cell directly expels CO_2 gas to the ambient through the surface film. However, actual DMFC system may consist of several cells by building a stack. In that case, CO_2 breathing DMFC should expel anode effluent to the cathode channel through the surface film separating the anode from the cathode. This anode effluent contains not only CO_2 but also methanol vapor and water vapor. Therefore, it is meaningful to understand what influence this effluent has on the cell performance.

FIGURES

(a)

(b)
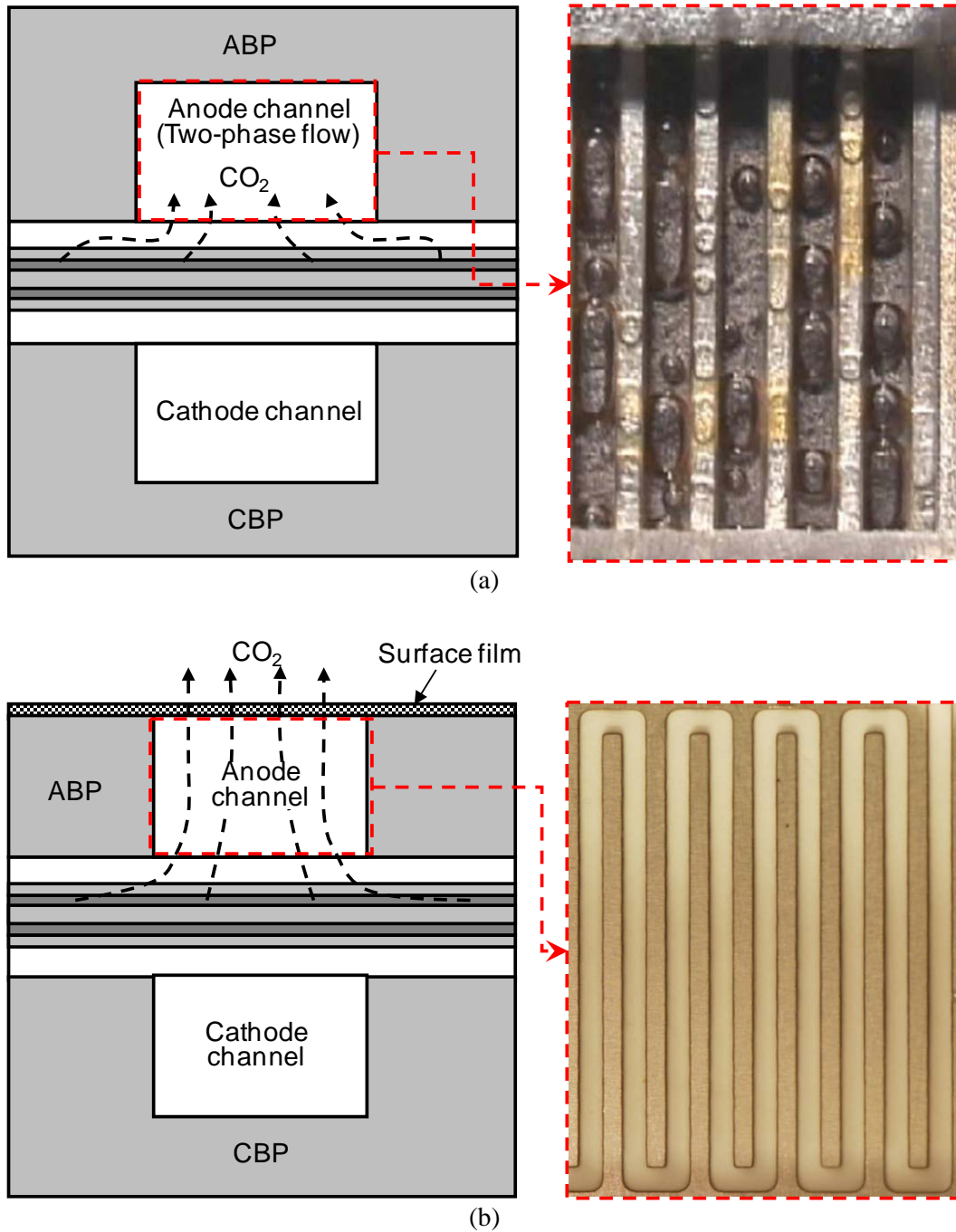
Figure [3-1]   (a) Schematic of conventional DMFC showing CO_2 removal route and two-phase flow in anode channel [34], (b) Schematic of CO_2 breathing DMFC showing CO_2 removal route and almost pure liquid flow in anode channel without CO_2 bubbles (photo by Y.J. Leng)
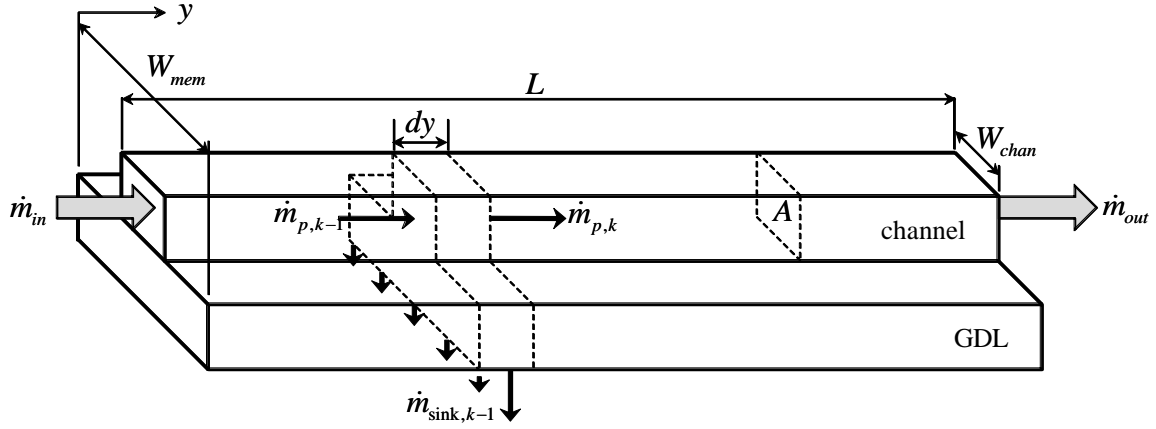
(a) Schematic of 1-D anode channel model in a DMFC
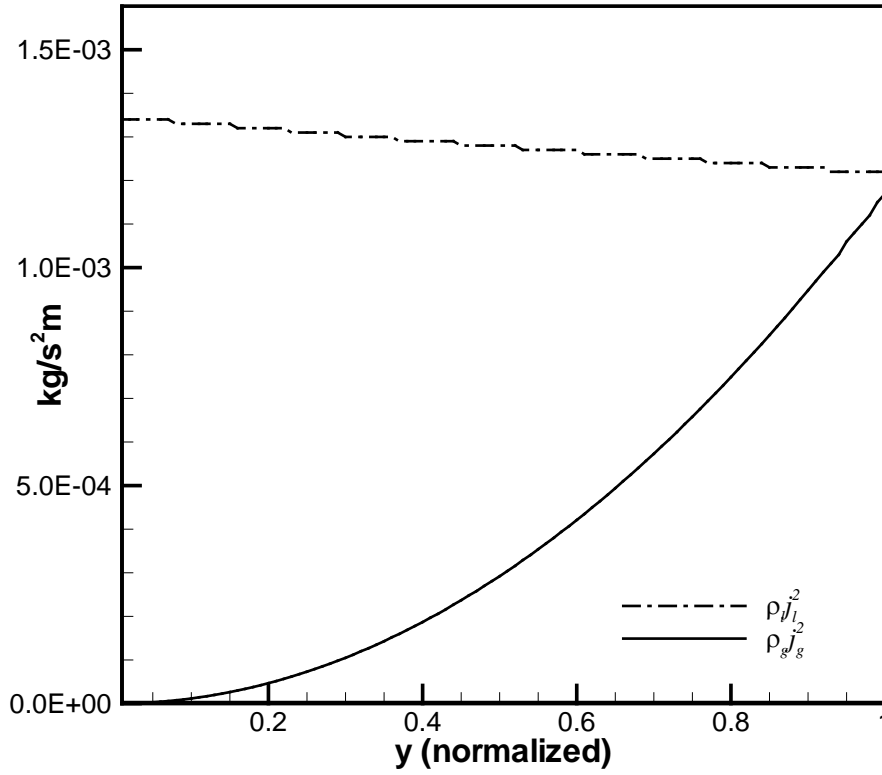
(b) $\rho_l j_l^2$ and $\rho_g j_g^2$

Figure [3-2]　Schematic of 1-D anode channel model in a DMFC (T_{cell} = 333 K, I=150 mA/cm^2, ξ_a=3.0, ξ_c=3.0) and flow pattern parameters
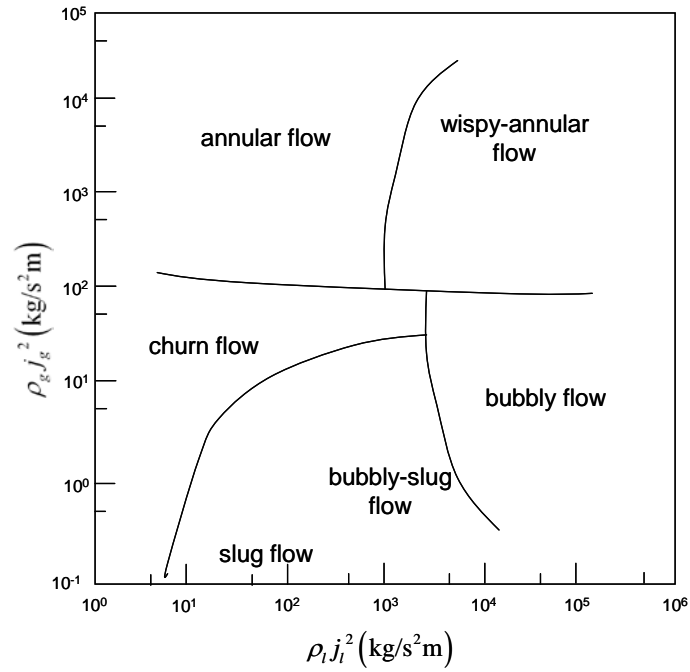
(b) Flow regime map obtained by Hewitt and Roberts [48] for vertical upward two-phase flow
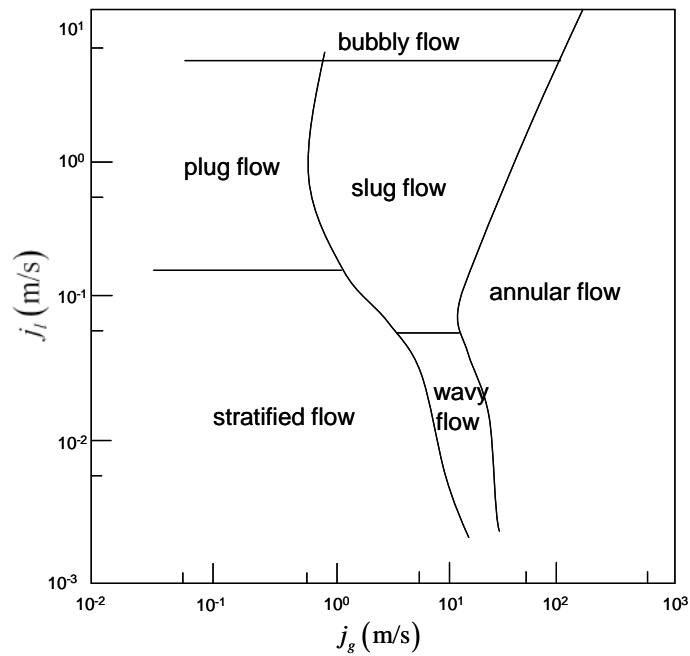
(b) Flow regime map obtained by Mandhane [49] for horizontal two-phase flow

Figure [3-3]   Referenced two-phase flow regime maps
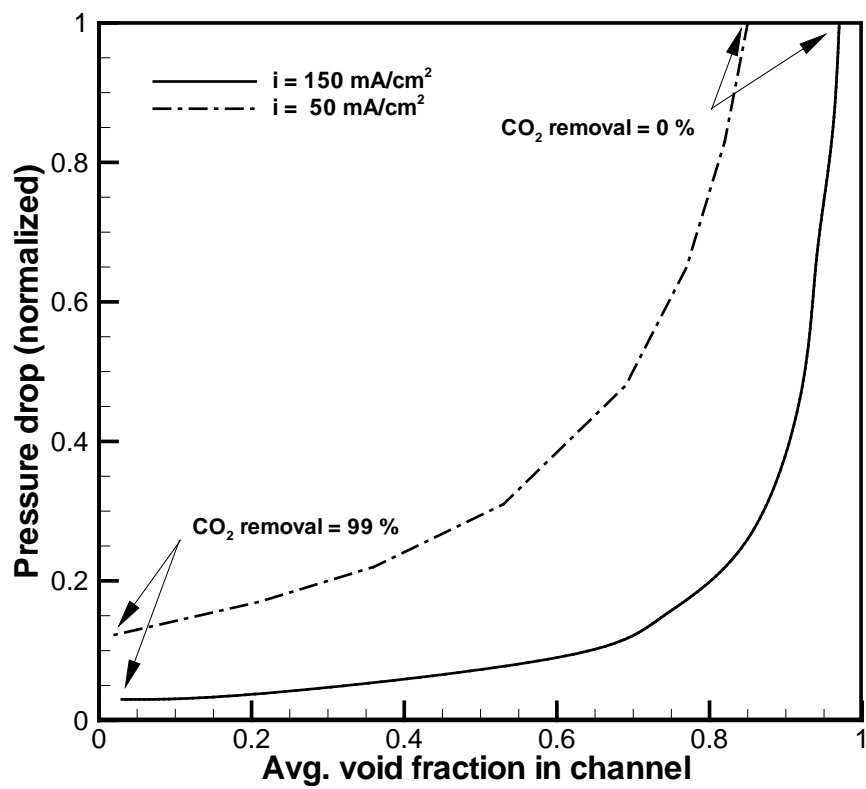
Figure [3-4]   Calculation result of 1-D anode channel model (normalized pressure drop according to CO_2 removal)
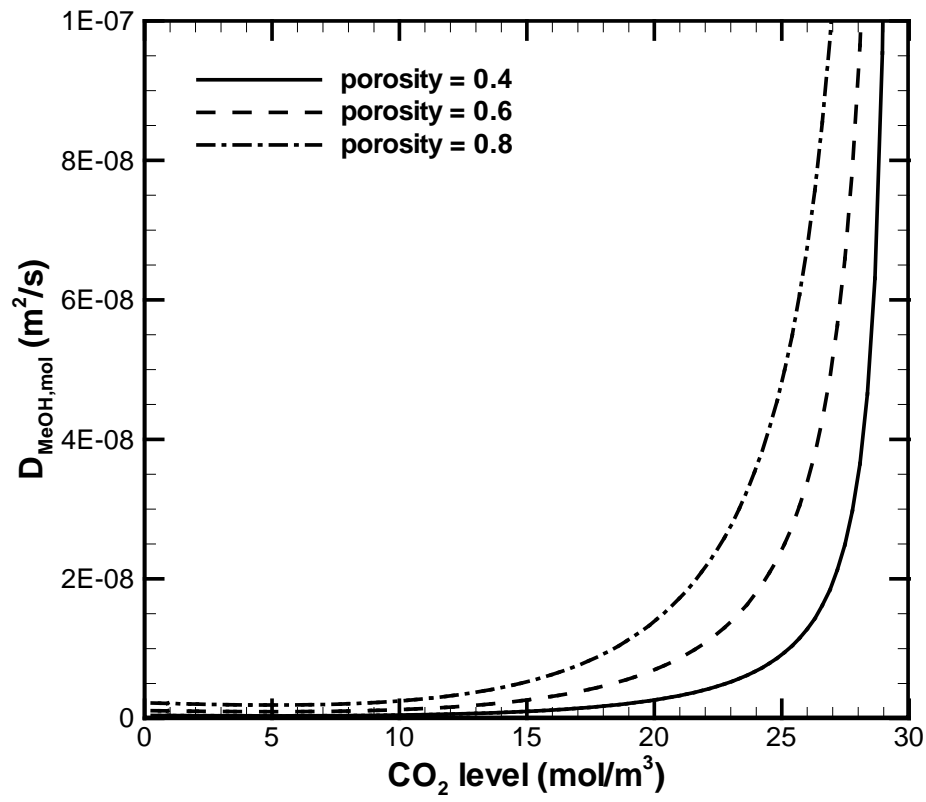
Figure [3-5]   Molecular diffusivity of methanol in GDL according to CO_2 level and GDL porosity
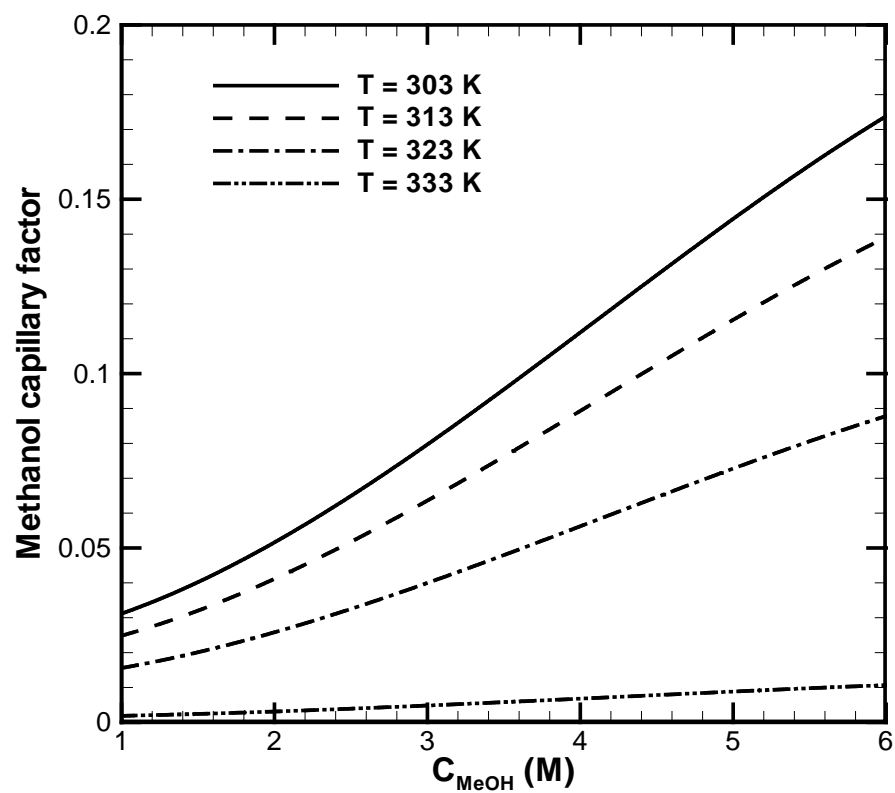
Figure [3-6]   Methanol capillary factor according to the cell temperature and methanol concentration
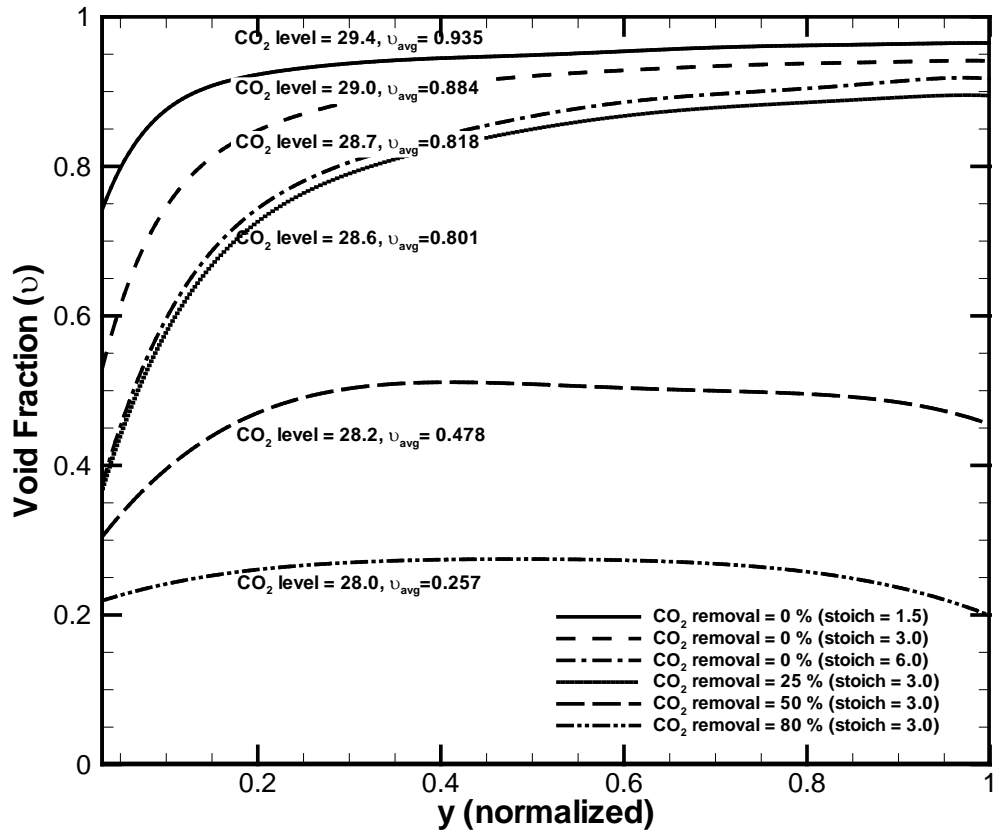
Figure [3-7]   Void fraction in the anode channel according to anode stoichiometry and CO_2 surface removal rate (T_{cell} = 333 K, I=150 mA/cm^2)

Section A   Section B   Section C

(a)

Section A   Section B   Section C

(b)
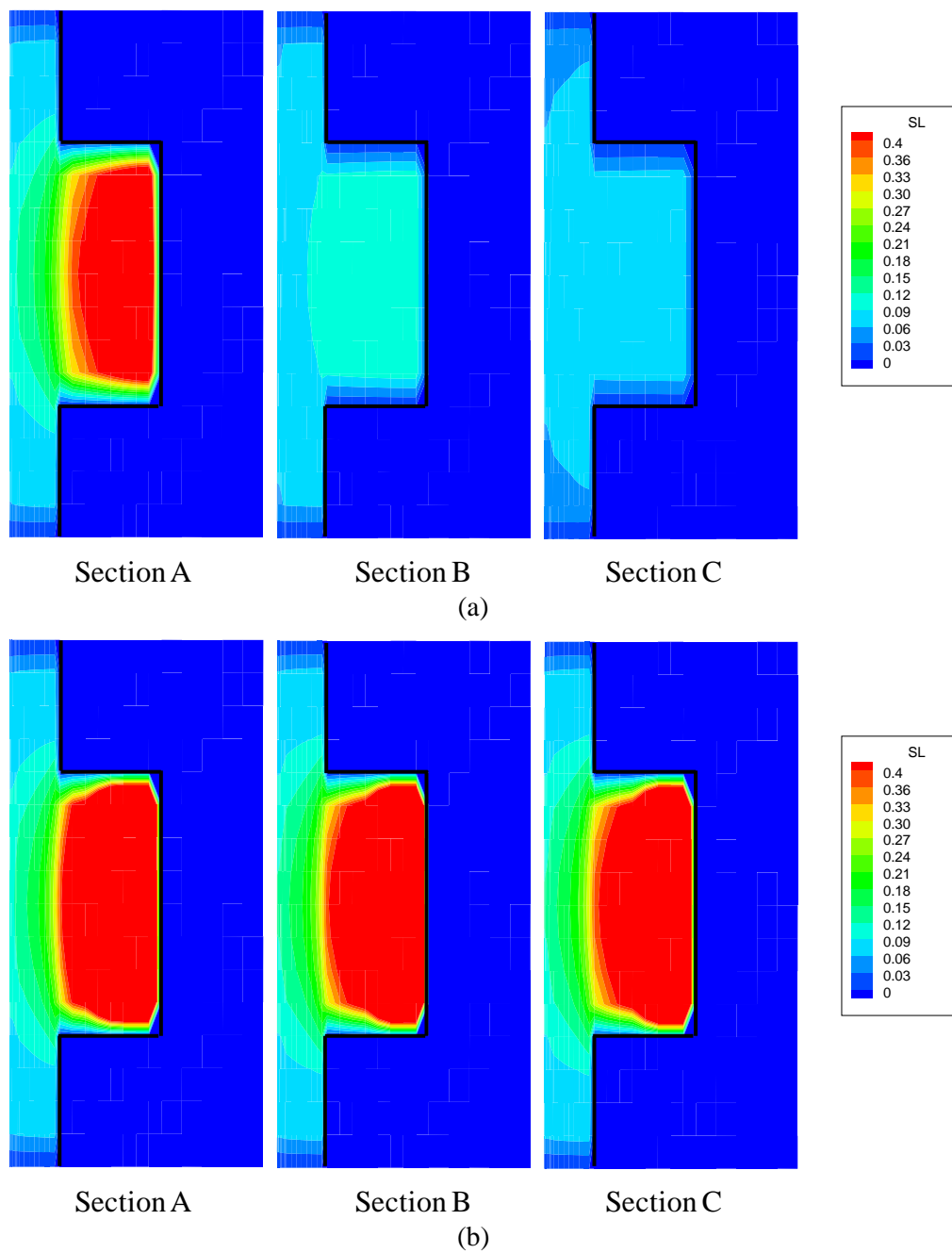
Figure [3-8]   Liquid saturation distribution in the anode: (a) conventional DMFC, (b) CO_2 breathing DMFC (T_{cell} = 333 K, I=150 mA/cm^2, ξ_a=3.0, ξ_c=3.0)
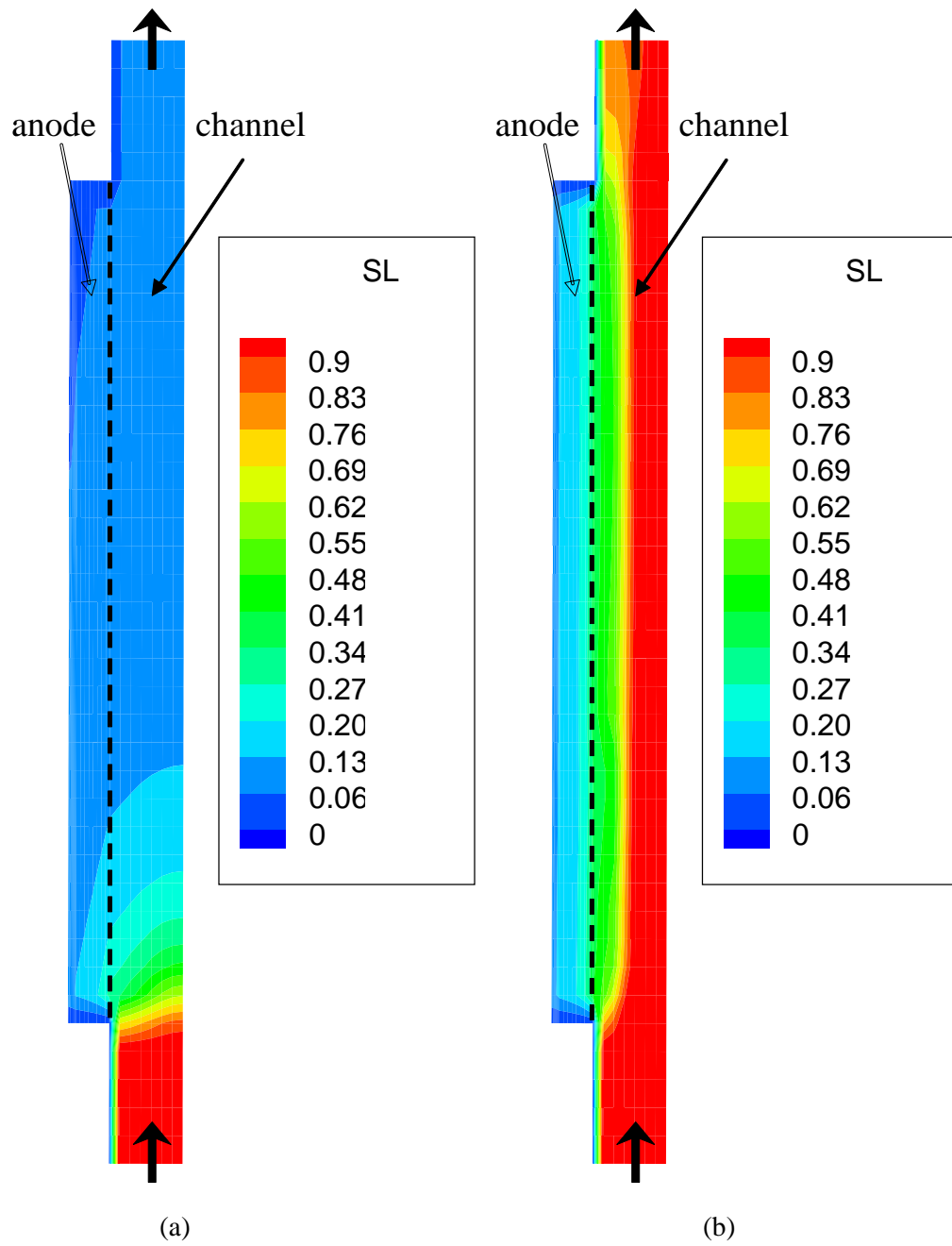
Figure [3-9]   Liquid saturation distribution in the anode (Section E): (a) conventional DMFC, (b) CO_2 breathing DMFC (T_{cell} = 333 K, I=150 mA/cm^2, ξ_a=3.0, ξ_c=3.0)
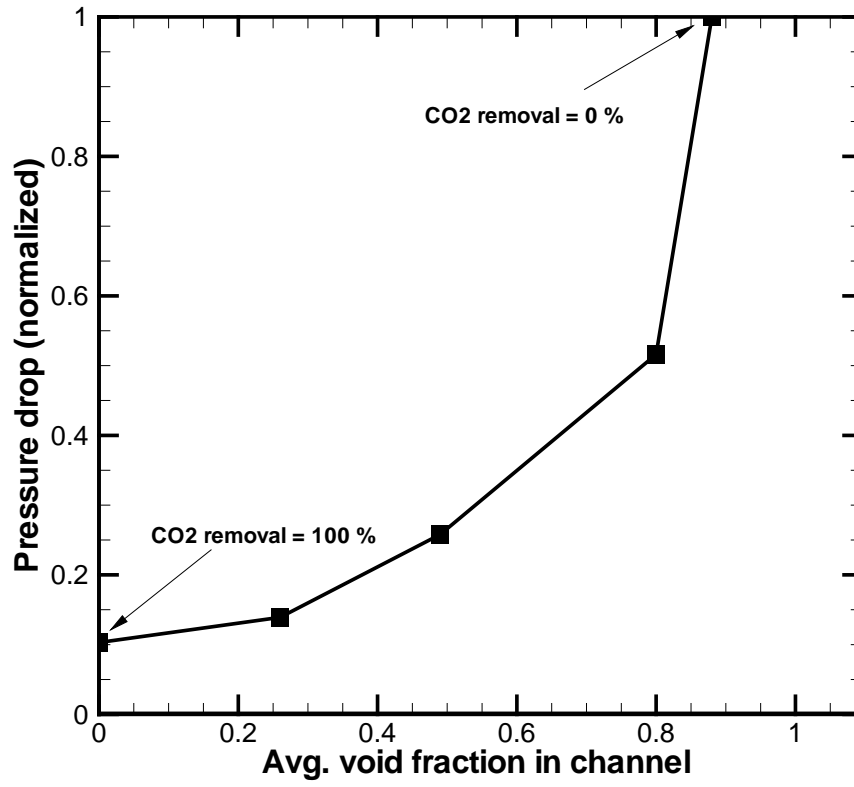
Figure [3-10]   Calculation result from multi-D DMFC model: Normalized pressure drop according to average void fraction in the anode channel due to CO_2 face removal. (T_{cell} = 333 K, I=150 mA/cm^2, ξ_a=3.0, ξ_c=3.0)
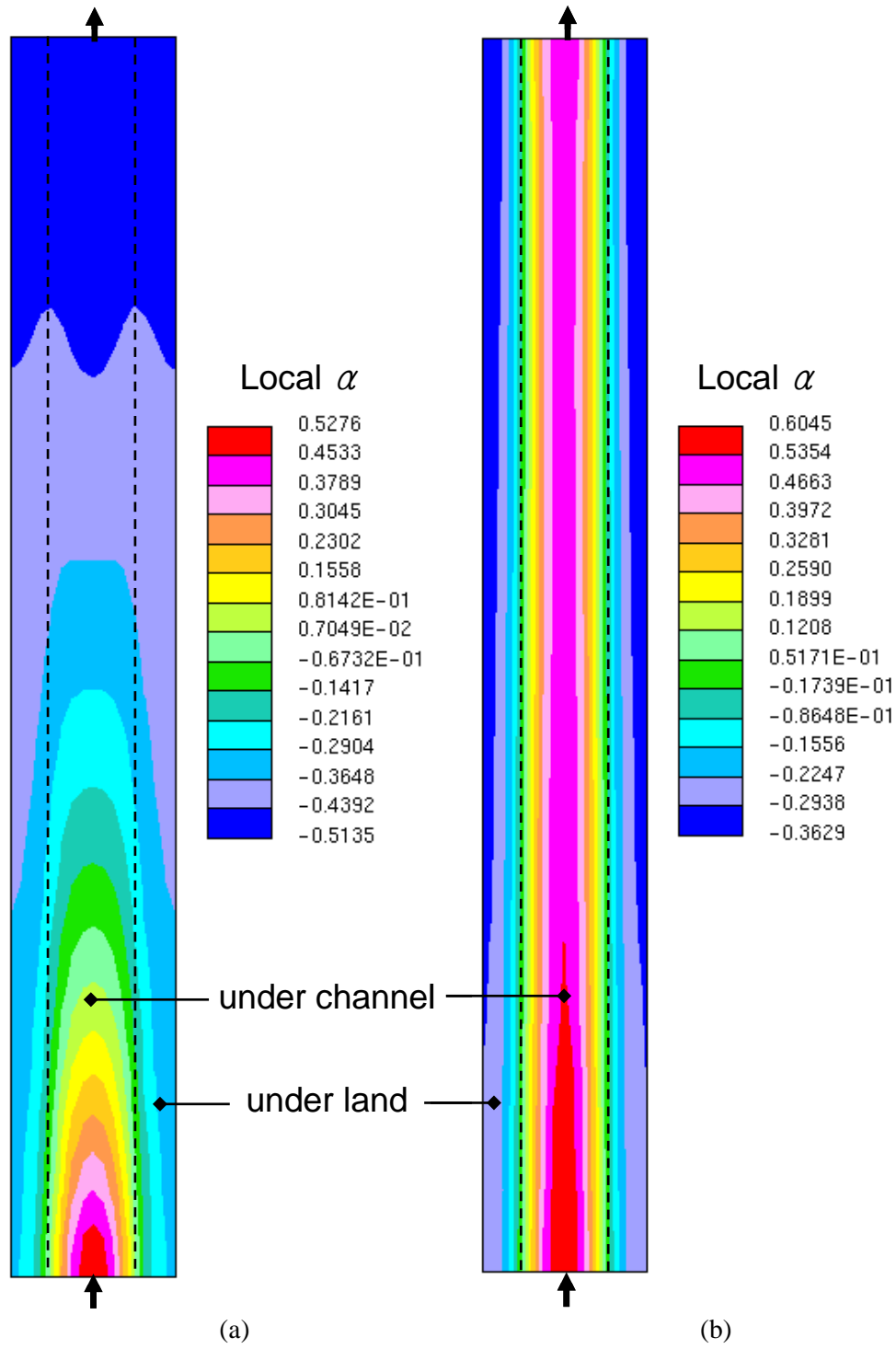
Figure [3-11] Local water transfer coefficient distribution in the membrane: (a) conventional DMFC, (b) CO_2 breathing DMFC (T_{cell} = 333 K, I=150 mA/cm^2, ξ_a=3.0, ξ_c=3.0)
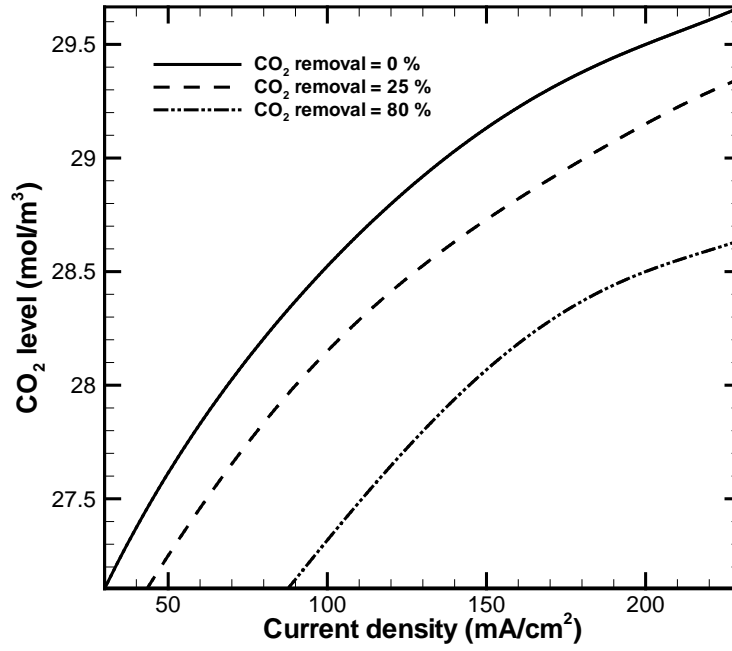
(a)
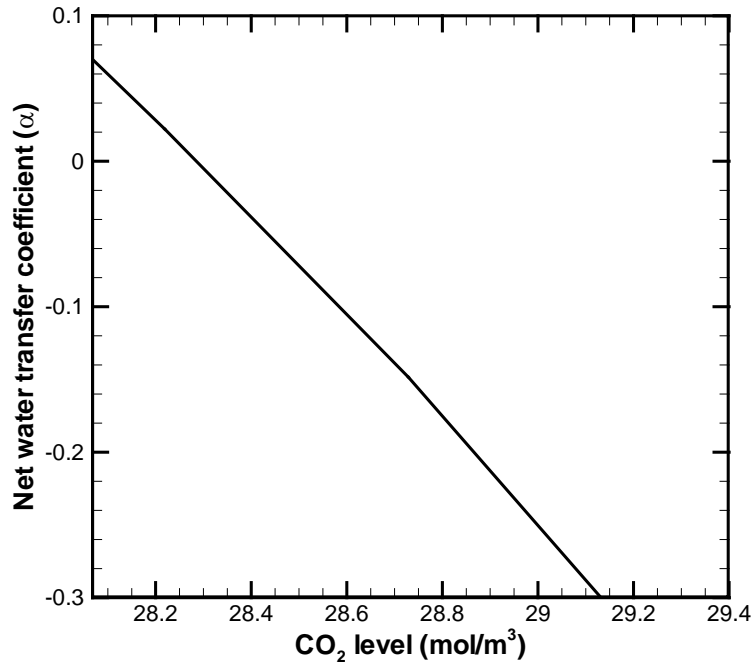
(b)

Figure [3-12]   (a) CO_2 level according to current density, (b) water transfer coefficient according to CO_2 level. (T_{cell} = 333 K, I=150 mA/cm^2, ξ_a=3.0, ξ_c=3.0)
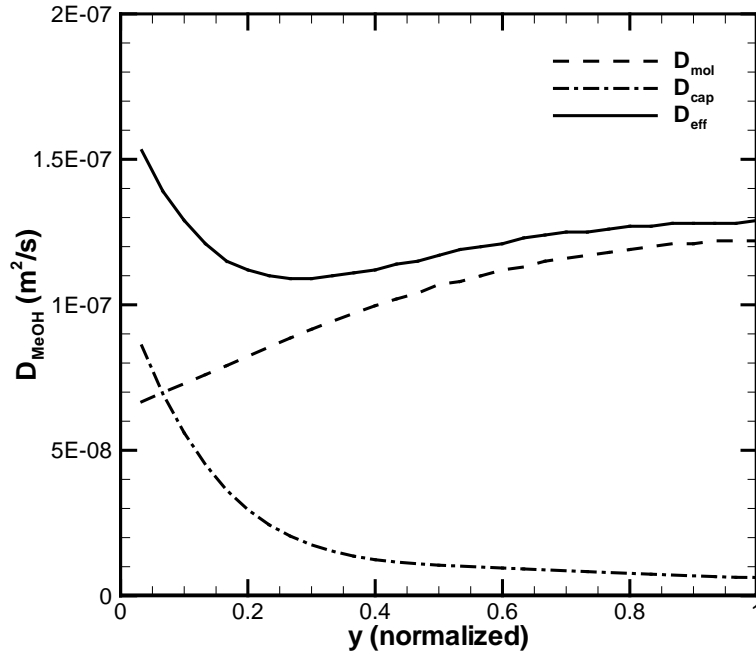
(a) Conventional DMFC (T_{cell} = 333K, I=150 mA/cm^2, ξ_a=3.0, ξ_c=3.0)
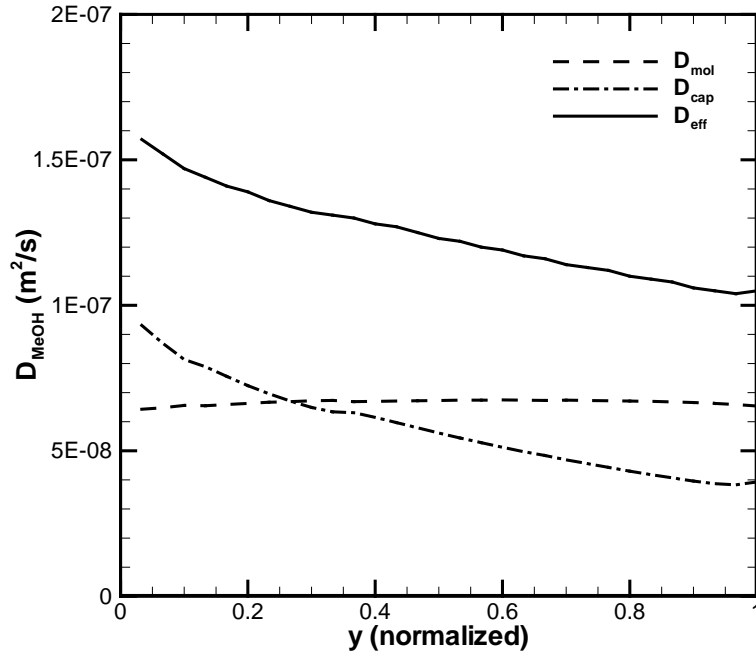
(b) CO$_2$ breathing DMFC (T_{cell} = 333K, I=150 mA/cm^2, ξ_a=3.0, ξ_c=3.0)

.
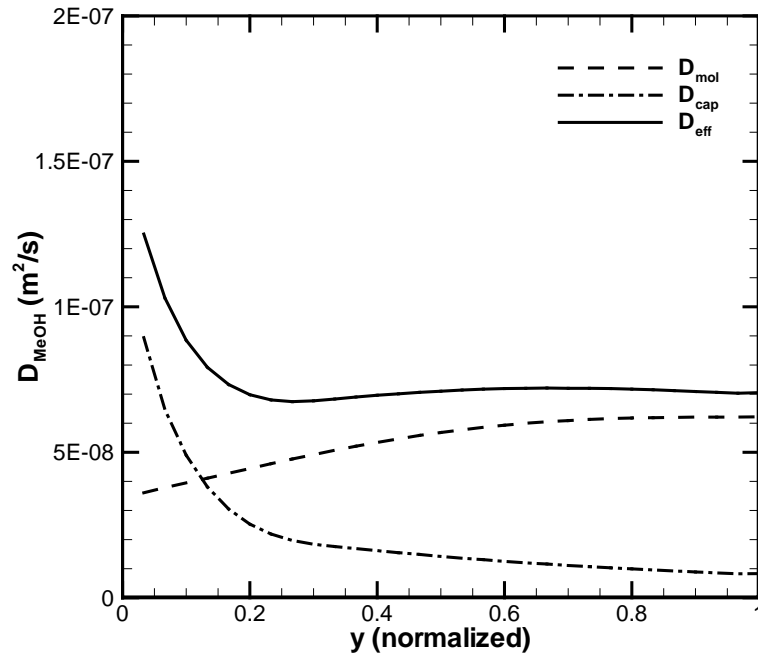
(c) Conventional DMFC (T_{cell} = 313K, I=150 mA/cm^2, ξ_a=3.0, ξ_c=3.0)
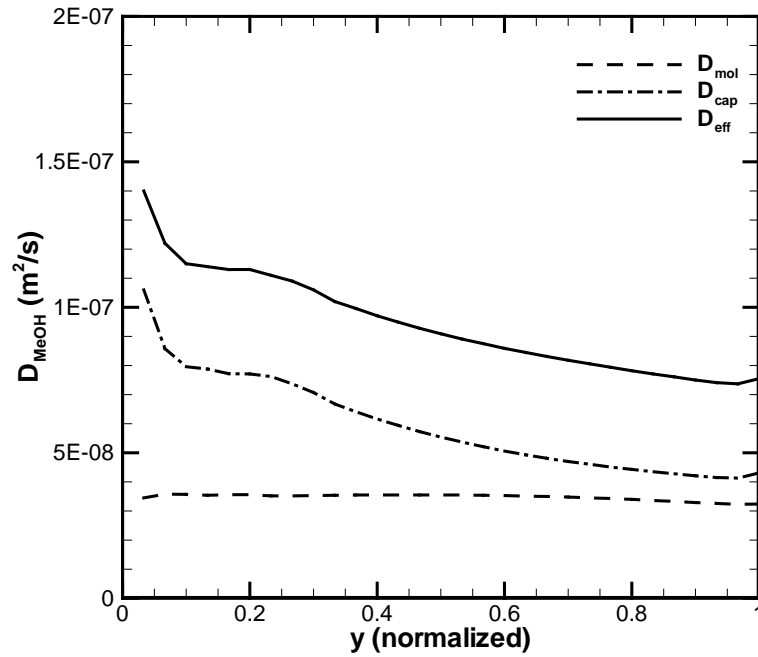
(d) CO$_2$ breathing DMFC (T_{cell} = 313K, I=150 mA/cm^2, ξ_a=3.0, ξ_c=3.0)

Figure [3-13]   Methanol diffusivity distribution in the channel direction

114
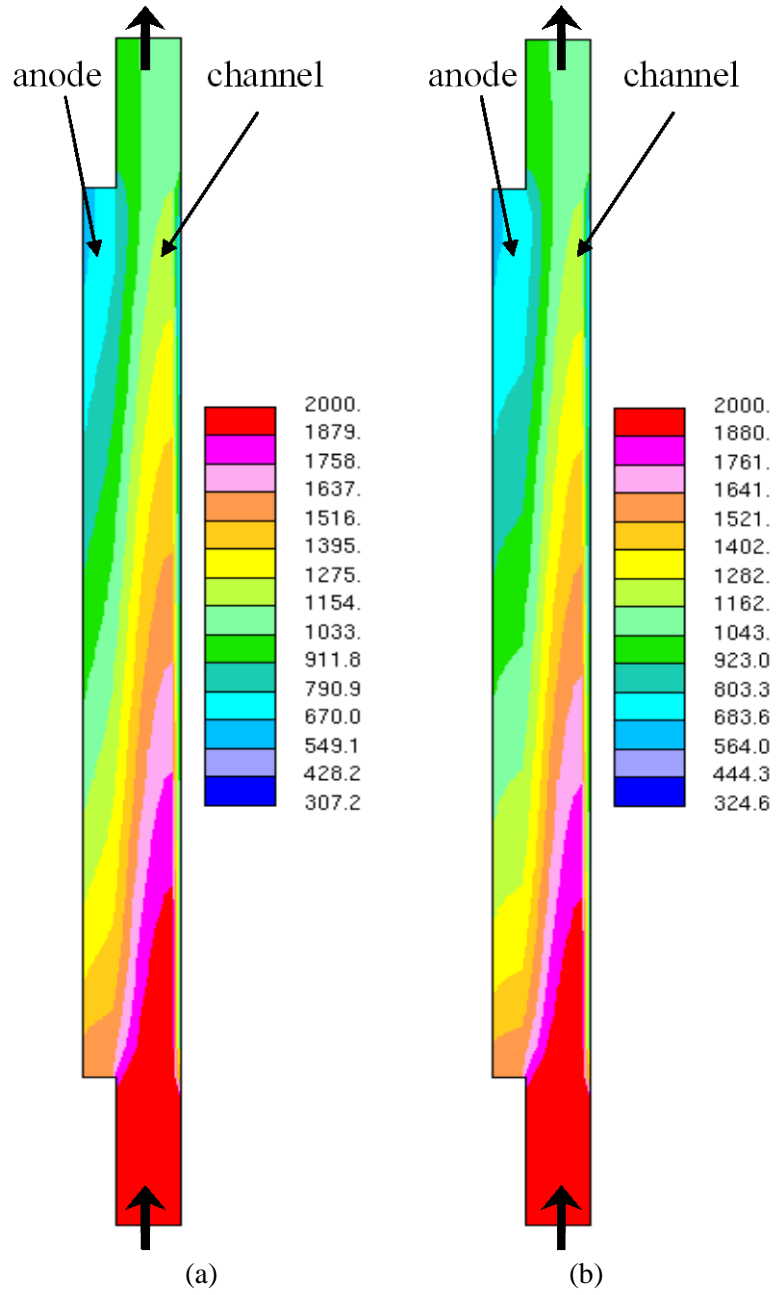
Figure [3-14]   Methanol concentration distribution (Section E), (a) conventional cell, (b) CO_2 breathing cell ($T_{cell} = 333$ K, I=150 mA/cm^2, ξ_a=3.0, ξ_c=3.0)
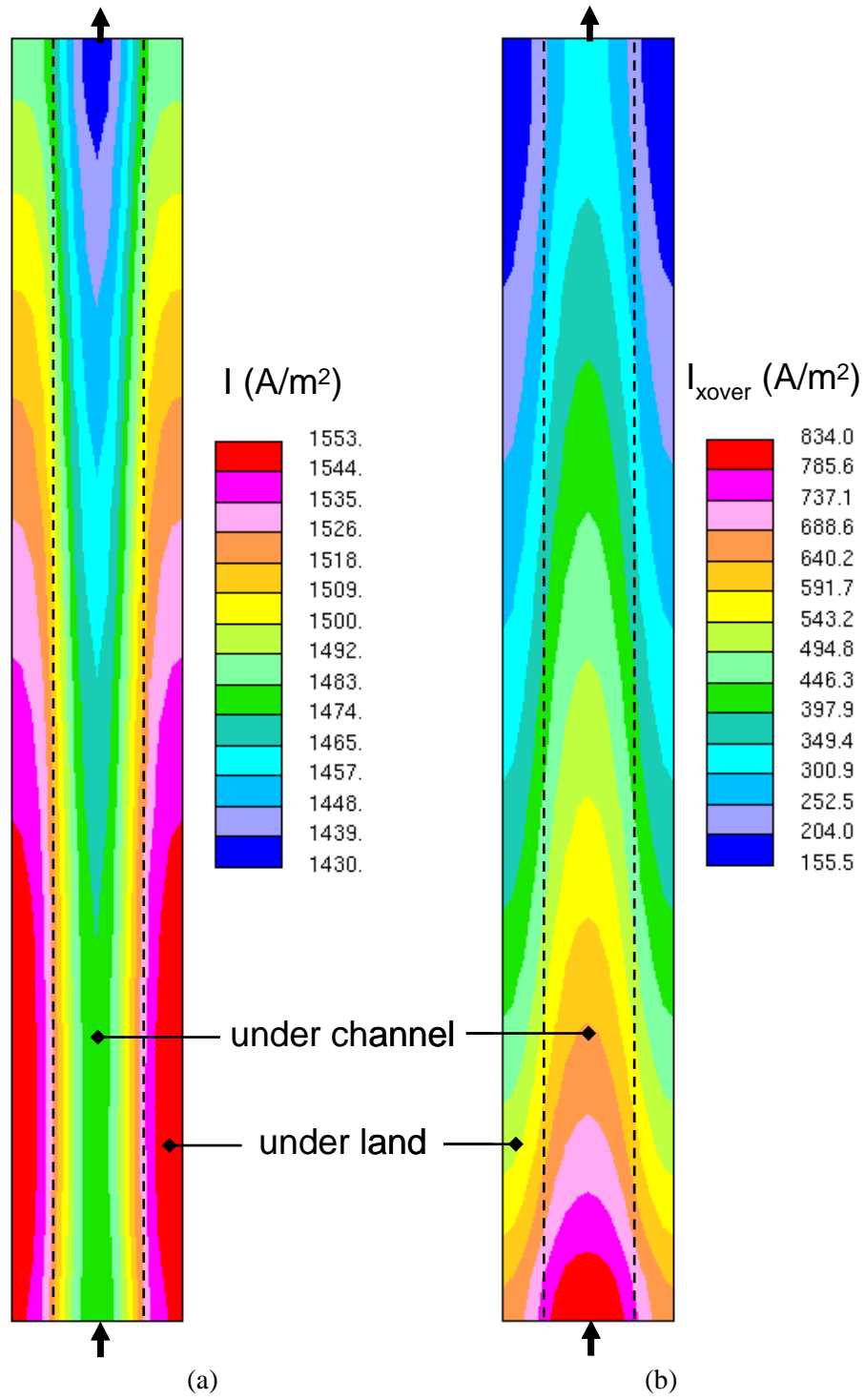
Figure [3-15] (a) Local current density, (b) local crossover current density distribution in the conventional DMFC (T_{cell} = 333 K, I=150 mA/cm^2, ξ_a=3.0, ξ_c=3.0)
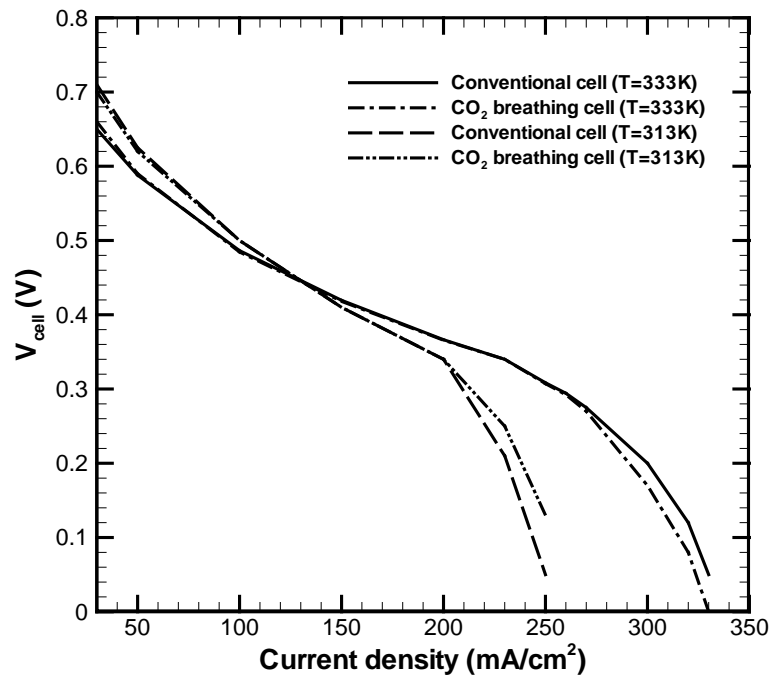
Figure [3-16]   Polarization curve from the simulation result (ξ_a=3.0, ξ_c=3.0)
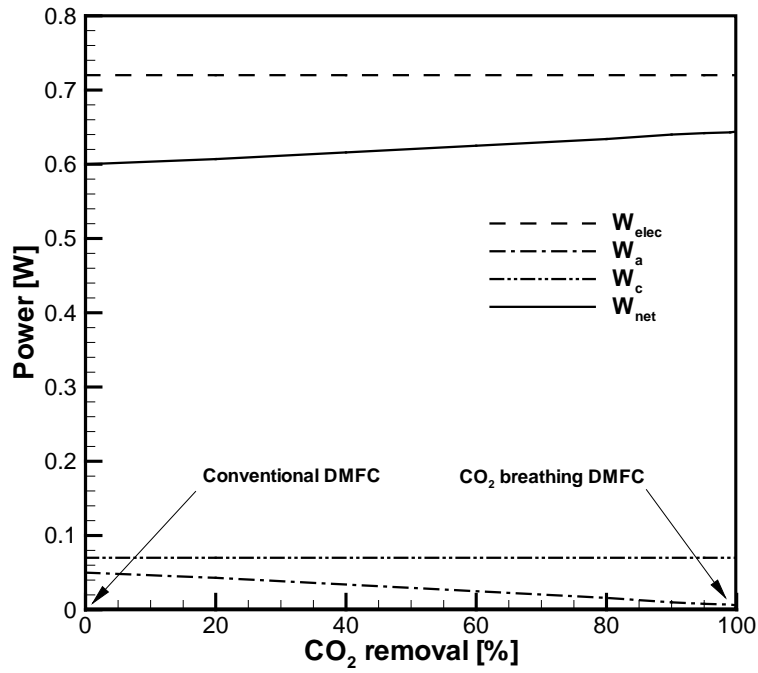
(a) Power throughput according to the CO_2 surface removal amount ($A_{cell} = 12$ cm^2)
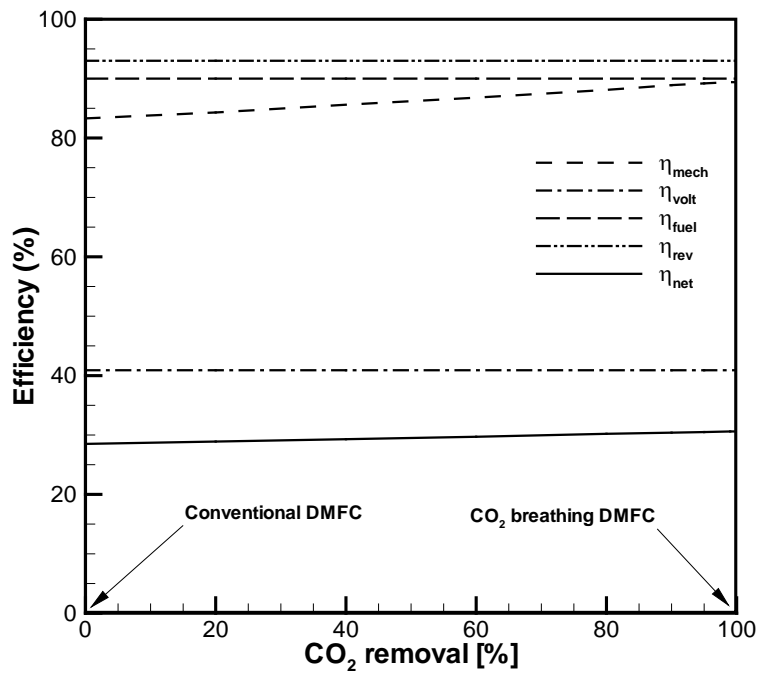
(b) DMFC system efficiency

Figure [3-17]   Power throughput and system efficiency according to CO_2 removal
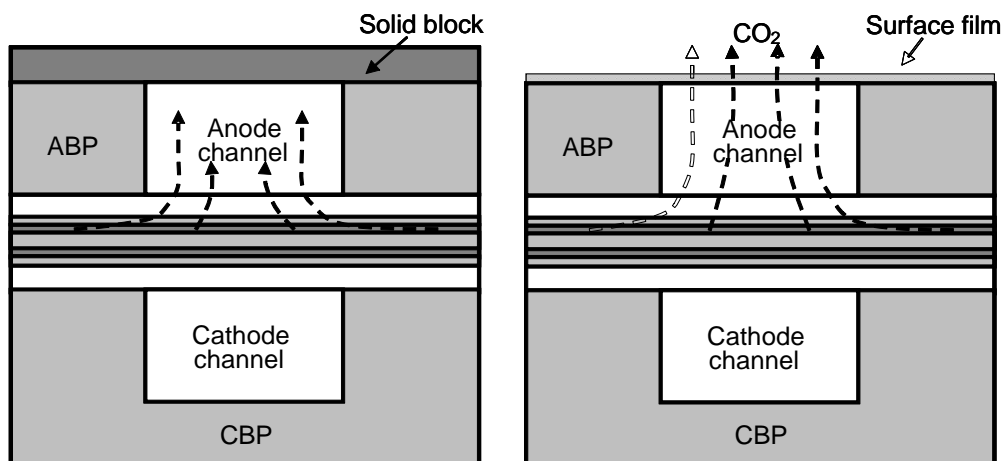
(a) Schematics of the test cell (Left: conventional cell, right: CO_2 breathing cell)
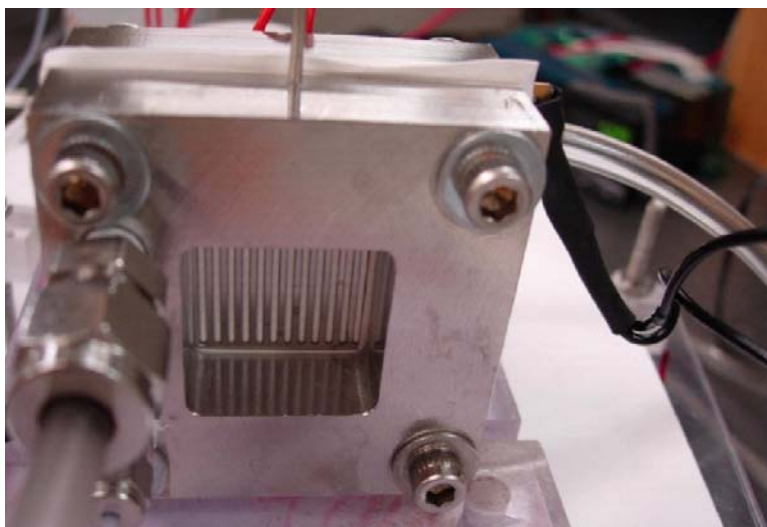
(b) Experimental view of the test cell

Figure [3-18]   Visualized DMFC for examining the effect of CO_2 in this study (test cell fabricated by Y.J. Leng, The Pennsylvania State University, 2009)
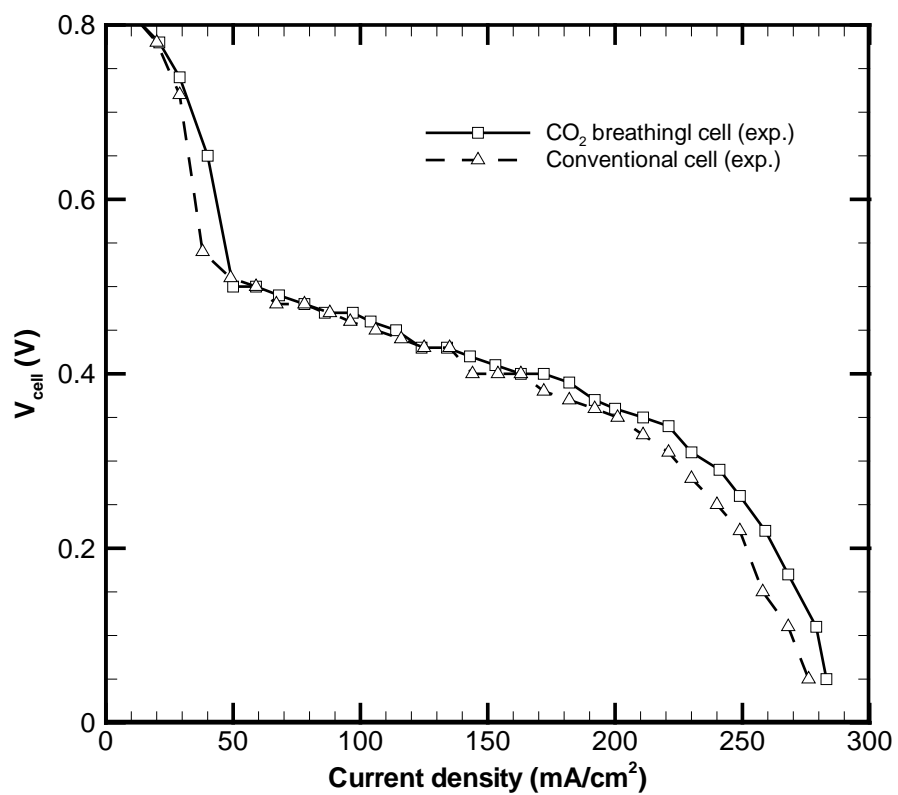
Figure [3-19]   Polarization curve from the experimental result (T_{cell} = 313K, C_{MeOH} = 2M, ξ_a=3.0, ξ_c=3.0). Experiment was conducted by Y.J. Leng, 2009.

Chapter 4

DMFC with Streamline-Graded Structures for Mitigating Anode Non-Uniformity under Ultra-Low Stoichiometry

4.1 Introduction

In order to develop a compact, portable DMFC system, there are several objectives to achieve, such as high energy density, small system size and high fuel efficiency. First, energy density of the DMFC system must be increased by using highly concentrated fuel. Many DMFCs carry a diluted fuel solution which consists of water and methanol. Although cell operation with dilute solution has benefits of reducing methanol crossover and increasing cell voltage, it is not good for developing portable DMFCs because dilute solution lowers the energy density of the system. As water is produced in the cathode catalyst layer (CCL) by the oxygen reduction reaction (ORR), it is theoretically possible to achieve a water-neutral condition to operate DMFC without external water supply to the anode side. Blum *et al.* [53] first proposed this water-neutral condition and they concluded that carrying pure liquid methanol is theoretically possible when the water transfer coefficient (α) is equal to -1/6. However, supplying pure methanol to a DMFC causes severe methanol crossover and it is difficult to uniformly supply fuel to a DMFC with low stoichiometry. Even though a DMFC system carries a pure methanol tank, it must dilute pure methanol internally with produced water.

Balance of plant (BOP) occupying a large volume of a DMFC system should be reduced also. The gas-liquid separator located at the anode outlet can be removed if CO_2 gas is vented through alternate routes as discussed in Chapter 3. The air supplying system

can be simplified by replacing the air blower with an air breathing pad, although the performance of air breathing type of DMFC is strongly affected by ambient condition [54, 55].

Conventional DMFCs use pumps to supply liquid fuel on the anode side. If anode flow rate is minimized, this pump size can be reduced and required power operating the pump can be reduced also. Due to CO_2 production by MOR in the anode, usually, a strong two-phase flow exists in the anode channel. This two-phase flow causes a large pressure drop by two-phase frictional loss and inertial loss. CO_2 breathing type DMFC removes CO_2 through the cell surface and almost pure liquid flows in the anode channel. Therefore, anode pressure drop can be significantly reduced as shown in Chapter 3.

Maintaining ultra-low anode stoichiometry is another way for constructing a compact DMFC system and reducing the manufacturing cost. However, it is difficult to uniformly distribute concentrated fuel in the anode since a large amount of methanol may diffuse through the proton exchange membrane in the inlet region, which lowers fuel efficiency. In contrast, the outlet region may suffer from fuel shortage, which degrades cell performance. In this chapter, this phenomenon is called 'fuel concentration non-uniformity'. Fuel concentration non-uniformity eventually leads to current density non-uniformity, temperature non-uniformity and even cell shut-down. All of those non-uniformities are called 'anode non-uniformity'. Therefore, it can be easily conjectured that anode non-uniformity has a strong influence on the cell performance and fuel efficiency.

Fuel efficiency is particularly important for portable power sources since it determines the total operational time of the system. A large amount of unused methanol

in the anode catalyst layer (ACL) is lost by cathode due to diffusion and electro-osmosis drag through the membrane, which is called methanol crossover. Methanol crossover degrades not only cell performance but also fuel efficiency. The easiest way to minimize methanol crossover is to operate a DMFC with ultra-low anode stoichiometry. However, low anode stoichiometry causes anode non-uniformity problems as explained above.

In this chapter, we investigate the anode non-uniformity phenomena when a DMFC operates at ultra-low anode flow stoichiometry, and identify the relationship between non-uniformity and cell performance. Then, two strategies to mitigate the anode non-uniformity are introduced in order to achieve both high cell performance and high fuel efficiency required for a portable power source.

4.2   Physical model

First, the fuel transport mechanism and the fuel transport resistance of DMFC are introduced. After that, anode non-uniformity is introduced through 1-D analysis. Finally, the anode non-uniformity and the mitigating methods will be presented with multi-D simulation.

4.2.1   *Two-phase transport of methanol*

In Chapter 3, we derived the two-phase methanol transport equation as follows:

$$\nabla \cdot \left(\rho \vec{u} Y_1^{\text{MeOH}} \right) = \nabla \cdot \left[\rho D_{\text{eff}}^{\text{MeOH}} \nabla \cdot Y_1^{\text{MeOH}} \right] + M^{\text{MeOH}} S^{\text{MeOH}} \tag{4-1}$$

The effective methanol diffusivity consists of the effective methanol molecular diffusivity and the methanol capillary diffusivity as follows:

$$D_{\text{eff}}^{\text{MeOH}} = D_{\text{mol}}^{\text{MeOH}} + D_{\text{capill}}^{\text{MeOH}}$$
(4-2)

Molecular diffusivity (Eq. (4-3)) is a strong function of both operating condition (liquid saturation) and material property (porosity).

$$D_{\text{mol}}^{\text{MeOH}} = \frac{\rho_1}{\rho}\left(D_{\text{l,eff}}^{\text{MeOH}} + \frac{D_{\text{g,eff}}^{\text{MeOH}}}{k_{\text{H}}} \right) = \frac{\rho_1}{\rho}\left(D_{\text{l}}^{\text{MeOH}} s^n + \frac{D_{\text{g}}^{\text{MeOH}}(1-s)^n}{k_{\text{H}}} \right)\varepsilon^n$$
(4-3)

Methanol molecular diffusivity is determined by liquid-phase diffusivity, temperature and methanol concentration as follows:

$$D_{\text{capill}}^{\text{MeOH}} = D_{\text{capill}}\psi$$

$$\text{where} \quad \psi = \left(1 - \frac{\rho_1}{\rho_{\text{g}} k_{\text{H}}} \right)\frac{Y_1^{\text{MeOH}}}{Y_1^{\text{H}_2\text{O}} - Y_{\text{g}}^{\text{H}_2\text{O}}}$$
(4-4)

It is easily predicted that the contribution of methanol capillary diffusion to the total methanol transport in porous media becomes small when the liquid mixture is dilute and temperature is high. Under ultra-low anode flow stoichiometry condition, however, D_{capill} itself becomes very low since the anode porous media becomes gaseous, which means methanol molecular diffusion is dominant over methanol capillary diffusion.

4.2.2 *Effective methanol transport resistance*

Figure [4-1] schematically shows methanol transport in the anode. Supplied methanol from the channel inlet spreads out through the anode porous media and the remaining amount moves out of the channel. Methanol is convection-dominantly transported from the channel to the GDL surface. Then, methanol is diffusively transported to the catalyst

124

layer through porous media. Therefore, methanol transported from the channel to the catalyst layer at location y can be expressed as Eq. (4-5),

$$J^{\text{MeOH}} = \frac{A_{\text{mem}}\left(C_{\text{chn}}^{\text{MeOH}} - C_{\text{cl}}^{\text{MeOH}}\right)}{\dfrac{1}{h_{\text{m}}A_{\text{R}}} + \dfrac{\delta}{D_{\text{eff}}^{\text{meoh}}\left(1 - 2^{-1/n}\left(1 - A_{\text{R}}\right)\right)}} \tag{4-5}$$

$$\text{where} \quad A_{\text{R}}(y) = \frac{A_{\text{chn}}}{A_{\text{mem}}} \quad \text{(opening ratio)}$$

The effective resistance which consists of convective resistance and diffusive resistance expresses the total resistance controlling methanol transport as follows:

$$R_{\text{eff}} = R_{\text{conv}} + R_{\text{diff}} = \frac{1}{h_{\text{m}}A_{\text{R}}} + \frac{\delta}{D_{\text{eff}}^{\text{MeOH}}\left(1 - 2^{-1/n}\left(1 - A_{\text{R}}\right)\right)} \tag{4-6}$$

Convective resistance (R_{conv}) is determined by opening ratio (A_{R}) and convective coefficient which is a function of flow rate (Re_{D}) as follows [56]:

$$h_{\text{m}} = \frac{D_{\text{chn}}^{\text{MeOH}}}{H} Sh = \left(\frac{D_{\text{chn}}^{\text{MeOH}}}{H}\right) 1.86 \left(\frac{Re_{D_{\text{H}}} Sc}{L D_{\text{H}}}\right)^{1/3} \tag{4-7}$$

Effective methanol diffusivity shown in Eq. (4-6) came from Eq. (4-2). Therefore, diffusive resistance (R_{diff}) is a function of both material property (porosity) and channel geometry (A_{R}). For simple analysis, liquid saturation in the anode porous media is assumed constant value (0.2) and $D_{\text{capill}}^{\text{MeOH}}$ is neglected here. The dependence of the methanol diffusive resistance on the channel geometry is presented in Figure [4-2 (b)].

Based on the schematic of Figure [4-1], the relationship among fuel concentration distribution, current density distribution, and fuel transport resistance is analyzed through 1-D fuel distribution model which is extended from 1-D anode channel model introduced

in Chapter 3. Basic assumptions for the model are, *i*) uniform liquid saturation in porous media (0.2), *ii*) CO_2 is the only gas, and *iii*) zero water transfer coefficient ($\alpha = 0$).

For the control volume of Figure [4-1], gas mass flow rate (kg/s) is calculated by

$$\dot{m}_{g,k} = \frac{M^{CO_2}}{6F} i(y) W_{mem} y \qquad (4\text{-}8)$$

and liquid mass flow rate is calculated by species consumption from MOR and methanol crossover as follows:

$$\dot{m}_{l,k} = \dot{m}_{l,k-1} - \frac{i(y)}{6F} \left(M^{H_2O} + M^{MeOH} \right) W_{mem} dy - D_{mem}^{MeOH} M^{MeOH} W_{mem} dy \frac{C_{acl}^{MeOH}(y)}{\delta_{mem}} \qquad (4\text{-}9)$$

Then, gas mass fraction becomes,

$$Y_g(y) = \frac{\dot{m}_g(y)}{\dot{m}_l(y) + \dot{m}_g(y)} \qquad (4\text{-}10)$$

And liquid saturation, void fraction, and quality are found by,

$$s_l(y) = \frac{\rho_g Y_l}{\rho_l(1 - Y_l) + \rho_g Y_l}$$
$$\alpha(y) = 1 - s_l(y) \qquad (4\text{-}11)$$
$$x(y) = \frac{\rho_g(1 - s_l(y))}{\rho}$$

Therefore, velocities can be found as follows:

$$u_l(y) = \frac{\dot{m}_l(y)}{\rho_l A_l(y)} = \frac{\dot{m}_l(y)}{\rho_l A(y) s_l(y)}$$
$$u_g(y) = \frac{\dot{m}_g(y)}{\rho_g A_g(y)} = \frac{\dot{m}_g(y)}{\rho_l A(y)(1 - s_l(y))} \qquad (4\text{-}12)$$
$$u(y) = s_l u_l + (1 - s_l) u_g$$

Now, the methanol concentration distribution in the channel can be calculated. Methanol sink at location y can be expressed as follows:

$$\dot{m}_{\text{sink}}\left(y\right) = \frac{i_y}{6F} M^{\text{MeOH}} dy W_{\text{mem}} + D_{\text{mem}}^{\text{MeOH}} M^{\text{MeOH}} W_{\text{mem}} dy \frac{C_{\text{acl}}^{\text{MeOH}}(y)}{\delta_{\text{mem}}} \qquad (4\text{-}13)$$

Therefore, methanol mass fraction in the channel can be found according to the methanol conservation with the previously calculated velocity distribution.

$$Y_k = \left(\frac{s_{k-1} W_{k-1} u_{1,k-1}}{s_k W_k u_{l,k}}\right) Y_{k-1} - \frac{i_x dy W_{\text{mem}}}{6F \rho_1 s_k W_k H u_{1,k}} M^{\text{MeOH}} - \frac{D_{\text{mem}}^{\text{MeOH}} M^{\text{MeOH}} dx C_{\text{B}}^{\text{MeOH}}(y)}{\rho_1 s_k H u_{1,k} \delta_{\text{mem}}} \qquad (4\text{-}14)$$

Methanol concentration in ACL can be found by using the methanol transport resistance discussed previously. The effect of methanol concentration in ACL on cell performance is considered by the Tafel approximation as follows [22, 23, 24]:

$$j_a = \frac{a j_{0,a}^{\text{ref}} C_{\text{acl}}^{\text{MeOH}} \exp(\frac{\alpha_a F}{RT} \eta_a)}{C_{\text{acl}}^{\text{MeOH}} + K \exp(\frac{\alpha_a F}{RT} \eta_a)} \quad \text{where} \quad a = a_0 \left(\frac{\omega_{\text{acl}}}{\omega_{\text{acl,ref}}}\right)^n \qquad (4\text{-}15)$$

Eq. (4-15) explains reaction order shifts from 0th to 1st when methanol concentration becomes lower than the threshold value. Generally, adding more catalyst to the catalyst layer increases the specific reaction area ($a = \frac{A}{V}$) and improves kinetics by lowering activation energy. Catalyst loading effect is considered simply by multiplying relative catalyst loading amount to the reference specific reaction area.

Calculation results showing the dependence of methanol concentration distribution on the methanol transport resistance when a conventional DMFC operates at average current density 150 mA/cm^2 is presented in Figure [4-3]. The effective methanol transport

resistance slightly decreases in the channel direction due to improved convectional effects. Methanol concentration in ACL rapidly decreases and local current density significantly deviates from the average value, especially in the outlet region where fuel supply is insufficient.

4.2.3   *Multi-D DMFC model*

Although the 1-D fuel distribution model gives a quick glance about anode non-uniformity and its consequence, actual transport phenomena in a DMFC takes place three-dimensionally. Therefore, we further extend our analysis with the multi-dimensional model. The multi-dimensional DMFC model in this study is extended from the baseline model introduced in Chapter 2 and 3. A brief summary of governing equations is presented in Appendix A and B. MPL is inserted between the GDL and CL on both the anode and cathode in the present model.

4.3   Anode Non-Uniformity and Mitigating Strategies

As discussed in Chapter 2, the ideal method to get maximum cell performance with maximum fuel efficiency is to operate a DMFC near the threshold value of methanol concentration in ACL where methanol crossover is almost zero. This is same meaning as operating a DMFC at ultra-low anode stoichiometry. However, it is very difficult to achieve this condition because DMFC has a three-dimensional structure, which means fuel spreads in three dimensions. Therefore, when liquid fuel is supplied from the inlet at ultra-low flow rate, some region will operate with excessive fuel and some region will

operate with insufficient fuel. Here we investigate this anode non-uniformity in detail, its consequences and strategies to mitigate it.

4.3.1   *Anode non-uniformity under ultra-low stoichiometry*

The effect of anode stoichiometry on cell performance and anode non-uniformity is investigated with the multi-D simulation. Methanol concentration distribution in ACL for stoichiometry 1.4 and 2.4 are presented in Figure [4-4(a)] and [4-4(b)]. Under ultra-low anode stoichiometry condition ($\xi_a = 1.4$), methanol is concentrated in the inlet region and the outlet half region suffers from fuel shortage. Current density or anode reaction rate is strongly affected by methanol concentration when methanol concentration is insufficient. For the same operating current condition (150 mA/cm^2), the outlet half region has lower current density than the average value, whereas the inlet half region has high current density compared to the average value, which means large anode non-uniformity of current density (see Figure [4-5]). Crossover current density is presented in Figure [4-6]. As methanol crossover consists of diffusion through the membrane and electro-osmosis by electric current, methanol crossover is concentrated in the inlet region where both current density and methanol concentration are high under ultra-low anode stoichiometry condition. When stoichiometry is large, methanol crossover becomes more uniform. Methanol crossover rate affects temperature distribution also. As discussed in Chapter 2, crossover current density contributes to heat generation in the cathode. As methanol crossover is concentrated in the inlet region, low anode stoichiometry case shows a larger temperature gradient along the streamline direction compared to the large stoichiometry case (see Figure [4-7(a)] and [4-7 (b)]).

129

Although large anode flow stoichiometry assures better cell voltage due to lowered mass transport overpotential and good anode uniformity, it causes large methanol crossover rate and requires large fuel pumping power. In contrast, the cell may suffer severe fuel shortage at the outlet region under ultra-low stoichiometry condition, which results in large anode overpotential and poor anode uniformity.

4.3.2 *Effect of cell temperature on anode non-uniformity*

High temperature leads to better methanol diffusion in porous media due to the Arhenius relationship of diffusivity as shown in Figure [4-2(c)]. In addition, MOR is enhanced also from Eq. (4-15). Therefore, generally, high temperature leads to better cell performance. However, this may become a different story when the cell operates at ultra-low anode stoichiometry. High temperature increases not only the effective diffusivity in the anode porous media but also methanol diffusivity of the proton exchange membrane, which is not desired for fuel management since it may cause large methanol crossover. The effect of temperature on fuel distribution is presented in Figure [4-4(b)] and [4-4(c)]. As a large amount of methanol is transported to ACL in the inlet region due to increased effective methanol diffusivity, much more methanol is consumed there by both MOR and MCO when the temperature is high under ultra-low anode stoichiometry condition. Therefore, the outlet half region suffers from fuel shortage and poor anode kinetics, which worsens anode non-uniformity (see Figure [4-5]-[4-7]). It is estimated that the cell may shut down with severe anode non-uniformity when the cell temperature exceeds 70 °C under ultra-low anode stoichiometry in the present study. Therefore, the cell temperature should not be so high under ultra-low anode stoichiometry condition. In order to operate the cell at high temperature while maintaining low methanol crossover

under ultra-low anode flow stoichiometry condition, a hydrocarbon membrane which has low methanol diffusivity can be selected as proton exchange membrane instead of a fluorocarbon membrane.

4.3.3   *Mitigation of non-uniformity by controlling transport resistance*

It is clear that non-uniform fuel distribution leads to other anode non-uniformities such as current density, crossover current density and temperature, as discussed. In additional, severe anode non-uniformity leads to poor cell voltage and poor fuel efficiency. Therefore, if we mitigate methanol concentration non-uniformity, we can improve both cell performance and fuel efficiency. In other words, cell operation under ultra-low anode stoichiometry becomes possible without sacrificing cell performance. In order to mitigate non-uniform fuel distribution, we should find clues about this in the methanol transport mechanism discussed previously.

It is shown that the effective resistance in Eq. (4-6) controls methanol transport in a DMFC. The conventional DMFC has almost uniform effective methanol transport resistance in the streamline direction, which results in large methanol concentration gradient in the streamline direction, i.e., methanol concentration non-uniformity. In order to build a more uniform methanol concentration distribution in the streamline direction, we should vary the effective methanol transport resistance itself. The inlet region where large methanol crossover occurs must have large methanol transport resistance to reduce methanol transport. In contrast, the outlet region must have small methanol transport resistance to enhance methanol transport. Hereafter, we call this concept 'streamline-graded structure (SGS)'. Although cell temperature and methanol concentration affect the effective methanol diffusivity also, they are not design parameters but operating

131

conditions. Opening ratio and porosity are important design parameters affecting the effective methanol transport resistance as shown in Figure [4-2].

Opening ratio affects not only convective transport but also diffusive transport. Narrow channel width (small A_R) in the inlet region reduces diffusive transport by increasing diffusion length. Deepening channel depth can be helpful for reducing convective effect and delaying methanol diffusion in inlet region. On the contrary, in the outlet half region where methanol concentration is low, a wide channel is beneficial due to short diffusion length, and shallow depth improves the convective effect. In summary, the final anode channel design has a three-dimensionally tapered shape as shown in Figure [4-8]. Although the tapered channel is good for uniform fuel distribution, one problem expected is a large pressure drop. Basically, the tapered channel is a nozzle which exerts large pressure in the wide open area. The present tapered channel has around 5 times greater pressure than the straight channel.

Molecular methanol diffusivity (D_{mol}^{MeOH}) is a strong function of porosity. In order to get a linearly varying diffusivity in streamline direction as,

$$D_{mol}^{MeOH}(y) = D_{min}^{MeOH} + \left(\frac{D_{max}^{MeOH} - D_{min}^{MeOH}}{L} \right) y \qquad (4\text{-}16)$$

GDL porosity can be set up as,

$$\varepsilon(y) = \left[\varepsilon_{min}^n + \left(\frac{\varepsilon_{max}^n - \varepsilon_{min}^n}{L} \right) y \right]^{\frac{1}{n}} \qquad (4\text{-}17)$$

However, it is not easy to fabricate such a material which has smoothly varying porosity as above. Instead, porosity can be distributed as a stepping shape as shown in Figure [4-10].

4.4   Results and Discussion

4.4.1   Methanol transfer resistance

In contrast to the 1-D fuel distribution model which assumes uniform liquid saturation in GDL, liquid saturation in the anode of the multi-D model decreases along the channel due to CO_2 gas accumulation as shown in Figure [4-9]. Therefore, molecular methanol diffusivity, which is a strong function of liquid saturation (see Eq. (4-3)), increases and methanol transport resistance decreases in the channel direction in the base model as shown in Figure [4-11]. SGS models show much larger resistance in the inlet region compared to the base model. Although they use a different approach to control methanol transport, the result (resistance) is similar.

4.4.2   Methanol concentration distribution

It is important to avoid 1st order MOR in ACL for high uniformity of current density along with maintaining sufficiently low methanol concentration near the ACL to avoid severe methanol crossover which deteriorates both cell performance and fuel efficiency. This requirement eventually leads to achieving high uniformity of methanol concentration, which is the main goal of the present study.

Methanol concentration in the channel direction is presented in Figure [4-12(a)]. On the contrary to the base model which shows large variation along the channel, SGS

models show more uniform distribution of methanol concentration thanks to the effect of redistribution of methanol transport resistance. Figure [4-13] shows methanol concentration contours in ACL. Again, methanol concentration in the outlet region increased whereas it decreased in the inlet region.

4.4.3 Current density distribution

Calculation results of current density distribution in the channel direction of multi-D model are presented in Figure [4-12 (b)]. As the cathode side is same for all cases, different current density distribution comes from the anode side. Similar to the result of the 1-D model, the base model shows severe non-uniformity which is direct consequence of non-uniform distribution of methanol concentration.

In the base model, peak current occurs not just in the inlet region but around the center region in the channel direction due to large methanol crossover at the inlet. SGS models have improved uniformity, and peak current density is observed almost in the inlet region due to reduced methanol crossover. A contour plot of current density is shown in Figure [4-14]. Note that peak current density is observed under the land region in the inlet half where excessive methanol concentration causes severe methanol crossover which leads to negative mixed potential there. In the outlet half region where methanol concentration is low, peak current density is observed under the channel region where methanol concentration is high compared to under the land region.

4.4.4 Crossover current density distribution

As crossover current is defined by the sum of electro-osmosis drag and methanol diffusion through the membrane, which is strongly affected by methanol concentration in

ACL, the plot from the calculation results of the multi-D model is similar to methanol concentration distribution as shown in Figure [4-12(c)]. The base model has strong crossover current density in the inlet region, which degrades cell performance by mixed potential. As SGS models have reduced current strength in the inlet region, crossover current by EOD is lower than that of the base model there. In addition, lowered methanol concentration of SGS models also reduces crossover current by diffusion in the inlet region. Hence, SGS models have reduced overpotential in inlet region. Figure [4-15] is the contour plot of crossover current density, which is similar to the methanol concentration distribution.

4.4.5 Temperature distribution

It is important to maintain uniform temperature of the membrane to avoid local thermal degradation, especially in large cells. Main heat sources increasing cell temperature by methanol are current and crossover current. Therefore, non-uniform distribution of them leads to large in-plane gradient of temperature. As Figure [4-16] shows, SGS models have a better distribution of temperature than the others. The region under the channel at the inlet is the hottest area due to large MOR and MCO.

4.4.6 Overpotential and cell performance

Overpotentials of each model are presented in Table [4-1]. As all models share the same cathode, cathode overpotentials are almost the same for each case. SGS models show better performance than the baseline model and this performance improvement came from the reduced anode overpotential by delaying MOR order shift.

Finally, polarization curves are shown in Figure [4-17]. SGS models show improved performance. In addition, SGS models have a bit extended limiting current density. This is because saved fuel in the inlet region due to reduced MCO was utilized in the outlet region, which prevented the cell from shutting down at high current operation.

4.5   Conclusion

It is found that DMFC which has conventional anode structure suffers from severe methanol crossover in the inlet region (low fuel efficiency) and methanol shortage in outlet region (low cell voltage) under ultra-low anode stoichiometry condition. Additionally, under such a condition, it is estimated that high cell temperature greater than 70 °C degrades cell performance by severe methanol crossover in the inlet region.

In order to overcome such problems occurring under ultra-low stoichiometry conditions, the present study suggested streamline-graded anode structures (SGS) which are designed to boost cell performance and fuel efficiency by mitigating anode non-uniformity. Calculation results showed that SGS models achieved about 10 % improvement of voltage and 3 % improvement of fuel efficiency (see Table 4-1).
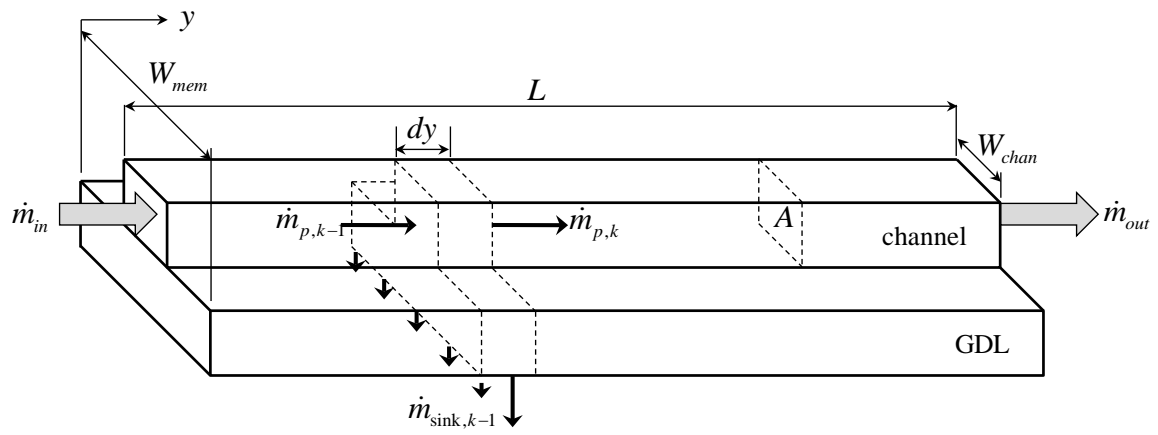
Figure [4-1]   Schematic of 1-D methanol transport model in a DMFC

(a)

(b)

138
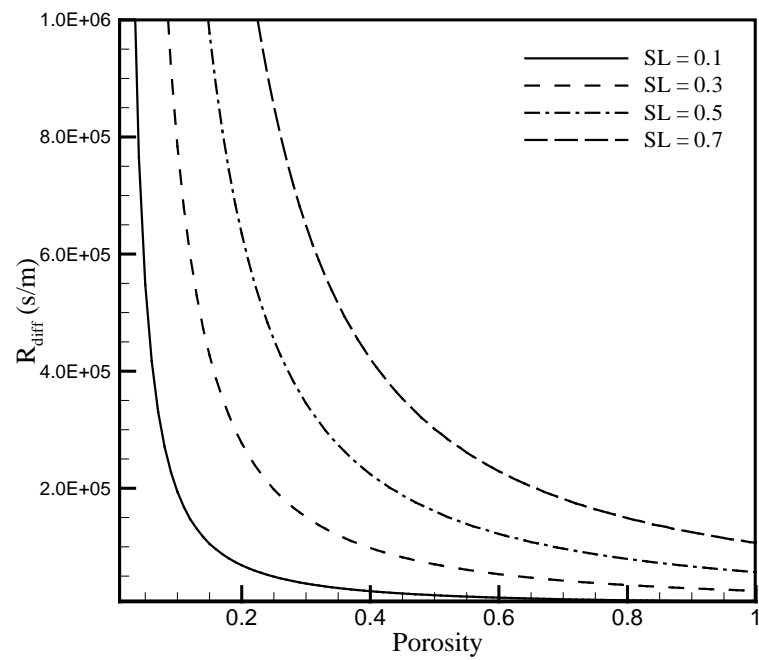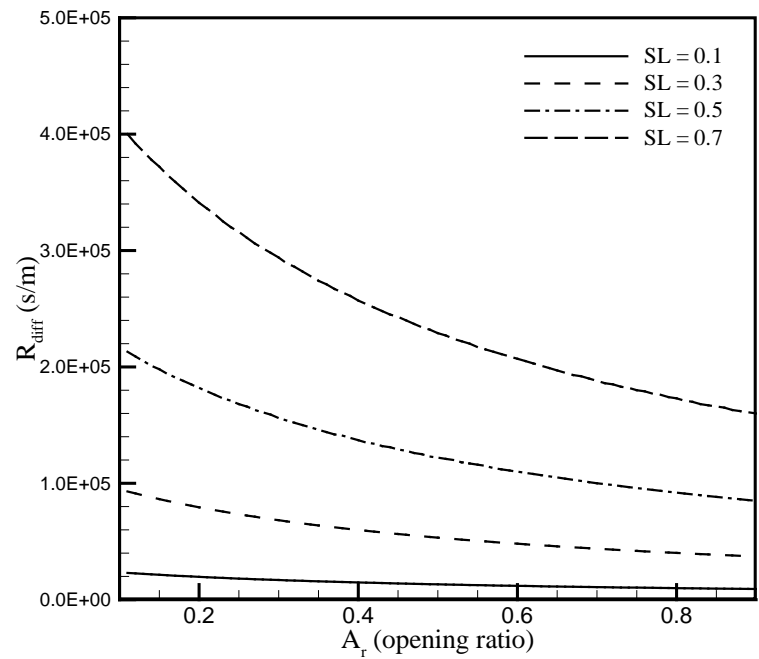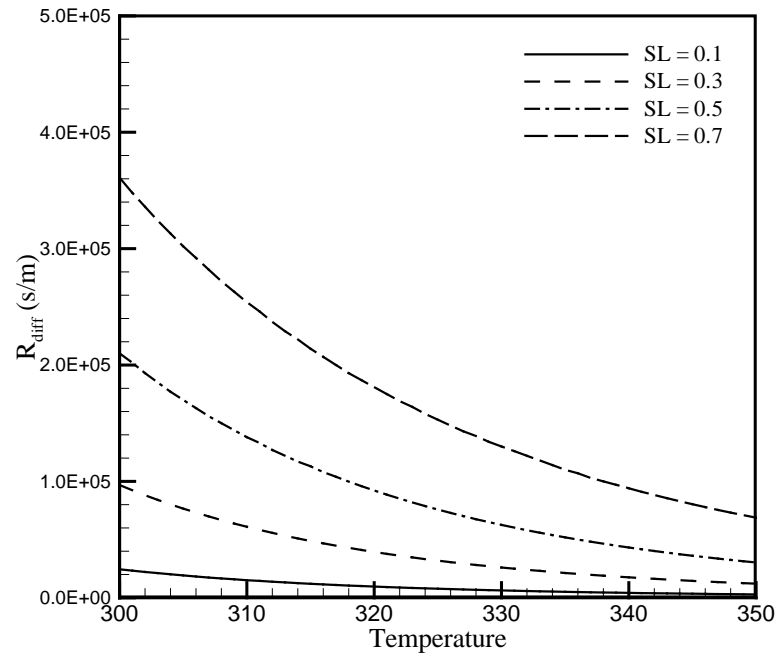
Figure [4-2]   Diffusive resistance according to (a) GDL porosity (ε), (b) opening ratio (A_R), (c) Temperature
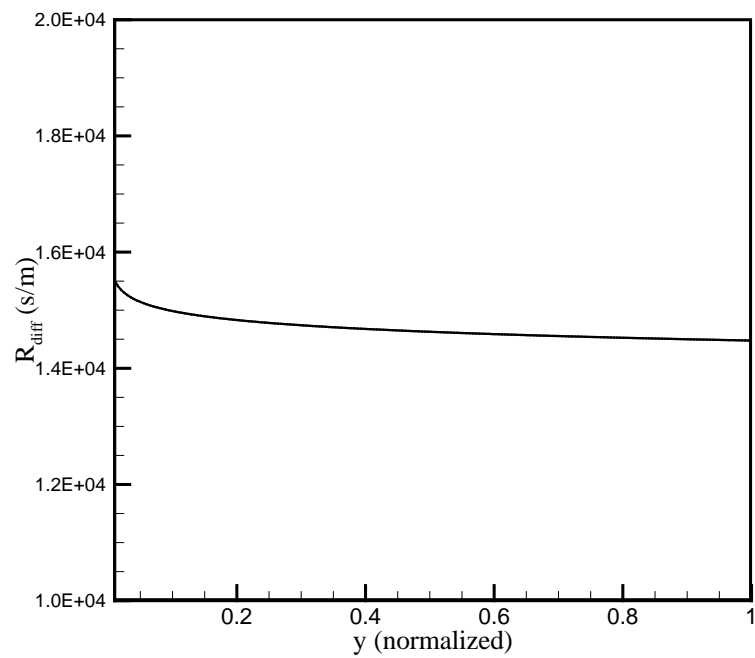
(a) Fuel transport resistance
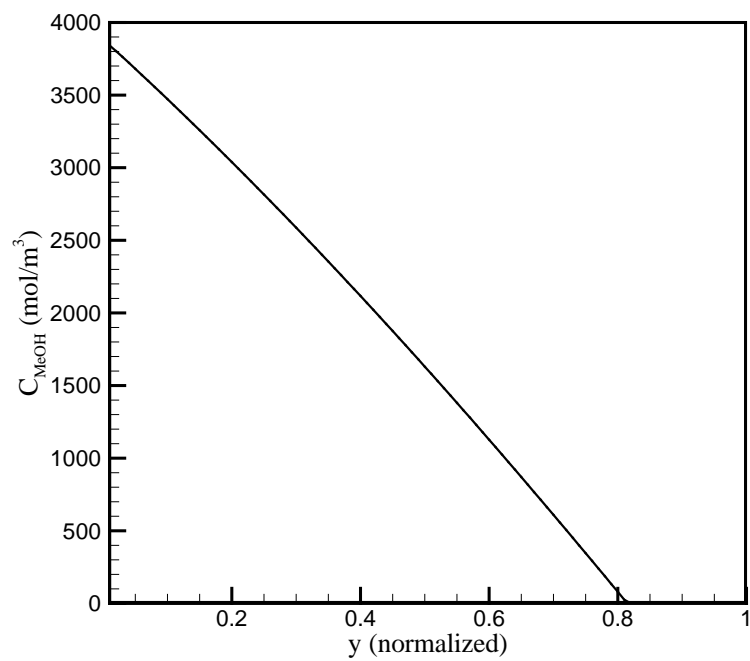
(b) Methanol concentration in anode catalyst layer
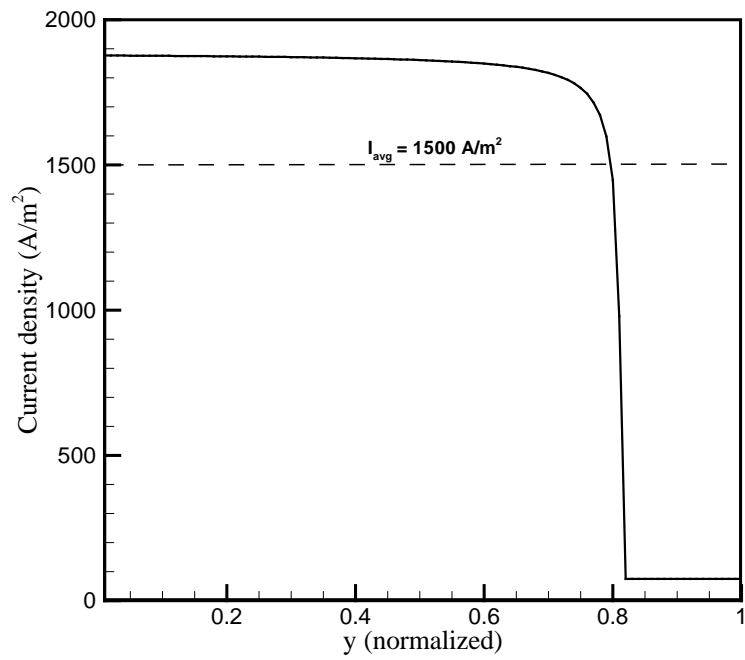
(c) Current density distribution

Figure [4-3]　　Calculation result of the 1-D model (T_{cell} = 313 K, I=150 mA/cm^2, ξ = 1.4)
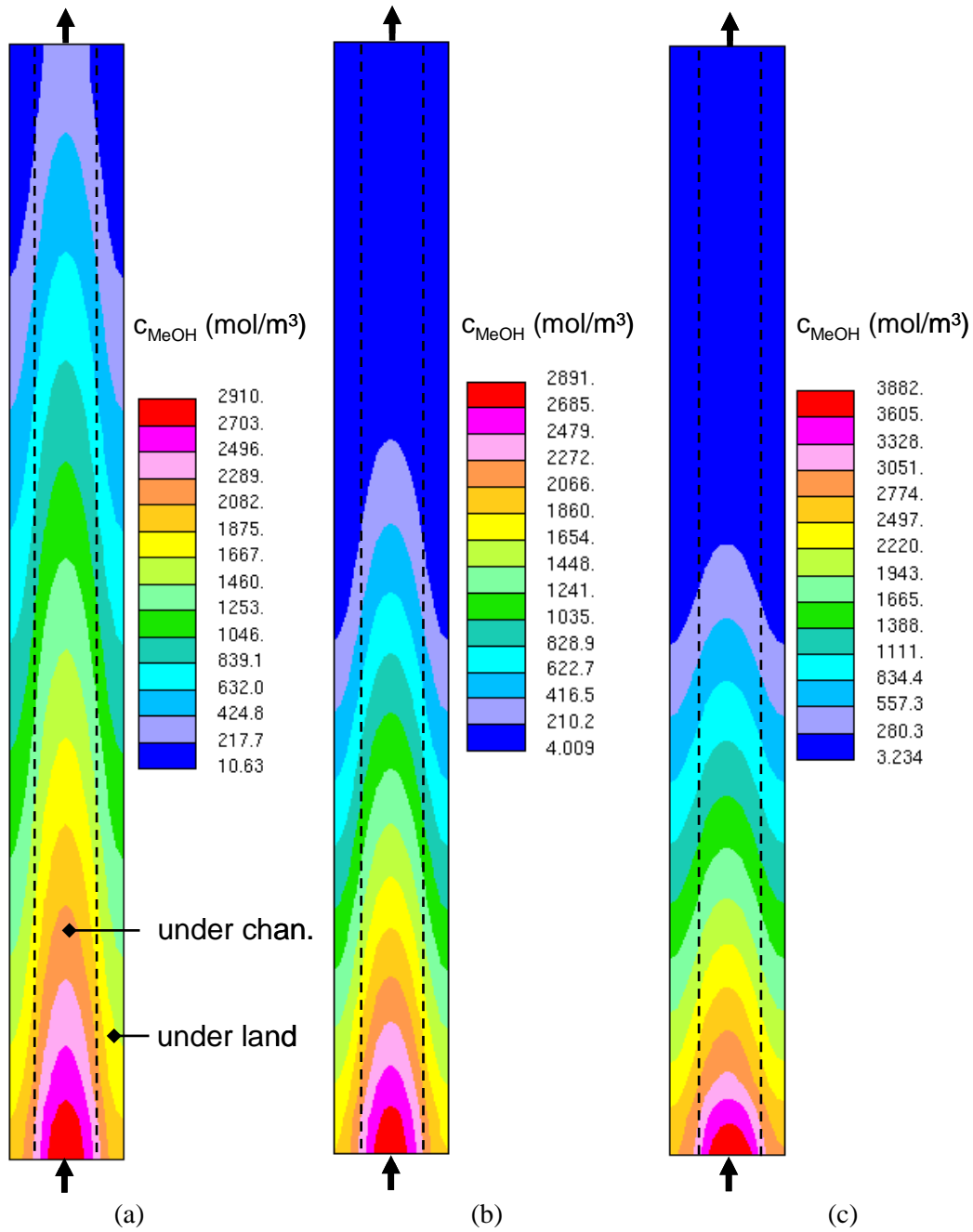
Figure [4-4]   Methanol concentration distribution in ACL, (a) T_{cell}=313K, ζ= a2.4c2.4, (b) T_{cell}=313K, ζ=a1.4c2.0, (c) T_{cell} =323K, ζ=a1.4c2.0
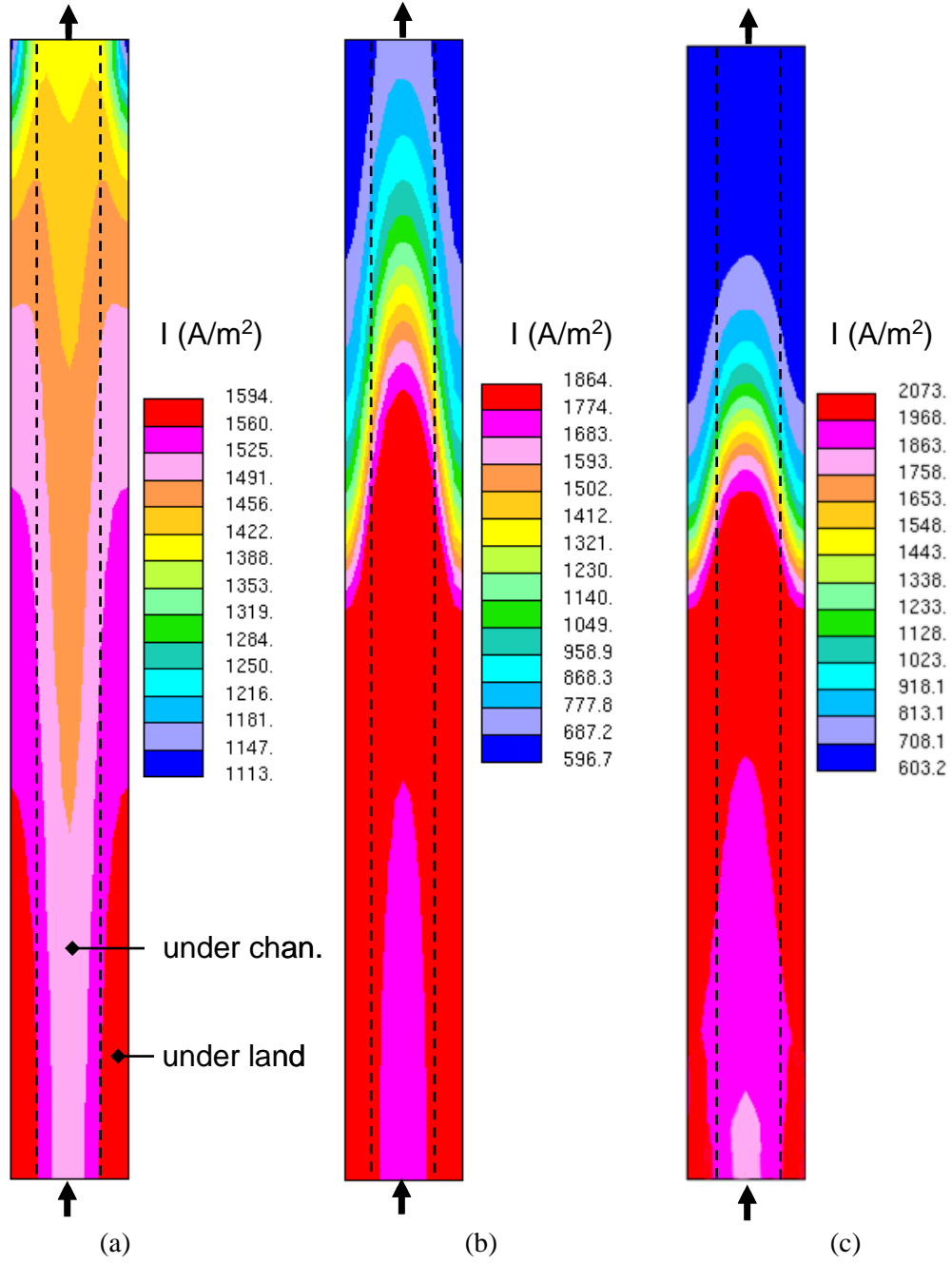
Figure [4-5] Current density distribution, (a) T_{cell}=313K, ζ= a2.4c2.4, (b) T_{cell}=313K, ζ=a1.4c2.0, (c) T_{cell} =323K, ζ=a1.4c2.0
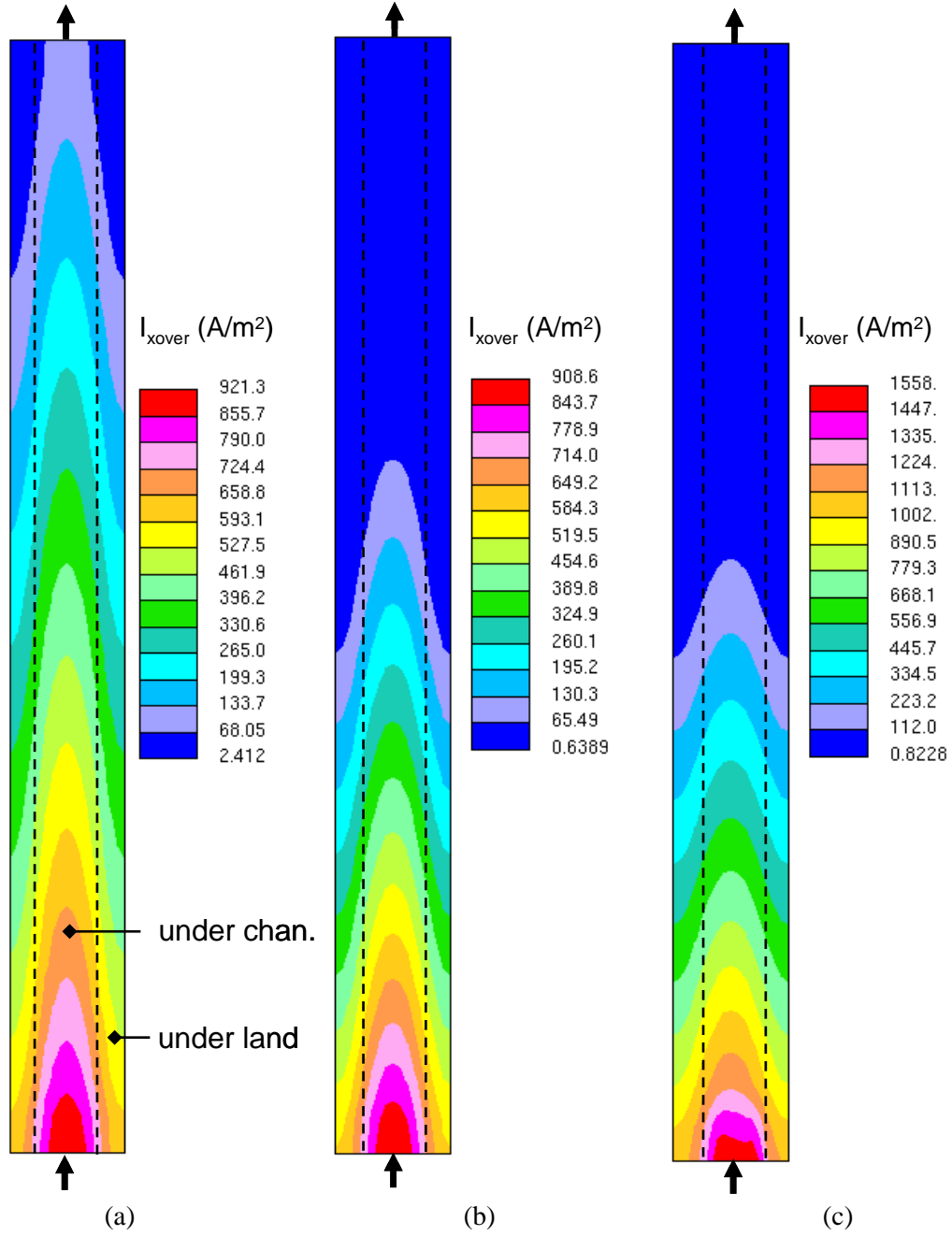
Figure [4-6]   Crossover current density distribution, (a) T_{cell}=313K, ζ= a2.4c2.4, (b) T_{cell}=313K, ζ=a1.4c2.0, (c) T_{cell} =323K, ζ=a1.4c2.0
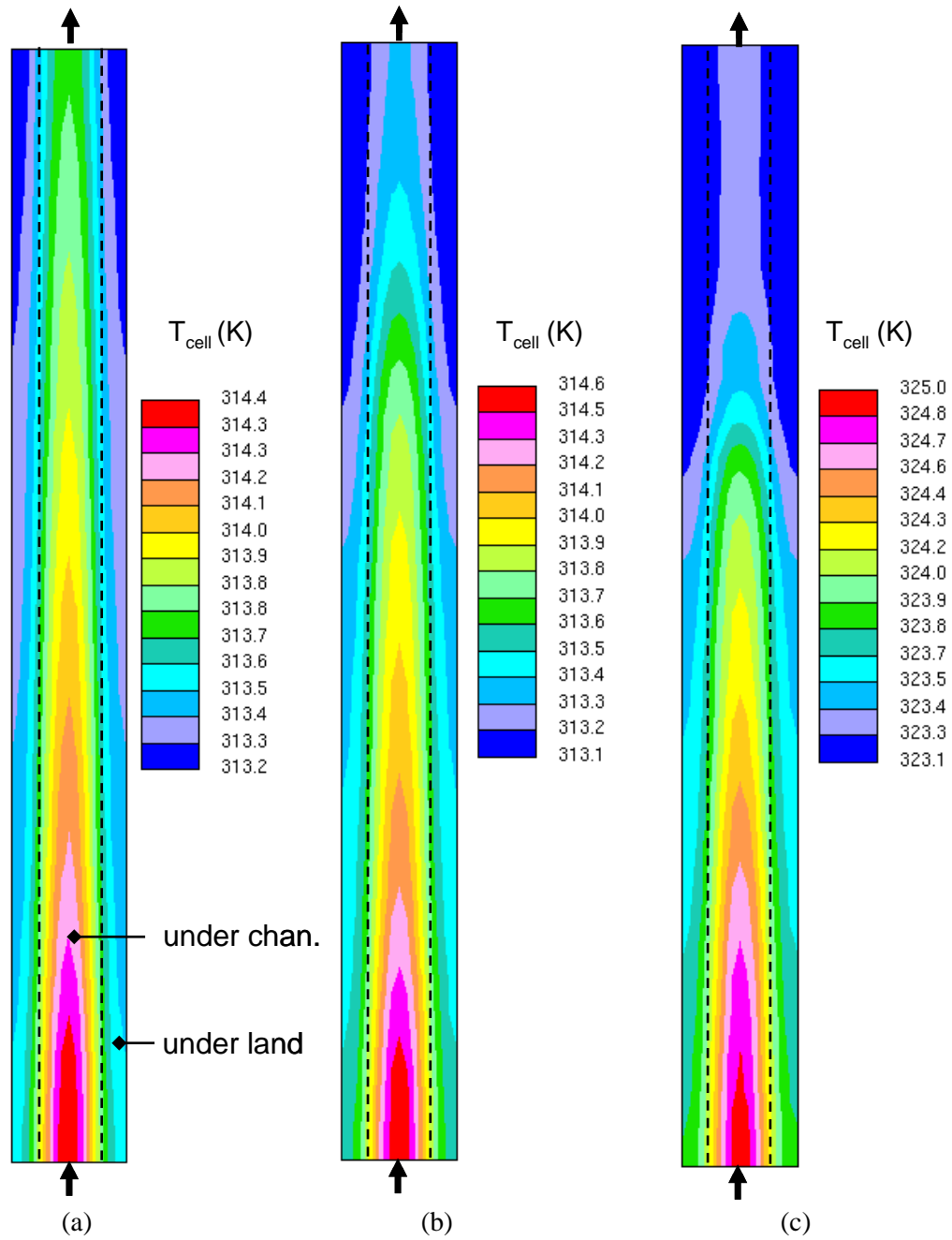
Figure [4-7]   Temperature distribution in membrane, (a) T_{cell}=313K, ζ= a2.4c2.4, (b) T_{cell}=313K, ζ=a1.4c2.0, (c) T_{cell} =323K, ζ=a1.4c2.0
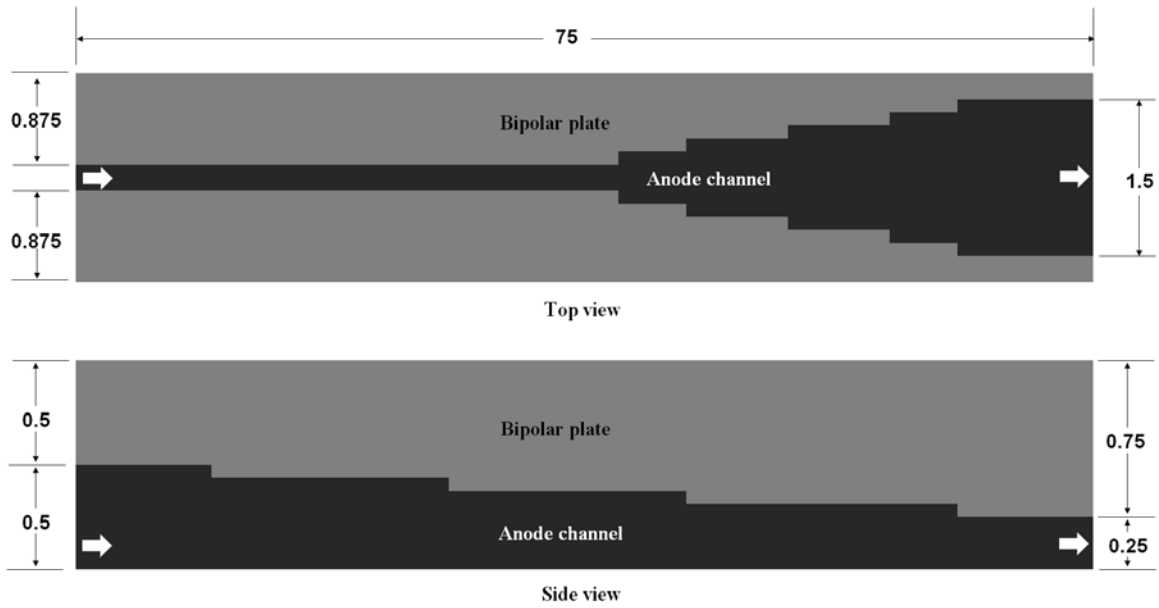
(a) 2-D schematic (not to actual scale)
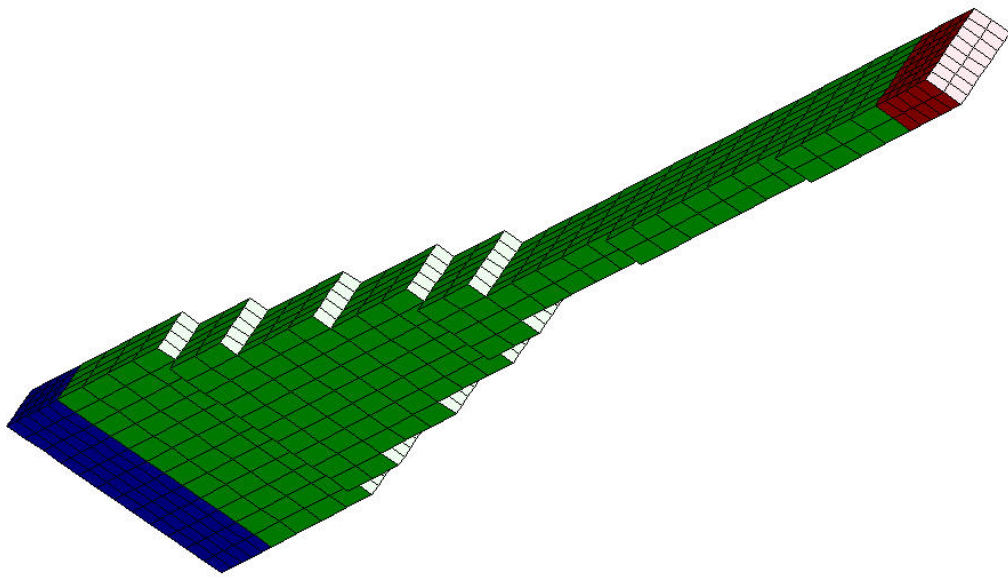
(b) 3-D mesh for CFD analysis

Figure [4-8]   Geometry of three-dimensionally tapered anode channel
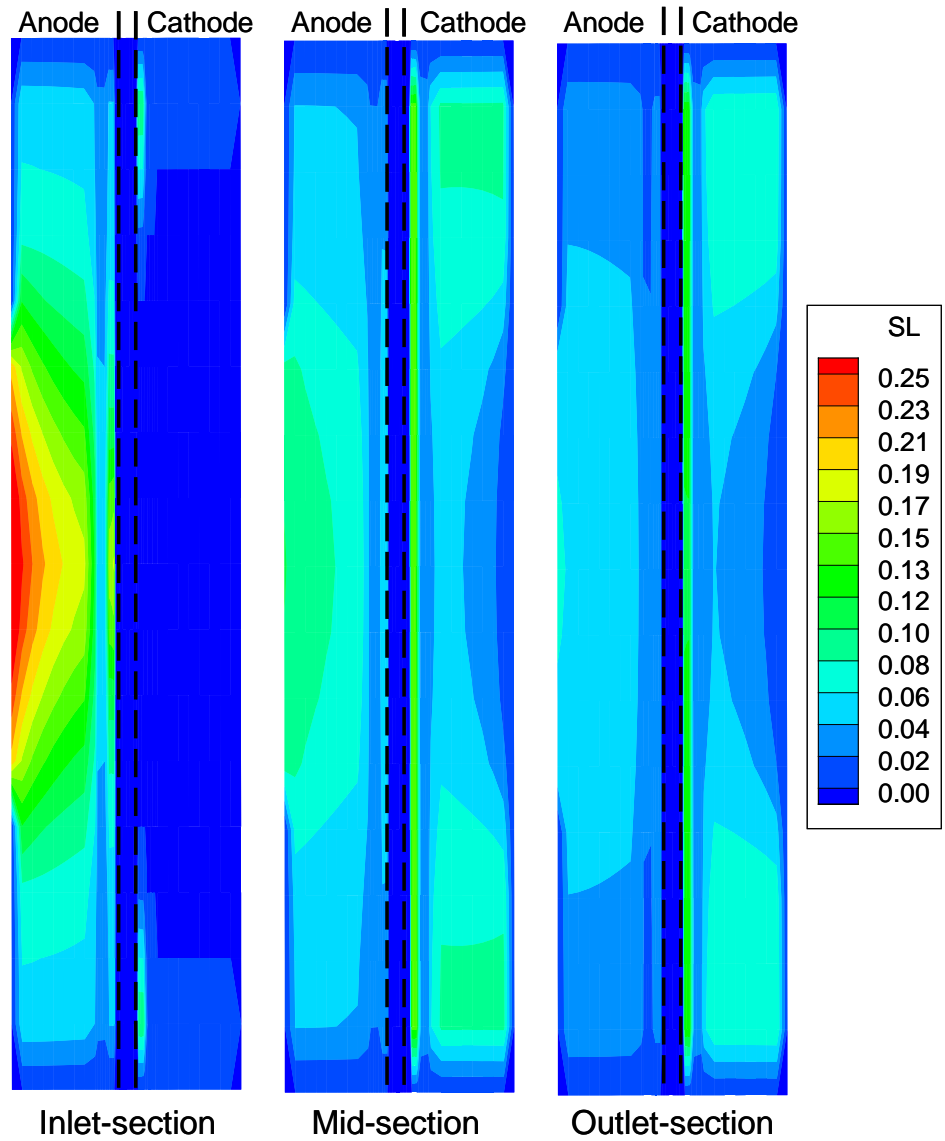
Figure [4-9]   Liquid saturation distribution at cross-section A, B, C showing saturation jumps at AGDL/AMPL, AMPL/ACL, CCL/CMPL, CMPL/CGDL, which effectively reduce water transfer coefficient of DMFC
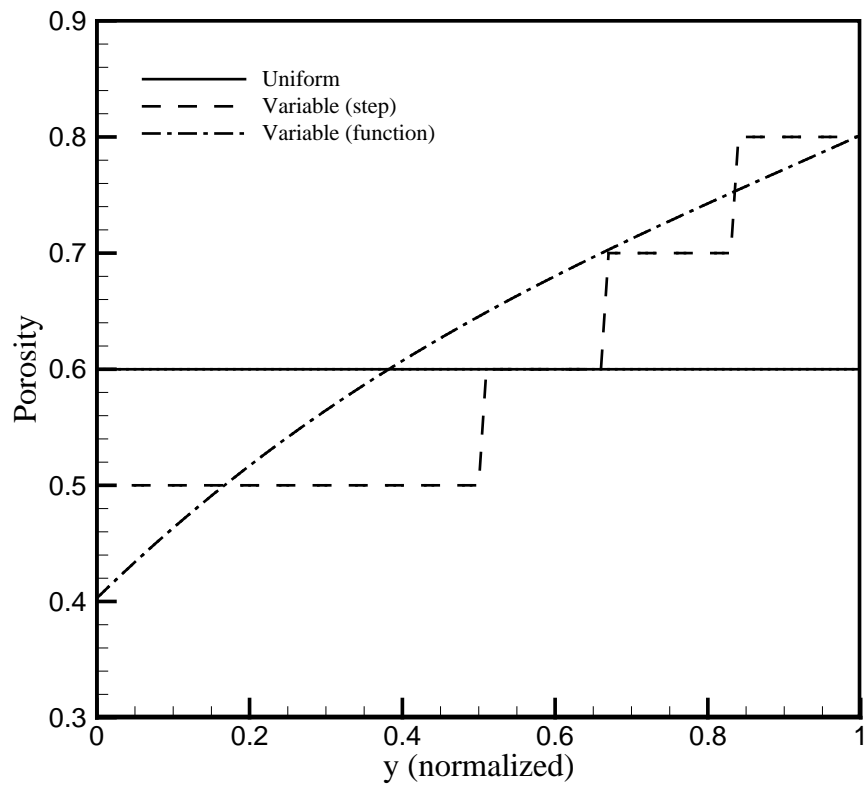
Figure [4-10]   Variable GDL porosity distribution for this study
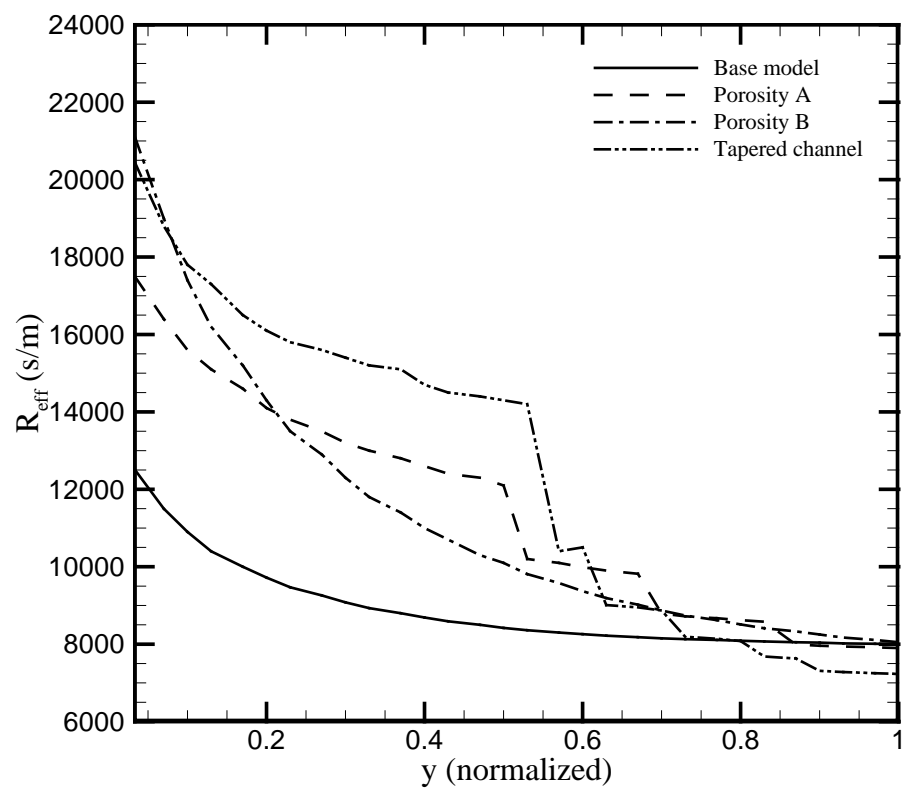
Figure [4-11]   Methanol transfer resistance distribution along streamline direction

	mean	sigma
Base model	934	867
SGS (Porosity A)	967	625
SGS (Porosity B)	972	611
SGS (Tapered)	794	325

(a) Methanol concentration distribution

	mean	sigma
Base model	1500	466
SGS (Porosity A)	1500	201
SGS (Porosity B)	1500	244
SGS (Tapered)	1500	79
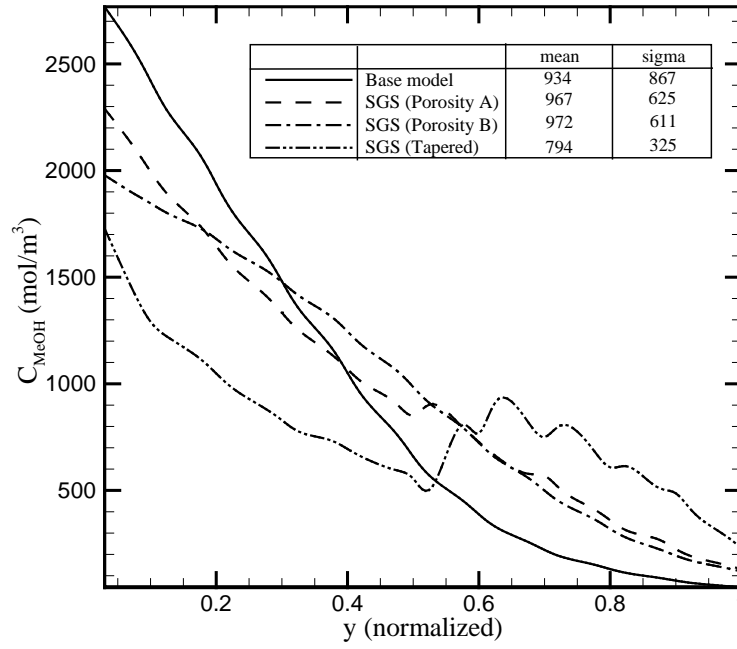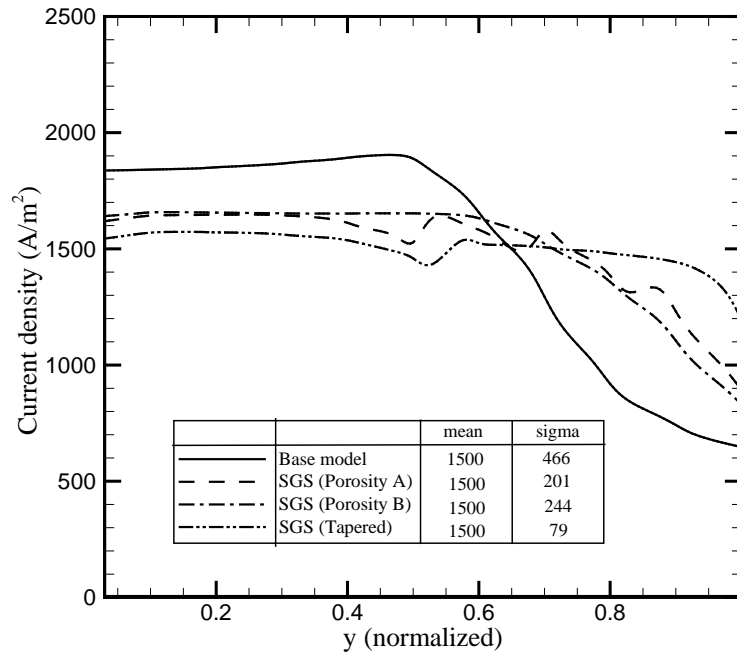
(b) Current density distribution
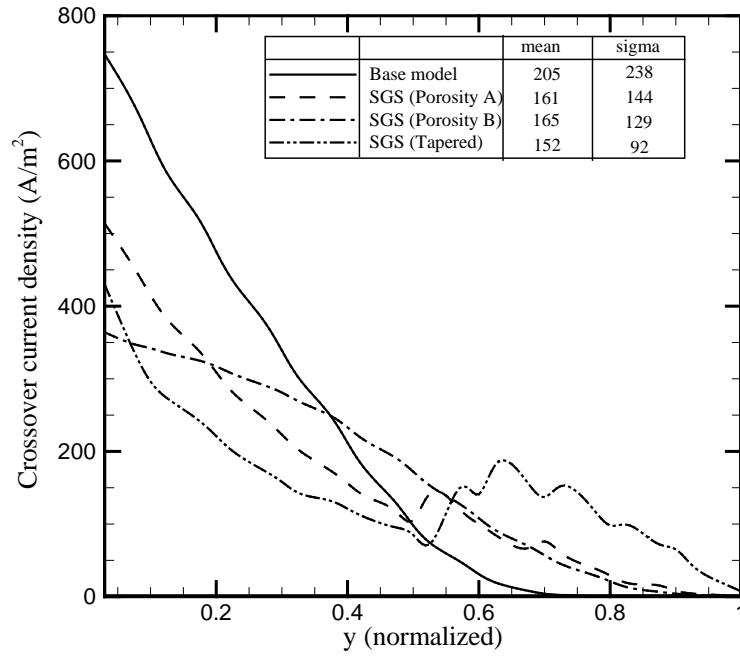
(c) Crossover density distribution

Figure [4-12]   Calculation result of multi-D DMFC model with streamline-graded structure (T_{cell} = 313 K, I=150 mA/cm^2, ξ_a = 1.4, ξ_c = 2.0)
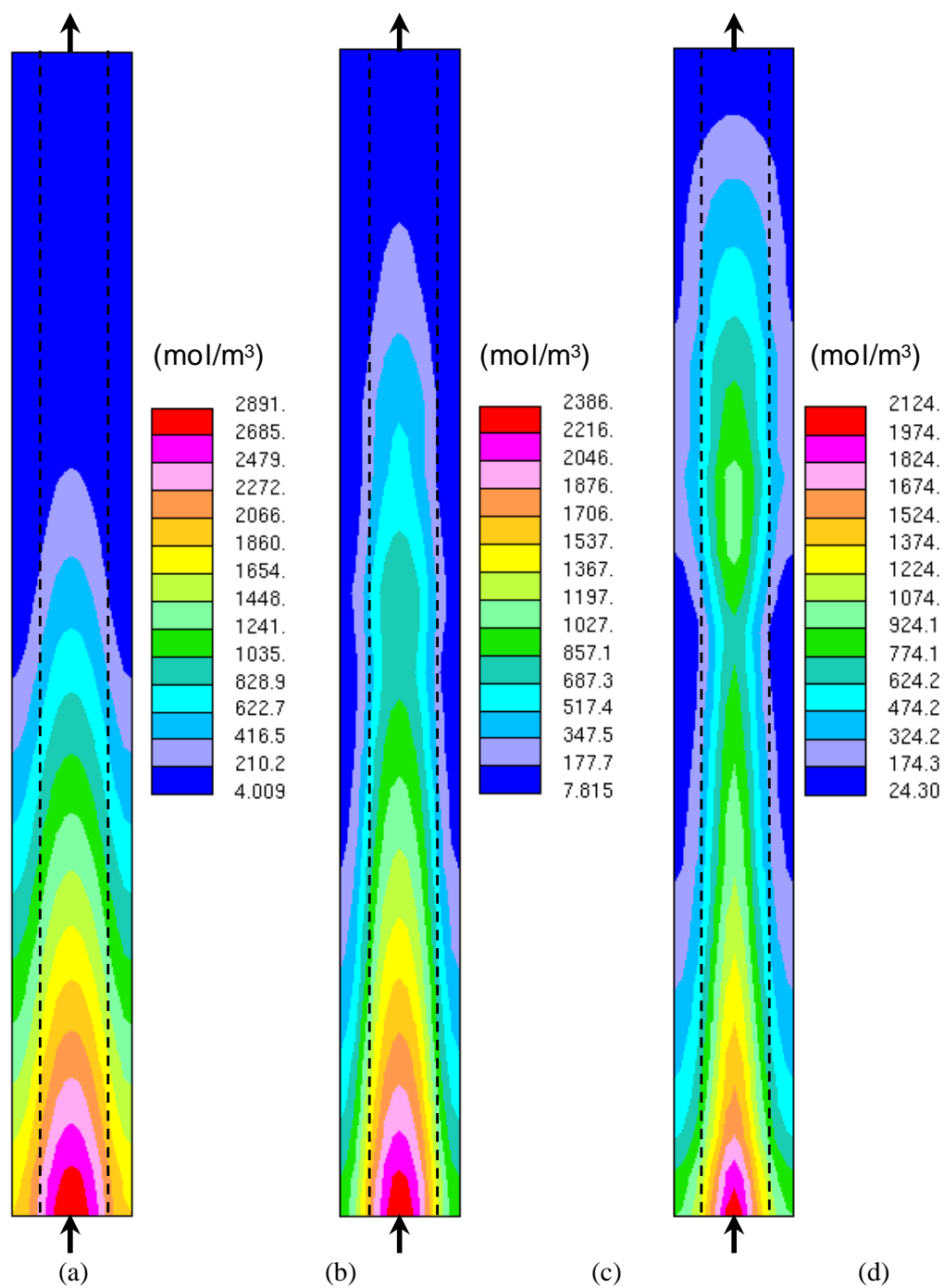
Figure [4-13]   Methanol concentration distribution in ACL, (a) baseline, (b) SGS (variable porosity), (c) SGS (tapered channel)

152
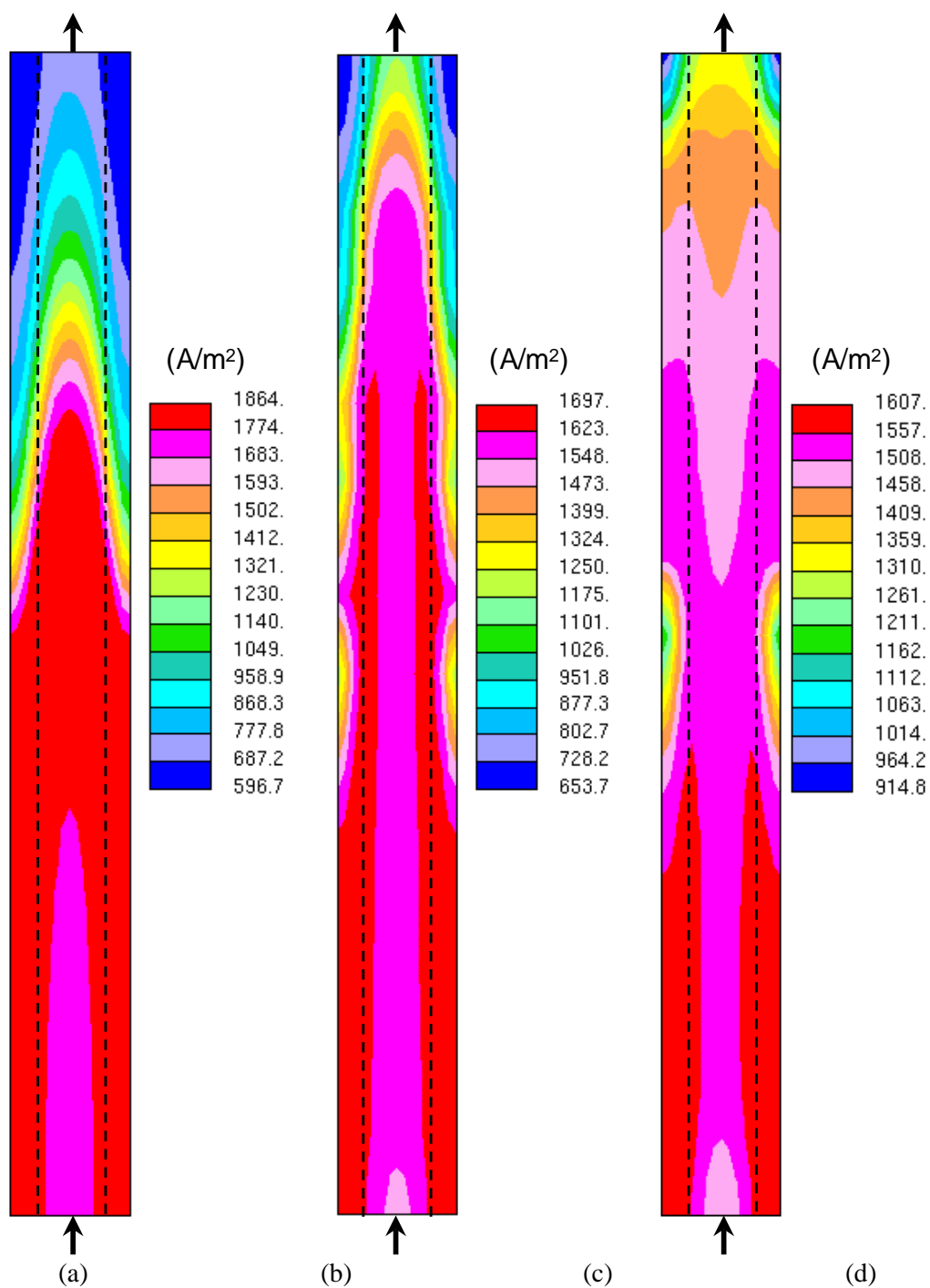
Figure [4-14]   Current density distribution, (a) baseline, (b) SGS (variable porosity), (c) SGS (tapered channel)
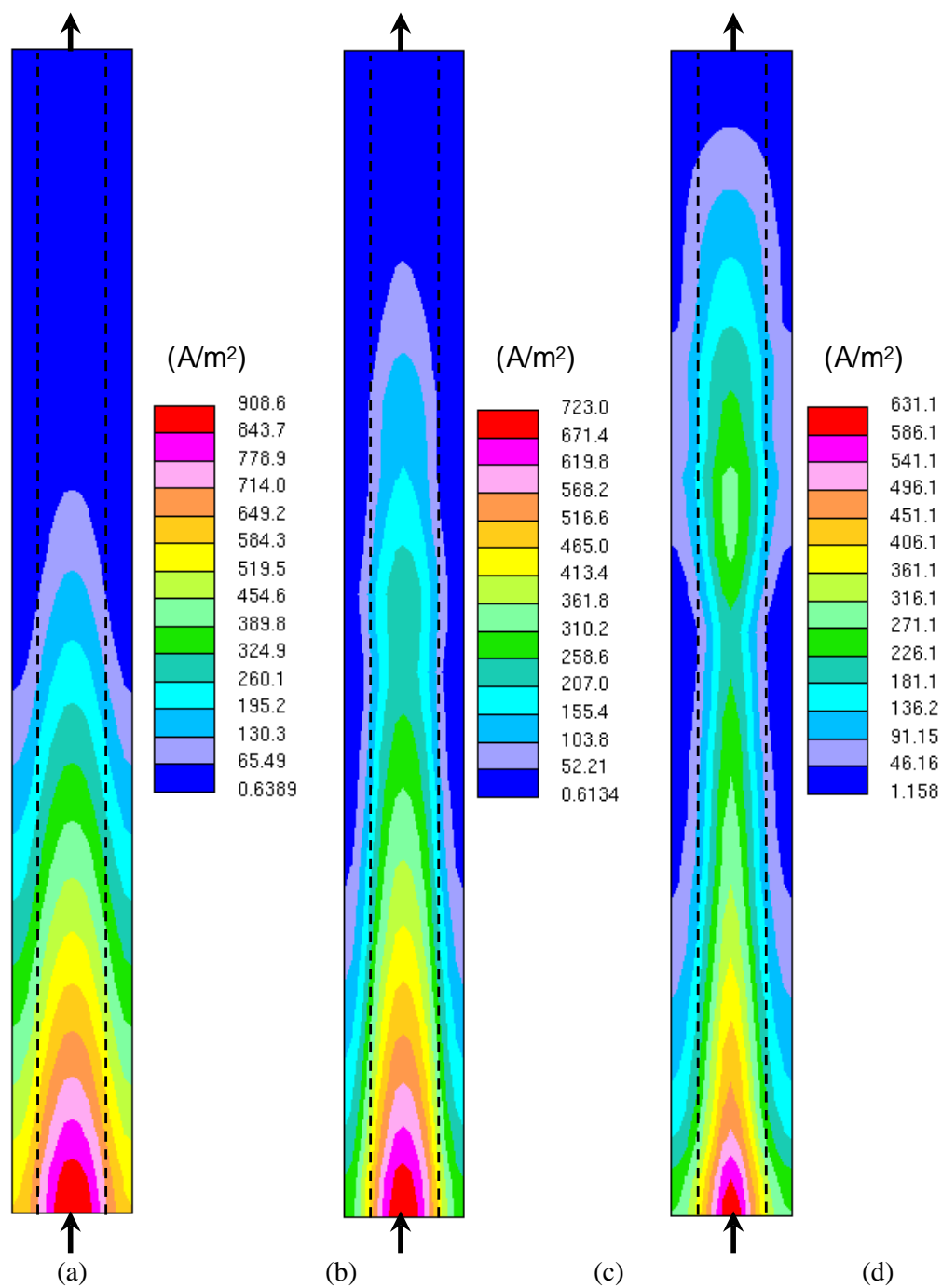
Figure [4-15]   Crossover current density distribution, (a) baseline, (b) SGS (variable porosity), (c) SGS (tapered channel)
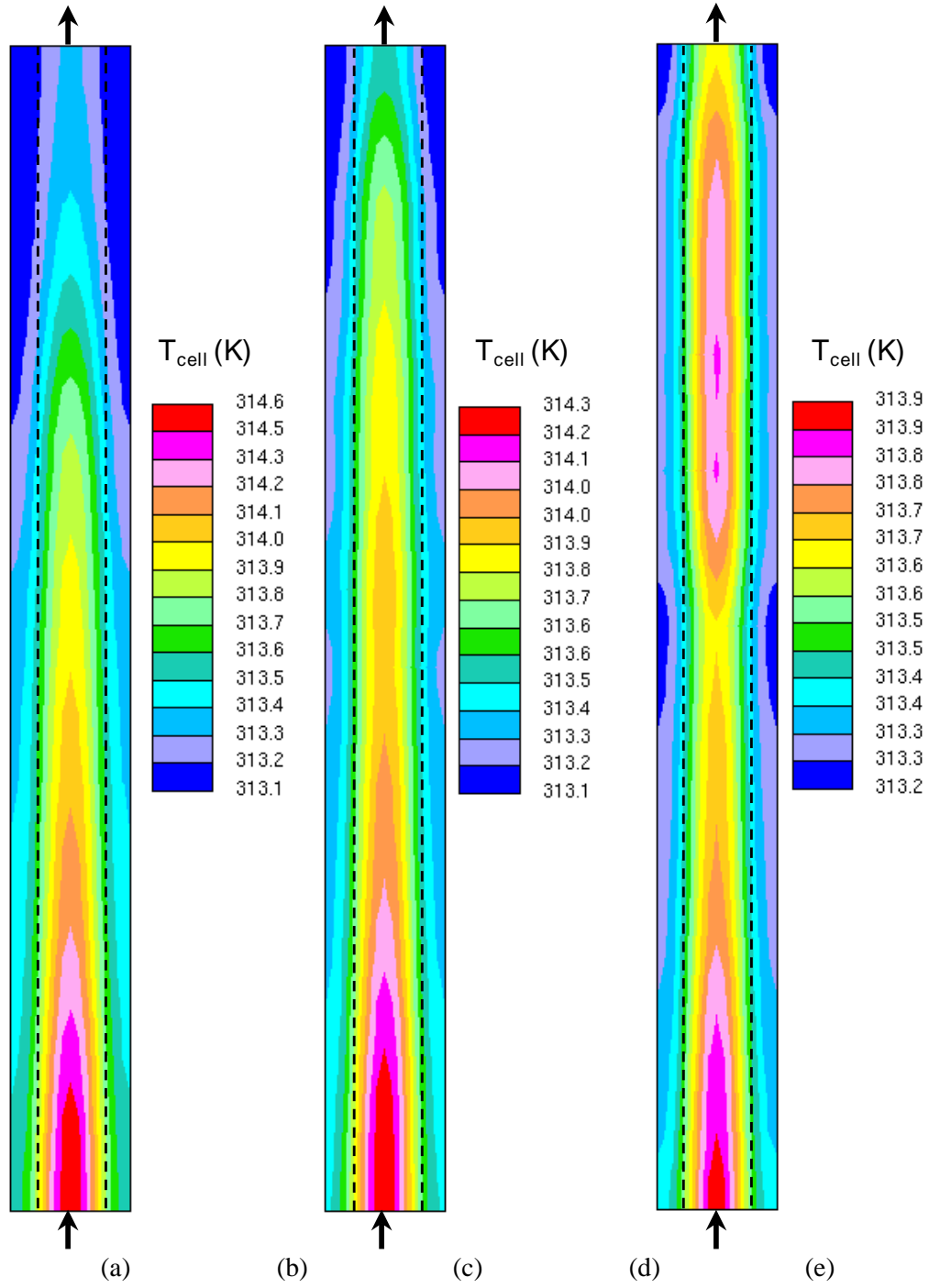
Figure [4-16]   Temperature distribution in membrane, (a) baseline ($\sigma = 0.26$ K), (b) SGS with variable GDL porosity ($\sigma = 0.13$ K), (c) SGS with tapered channel ($\sigma = 0.05$ K)
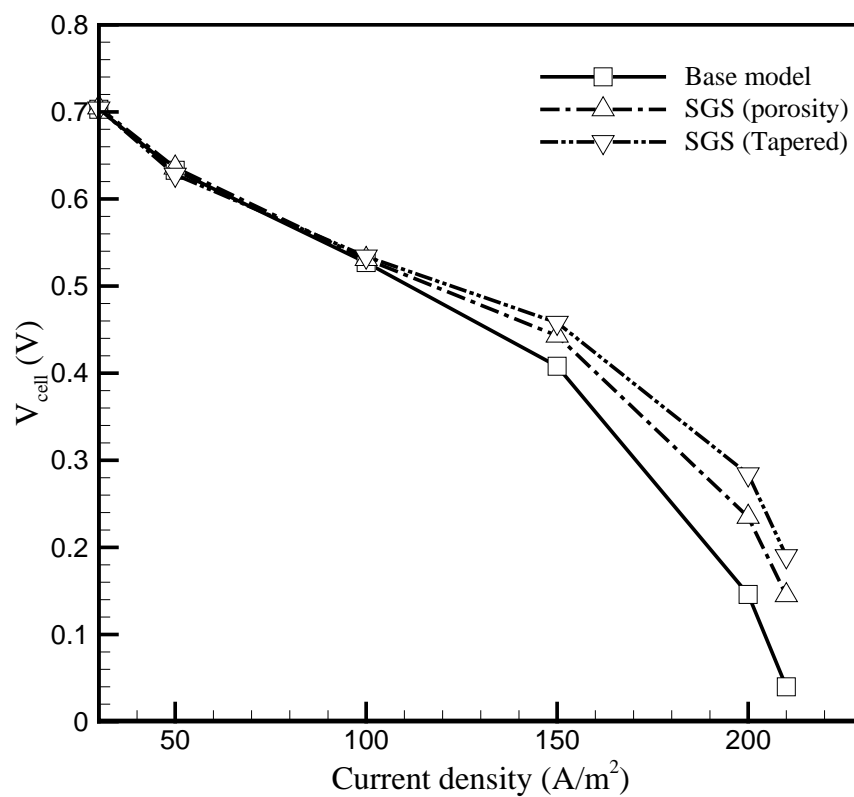
Figure [4-17]   Polarization curve comparison among the models discussed

TABLES

Table [4-1]   Calculation summary

	ξ_a	ξ_c	T_{cell}	$I\,(\text{A.}/\text{m}^2)$	$\eta_a\,(\text{V})$	$\eta_c\,(\text{V})$	$V_{\text{cell}}\,(\text{V})$	MCO (%)
Baseline	1.4	2.0	313	1500	0.444	0.274	0.408	12.0
SGS (Porosity A)	1.4	2.0	313	1500	0.413	0.277	0.443	9.7
SGS (Porosity B)	1.4	2.0	313	1500	0.415	0.276	0.441	9.9
SGS (Tapered)	1.4	2.0	313	1500	0.399	0.276	0.458	9.0

Chapter 5

DMFC with Interdigitated Fuel Distributor

5.1   Introduction

In addition to the cell unit, a DMFC system requires several mechanical components such as a fuel pump, air blower, gas-liquid separator, heat exchanger and so on. This is why a DMFC system is called a small power plant. As those mechanical parts consume power, it is important to minimize power consumption in order to maximize the net throughput. Additionally, minimizing power consumption provides us with more silent systems.

Various efforts have been applied to this challenging work to date. Instead of applying forced-convective air supply with blowers, some DMFCs adopt passive air supply on the cathode side which is often called an air-breathing cathode [54, 55, 57]. On the anode side, several different approaches to achieve minimizing parasitic power loss have been made. Generally, a passive anode structure delivers fuel in vapor-phase by using a vaporizer [58] or phase-separation film [59, 60] with liquid fuel cartridge, which makes the anode simpler. However, the reported cell performance of such a passive anode structure is not high enough compared to force-fed cells.

As discussed in Chapter 4, DMFCs with conventional anode structure suffer from severe performance loss due to anode non-uniformity when cells operate at ultra-low anode stoichiometry. In order to mitigate anode non-uniformity which degrades both cell voltage and fuel efficiency, we proposed the use of the streamline-graded structures (SGS) which enable a DMFC to operate with minimum fuel supply in Chapter 4.

158

In this chapter, we introduce a new anode structure design that improves cell performance under ultra-low anode stoichiometry condition based on the understanding of anode non-uniformity theory.

5.2   Physical model

5.2.1   *Interdigitated fuel distributor*

Figure [5-1] compares the anode structure of the conventional DMFC with the interdigitated DMFC which has a porous fuel distributor. In contrast to the conventional DMFC whose liquid fuel is supplied from the channel inlet, DMFC with fuel distributor delivers liquid fuel through the porous fuel distributor inserted between the liquid fuel chamber and the anode channel. Because the fuel chamber has a dead-end, all of supplied liquid fuel is forced to move though the porous fuel distributor by convection. In order to prevent CO_2 bubbles from penetrating the fuel chamber, the porous fuel distributor is made of hydrophilic materials such as Nafion. Therefore, we assume pure liquid exists in both the fuel chamber and the fuel distributor in this study. The anode channel whose inlet port is blocked receives liquid fuel from the surface of the fuel distributor. This is why the present DMFC is called 'interdigitated DMFC'. In order to uniformly distribute liquid fuel to the anode channel from the fuel chamber, it is important to address the design specification (thickness, porosity, permeability and hydrophobicity) of the fuel distributor.

5.2.2   1-D fuel distribution model

The 1-D fuel distribution model introduced in Chapter 4 is extended to compare the conventional DMFC with the interdigitated DMFC. Basic assumptions for the model are, *i*) uniform liquid saturation in porous media (0.2), *ii*) CO_2 is the only gas, and *iii*) zero water transfer coefficient ($\alpha = 0$).

Through-plane velocity of the fuel distributor can be easily found when anode stoichiometry and fuel concentration is given.

$$u_{\text{fd}} = \frac{\dot{m}}{\rho_l A_{\text{mem}}} = \frac{i_{\text{avg}}}{6\rho_l F}\left(M^{\text{MeOH}} + M^{\text{H}_2\text{O}}\right) \tag{5-1}$$

When uniform through-plane velocity distribution is assumed, along-channel velocity in the fuel chamber is found as follows:

$$u_{\text{fc}}(y) = u_{\text{in}}\left(1 - \frac{y}{L}\right) = \frac{i_{\text{avg}} A_{\text{mem}} \xi_a}{6\rho_l A_{\text{in}} F}\left(M^{\text{MeOH}} + M^{\text{H}_2\text{O}}\right)\left(1 - \frac{y}{L}\right) \tag{5-2}$$

When CO_2 is the only gas in the anode, the gas mass flow rate (kg/s) through the anode channel at location *y* is defined as follows:

$$\dot{m}_{\text{g},k} = \frac{M^{\text{CO}_2}}{6F} i(y)W_{\text{mem}} y \tag{5-3}$$

The liquid flow rate though anode channel is found by considering fuel supply from the fuel distributor and fuel consumption by MOR and MCO as follows:

$$\begin{aligned}
\dot{m}_{\text{l},k} = \dot{m}_{\text{l},k-1} &- \frac{i(y)}{6F}\left(M^{\text{H}_2\text{O}} + M^{\text{MeOH}}\right)W_{\text{mem}}dy \\
&- D_{\text{mem}}^{\text{MeOH}} M^{\text{MeOH}} W_{\text{mem}} dy \frac{C_{\text{cl}}^{\text{MeOH}}(y)}{\delta_{\text{mem}}} + \rho_l u_{\text{fd}} W_{\text{chn}} dy
\end{aligned} \tag{5-4}$$

Gas mass fraction is found by

$$Y_g(y) = \frac{\dot{m}_g(y)}{\dot{m}_l(y) + \dot{m}_g(y)} \tag{5-5}$$

And liquid saturation is determined as

$$s_l(x) = \frac{\rho_g Y_l}{\rho_l(1-Y_l) + \rho_g Y_l} = \frac{\rho_g(1-Y_g)}{\rho_l Y_g + \rho_g(1-Y_g)} \tag{5-6}$$

Therefore, liquid and gas phase velocity in the anode channel can be found as follows:

$$u_l(y) = \frac{\dot{m}_l(y)}{\rho_l A_l(y)} = \frac{\dot{m}_l(y)}{\rho_l A(y) s_l(y)}$$

$$u_g(y) = \frac{\dot{m}_g(y)}{\rho_g A_g(y)} = \frac{\dot{m}_g(y)}{\rho_l A(y)(1-s_l(y))} \tag{5-7}$$

$$u(y) = s_l u_l + (1-s_l) u_g$$

Methanol mass fraction in the anode channel can be found according to the methanol conservation in a control volume k with previously calculated velocity distribution as follows:

$$Y_k = \frac{(s_{l,k-1})u_{l,k-1}}{(s_{l,k})u_{l,k}} Y_{k-1} + \frac{u_{fd} dy}{(s_{l,k} H_{chn})u_{l,k}} Y_{fc,k} - \frac{i_{avg} M^{MeOH} dy}{6F\rho_l(s_{l,k} H_{chn})u_{l,k}} \left(\frac{W_{mem}}{W_{chn}}\right)$$
$$- \frac{D_{mem}^{MeOH} M^{MeOH} dx C_{cl}^{MeOH}(y)}{\delta_{mem}\rho_l(s_{l,k} H_{chn})u_{l,k}} \left(\frac{W_{mem}}{W_{chn}}\right) \tag{5-8}$$

Methanol concentration in ACL is found by

$$N^{MeOH} = \frac{i_{avg}}{6F} = D_{eff}^{MeOH} \frac{C_{chn}^{MeOH} - C_{acl}^{MeOH}}{\delta_{gdl}} \tag{5-9}$$

According to the methanol concentration in ACL, local reaction current density is determined by the Tafel approximation.

5.2.3 Multi-D DMFC model

In order to investigate the effect of fuel distributor properties on anode uniformity and cell performance, multi-D model is applied for the present study. Present multi-D model is extended from the baseline model introduced in Chapter 4. Governing equations and parameters are found in the Appendix.

Figure [5-2] shows the three dimensional model geometry and Figure [5-3] presents the cross-sectional cell structure of the interdigitated DMFC used for the present multi-D simulation. The cell has seven sandwich layers composed by proton exchange membrane, two MPLs, two CLs and two GDLs.

5.3   Results and Discussion

5.3.1 1-D model result

Methanol concentration near the ACL is presented in Figure [5-4]. Under ultra-low stoichiometry condition, the conventional DMFC suffers from severe methanol crossover in the inlet region and methanol shortage in the outlet region, which is called anode non-uniformity. In the case of the interdigitated DMFC, fuel distribution is more uniform compared to the conventional cell since fuel is uniformly supplied from the fuel distributor along the channel direction. Figure [5-5] shows the current density distribution when both cells operate at the same average current density (150 mA/cm^2). In the outlet region of the conventional DMFC, current density sharply decreases since MOR shifts

from 0th order to 1st order there. The interdigtated cell shows relatively uniform distribution of current density.

5.3.2 Design of fuel distributor

In order to achieve uniform fuel distribution in the anode channel from the fuel distributor, mass flux through the porous fuel distributor should first be uniform. Although the entire mass in the fuel chamber moves to the anode channel through the porous fuel distributor, local mass flux can vary according to the pressure gradient formed in the fuel supply assembly (fuel chamber, fuel distributor and flow field) and the pressure gradient is strongly affected by the permeability of the porous fuel distributor. Pressure drop through the porous fuel distributor is governed by Darcy's law as follows:

$$\Delta p = \frac{\mu_l u_{fd}}{K_{fd} \delta_{fd}}$$

(5-10)

Figure [5-6] shows pressure field formed in the fuel supply assembly according to the permeability of the porous fuel distributor. When the porous fuel distributor is highly permeable, the fuel supply assembly is nothing more than a normal flow channel which has channel direction favored pressure gradient (Figure [5-6(a)]). In this case, mass flux from the fuel chamber to the flow channel is concentrated in region A and B. As region A has a sudden expansion and region B has sudden contraction, those regions have the largest pressure gradient inducing most of the mass flux from the fuel chamber. Pressure gradient shifts to the through-plane direction as the permeability of the fuel distributor becomes lower, and mass flux distribution becomes more uniform as shown in Figure [5-6(d)]. However, practical permeability should be selected by considering allowed

pressure drop for cell design. Figure [5-6(c)] is a reasonable choice for that reason in this study.

The purpose of using the porous fuel distributor is to change diffusion-dominant transport to convection-dominant transport. The Peclet number (*Pe*) in Eq. (5-11) explains which transport mechanism is strong in the porous fuel distributor. If Peclet number is greater than 1, convection is dominant over diffusion. Peclet number of a conventional DMFC (GDL) is very small ($\sim 10^{-3}$).

$$Pe = \frac{\delta_{\text{fd}}}{D_{\text{eff}}^{\text{MeOH}}} u_{\text{fd}} = \frac{\delta_{\text{fd}}}{D_{\text{l}}^{\text{meoh}} \varepsilon^n} u_{\text{fd}} \tag{5-11}$$

When the thickness of the porous fuel distributor and flow rate are given, Peclet number is a function of porosity as shown in Figure [5-7]. If we correlate permeability with porosity by using an empirical relationship (*the Carman-Kozney equation*) as Eq. (5-12), the approximate porosity of the porous fuel distributor can be determined.

$$K = \frac{\varepsilon^3}{150\left(1-\varepsilon^2\right)} d_{\text{p}}^2 \tag{5-12}$$

As K_{fd} is selected about 10^{-13} in the present study, the porosity of the fuel distributor is around 0.3 and Peclet number is around 0.6 by Figure [5-7].

For practical applications, it is important to prevent CO_2 bubbles from penetrating the fuel chamber for steady cell operation. Once a CO_2 bubble penetrates the fuel chamber, it remains there and hinders fuel delivery to the anode flow channel because of the dead-end structure of the fuel chamber. From that reason, the porous fuel distributor must be made of hydrophilic material which expels CO_2 bubbles. As the liquid pressure in the fuel chamber is higher than the anode flow channel, it is possible for liquid fuel to penetrate

the GDL with large hydraulic force. This may lead to catastrophic results such as severe methanol crossover and voltage loss. To prevent this problem, low permeability of the fuel distributor is suggested with hydrophobic anode MPL.

5.3.3 Multi-D simulation result

Figure [5-8] compares methanol concentration distribution of the conventional DMFC with the interdigitated DMFC. With help from the porous fuel distributor, the interdigitated DMFC has reduced fuel concentration near the inlet region and increased fuel concentration near the outlet region, which means improved fuel concentration uniformity compared to the conventional DMFC. Reduced methanol concentration in the inlet region mitigates local methanol crossover while increased methanol concentration in the outlet region relieves the cell from voltage loss due to methanol concentration loss.

Local current density distribution is presented in Figure [5-9]. As predicted in the 1-D model analysis, the conventional DMFC has a sharply decreasing distribution near the outlet region since MOR shifts to first-order whereas the interdigitated DMFC shows a more uniform distribution due to improved methanol concentration uniformity. Local crossover current density follows a similar distribution trend with methanol concentration as shown Figure [5-10], since it is a strong function of methanol concentration. The interdigitated DMFC shows reduced average crossover current density with improved uniformity compared to the conventional DMFC.

Local temperature distribution is strongly affected by heat sources due to local current density and local crossover current density. As the interdigitated DMFC has more uniform distribution of local current density and local crossover current density, it shows better uniformity of temperature as shown in Figure [5-11].

5.3.4   *Overall cell performance*

Anode uniformity and cell overpotentials are summarized in Table [5-1]. With the newly designed fuel supply structure, anode non-uniformity is mitigated (low standard deviations) and anode overpotential due to concentration loss is reduced. Around 30 mV voltage increment by changed anode structure is predicted in this study, which is close to the performance improvement done by streamline-graded structure (SGS) studied in Chapter 4. In addition, better fuel efficiency (lower MCO) is achieved also by saving excessive fuel in the inlet region and utilizing it in the outlet region.

Finally, a polarization curve comparison between the conventional DMFC and the interdigitated DMFC is presented in Figure [5-12], which clearly shows the benefit of the interdigitated anode structure.

5.4   Conclusion

Mitigating anode non-uniformity is crucial for achieving high cell voltage and high fuel efficiency under ultra-low anode stoichiometry conditions. Instead of manipulating fuel transport resistance, interdigitated fuel supply structure achieves a similar effect of mitigating anode non-uniformity by converting diffusive transport mechanism to convective transport mechanism through the porous fuel distributor, which results in both uniform flow rate and uniform fuel concentration. Calculation results with multi-D simulation predicted a similar level of performance improvement with the present interdigitated structure compared to the streamline-graded structure.

(a)

(b)
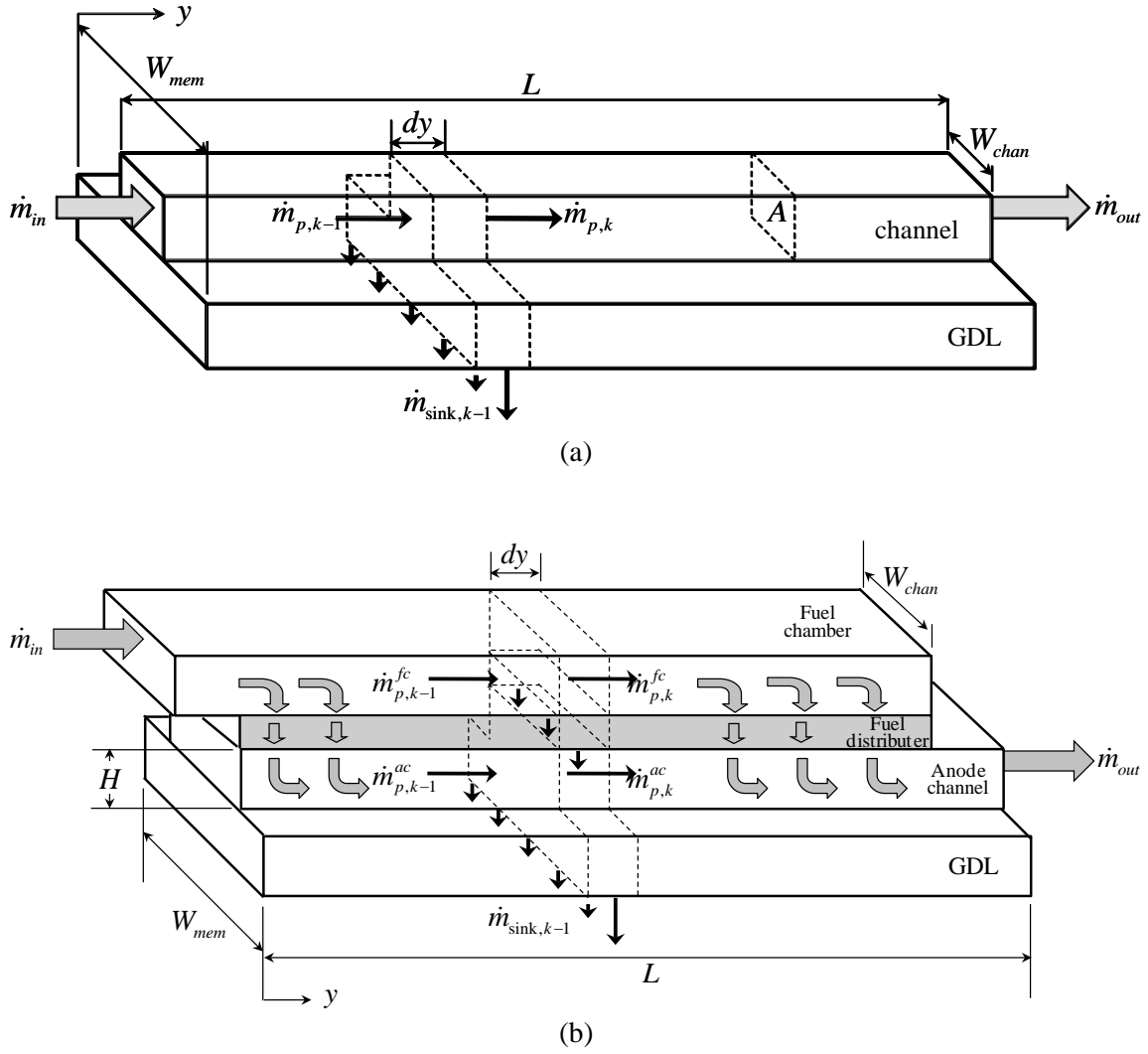
Figure [5-1]   Schematics showing fuel flow route in the conventional DMFC (upper) and interdigitated DMFC (lower) used for 1-D fuel distribution model
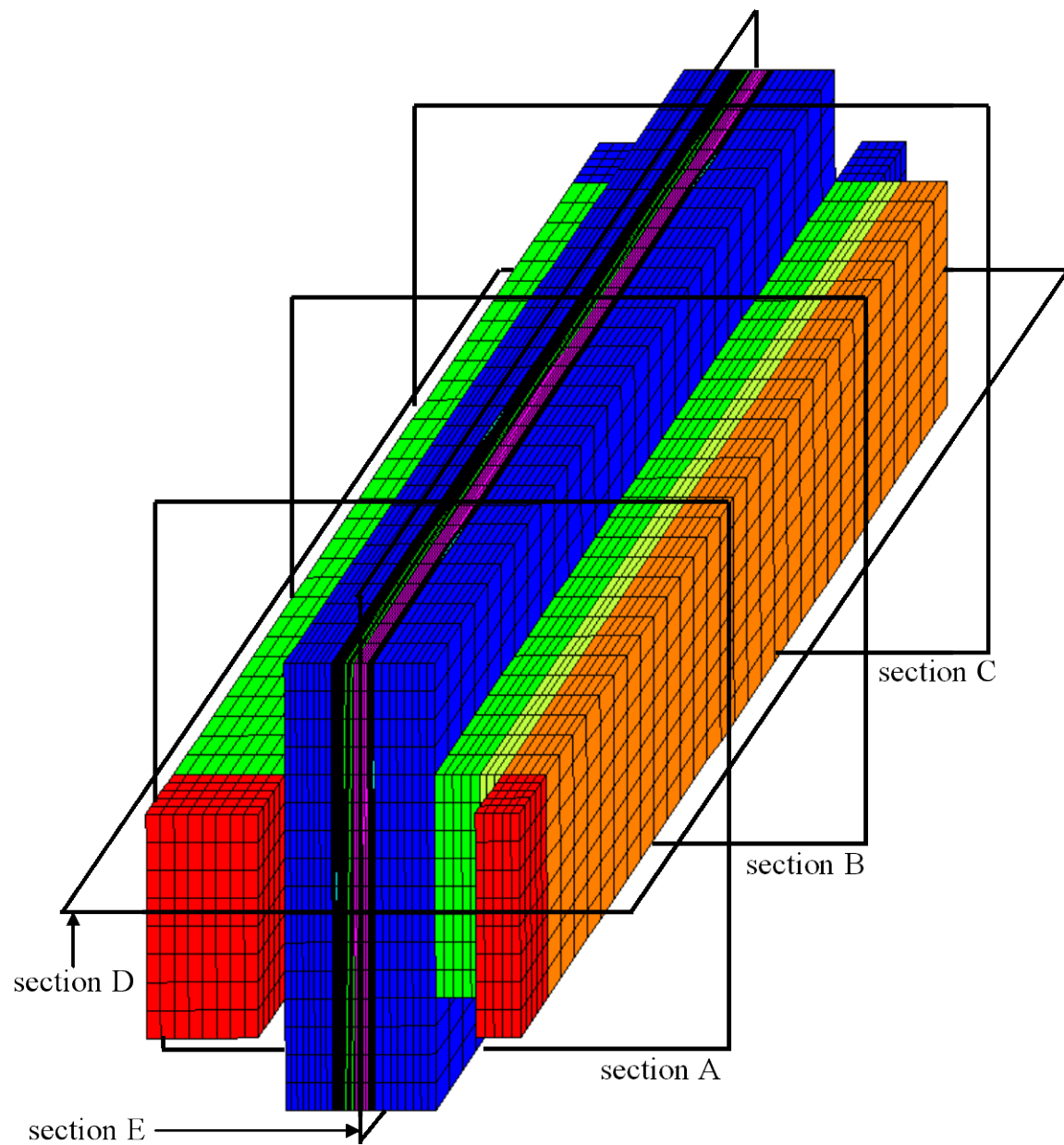
Figure [5-2]   Three-dimensional geometry of DMFC model with the fuel distributor used for the multi-D simulation in the present study
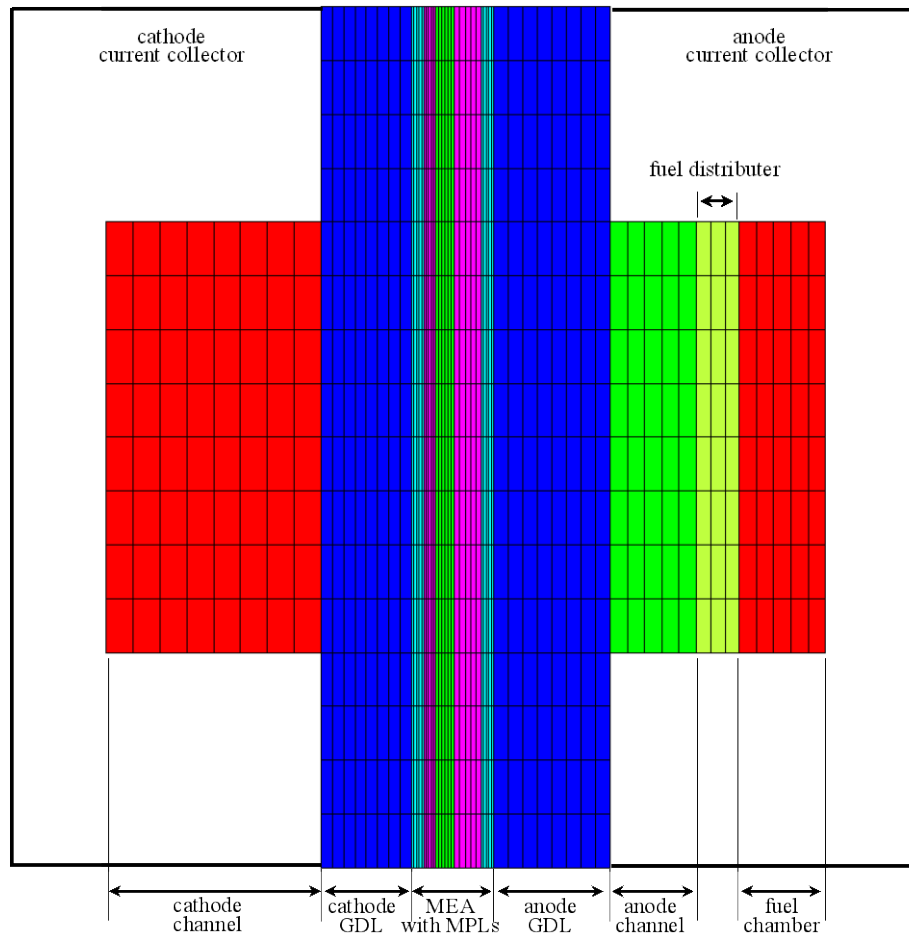
Figure [5-3]   Cross-section of the DMFC with the fuel distributor used for multi-D simulation
in the present study
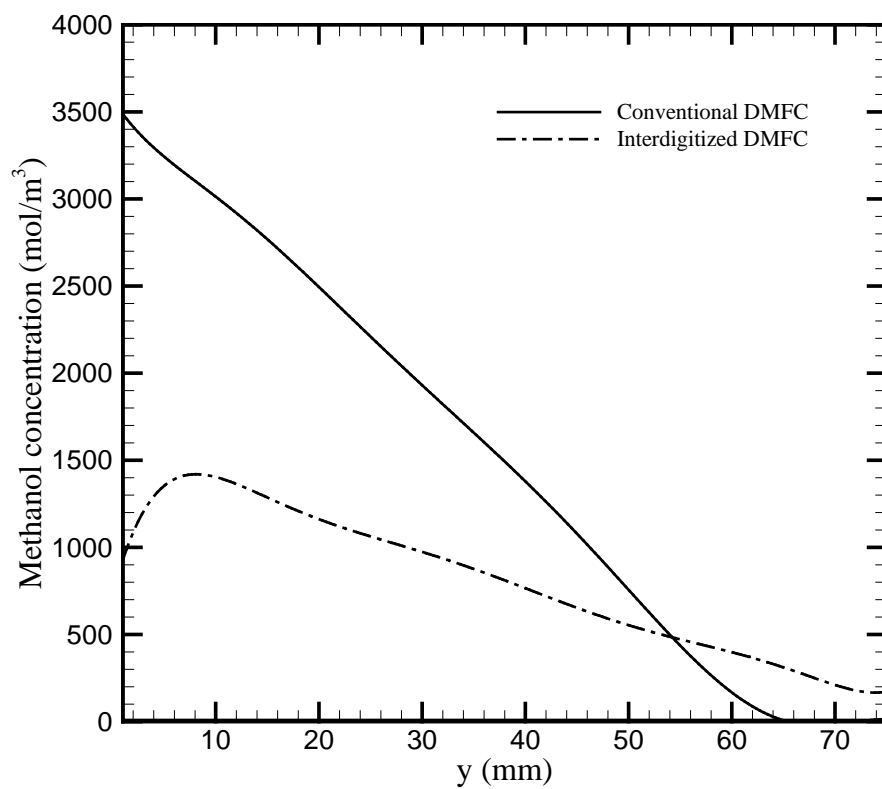
Figure [5-4]   Comparison of methanol concentration distribution near anode catalyst layer along the flow channel. Interdigitated cell shows more uniform fuel concentration distribution than the conventional cell
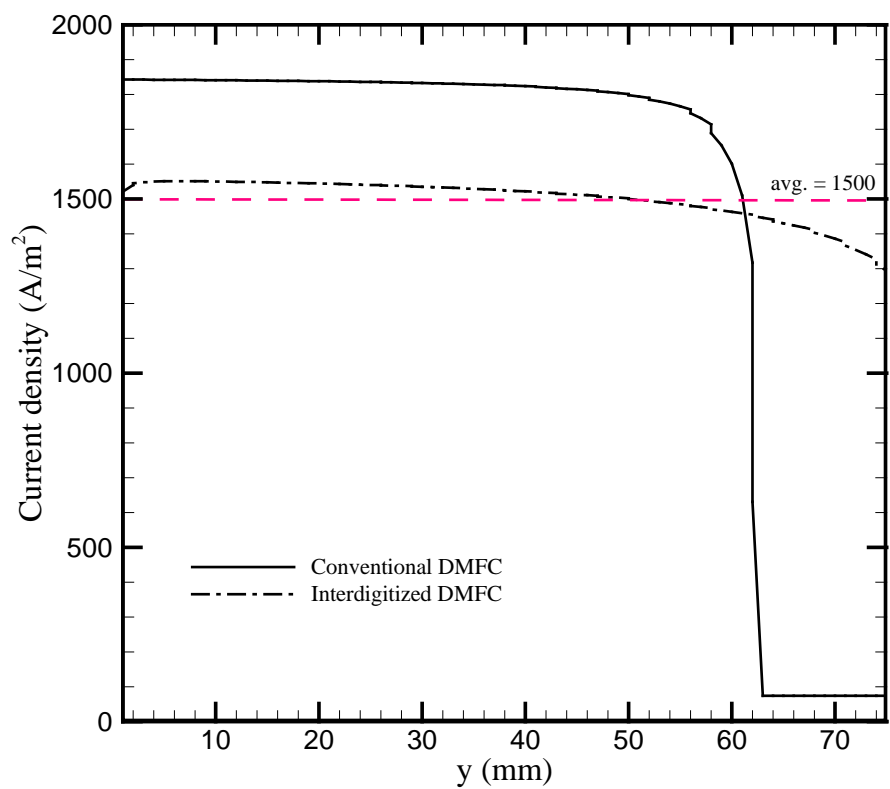
Figure [5-5]   Comparison of current density distribution along the flow channel. Interdigitated structure helps the cell avoid 1st order MOR regime by distributing fuel uniformly in the anode
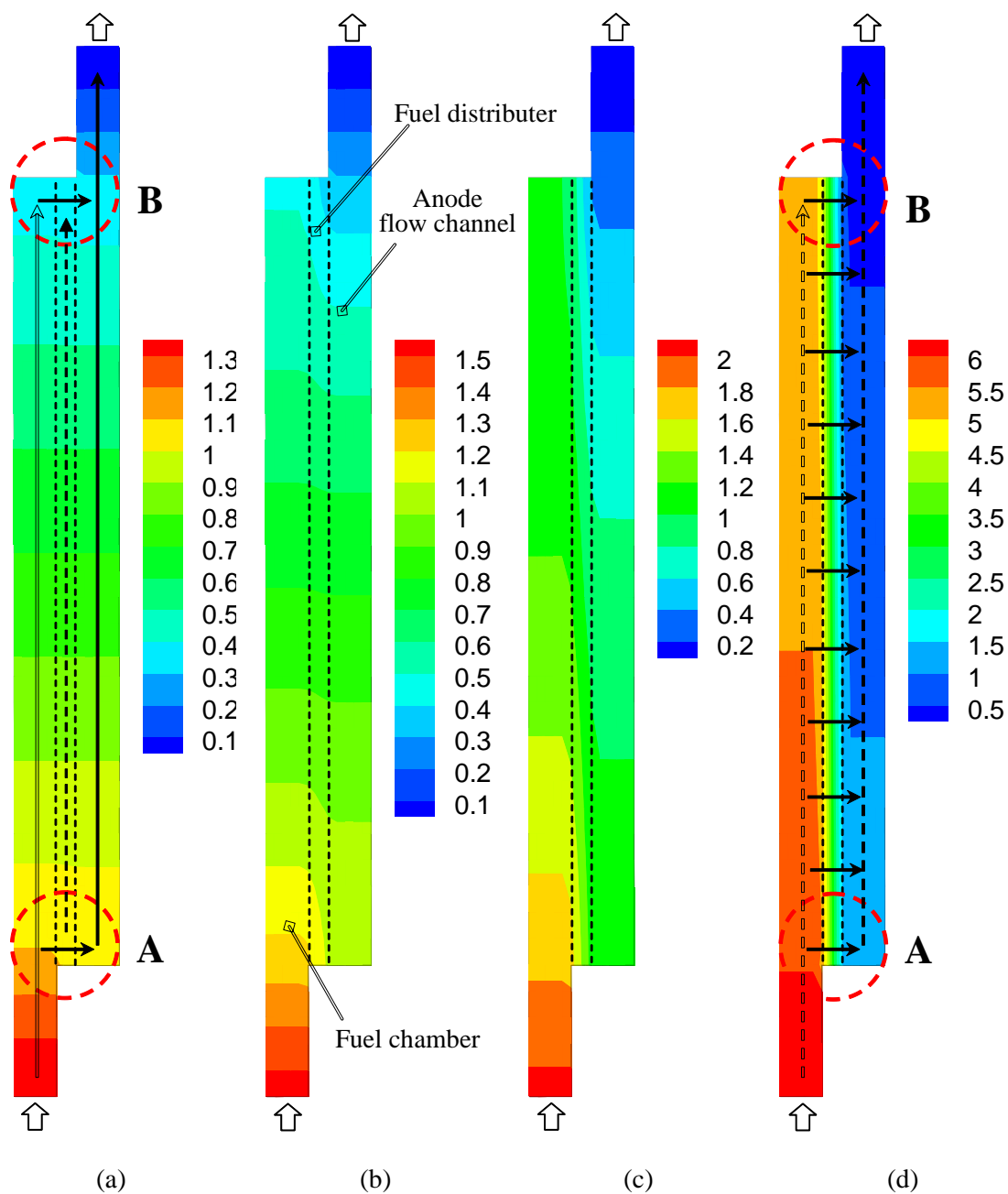
Figure [5-6]   Pressure field and mass flux direction in the fuel supply assembly (fuel chamber, fuel distributor and anode channel) according to the permeability of the porous fuel distributor. (a) $K_{fd} = 2.84 \times 10^{-11}\,\text{m}^2$, (b) $K_{fd} = 2.84 \times 10^{-12}\,\text{m}^2$, (c) $K_{fd} = 2.84 \times 10^{-13}\,\text{m}^2$, (d) $K_{fd} = 2.84 \times 10^{-14}\,\text{m}^2$
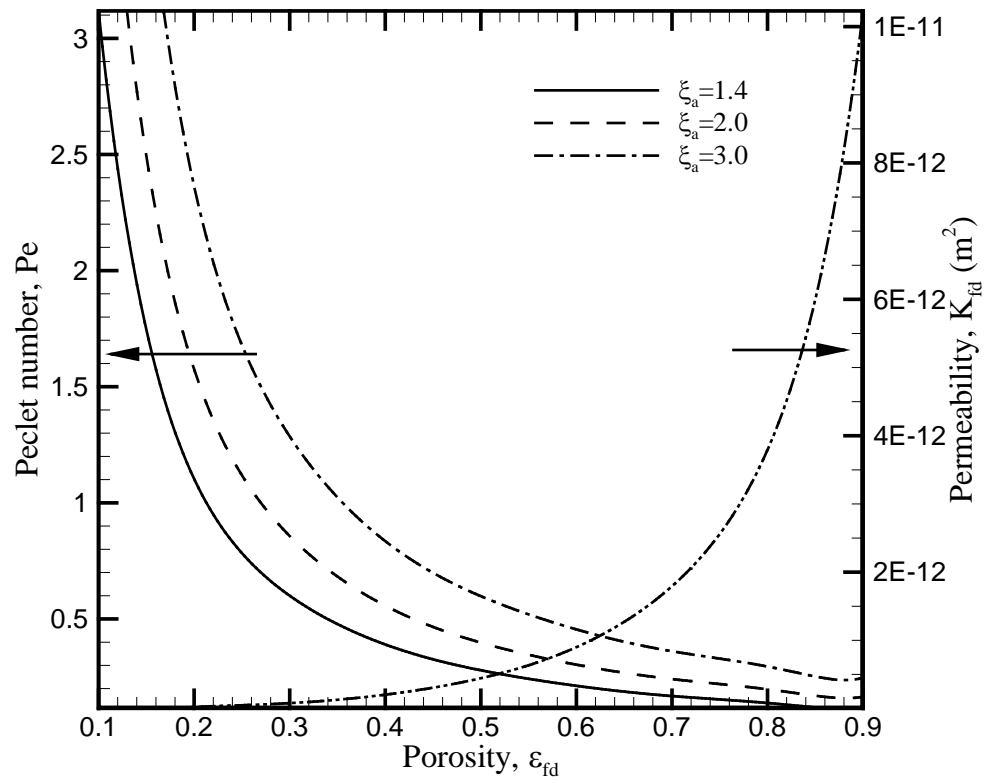
Figure [5-7]   Relationship between porosity, permeability and *Pe* of the porous fuel distributor
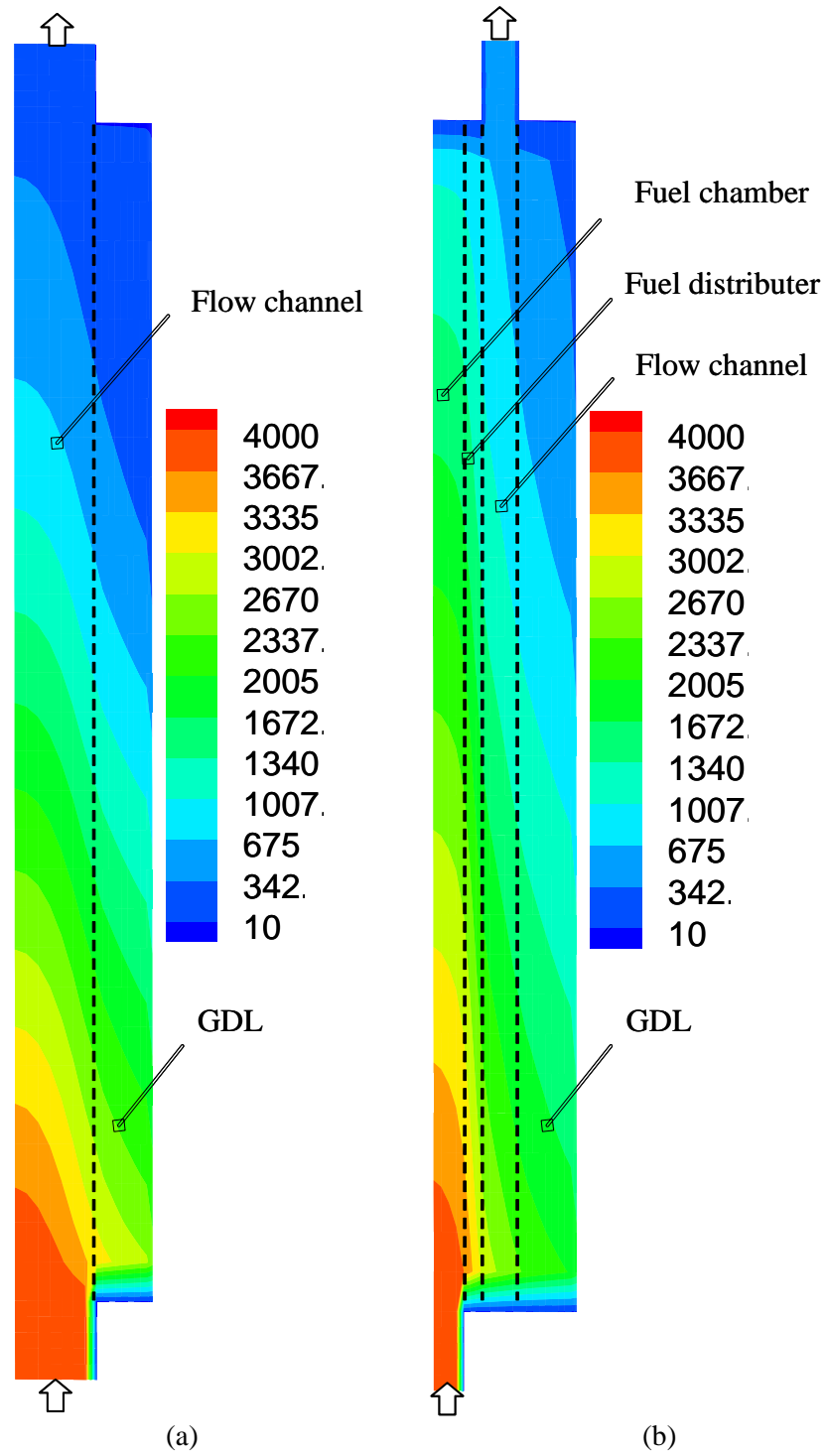
Figure [5-8]   Methanol concentration distribution in cross-section D. (a) conventional DMFC,
(b) DMFC with interdigitated fuel distributor

(a)   (b)
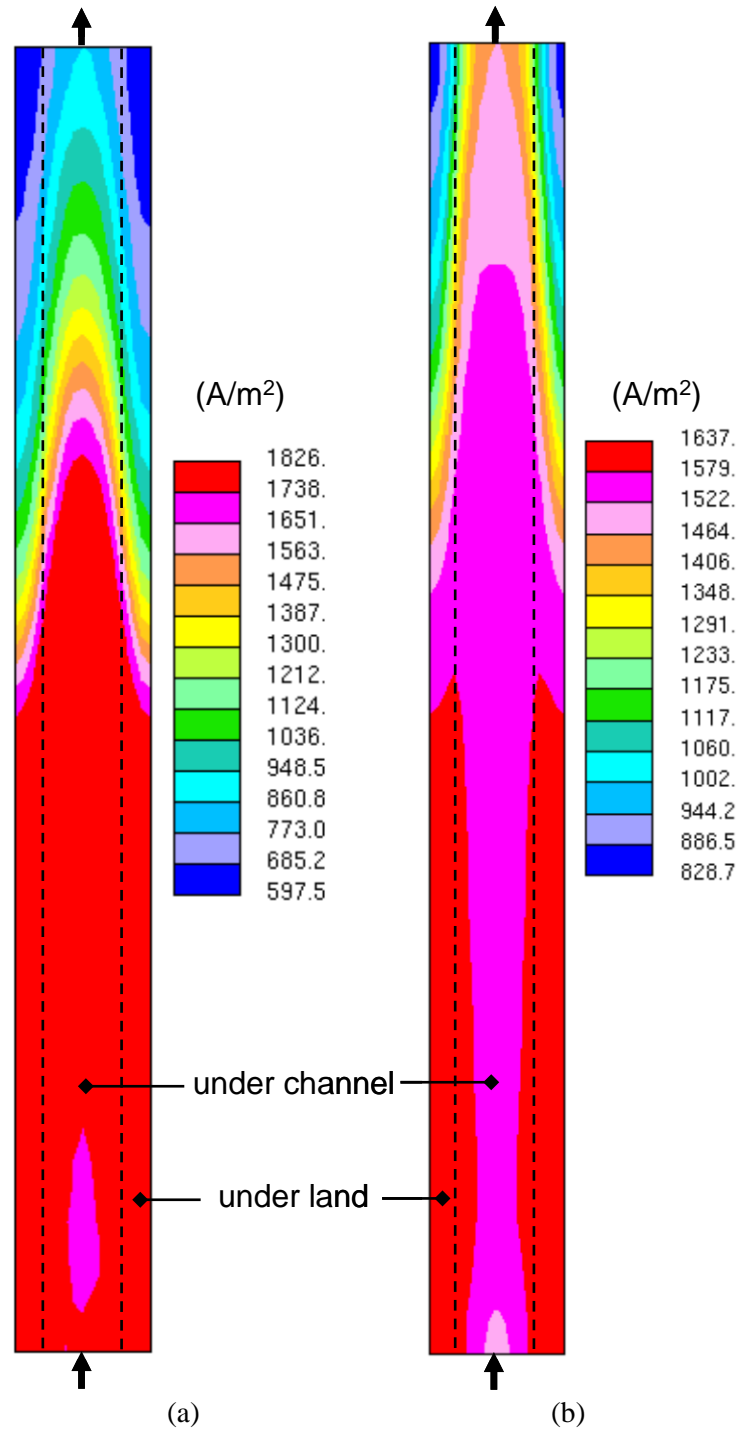
Figure [5-9]   Current density distribution in the mid-section of the membrane. (a) conventional DMFC, (b) DMFC with interdigitated fuel distributor

(A/m²) 799.9 742.7 685.6 628.5 571.4 514.3 457.2 400.1 342.9 285.8 228.7 171.6 114.5 57.36 0.2474

(A/m²) 559.9 520.0 480.1 440.1 400.2 360.3 320.4 280.4 240.5 200.6 160.6 120.7 80.78 40.85 0.9156

under channel

under land

(a)

(b)
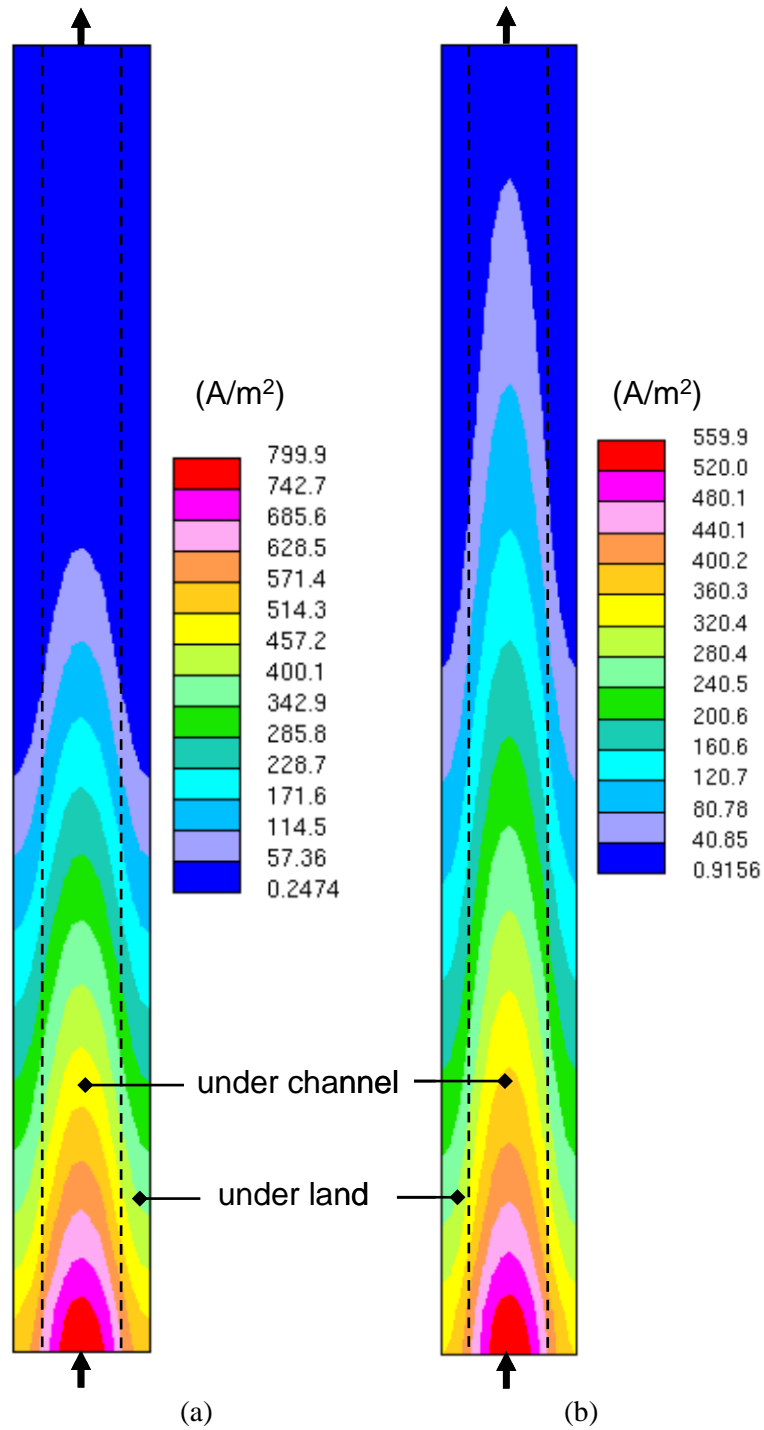
Figure [5-10]   Crossover current density distribution through the membrane. (a) conventional DMFC, (b) DMFC with interdigitated fuel distributor
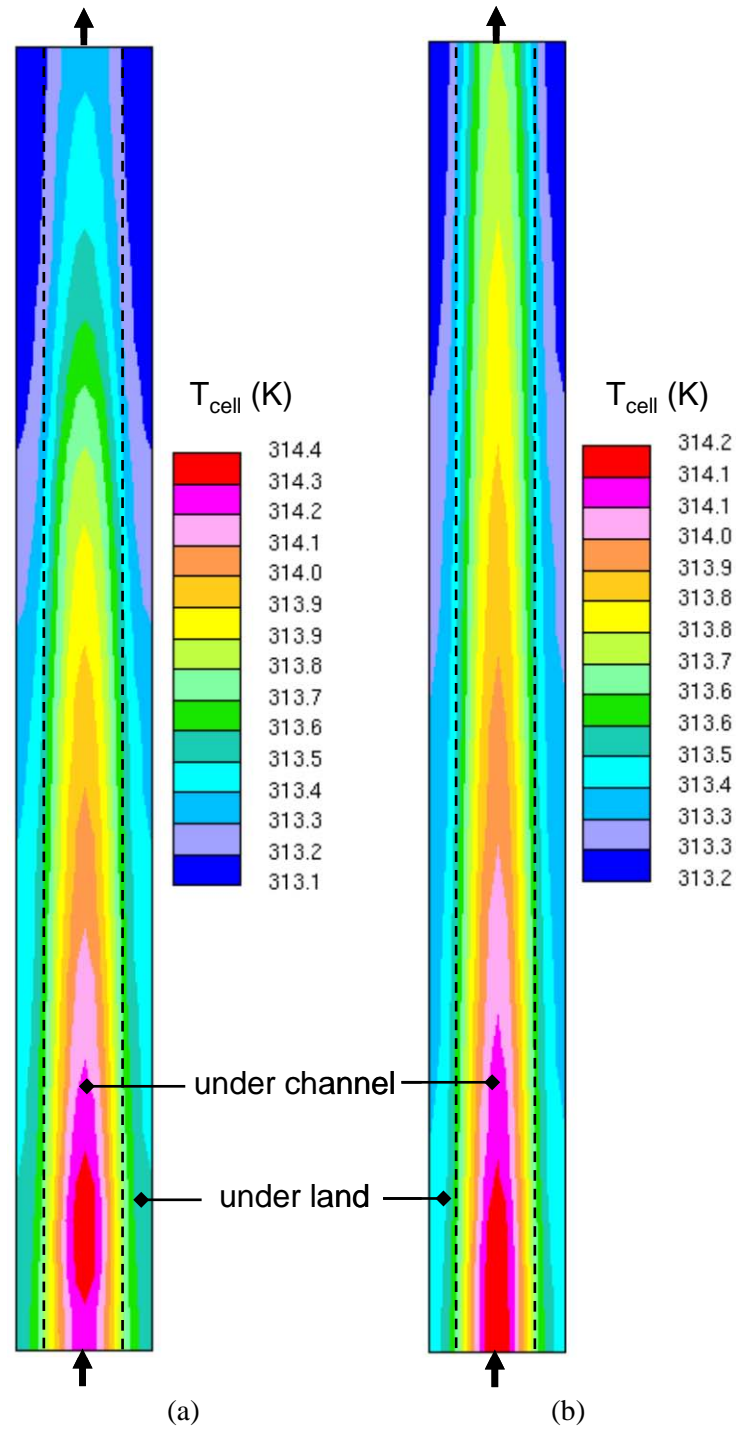
Figure [5-11]   Temperature distribution in the membrane. (a) conventional DMFC, (b) DMFC with interdigitated fuel distributor
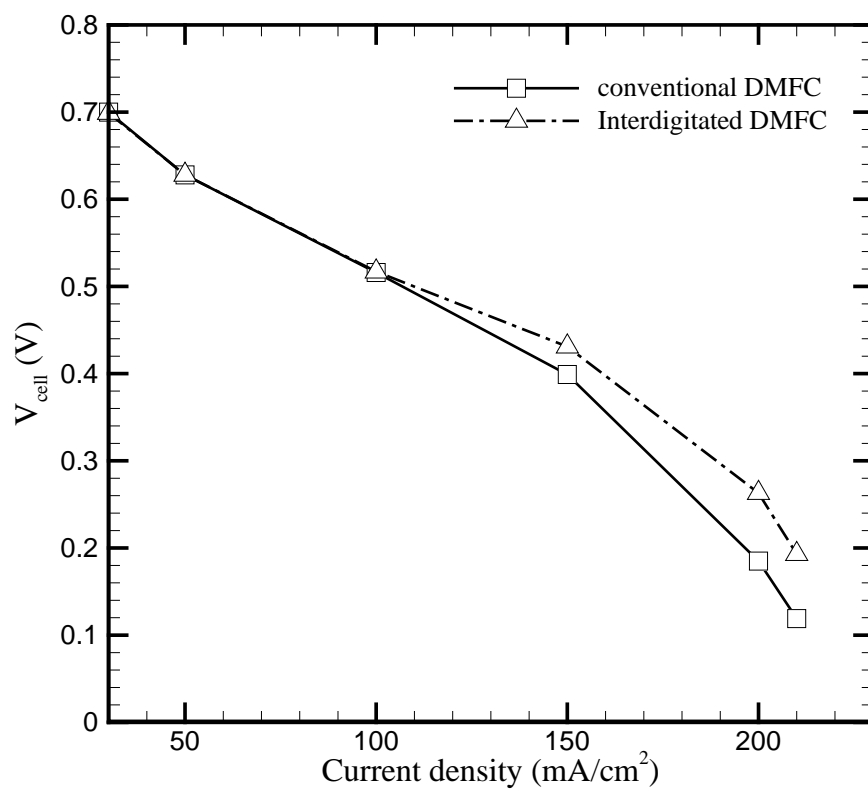
Figure [5-12]   Polarization curves showing the performance improvement by interdigitated fuel distributor

TABLES

Table [5-1]   Calculation summary

	$\sigma_{\text{cmeoh, gdl}}$	σ_{cd}	σ_{xcd}	σ_{temp}	η_a (V)	η_c (V)	V_{cell} (V)	MCO (%)
Conventional	780	382	209	0.21	0.438	0.229	0.398	11.0
Interdigitated	492	123	135	0.10	0.405	0.234	0.431	9.5

Chapter 6
Summary and Future Work

6.1   Summary

In order to understand the fundamentals of two-phase flow in DMFC, a two-phase, non-isothermal multi-dimensional DMFC model is developed in this thesis. This model has the capability of simulating saturation jump at the interface between different porous media, which is important for investigating the effect of micro-porous layers (MPL). The present multi-D model confirmed the effectiveness of MPLs which reduced water/methanol crossover and improved cell performance and fuel efficiency.

As two-phase mass transport is strongly coupled with heat transport, the present model includes a detailed two-phase heat transport model which is capable of simulating the latent heat effect and thermal diffusion by three-dimensionally visualizing phase-change rate on the cathode side. The calculation result showed that material property (heat conductivity) and operating condition (temperature and humidity) strongly affect two-phase heat and water transfer that are strongly coupled with each other.

Typically, a DMFC experiences a strong two-phase flow in the anode channel, which is caused by CO_2 gas produced from methanol oxidation reaction in the anode catalyst layer. As this two-phase flow in the channel causes several problems such as channel clogging, large pressure drop and voltage instability, a new method of venting CO_2 gas directly to the ambient is developed in order to make a pure liquid flow in the anode channel. Instead of removing CO_2 through the anode channel, an alternate CO_2 removal route is suggested with a gas permeable surface film attached on the surface of the anode

channel. This is called a CO_2 breathing DMFC. The calculation results showed that the anode channel pressure drop is significantly reduced with water transfer coefficient a bit increased due to the wetter environment of CO_2 breathing DMFC. During study of CO_2 breathing DMFC, the nature of the anode two-phase flow which is controlled by CO_2 level is enlightened for the first time. It is found that methanol transport in anode porous media is conducted by both methanol molecular diffusion and methanol capillary diffusion. Computational results showed that CO_2 level strongly affects both methanol transport mechanisms. High CO_2 level improves molecular diffusion, whereas it reduces methanol capillary diffusion. However, effective methanol diffusivity remained at constant level and cell performance was not greatly affected by CO_2 level, which was confirmed by experimental results.

In order to build a compact, highly efficient DMFC, operation of the cell under ultra-low anode stoichiometry is required. This thesis investigated problems occurring in a conventional DMFC operating under this condition with a computational method. As a large amount of fuel is lost just at the inlet region under ultra-low stoichiometry condition, the outlet half region suffers from fuel shortage, which is called anode non-uniformity. It is predicted that a cell may suffer from large voltage loss or even shut-down when the anode non-uniformity is severe. Two strategies are suggested to mitigate this anode non-uniformity. One is controlling methanol transfer resistance along the streamline direction, which is called streamline-graded structure (SGS). The other is converting diffusive methanol transport to convective methanol transport by applying an interdigitated fuel supply assembly with a porous fuel distributor. Multi-D simulation predicted that both

181

methods effectively mitigated anode non-uniformity, and boosted cell performance as well as fuel efficiency.

6.2   Future Work

6.2.1   Bubble dynamics of CO_2

In an actual DMFC, anode channel flow is a bit complex due to the CO_2 formation and removal process. Although the present work assumes an ideal mixture of liquid and CO_2 gas in order to solve the continuum equation set, experiments show that CO_2 bubble formation on the anode GDL surface and detaching motion of CO_2 bubbles from the GDL surface are very complex, especially under ultra-low stoichiometry conditions. In addition, it is observed that some CO_2 bubbles merge together to form large CO_2 slugs floating in the channel, which makes it very difficult to analyze the anode channel flow. Bubble formation and removal is basically a transient process which is strongly affected by material properties (hydrophobicity, porosity) and flow conditions. Surface tension, flow drag and CO_2 growing rate by MOR are strongly coupled and determine the bubble movement. Kulikovsky [42, 43] conducted a 1-D analytical modeling to identify the dynamics of bubble and the effect in a DMFC. Following are steps of the future research plan.

First, the fundamental mechanism of CO_2 bubble formation, coalescence and removal process will be explored. This step is focused on fluid mechanics.

Second, after identifying the bubble dynamics, the effect of CO_2 bubble dynamics on the mass transport of DMFC will be explored. This step is focused on mass transport.

Third, the effect of CO_2 bubble dynamics on the actual cell performance will be explored.

6.2.2   Multi-dimensional modeling of flow batteries

Storage of renewable energy such as solar and wind is tremendously important for a sustainable energy future. Energy storage devices or batteries for stationary applications should be inexpensive and long-lasting (high durability). Although Li-ion batteries have the highest energy density among all commercially available batteries, they are too expensive and not so durable for stationary purposes. Valve-regulated lead acid batteries (VRLA) can be used for this application, but their price is still expensive for large-scale load leveling system and maintenance of such a large battery system is not a simple problem.

Recently, the Redox flow batteries (RFB) gained much attention. RFBs are aqueous electrochemical systems with structure very similar to fuel cells as shown in Figure [6-1]. RFBs store energy in two solution tanks which contain different redox couples. Electrochemical potential by those redox couples makes RFBs charge or discharge electricity through reduction-oxidation reactions [69]. As RFBs have relatively lower kinetics losses due to active reactants, precious metal catalyst such as platinum is not or less required [70, 71]. In addition, maintenance cost is lower than other battery systems due to the simple cell structure. The energy capacity is determined by the size of the solution tank whereas the power is determined by the size of the cell stack. In contrast to DMFCs which typically have two-phase flow (even CO_2 breathing DMFC has two-phase flow inside porous media), RFBs have single-phase flow (liquid) which has very low

183

diffusivity ($\sim 10^{-10}$ m^2/s) compared to two-phase flow. In order to compensate low diffusivity, RFBs typically use highly concentrated solution. For this reason, severe redox solution crossover occurs through the ion exchange membrane, which degrades cell performance like methanol crossover in DMFCs.

As RFBs share similar features such as porous electrodes and flow channels with fuel cells, fuel cell technologies such as modeling methodologies are applicable for RFB development also [72]. For that reason, several modeling papers have been published during past few years [73, 74, 75]. Multi-D modeling is a good tool for identifying the fundamentals of RFBs in that it can predict species distribution, cell performance and the effect of redox crossover. Mitigating strategies of anode non-uniformity in DMFCs are applicable to assure uniform distribution of reduction-oxidation reactions in RFBs also. MEA design techniques such as using MPLs to reduce water/methanol crossover in DMFCs is also applicable to RFBs for reducing redox solution crossover. As most of RFCs such as Zinc Bromine redox flow battery (ZrBr), Vanadium redox flow battery (VRB) or Sodium polysulfide Bromine redox flow battery (PSB) have the same cell structure and operating mechanism, one multi-D model framework can be applied commonly for all types of batteries. Developing a universal multi-dimensional RFB model framework will be future work.
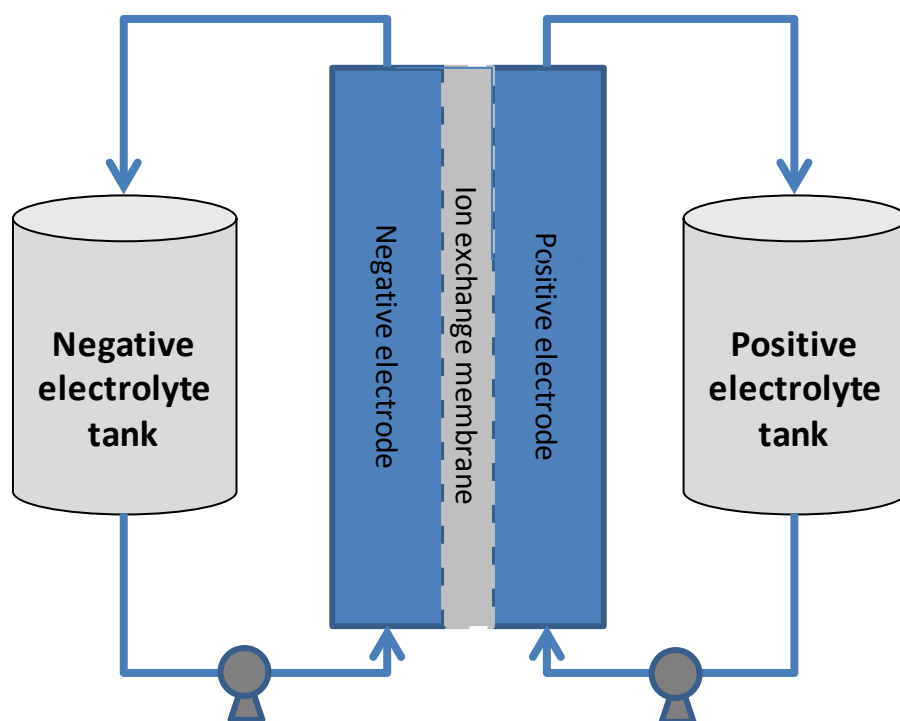
Figure [6-1]   Schematic of a unit redox flow cell system

BIBLIOGRAPHY

1   R. O'Hayre, S.W. Cha, W. Colella, and F.B. Prinz, Fuel Cell Fundamentals, Wiley, (2006)

2   W. Liu, C.Y. Wang, "Modeling water transport in liquid feed direct methanol fuel cell", Journal of Power Sources, vol. 164, pp. 189-195 (2007)

3   F.Q. Liu, G.Q. Lu and C.Y. Wang, "Low crossover of methanol and water though thin membranes in Direct Methanol Fuel Cells" Journal of the Electrochemical Society, vol. 153, pp. A543-553 (2006)

4   K. Scott, P. Argyropoulos, P. Yiannopoulos and W.M. Taama, "Electrochemical and gas evolution characteristics of direct methanol fuel cells with stainless steel mesh flow beds", Journal of Applied Electrochemistry, vol. 31, pp. 823-832 (2001)

5   M. D. Lundin, M. J. McCready, "Reduction of carbon dioxide gas formation at the anode of a direct methanol fuel cell using chemically enhanced solubility", Journal of Power Sources, vol. 172, pp. 553-559 (2007)

6   G. Lu and, C.Y. Wang, "Two-phase microfluidics, heat and mass transport in direct methanol fuel cells", an invited chapter for New Developments in Heat Transfer, Chapter 9, pp. 317-358 (2005)

7   J.A. Kerres, J. Membr. Sci. vol. 185, pp. 3-27 (2001)

8   F. Bauer, M. Willert-Porada, J. Membr. Sci. vol. 233, pp. 141-149 (2004)

9   G.Q. Lu, F.Q. Liu, C.Y. Wang, "Water Transport Through Nafion 112 Membrane in DMFCs", Electrochemical and Solid-State Letters, vol. 8(1), pp. A1-A4 (2005)

10 U. Pasaogullari, C.Y. Wang, "Two-phase transport and the role of micro-porous layer in polymer electrolyte membrane fuel cells", Electrochemical Acta, vol. 49, pp. 4559-4369 (2004)

11 F. Liu, C.Y. Wang, "Water and methanol crossover in direct methanol fuel cells-Effect of anode diffusion media", Electrochemica Acta, vol.53, pp. 5517-5522 (2008)

12 X.M. Ren, S.B. Gottesfeld, R.S. Hisch, "Fluid Management Component for Use in a Fuel Cell", U.S. Patent Pub. No. 2004/0062980

13 X.M. Ren, F.W. Kovacs, K.J. Shufon, S.B. Gottesfeld, "Passive Water Management Techniques in Direct Methanol Fuel Cells", U.S. Patent Pub. No. 2004/0209154

14 X.M. Ren, J.J. Becerra, S.B. Gottesfeld, J.S. Kovacs, "Controlled Direct Liquid Injection Vapor Feed for a DMFC", U.S. Patent Pub. No. 2005/0170224

15 Z. Guo, A. Faghri, "Vapor feed direct methanol fuel cells with passive thermal-fluids management system", Journal of Power Sources, vol. 167, pp. 378-390 (2007)

16 J. Rice, Amir Faghri, "Analysis of a passive vapor feed direct methanol fuel cell", Int. Journal of Heat and Mass Transfer, vol. 51, pp. 948-959 (2008)

17 E. Barendrecht, "Fuel cell systems", L.J.M.J. Blowen & M.N. Mugerwa, New York, pp. 75 (1993)

18 C.Y. Wang, "Lecture Note; Electrochemical Engine Fundamental (ME597G)", Pennsylvania State University (2007)

19 Z. H. Wang and C. Y. Wang, "Mathematical Modeling of Liquid-Feed Direct Methanol Fuel Cells" Journal of the Electrochemical Society, vol. 150, ppA508-A519 (2003)

20 W. Liu and C. Y. Wang "Three-Dimensional Simulations of Liquid Feed Direct Methanol Fuel Cells" Journal of the Electrochemical Society, vol. 154, pp. B352-B361 (2007)

21 C.Y. Wang and P. Cheng, "A multiphase mixture model for multiphase, multicomponent transport in capillary porous media – I. Model development", Int. Journal of Heat Mass Transfer, vol. 39, No. 17, pp. 3607-3618 (1996)

22 J.P. Meyers and J. Newman, J. Electrochem. Soc., vol. 149, pp. A710 (2002)

23 J.P. Meyers and J. Newman, J. Electrochem. Soc., vol. 149, pp. A718 (2002)

24 J.P. Meyers and J. Newman, J. Electrochem. Soc., vol. 149, pp. A729 (2002)

25 Z. H. Wang and C. Y. Wang, Journal of Power Sources, vol. 94(1), pp.40-50 (2001)

26 Z. Qi and A. Kaufman, Journal of the Power Sources, vol. 109, pp. 38 (2002)

27 J.H. Nam and M. Kaviany, Int. Journal of Heat Mass Transfer, vol. 46, pp. 4595-4611 (2003)

28 C. E. Shaffer and C. Y. Wang, Electrochimica Acta, vol.54, pp. 5761-5769 (2009)

29 F. Liu and C.Y. Wang, "Water and Methanol Crossover in Direct Methanol Fuel Cells – Effect of Anode Diffusion Media", Electrochemica Acta, vol. 53, pp. 5517-5522 (2008)

30 H. Ju, "Coupled heat and water management in polymer electrolyte fuel cells", Ph.D. thesis, The Pennsylvania State University, 2006

31 Y. Wang and C.Y. Wang, Journal of the Electrochemical Society, vol. 153 pp. A1193-1200 (2006)

32 S. Basu, C.Y. Wang and K.S. Chen, Journal of the Electrochemical Society, vol. 156, pp. B748-B756 (2009)

33 P. Argyropoulos, K. Scott, W.M. Taama, "Carbon dioxide evolution patterns in direct methanol fuel cells", Electrochemica Acta, vol. 44, pp. 3575-3584 (1999)

34 G.Q. Lu, C.Y. Wang, "Electrochemical and flow characterization of a direct methanol fuel cell", Journal of Power Sources, vol. 134, pp. 33-40 (2004)

35 H. Yang, T.S. Zhao, Q. Ye, "In situ visualization study of CO2 gas bubble behavior in DMFC anode flow fields", Journal of Power Sources, vol. 139, pp. 79-90 (2005)

36 H. Yang, T.S. Zhao, "Effect of anode flow field design on the performance of liquid feed direct methanol fuel cells", Electrochemica Acta, vol. 50, pp. 3243-3252 (2005)

37 M.M. Mench, S. Boslet, S. Thynell, J. Scott and C.Y. Wang, "Experimental study of a direct methanol fuel cell", Proceeding of the Symposium on Direct Methanol Fuel Cells, 199th Electrochemistry Society Proc. Series, Princeton, NJ, 2001.

38 T. Bewer, T. Beckmann, H. Dohle, J. Mergel, D. Stolten, "Novel method for investigation of two-phase flow in liquid feed direct methanol fuel cells using an aqueous H_2O_2 solution", Journal of Power Sources, vol. 125, pp. 1-9 (2004)

39 Qiang Liao, Xun Zhu, Xueyan Zheng, Yudong Ding, "Visualization study on the dynamics of CO_2 bubbles in anode channels and performance of a DMFC", Journal of Power Sources, vol. 171, pp. 644-651 (2007)

40 C.W. Wong, T.S. Zhao, Q. Ye, J.G. Liu, "Transient capillary blocking in the flow filed of a micro-DMFC and its effect on cell performance", Journal of the Electrochemical Society, vol.152 (8), pp. A1600-A1605 (2005)

41 P. Argyropoulos, K. Scott, W.M. Taama, "Modeling pressure distribution and anode/cathode streams vapor-liquid equilibrium composition in liquid feed direct methanol fuel cells", Chemical Engineering Journal vol. 78, pp. 29-41(2000)

42 A.A. Kulikovsky, "Model of the flow with bubbles in the anode channel and performance of a direct methanol fuel cell", electrochemical communications vol. 7, pp. 237-243 (2005)

43 A.A. Kulikovsky, "Bubbles in the anode channel and performance of a DMFC: Asymptotic solutions", Electrochemica Acta, vol. 51, pp. 2003-2001 (2006)

44 J. Ge, H. Liu, "A three-dimensional two-phase flow model for a liquid-fed direct methanol fuel cell", Journal of Power Sources, vol.163, pp. 907-915 (2007)

45 M.S. DeFilippis, MTI Mcirofuel Cells, Inc. "Bipolar Plate having integrated gas-permeable membrane", U.S. Patent 7,081,310 B2 (2006)

46 W.P. Acker, MTI Mcirofuel Cells, Inc. "Fuel cell membrane and Fuel cell system with integrated gas separation", U.S. Patent 7,125,620 B2 (2006)

47 D.D. Meng and C.J. Kim, Journal of Power Sources, Vol. 194, pp. 445-450 (2009)

48 G.F. Hewitt and D.N. Roberts, "Studies of Two-Phase Flow Patterns by Simultaneous X-ray and Flash Photography", AERE-M 2159, HMSO (1969)

49 J.M. Mandhane, G.A. Gregory and K. Aziz, "A Flow Pattern Map for Gas-Liquid Flow in Horizontal Pipes", In. J. Multiphase Flow, vol. 1, pp. 537-553 (1974)

50 F.B. Cheung, ME515 "Two-Phase Heat Transfer" Lecture note, The Pennsylvania State University (2006)

51 F. Amir, Y. Zhang, Transport Phenomena In Multiphase Systems, 1st edition, Elsvier Academic Press (2006)

52 R.C. Martinelli, D.B. Nelson, "Prediction of Pressure Drop During Forced Circulation Boiling of Water", Trans. ASME, vol. 70, pp.695 (1948)

53 A. Blum, T. Duvdevani, M. Philosoph, N. Rudoy, and E. Peled, "Water-neutral micro direct-methanol fuel cell (DMFC) for portable applications", Journal of Power Sources, vol. 117, pp. 22-25 (2003)

54 G.Q. Lu, P.C. Lim, F.Q. Liu and C.Y. Wang, International Journal of Energy Research, vol. 29, pp. 1041-1050 (2005)

55 G.Q. Lu, C.Y. Wang, Journal of Fuel Cell Science and Technology, vol. 3, pp. 131-136 (2006)

56 F.P. Incropera and D.P. DeWitt, Fundamentals of Heat and Mass Transfer, Fifth edition (2002)

57 Z. Guo, A. Faghri, Journal of Power Sources, vol. 160, pp. 1183-1194 (2006)

58 H. Kim, Journal of Power Sources, vol. 162, pp. 1232-1235 (2006)

59 S. Eccarius, F. Krause, K. Beard, C. Agert, Journal of Power Sources, vol. 182, pp. 565-579 (2008)

60 M. A. Abdelkareem, N. Nakagawa, Journal of Power Sources, vol. 162, pp. 114-123 (2006)

61 R.H. Brooks and A.T. Corey, "Hydraulic Properties of Porous Media", Hydrology Papers, Colorado State University, vol. 3, pp. 1-27 (1964)

62 R.B. Mrazek, C.E. Wicks and K.N.S. Prabhu, "Dependence of the Diffusion Coefficient on Composition in Binary Gaseous Systems", Journal of Chemical and Engineering Data, vol. 13, pp. 508-510 (1968)

63 B.E. Poling, J.M. Prausnitz, J.P. O'Connell, "The properties of Gases and Liquids", 5th ed., McGraw-Hill, New York (2001)

64 Z.J. Derlacki, A.J. Easteal, V.J. Edge, L.A. Woolf and Z. Roksandic, "Diffusion Coefficients of Methanol and Water and the Mutual Diffusion Coefficient in Methanol-water solutions at 278 and 298 K", Journal of Physical Chemistry, vol. 89, pp. 5318-5322 (1985)

65 T.A. Zawodzinski, C. Derouin, S. Radzinski, R.J. Sherman, V.T. Smith, T.E. Springer and S. Gottesfeld, "Water Uptake and Transport Through Nafion®117 Membranes", Journal of the Electrochemical Society, vol. 140, pp. 1041-1047 (1993)

66 T.A. Zawodzinski, J. Davey, J. Valerio and S. Gottesfeld, "The Water Content Dependence of Electro-osmotic Drag in Proton-conducting Polymer Electrolytes", Electrochemica Acta, vol. 40, pp. 297-302 (1995)

67 T.E. Springer, T.A. Zawodzinski, S. Gottesfeld, "Polymer Electrolyte Fuel Cell Model", Journal of the Electrochemical Society, vol. 138, pp. 2334-2342 (1991)

68 G.Q. Lu, C.Y. Wang, "Electrochemical and flow characterization of a direct methanol fuel cell", Journal of Power Sources, vol. 134, pp. 33-40 (2004)

69 C. Ponce de León, A. Frias-Ferrer, J. González-Garcia, D.A. Szánto, F.C. Walsh, "Review: Redox flow cells for energy conversion", Journal of Power Sources, vol. 160, pp. 716-732 (2006)

70 Y.D. Chen, K.S.V. Santhanam and A.J. Bard, "Solution Redox Couples for Electrochemical Energy Storage I", Journal of the Electrochemical Society, vol. 128 (n7), pp. 1460-1467 (1981)

71 Y.D. Chen, K.S.V. Santhanam and A.J. Bard, "Solution Redox Couples for Electrochemical Energy Storage II", Journal of the Electrochemical Society, vol. 129 (n1), pp. 61-69 (1982)

72 M.L. Perry, "Advanced Flow-Battery Systems", MS&T'09 conference at Pittsburgh (2009)

73 A.A. Shah, M.J. Watt-Smith, F.C. Walsh, "A dynamic performance model for redox-flow batteries involving soluble", Electrochemica Acta, vol. 53, pp. 8087-8100 (2008)

74 H. Al-Fetlawi, A.A. Shah, and F.C. Walsh, "Non-isothermal modeling of the all-vanadium redox flow battery", Electrochemica Acta, vol. 55, pp. 78-89 (2009)

75 M. Li, and T. Hikihara, "A Coupled Dynamical Model of Redox Flow Battery Based on Chemical Reaction, Fluid Flow, and Electrical Circuit", IEICE Trans. Fundamentals, vol. E91-A, no.7 (2008)

APPENDIX A: Governing equations of the baseline multi-D DMFC model

	Conservation equations	Source terms
Mass	$\nabla \cdot (\rho \vec{u}) = \dot{m}'''$	$\dot{m}'''_{\text{acl}} = M^{\text{MeOH}} S^{\text{MeOH}} + M^{\text{H}_2\text{O}} S^{\text{H}_2\text{O}} + \dfrac{jM^{\text{CO}_2}}{6F}$ $\dot{m}'''_{\text{ccl}} = M^{\text{H}_2\text{O}} S^{\text{H}_2\text{O}} + M^{\text{O}_2} S^{\text{O}_2} + \dfrac{j_{\text{xover}}M^{\text{CO}_2}}{6F}$
Momentum	$\nabla \cdot (\rho \vec{u}\vec{u}) = -\nabla p + \nabla \cdot \vec{\tau} + S^{\text{u}}$	$S^{\text{u}} = -\dfrac{\mu}{K}\vec{u}$ (in porous media domain)
Water transport	$\nabla \cdot (\gamma\rho\vec{u}Y^{\text{H}_2\text{O}}) = \nabla \cdot [\rho D_{\text{capill}}\nabla Y^{\text{H}_2\text{O}}] + M^{\text{H}_2\text{O}}S^{\text{H}_2\text{O}}$	$S_{\text{acl}}^{\text{H}_2\text{O}} = -\dfrac{j}{6F} - \dfrac{j}{F}\alpha$ $S_{\text{ccl}}^{\text{H}_2\text{O}} = \dfrac{j}{2F} + \dfrac{j_{\text{xover}}}{3F} + \dfrac{j}{F}\alpha$
Methanol transport	$\nabla \cdot (\gamma^*\rho\vec{u}Y_1^{\text{MeOH}}) = \nabla \cdot [\rho D_{\text{eff}}^{\text{MeOH}}\nabla \cdot Y_1^{\text{MeOH}}] + M^{\text{MeOH}}S^{\text{MeOH}}$	$S_{\text{acl}}^{\text{MeOH}} = -\dfrac{j}{6F} - \dfrac{j_{\text{xover}}}{6F}$
CO$_2$ transport	$\nabla \cdot (\gamma\rho\vec{u}Y^{\text{CO}_2}) = \nabla \cdot \left[\rho\left(\dfrac{\rho_{\text{g}}}{\rho}D_{\text{g,eff}}^{\text{CO}_2}\right)\nabla Y^{\text{CO}_2}\right] + \nabla \cdot [Y^{\text{CO}_2}\vec{j}_1]$ $+ M^{\text{CO}_2}S^{\text{CO}_2}$	$S_{\text{acl}}^{\text{CO}_2} = \dfrac{j}{6F}$ $S_{\text{ccl}}^{\text{CO}_2} = \dfrac{j_{\text{xover}}}{6F}$
Oxygen transport	$\nabla \cdot (\gamma\rho\vec{u}Y^{\text{O}_2}) = \nabla \cdot \left[\rho\left(\dfrac{\rho_{\text{g}}}{\rho}D_{\text{g,eff}}^{\text{O}_2}\right)\nabla Y^{\text{O}_2}\right] + \nabla \cdot [Y^{\text{O}_2}\vec{j}_1]$ $+ M^{\text{O}_2}S^{\text{O}_2}$	$S_{\text{ccl}}^{\text{O}_2} = -\dfrac{j}{4F} - \dfrac{j_{\text{xover}}}{4F}$
Proton	$0 = \nabla \cdot (\kappa_{\text{e,eff}}\nabla \phi_{\text{e}}) + S_{\text{e}}^{\phi}$	$S_{\text{e,acl}}^{\phi} = j$ $S_{\text{e,ccl}}^{\phi} = -j_{\text{c}} + j_{\text{xover}}$
Electron	$0 = \nabla \cdot (\kappa_{\text{s,eff}}\nabla \phi_{\text{s}}) + S_{\text{s}}^{\phi}$	$S_{\text{s,acl}}^{\phi} = -j$ $S_{\text{s,ccl}}^{\phi} = j_{\text{c}} - j_{\text{xover}}$
Energy	$\nabla \cdot (\rho\vec{u}c_{\text{p}}^{\text{g}}T) = \nabla \cdot (k_{\text{eff}}\nabla T) + S^{\text{T}}$ where $\begin{cases} k_{\text{eff}} = k_{\text{gdl}} + h_{\text{fg}}^{\text{o}}M^{\text{H}_2\text{O}}D_{\text{g,eff}}^{\text{H}_2\text{O}}\dfrac{dC_{\text{sat}}^{\text{H}_2\text{O}}}{dT} \\ S^{\text{T}} = S_{\text{acl}}^{\text{T}} + S_{\text{ccl}}^{\text{T}} + S_{\text{mem}}^{\text{T}} + S_{\text{latent}}^{\text{T}} \end{cases}$	$S_{\text{acl}}^{\text{T}} = j\left(\eta + T\dfrac{dU_0}{dT}\right) + \dfrac{I^2}{\kappa_{\text{eff}}}$ $S_{\text{mem}}^{\text{T}} = \dfrac{I^2}{\kappa_{\text{eff}}}$ $S_{\text{ccl}}^{\text{T}} = j\left(\eta + T\dfrac{dU_0}{dT}\right) + \dfrac{I^2}{\kappa_{\text{eff}}} + j_{\text{xover}}\left(\eta + T\dfrac{dU_0}{dT}\right)$ $S_{\text{latent}}^{\text{T}} = \dot{m}_{\text{fg}}h_{\text{fg}}^{\text{o}} = \nabla \cdot (h_{\text{fg}}^{\text{o}}\rho_1\vec{u}_1)$

APPENDIX B: Constitutive relationships of the baseline DMFC model

Parameters	Expression	Reference
Relative permeability	$k_{rl} = s^n; \quad k_{rg} = (1-s)^n$	[61]
Methanol diffusivity (vapor)	$D_g^{MeOH} = 1.96 \times 10^{-5} \left(\dfrac{T}{328.15} \right)^{1.823} \dfrac{1.013 \times 10^5}{p} \; \left[m^2/s \right]$	[62]
Water diffusivity (vapor)	$D_g^{H_2O} = 2.01 \times 10^{-5} \left(\dfrac{T}{307} \right)^{1.823} \dfrac{1.013 \times 10^5}{p} \; \left[m^2/s \right]$	[63]
Methanol diffusivity (liquid)	$D_l^{MeOH} = 1.4 \times 10^{-9} \left(\dfrac{647.3 - 298.15}{647.3 - T} \right)^6 \; \left[m^2/s \right]$	[64]
Oxygen diffusivity (gas)	$D_g^{O_2} = 3.57 \times 10^{-5} \left(\dfrac{T}{352} \right)^{1.823} \dfrac{1.013 \times 10^5}{p} \; \left[m^2/s \right]$	[63]
Water content in Nafion-membrane	$\lambda = \begin{cases} 22 & (s > 0.3) \\ 14 + 8s/0.3 & (s \leq 0.3) \\ 0.043 + 17.81RH - 39.85RH^2 + 36.0RH^3 & \text{(vapor)} \end{cases}$	[67, 65]
Water diffusivity in Nafion-membrane	$D_{mem}^{H_2O} = 4.80 \times 10^{-11} \exp \left[2416 \left(\dfrac{1}{303} - \dfrac{1}{T} \right) \right] \; \left[m^2/s \right]$	Calibrated based on [67]
Methanol diffusivity in Nafion-membrane	$D_{mem}^{MeOH} = 1.5 \times 10^{-10} \exp \left[2416 \left(\dfrac{1}{303} - \dfrac{1}{T} \right) \right] \; \left[m^2/s \right]$	Calibrated based on [67]
Water EOD coefficient in Nafion-membrane	$n_d^{H_2O} = \begin{cases} \left[\dfrac{\lambda - 14}{8} \right] \left(n_{d,ref}^{H_2O} - 1 \right) + 1 & \text{(for } \lambda \geq 14) \\ 1 & \text{(for } \lambda < 14) \end{cases}$	[6], [66]
Water reference EOD coefficient in Nafion-membrane	$n_{d,ref}^{H_2O} = 1.6767 + 0.0155(T - 273) + 8.9074 \times 10^{-5}(T - 273)^2$	[6]
Ion conductivity of Nafion-membrane	$k_{mem} = 0.1$ (S/cm) @ 60°C (fully hydrated)	
J-Leverett function	$J(s) = \begin{cases} -1.263s^3 + 1.669s^2 - 0.966s + 0.56 & \text{(when } \theta_c < 90^o) \\ 1.263s^3 - 2.120s^2 + 1.417s & \text{(when } \theta_c > 90^o) \end{cases}$	

APPENDIX C: Cell geometry and material properties of the baseline DMFC model

Description	Symbol	Value
Anode GDL thickness	δ_{adl}	270 µm
Anode MPL thickness	δ_{aml}	30 µm
Anode CL thickness	δ_{acl}	62 µm
Membrane thickness	δ_{mem}	45 µm
Cathode CL thickness	δ_{ccl}	25 µm
Cathode MPL thickness	δ_{cml}	30 µm
Cathode GDL thickness	δ_{cdl}	210 µm
GDL porosity	ε_{gdl}	0.6
MPL porosity	ε_{mpl}	0.4
CL porosity	ε_{cl}	0.4
FD porosity	ε_{fd}	0.3
GDL permeability	K_{gdl}	2.0×10^{-12} m^2
MPL permeability	K_{mpl}	5.0×10^{-14} m^2
CL permeability	K_{cl}	1.0×10^{-13} m^2
FD permeability	K_{fd}	2.84×10^{-13} m^2
Membrane permeability	K_{mem}	4.0×10^{-20} m^2
GDL contact angle	θ_{gdl}	110°
MPL contact angle	θ_{mpl}	114°
CL contact angle	θ_{cl}	96°
Cell length	L_{cell}	75 mm
Channel width	W_{chn}	1 mm
Channel height	H_{chn}	0.5 mm
Land width	W_{land}	1 mm
Bipolar plate thickness	H_{bp}	0.5 mm

APPENDIX D: Simulation parameters of the baseline DMFC model

Description	Symbol	Value
Reference current density	i_{ref}	150 mA/cm^2
Anode reference exchange current density	$i_{ex,a}$	45.51 A/m^2
Cathode reference exchange current density	$i_{ex,c}$	0.12 A/m^2
Anode catalyst ionomer		25 vol.%
Cathode catalyst ionomer		25 vol.%
Anode catalyst loading		4 mg/cm^2
Cathode catalyst loading		2 mg/cm^2
Surface tension	σ	0.0625 N/m
Inlet methanol concentration	C_{in}^{MeOH}	4000 mol/m^3
Pure liquid methanol concentration	$C_{l,pure}^{MeOH}$	24719 mol/m^3
Pure liquid water concentration	$C_{l,pure}^{H_2O}$	55556 mol/m^3
Total anode transfer coefficients	α_a	0.239
Total cathode transfer coefficients	α_c	0.875
Faraday constant	F	96487 C/mol
Universal gas constant	R	8.314 J/mol K
Equivalent weight of dry membrane	EW	1.1 kg/mol
Dry membrane density	ρ_{dry}	1980 kg/m^3
Cell temperature	T_{cell}	313 K
Anode stoichiometry	ξ_a	1.4
Cathode stoichiometry	ξ_c	2.0

APPENDIX E: Derivation of Energy Equation from M^2 model

The energy conservation equation in phase a is given by,

$$\frac{\partial(\varepsilon s_\alpha \rho_\alpha h_\alpha)}{\partial t} + \nabla \cdot \left(\rho_\alpha \vec{u}_\alpha h_\alpha \right) = \nabla \cdot \left(s_\alpha k_{\alpha,\text{eff}} \nabla T \right) + S^{\text{T}} \tag{E1}$$

Summation of all phase energy equations becomes

$$\frac{\partial \left[(1-\varepsilon)\rho_s h_s + \varepsilon \sum_\alpha s_\alpha \rho_\alpha h_\alpha \right]}{\partial t} + \nabla \cdot \left(\sum_\alpha \rho_\alpha \vec{u}_\alpha h_\alpha \right) = \nabla \cdot (k_{\text{eff}} \nabla T) + S^{\text{T}}$$

Gas mixture enthalpy (ideal gas law): $h_g = \sum_k m_g^k h_{g,o}^k \approx \sum_i m_g^k c_{p,g}^k (T - T_o) = c_{p,g}(T - T_o)$

where $c_{p,g}$ is a gas mixture specific heat (i.e. $c_{p,g} = \sum_k m_g^k c_{p,g}^k$)

Liquid enthalpy (water): $h_l = c_{p,l}(T - T_o) - h_{fg}^o$ where $c_{p,l}$ is a liquid water specific heat and

h_{fg}^o denotes latent heat of water at the reference temperature, $T_o = 298.15$ K (i.e.

$h_{fg}^o = 2445$ kJ/kg).

Therefore, $h_g - h_l = h_{fg}^o + \left(c_{p,g} - c_{p,l} \right)(T - T_0)$

Using $\rho_\alpha \vec{u}_\alpha = j_\alpha + \lambda_\alpha \rho \vec{u}$, one has

$$\frac{\partial \left[(1-\varepsilon)\rho_s h_s + \varepsilon \sum_\alpha s_\alpha \rho_\alpha h_\alpha \right]}{\partial t} + \nabla \cdot \left(\sum_\alpha \left(j_\alpha + \lambda_\alpha \rho \vec{u} \right) h_\alpha \right) = \nabla \cdot (k_{\text{eff}} \nabla T) + S^{\text{T}}$$

$$\frac{\partial \left[(1-\varepsilon)\rho_s h_s + \varepsilon \sum_\alpha s_\alpha \rho_\alpha h_\alpha \right]}{\partial t} + \nabla \cdot \left(\sum_\alpha \lambda_\alpha \rho \vec{u} h_\alpha \right) = \nabla \cdot (k_{\text{eff}} \nabla T) - \nabla \cdot \left(\sum_\alpha j_\alpha h_\alpha \right) + S^{\text{T}}$$

$$\frac{\partial \left[(1-\varepsilon)\rho_s h_s + \varepsilon \sum_\alpha s_\alpha \rho_\alpha h_\alpha \right]}{\partial t} + \nabla \cdot \left(\lambda_l \rho \vec{u} h_l + (1-\lambda_l)\rho \vec{u} h_g \right) = \nabla \cdot (k_{\text{eff}} \nabla T) + \nabla \cdot \left(j_l \left(h_g - h_l \right) \right) + S^{\text{T}}$$

$$\frac{\partial\left[(1-\varepsilon)\rho_s h_s + \varepsilon\sum_\alpha s_\alpha\rho_\alpha h_\alpha\right]}{\partial t} + \nabla\cdot\left(\rho\vec{u}_{\,g} - h\lambda_1\rho\vec{u}\left(h_g - h_1\right)\right) = \nabla\cdot(k_{\text{eff}}\nabla T) + \nabla\cdot\left(j_1\left(h_g - h_1\right)\right) + S^T$$

$$\frac{\partial\left[(1-\varepsilon)\rho_s h_s + \varepsilon\sum_\alpha s_\alpha\rho_\alpha h_\alpha\right]}{\partial t} + \nabla\cdot\left(\rho\vec{u}h_g\right) = \nabla\cdot(k_{\text{eff}}\nabla T) + \nabla\cdot\left(\left(j_1 + \lambda_1\rho\vec{u}\right)\left(h_g - h_1\right)\right) + S^T$$

By plugging $h_g \approx c_{p,g}(T - T_o)$ into the advection term,

$$\frac{\partial\left[(1-\varepsilon)\rho_s h_s + \varepsilon\sum_\alpha s_\alpha\rho_\alpha h_\alpha\right]}{\partial t} + \nabla\cdot\left(\rho\vec{u}c_{p,g}T\right) - \nabla\cdot\left(\rho\vec{u}c_{p,g}T_o\right)$$
$$= \nabla\cdot(k_{\text{eff}}\nabla T) + \nabla\cdot\left(\rho_1\vec{u}_1\left(h_{fg}^o + \left(c_{p,g} - c_{p,1}\right)(T - T_0)\right)\right) + S^T$$

By assuming that $c_{p,g}T_o \approx$ const. and $h_{fg}^o \gg \left(c_{p,g} - c_{p,1}\right)(T - T_0)$

$$\frac{\partial\left[(1-\varepsilon)\rho_s h_s + \varepsilon\sum_\alpha s_\alpha\rho_\alpha h_\alpha\right]}{\partial t} + \nabla\cdot\left(\rho\vec{u}_{\,p,g}T\right) - c_{p,g}T_o\nabla\cdot\left(\rho\vec{u}\right) = \nabla\cdot(k_{\text{eff}}\nabla T) + \nabla\cdot\left(h_{fg}^o\rho_1\vec{u}_1\right) + S^T$$

From the continuity equation (i.e. $\nabla\cdot\left(\rho\vec{u}\right) = 0$)

$$\frac{\partial\left[(1-\varepsilon)\rho_s h_s + \varepsilon\sum_\alpha s_\alpha\rho_\alpha h_\alpha\right]}{\partial t} + \nabla\cdot\left(\rho\vec{u}c_{p,g}T\right) = \nabla\cdot(k_{\text{eff}}\nabla T) + \nabla\cdot\left(h_{fg}^o\rho_1\vec{u}_1\right) + S^T \qquad \text{(E2)}$$

Implementation of the source term, $\nabla\cdot\left(h_{fg}^o\rho_1\vec{u}_1\right)$, is described here briefly.

Using $\rho_1\vec{u}_1 = j_1 + \lambda_1\rho\vec{u}$, $\rho\vec{u} = -\dfrac{K}{\nu}\nabla p$, and $j_1 = \dfrac{\lambda_1\lambda_g\sigma\cos\left(\theta_c\right)}{\upsilon}\left(K\varepsilon\right)^{1/2}\dfrac{dJ}{ds}\nabla s$, one has

$$\nabla\cdot\left(h_{fg}^o\rho_1\vec{u}_1\right) = \nabla\cdot\left[h_{fg}^o\left(j_1 + \lambda_1\rho\vec{u}\right)\right]$$

$$= \nabla\cdot\left(h_{fg}^o\frac{\lambda_1\lambda_g\sigma\cos\left(\theta_c\right)}{\upsilon}\left(K\varepsilon\right)^{1/2}\frac{dJ}{ds}\nabla s - h_{fg}^o\lambda_1\frac{K}{\nu}\nabla p\right) \qquad \text{(E3)}$$

VITA

Seung Hun Jung

Seung Hun Jung was born on February 29th, 1976 to Mr. Hwa-Sung Jung and Mrs. Deok-Chi Kim at Gwang-ju, Korea. He attended Seoul National University, Seoul, Korea, earning his Bachelor of Science degree in February 2001 and Master of Science degree in February 2006. He then entered the United States to proceed with his Ph.D. study in Mechanical Engineering at the Pennsylvania State University in September 2006. He has since been working in the area of computational modeling of electrochemical systems such as batteries and fuel cells.